UNIVERSIDAD DE GRANADA

Programa de Doctorado en Ciencias de la Tierra

Interaction between serpentinites and ore-forming fluids in the Bou Azzer mining district: clues to understand the genesis of Co-Ni ores.

Tesis doctoral presentada por:

Zaineb HAJJAR

Director de Tesis

Fernando GERVILLA LINARES

Editor: Universidad de Granada. Tesis Doctorales
Autor: Zaineb Hajjar
ISBN: 978-84-1117-658-3
URI: https://hdl.handle.net/10481/79677

My Lord, expand for me my breast [with assurance], and ease for me my task, and untie the knot from my tongue, that they may understand my speech.

Acknowledgments / Agradecimientos

I don't know exactly, is it a coincidence or a destiny? My family name is HAJJAR and I am a Geologist. This name comes from the profession of my great-grandfather who worked as a "hajjar" at the time (He prepared the rocks for the construction of houses). And today, I am a geologist. Although the angle of vision is different but my last name and function revolve around the rock. Thank you, Grandfather, for this surname.

After obtaining my first doctoral thesis in Morocco, I decided to embark on a new adventure far from the borders of my mother country, encouraged by my mother (may her soul rest in peace). That is why I dedicate this thesis to her.

Over the past four (almost five) years, I have met many people that made possible the development of this Ph.D. thesis. In the following lines, I would like to express my gratitude to everyone who has accompanied me along the way.

First of all, I would like to thank my thesis supervisor, *Fernando Gervilla*, for this opportunity and all the dedication and guidance he has provided me throughout this journey. Thank you very much Fernando for always being there, making things so easy and always coping with work "without pressure". Thanks to you I was able to learn a lot both scientifically and personally during these years.

This adventure began in November 2016, during a field mission with the deceased *Ignacio Subias* and *Isabel Fanlo* in the framework of the Spanish project RTI2018-099157-A-100 granted by the “Ministerio de Ciencia, Innovación y Universidades”. Therefore, I would like to thank researcher who helped from the beginning and with whom I collaborated during the thesis. Many thanks to Isabel Fanlo, José-Maria González-Jiménez, and K. Billström.

The survey was carried out thanks to many people from three research centres: (1) the Centers Científics i Teconològics de la Universitat de Barcelona (CCiTUB), I am particularly indebted to *Xavier Llovet* for his help and dedication during the EMPA sessions to analyze arsenide minerals. (2) the Universidad de Granada, I would like to thank *Jesús Montes* from the thin section laboratory, *Isabel* for her assistance during the SEM sessions, and *Miguel*

Ángel Hidalgo for the assistance during the EMPA sessions, and (3) the Servicio General de Apoyo a la Investigación-SAI, Universidad de Zaragoza.

This project would not have been possible without the organized fieldwork towards the Bou Azzer district. For this reason, I would like to thanks the CTT-mine geological survey represented by *Abdelhak Karfal* and *Youness Moundi,* and the Bou Azzer Exploration survey represented by *Said Ilmen*.

Por último, quiero dar mis gracias a mi familia que me ha suportado y apoyado durante esta aventura; mi padre, mis dos hermanas. Sin olvidar mis amigos y colegas.

Table of contents

Chapter I: General Introduction ---------- 1

1 Introduction ---------- 1

2 Justification for the research and aims ---------- 8

3 Sampling and Analytical methods ---------- 10

Chapter II: Formation of serpentinite-hosted, Fe-rich arsenide ores at the latest stage of mineralization of the Bou-Azzer mining district (Morocco) ---------- 11

Abstract ---------- 12

1 Introduction ---------- 13

2 Geology ---------- 15

3 Samples and analytical methods ---------- 18

4 The arsenide ore lenses ---------- 20

4.1 Petrography ---------- 20
4.2 Mineral chemistry of arsenides ---------- 24
4.3 Mineral chemistry of Chromite ---------- 26
4.4 Whole rock analyses ---------- 28

5 Discussion ---------- 33

5.1 Serpentinite-hosted versus contact ores at Bou Azzer ---------- 33
5.2 Mechanisms of ore formation: vein filling versus replacement ---------- 35
5.3 Sources for major ore-forming metals ---------- 38

6 Conclusions ---------- 40

Declaration of Competing Interest ---------- 42

Acknowledgements ---------- 42

Appendix 1. Supplementary data ---------- 42

References ---------- 42

Chapter III: Cr-spinel tracks genesis of Co-Fe ores by serpentinite replacement at Bou Azzer, Morocco 47

Abstract ---------- 48

1. Introduction ---------- 49

2. Geology ---------- 51

3. Serpentinite-hosted arsenide ores ---------- 53

4. Samples and methods ---------- 55

5. Cr-spinels in the Co-Fe ores and hosting serpentinites ---------- 56

5.1. Textural types ---- 56
5.2. Mineral chemistry ---- 59

6. Discussion ---- *68*
6.1. Pre-ore Cr-spinel ---- 68
6.2. Cr-spinel dissolution and serpentinite replacement during ore precipitation ---- 69

7. Conclusion ---- *71*

Declaration of competing interest ---- *72*

Acknowledgement ---- *72*

References ---- *73*

Chapter IV: Isotopic constraints on the age and source of ore forming fluids of the Bou Azzer arsenide ores (Morocco) ---- 79

Abstract ---- *80*

1 Introduction ---- *81*

2 Geology and ore deposits of the Bou Azzer district ---- *81*

3 Sampling and analytical techniques ---- *87*

4 Results ---- *92*
4.1 Pb isotopes: ---- 92
4.2 Sr isotopes: ---- 95
4.3 Nd isotopes: ---- 96
4.4 S isotopes: ---- 101
4.5 Geochemistry of rocks ---- 107

5 Discussion ---- *107*
1.1. Lead isotope constraints on the ore-forming conditions ---- 108
1.2. Source(s) of lead in ore fluids ---- 111
1.3. Sources of Sr, Nd ore components ---- 113
1.4. Source (s) of sulphur in ore fluids ---- 116
1.5. Crustal assimilation of ophiolite-forming magmas ---- 118
1.6. Ore-forming model ---- 120

6 Conclusions ---- *123*

Declaration of Competing Interest ---- *123*

Acknowledgements ---- *124*

References ---- *124*

Chapter V: Concluding remarks ---- 128

1 Pre-arsenide ores processes? ---- *129*

2 Sources of ore-forming fluids ---- *131*

3 Source of ore forming metals ---- *134*

4 Mechanisms of ore formation: Vein filling versus replacement ---- *136*

5 Ore forming model ---- *138*

References ---- 140

Appendix ---- 147

List of figures

Chapter I

Fig. I. 1: (A). Simplified geological map of the Anti-Atlas belt (Gasquet et al., 2008). (B). Geological map of Bou Azzer inlier (Central Anti Atlas, Morocco) (modified from El Hadi et al., 2010; Soulaimani et al., 2018), showing the studied Co-Fe deposits in the district. (C) Two-arc hypothesis of the Cryogenian evolution of the Anti-Atlas Pan-African belt (after Admou et al., 2013; Soulaimani and Hefferan, 2017)..... 2
Fig. I. 2: Simplified 3D sketch of mineralised ore-types from Bou Azzer district (modified after Tourneur et al., 2021). 3
Fig. I. 3 : Idealized paragenetic sequence for polymetallic Bou Azzer Co–As–Fe–Ni (±Ag ± Au) district (modified after Bouabdellah et al., 2016). 5
Fig. I. 4: Representative diagram of the dated minerals from stage I (bluish green), stage II (Red) and stage III (blue) of the Bou Azzer district..... 7

Chapter II

Fig. II. 1. (A). Simplified geological map of the Anti-Atlas belt. (B). Geological map of Bou Azzer inlier (Central Anti Atlas, Morocco) (modified from El Hadi et al., 2010), showing the main Co-Ni deposit in the district. 16
Fig. II. 2. Geological map of Ait Ahmane area (modified from Saquaque, 1992), showing the position of Fe-Co ores. 18
Fig. II. 3. Geological map of F55 and F56 lenses (Ait Ahmane area, Bou Azzer, Anti- Atlas); internal report of CTT mine Bou Azzer). 19
Fig. II. 4. (a). Field observation of the main F55 lens in the Ait Ahmane district. (b to e). Microphotographs of rocks hosted F55 ores observed by LPA. (b). serpentinite rock composed mainly by serpentine (srp). (c & d). calcite (Cal) filling of irregular veinlets affecting serpentine (srp) and talc minerals (tlc). (e). fibrous texture of talc (tlc), containing scattered small magnetite crystals. 22
Fig. II. 5. Microphotographs of ore minerals from F55 and F56 ores. (a). Chromite (Chr) replaced by löllingite (Lo). (b & c). löllingite rosettes (Lo) grains containing Co-Ni richdiarsenides bands (Rm-Sf-Lo) and Bi inclusion (Bi); scattered in calcite in disseminated ores from F55 lens. (d & e). aggregates of spindle-shaped, zoned crystals of löllingite-safflorite included in calcite (F56 lens). (e) is zoom of (d) (f). map of chromite (Chr) altered into Fe-Cr- rich hydroxides (hdr); scattered in chlorite (Chl). 23
Fig. II. 6. X-ray chemical distribution maps of Fe, Co, and Ni for two characteristic zoned löllingite rosettes from F55 ores (a. b. c) and F56 ores (d. e. f) (Ait Ahmane area, Bou Azzer district)..... 24
Fig. II. 7. (a). Plot of diarsenides composition from F55 and F56 ores from Ait Ahmane area in the system $CoAs_2$–$NiAs_2$–$FeAs_2$. (b). Plot of skutterudite composition from F56 ores from Ait Ahmane area in the system $CoAs_3$–$NiAs_3$–$FeAs_3$. The compositional fields of di- and tri-arsenides analyzed by others authors from ores of the Ait Ahmane Area (Bou Azzer district; (En-Naciri, 995; El Ghorfi, 2006; Lasobras, 2012)) are also shown for comparison. 25
Fig. II. 8. Compositional variations in terms of Cr–Fe^{3+}–Al of accessory chromite grains associated to Fe-arsenide ores in F55 lens from Ait Ahmane area. The omposition of chromite analyzed by others authors from Bou Azzer (peridotite mantle: Ahmed et al., (2005), serpentinite from Ait Ahmane area: Hodel et al., (2017); Ait Ahmane ores hosted in serpentinite: Fanlo et al., (2015); F7/5 deposit: Ares, (2018)) are also shown for comparison..... 27
Fig. II. 9. Primitive mantle-normalized As-Co-Ni-Fe spidergrams of ores from Ait Ahmane area (F56, F55 ores, and its host rocks), F7/5 and Aghbar deposits (Bou Azzer district, Morocco). Normalizing values are taken from Lyubetskaya and Korenaga, (2007). 29
Fig. II. 10. As-Co, As-Ni, and As-Fe diagrams of ores from Ait Ahmane area (F55 and F56), F7/5 and Aghbar deposits (Bou Azzer district, Morocco). 32

Fig. II. 11. Chondrite-normalized PGE spidergrams of ores from Ait Ahmane area (F56, F55 ores, and its host rocks), F7/5 and Aghbar deposit (Bou Azzer district, Morocco). Normalizing values are taken from Naldrett and Duke (1980)..... 32
Fig. II. 12. Schematic bloc diagram of ores zoning in the serpentinite hosted ores (F55 lens, A), and in contact-type ores (B)..... 37

Chapter III

Fig. III. 1. (A). Simplified geological map of the Anti-Atlas belt (Gasquet et al., 2008). (B). Geological map of Bou Azzer inlier (Central Anti Atlas, Morocco) (modified from El Hadi et al., 2010; Soulaimani et al., 2018), showing the studied Co-Fe deposit in the district. 52
Fig. III. 2. A: Panoramic view of F55 orebody (Ait Ahmane area) hosted in serpentinite. B: western edge of F55 orebody, composed by disseminated Fe arsenide ores. C: massive Fe arsenide ores from central part of F55 orebody. D: Panoramic view of F7/5 orebody in the contact with quartz diorite. F7/5 orebody correspond formed by Co-Ni rich carbonated serpentinite. 54
Fig. III. 3. Back scattered electron image of the different textural types of zoned Cr-spinel. a. Type 1A Cr-spinel crystal from talc rich serpentinite (F55 deposit). b. Type 1A Cr-spinel crystal associated to calcite from carbonated serpentinite (F55 deposit). c. Zoned Cr-crystal from F7/5 deposit with porrous homogenous core (Chr) evelving into a porrous rims constitued by Fe-Cr hydrxide (Hydrox); associated to calcite (Cal) and lollingite (Lo) with minor chlorite (Chl). d. e. Type 1B Cr-spinel crystals with porous core composed by Fe-Cr hydroxide, associatd to a chlroite (Chl) rich calcite matrix (Cal) (F55 deposit). f. Type 1B Cr-spinel crystals composed by Fe-Cr hydroxides core surrounded by ferrian chromite (Fe-Chr), partially replaced by lollingite (Lo)..... 57
Fig. III. 4. Back scattered electron image of Cr-spinel. a. Type 1B Cr-spinel crystals composed by Fe-Cr hydroxides core surrounded by ferrian chromite (Fe-Chr), partially replaced by lollingite (Lo).. b. Type 1B Cr-spinel with porrous core composed by Cr-Fe hydroxide surrinded by Ferrian chromite (Fe-Chr) associated to lollingite (Lo). c. Ferrian chromite (Fe-Chr) (Type 2) included in calcite (Cal) and chlorite (Chl), being replaced by löllingite (Lo) (F7/5 deposit). d. Type 2 Cr-spnel corresponding to Ferrian chromite (Fe-Chr) included in calcite (Cal) with minor chlorite (Chl), associated to löllingite (Lo) (F55 deposit). e. f. Type 3: disolved Cr-spinel (Fe-chr) with Fe-Cr hydroxide relics (Hydrox) associatd to calcite (Cal). 58
Fig. III. 5. Distribution of Cr# [=Cr/(Cr+Al)], Mg# [=Mg/(Mg=Fe^{2+})], and Fe^{3+}# [=Fe^{3+}/(Fe^{3+}+Cr+Al)] values in Cr-spinel grains associated to Co-Fe arsenide ores in F7/5 and F55 deposit (Bou Azzer district). Dark colors correspond to core composition, while ligh colors correspond to rim composition. The composition of Cr-spinel analyzed by others authors from Bou Azzer (peridotite mantle: Ahmed et al. (2005), serpentinite from Ait Ahmane area: Hodel et al. (2017). Serpentinite and ore assemblages from Aghbar, Tamdrost and Ait Ahmane: Fanlo et al., (2015)). 61
Fig. III. 6. Compositional variations in terms of Cr–Fe^{3+} –Al of Cr-spinel grains (A.B.C.D) and Cr-Fe-hydroxide (E) in F55 and F7/5 deposit. A. Type 1A Cr-spinel with homogenous core. B. Type 1B Cr-spinel with porous core. C. Type 2 homogenous Cr-spinel. D. Type 3 dissolved Cr-spinel. The composition of Cr-spinel analyzed by others authors from Bou Azzer (peridotite mantle: Ahmed et al. (2005), serpentinite from Ait Ahmane area: Hodel et al. (2017). Serpentinite and ore assemblages from Aghbar, Tamdrost and Ait Ahmane: Fanlo et al., (2015)). 65
Fig. III. 7. Distribution of traces elements (MnO, ZnO, CoO, NiO, TiO_2, V_2O_3) in Cr-spinel grains associated to Co-Fe arsenide ores in F7/5 and F55 deposit (Bou Azzer district). 66
Fig. III. 8. X-ray chemical distribution maps of Fe, Cr, Ca, Mn, and Zn for Type 1B zoned Cr-spinel (A,B) and Type 3 partially dissolved Cr-Fe hydroxide (C, D) from F55 deposit (Ait Ahmane area, Bou Azzer district). ... 67
Fig. III. 9. Schematic diagram of ores zoning in the serpentinite hosted ores, showing the distribution of different Cr-spinel texture over this cross section. 70

Chapter IV

Fig. IV. 1. (A). Simplified geological map of the Anti-Atlas belt. (B). Geological map of Bou Azzer inlier (Central Anti Atlas, Morocco) (modified from Soulaimani et al., 2018), showing the main Co-Ni deposit in the district 84
Fig. IV. 2. Paragenetic sequence of arsenide ores from Bou Azzer district. Nc: nickeline, Kru/Rmb: krutovite/rammelsbergite, Sk: skutterudite, R_mS_f: crystals of rammelsbergite-safflorite solid solution, $R_mS_fL_o$: crystals of rammelsbergite- safflorite-Löllingite solid solution, S_fL_o: crystals of safflorite-löllingite solid so- lution, Gdf: gersdorffite, CG: crystals of cobaltite-gersdorffite solid solution, Cbt: cobaltite, Sfl: safflorite, Lol: löllingite, Alo: alloclasite, Apy: arsenopyrite, Mlb: molybdenite, Py: pyrite, Cpy: chalcopyrite, Bn: bornite, Gn: galena, Rgr: realgar. 85

Fig. IV. 3. (A) Geological map of Aghbar deposit (modified after Leblanc, 1981). (B) Geological map of Tamdrost deposit (modified after Leblanc, 1981). (c) Geological map of Aït-Ahmane area (modified from Saquaque et al., 1992), showing the location of the differente ore deposits. 89
Fig. IV. 4. Reflected-light photomicrographs (A-D) and Back Scattered electron images (E-F) showing representative mineralogy of the studied ore deposits from Bou Azzer arsenide ores (Morocco). (A) Massive rammelsbergite exhibiting anisotropic colors with lamellae and inversion-induced polysynthetic twins; the crack in the middle of the masse is filled by millerite; #670a, Aghbar. (B) Euhedral crystals of skutterudite III, including small chromian spinel grains, scattered in serpentinite; #728, Aghbar. (C) Rammelsgergite-Safflorite solid-solution crystals with plumose textures; #1643–3, Tamdrost. (D) Idiomorphic crystals of alloclasite; #2449 Aït-Ahmane. (E) Crystals of arsenian- gersdorffite showing oscillatory replacement-induced zoning, very fine in scale along crystallographic directions; #759a, Filon7/5. (F) Rhythmic compositional zoning in löllingite–safflorite solid-solution crystals; #724, Aghbar. Abbreviations: Ram: rammelsbergite; Mlr: millerite; Sk III: skut- terudite from stage III; Chr: chromian spinel; Srp: serpentinite; R_mS_f: rammelsbergite-safflorite solid-solution series; Alo: alloclasite; Gdf: gersdorffite; S_fL_o: safflorite- löllingite solid-solution series..... 90
Fig. IV. 5. Lead isotopic compositions of ore phases from three deposits in the Bou Azzer area. A) a $^{207}Pb/^{204}Pb$ versus $^{206}Pb/^{204}Pb$ plot. The inset shows the full range of obtained compositions. Added is a reference line with a slope corresponding to the preferred ore formation age (350 Ma); B) a $^{208}Pb/^{204}Pb$ versus $^{206}Pb/^{204}Pb$ plot. The hatched line is likely depicting a potential syn-ore mixing effect, whereas the flat line illustrates the effect of an in-situ effect controlled by U-rich and Th- poor inclusions. 93
Fig. IV. 6. Lead isotopic compositions of selected whole rocks, occurring at distal positions from known ore occurrences, in the Bou Azzer area. The encircled areas in diagrams approximate the isotopic signature of the ophiolite magma ($^{206}Pb/^{204}Pb$ = 18, $^{207}Pb/^{204}Pb$ = 15.6 and $^{208}Pb/^{204}Pb$ = 38), and this composition is also used as a starting point of a line connecting samples with an ophiolitic chemistry. A) a $^{207}Pb/^{204}Pb$ versus $^{206}Pb/^{204}Pb$ plot. The steep dotted line in the inset aligns three samples (T-pegm, Tak-2a and T-ORGN) that might exemplify isolated remnants of a Proterozoic basement, whereas the hatched line in the main diagram is drawn to connect rocks with an ophiolitic chemistry; B) a $^{208}Pb/^{204}Pb$ versus $^{206}Pb/^{204}Pb$ plot..... 94
Fig. IV. 7. A Sm-Nd isotope plot of selected whole rocks and ore minerals from the Bou Azzer area. Rocks of the ophiolite suite have a common age of ca. 658 Ma, and this age is also indicated by the slope of an added reference line that crudely connects some rocks of this suite. 96
Fig. IV. 8. Frecuency histogram showing S isotope compositions of ore phases and associated whole rocks. Arsenide data (this study) are shown in dark blue, black, green, orange and red colors, and epithermal sulphides (Levresse, 2001; Dolansky, 2007, Maacha et al., 2015) in light blue, gray and green colors..... 102
Fig. IV. 9. A $^{207}Pb/^{204}Pb$ versus $^{206}Pb/^{204}Pb$ plot showing values representing the situation at the time of the inferred ore formation at t = 350 Ma. Ore mineral data correspond to the present-day ratios (cf. Table IV. 1), whereas rock data are re- calculated to t = 350 Ma. The indicated ore signature defined by the least radiogenic ore data (encircled area) overlaps with the least radiogenic values of rocks of the ophiolite suite, and there are also other rock types sharing this isotopic signature. Part of the Stacey-Kramers (1975) two-stage curve is added as a reference. 112
Fig. IV. 10. An epsilon-Nd versus Sr plot based on rock data calculated at the time of the inferred ore formation (350 Ma). Available mineral data do not allow the Nd isotope character of the ore-forming solutions to be constrained, however, its Sr isotopic signature is indicated (grayish field). Added is also the Sr isotope composition of Carboniferous carbonate rocks (vertical stippled line). 114
Fig. IV. 11. A $^{207}Pb/^{204}Pb$ versus $^{206}Pb/^{204}Pb$ plot representing the situation at the time of ophiolite formation (at 658 Ma), with a complementary inset covering the more extreme isotopic compositions. The range of values for rocks of the ophiolite suite may indicate a variable contamination of the ophiolite magma (cf. the dotted line). Symbols M and UC stand for the approximative Pb isotope composition at t = 658 Ma of the mantle and upper crust, respectively. To illustrate the possible role of deep-seated (basement?) and more surficial contamination (dolomite?) of the ophiolite -forming magma, calculated isotope values of other rock types (at 658 Ma) are also shown. However, the latter are uncertain given that certain rocks are believed to be younger than 658 Ma..... 119

Chapter V

Fig. V. 1. (A) A 207Pb/204Pb versus 206Pb/204Pb plot showing values representing the situation at the time of the inferred ore formation at t = 350 Ma. Ore mineral data correspond to the present-day ratios (cf. Table IV. 1), whereas rock data are recalculated to t = 350 Ma. The indicated ore signature defined by the least radiogenic ore data (encircled area) overlaps with the least radiogenic values of rocks of the ophiolite suite, and there are also other rock types sharing this isotopic signature. Part of the Stacey and Kramers (1975) two-stage curve is added as a reference. (B) An epsilon-Nd versus Sr plot based on rock data calculated at the time of the inferred ore formation (350 Ma). Available mineral data do not allow the Nd isotope character of the ore-forming solutions to

be constrained, however, its Sr isotopic signature is indicated (grays field). Added is also the Sr isotope composition of Carboniferous carbonate rocks (vertical stippled line). 133
Fig. V. 2. Schematic diagram of ores zoning in the serpentinite hosted ores, showing the distribution of different Cr-spinel texture over this cross section. 137
Fig. V. 3. Schematic bloc diagram of ores zoning in the serpentinite hosted ores (F55 lens, A), and in contact-type ores (B). 139

Abstract

Discovered for the first time randomly by a French geologist in 1929, The Bou Azzer district (Central Anti-Atlas, Morocco) become the only world producer of Co from primary, hydrothermal Co arsenide ores. Co-Ni -Fe orebodies in the Bou Azzer occurs in strong association with serpentinite (cryogenian time). They occur as (1) contact-type ore mainly distributed along the contact between serpentinite and adjacent cryogenian or ediacaran rocks (quartz diorite, gabbro, volcano-sedimentary rocks); (2) crosscutting ores consisting of N-S to NE-SW veins, cross-cutting the different lithologies (serpentinite, quartz diorite, gabbro and younger volcanic rocks), or (3) serpentinite-hosted ores consisting of flat lenses striking N120E. Ore establishment in contact-type and serpentinite-hosted type was accompanied by the development of an alteration halo. Multiple stages of ore formation were established including a pre-ore stage characterized by the presence of gold mainly associated to chlorite and quartz, a main arsenide stage and a late, post-ore, epithermal stage characterized by the precipitation sulfides associated to quartz and calcite. The main arsenide stage can be subdivided into three substages: (1) Ni-rich, Co ores (i.e., stage IIa) made up of nickeline, rammelsbergite, Ni-rich skutterudite, members of the rammelsbergite-safflorite – löllingite solid solution series and sulfarsenides (gersdorffite and minor cobaltite); (2) Co-Fe ores (i.e., stage IIb) consisting of Co-rich skutterudite, Co-Ni-Fe diarsenides deeply evolving from Co– and Ni-rich compositions to the löllingite corner of the rammelsbergite-safflorite-löllingite ternary system, members of the safflorite-löllingite solid solution series and cobaltite; and (3) Fe-Co ores (i.e., stage IIc) composed of a third generation of skutterudite, safflorite, löllingite, cobaltite, alloclasite, arsenopyrite and molybdenite. The ore assemblagre of this late substage further characterize the serpentinite-hosted ores (e.g., F56) as well as the distal, disseminated ores of some contact-type deposits (e.g., F7/5, Aghbar). Nevertheless, the ore assemblage of the studied serpentinite-hosted deposit (F55 orebody) is quite simple since it only consists of of löllingite with minor Ni and Co.

Cr-spinel occurs as a minor mineral associated to Fe-Co arsenides. Four textural relationships of Cr-spinel were recorded in the studied serpentinite-hosted ores: (1) zoned Cr-spinel consisting of a homogenous core rich in Cr- and Fe^{2+} surrounded by ferrian chromite

rims (i.e., Type 1A), which are usually found in carbonatized and talc-rich serpeninite and disseminated arsenide ore; (2) zoned Cr-spinel with porous cores of Cr-Fe hydroxides rimmed by ferrian chromite (i.e., Type 1B) identified in disseminated arsenide ores; (3) homogenous Cr-spinel (i.e., Type 2) corresponding to ferrian chromite hosted in löllingite and, at a lesser extent in calcite, from massive and disseminated arsenide ores, and partly dissolved Cr-spinel (i.e., Type 3), mainly consisting of ferrian chromite, commonly with Cr-Fe hydroxide, associated to chlorite, identified in highly carbonated serpentinites hosting disseminated arsenide ores.

Co-Ni-Fe arsenide ores post-date the regional Neoproterozoic rocks from the Bou Azzer inlier. This fact was justified by field relations and geochronological dating. Pb, S, Rb/Sr, Sm/Nd isotopes analysis of arsenide and sulfarsenide minerals from five ore deposits (Filon 7/5, Aghbar, Tamdrost, Ightem and Aït- Ahmane) and some whole-rock regional samples show that ores formed during multi-episodic hydrothermal events connected with Hercynian reactivation of Devonian-Carboniferous faults. These isotope data indicate that serpentine-related ophiolite acted as the main source of ore-forming elements, coupled with a number of isotopically different lithologies both from the inferred basement and the volcanic and sedimentary cover.

High-temperature ore-forming fluids infiltrated serpentinite from where they leached Co, Ni and Fe. These high temperature (>400 °C) slightly alkaline, oxidized and $CaCl_2$-rich fluids were channelized through faults separating serpentinite and quartz diorite (and locally gabbro and volcano-sedimentary rocks), where they deposited Ni- and Ni-Co-rich ores in these fault-related open spaces (contact-type ores). During the deposition of minerals, fluids became depleted in Ni, and infiltrated serpentinite (far away from the contact serpentinite/adjacent rocks) progressively by intergranular percolation, promoting dissolution of the infiltrated serpentinite and precipitation of Co-Fe ores. Further circulation of Ni-poor forming fluids through intraserpentinite weak fault zones tended to form serpentinite-hosted ores. These fluids evolved at low temperature (≤200ºC), increasing fO_2 (CO_2 and CO_3^{2-} increased over HCO_3^-) and producing dissolution of serpentinite coupled with precipitation of Co-Fe arsenide ores. Homogenous Cr-Fe^{2+}-rich cores from relict Cr-spinels (i.e., Type 1A) associated to disseminated arsenide ores were altered to Cr-Fe hydroxide giving rise to zoned Cr-spinel (Type 1B) under the physico-chemical conditions prevailing during precipitation of these low-temperature, serpentinite-hosted arsenide ores. On the course of Co-Fe arsenide precipitation both ferrian chromite and Cr-Fe hydroxide (i.e., Type 3) tended to be destabilized promoting

their dissolution. Only homogenous ferrian chromite grains (i.e., Type 2) included in calcite and löllingite in massive arsenide ores (and at lesser extent in disseminated ores) survived this process.

Resumen

Descubierto por primera vez de forma aleatoria por un geólogo francés en 1929, el distrito de Bou Azzer (Anti-Atlas Central, Marruecos) se ha convertido en el único productor mundial de Co a partir de minerales primarios hidrotermales de arseniuro de Co. Los yacimientos de Co-Ni-Fe de Bou Azzer se encuentran a menudo asociados a la serpentinita (de edad criogénica). Los depósitos se presentan como: (1) mineralizaciones tipo contacto, distribuidas principalmente a lo largo del contacto entre la serpentinita y las rocas criogénicas o ediacariensess adyacentes (cuarzo diorita, gabro y rocas volcanosedimentarias); (2) mineralizaciones discordantes consistentes en vetas de orientación N-S a NE-SW que atraviesan las diferentes litologías (serpentinitas, cuarzo dioritas, gabros y rocas volcanosedimentarias), y (3) mineralizaciones encajadas en serpentinitas constituidas por cuerpos lenticulares a tabulares alojados en zonas de falla intra-serpentinitas. La formación de las mineralizaciones de tipo contacto y de las encajadas en serpentinitas estuvo acompañada por el desarrollo de un halo de alteración carbonatada y/o silícea. En el proceso de formación de estos yacimientos, se han identificado varias etapas, incluyendo una etapa pre-mineralización caracterizada por la precipitación de oro asociado, principalmente a clorita y cuarzo, una etapa de mineralización principal en la que se forman las asociaciones de arseniuros de Ni y Co, y una etapa tardía, post-mineralización, de carácter epitermal, en la que se forman sulfuros asociados a cuarzo y calcita. La etapa de formación de arseniuros puede subdividirse en tres sub-etadios: (1) estadio IIa, en el que se forman arseniuros de Ni y Co, entre los que predominan niquelina, rammelsbergita, skutterudita rica en Ni, miembros de la serie de solución sólida rammelsbergita-saflorita-löllingita y, en menores proporciones sulfarseniuros de la serie de solución sólida gersdorfita-cobaltita; (2) estadio IIb, en el que se forman arseniuros de Co y Fe, principalmente skutterudita rica en Co, diarseniuros de la serie de solución sólida rammelsbergita-saflorita-löllingita (su composición evoluciona desde términos ricos en Co y Ni hasta los ricos en Fe) y de la serie saflorita-löllingita, y cobaltita, y (3) estadio IIc caracterizado por la formación de mineralizaciones de Fe-Co compuestas por una tercera generación de skutterudita, por saflorita, löllingita, cobaltita, aloclasita, arsenopirita y molibdenita. Los minerales de este último subestadio son los que caracterizan las

mineralizaciones alojadas en serpentinitas (por ejemplo, F56) y las mineralizaciones distales, de carácter diseminado de algunos yacimientos tipo contacto (por ejemplo, F7/5, Aghbar). No obstante, la asociación mineral del depósito encajado en serpentinitas estudiado (F55) es mucho más simple ya que está formada exclusivamente por löllingita con cantidades menores de Co y Ni.

La espinela cromífera es un mineral minoritario en las mineralizaciones de arseniuros de Fe-Co encajadas en las serpentinitas estudiadas. Se han identificado cuatro tipos de espinelas cromíferas con diferentes relaciones texturales: (1) espinela cromífera zonada formada por un núcleo homogéneo de espinela rica en Cr- y Fe^{2+} rodeado por bordes de ferian cromita (Tipo 1A) que se encuentra, normalmente, en la serpentinita carbonatizada rica en talco y en la mineralización de arseniuros diseminada; (2) espinela cromífera zonada con núcleos porosos compuestos por hidróxidos de Cr-Fe rodeados de ferian cromita (Tipo 1B), identificada en las mineralizaciones diseminadas de arseniuros; (3) espinela cromífera homogénea (Tipo 2) constituida solo por ferian cromita incluida en löllingita y, en menor medida en calcita, en mineralizaciones masivas y diseminadas de arseniuros de Fe, y (4) espinela cromífera parcialmente disuelta (Tipo 3) consistente principalmente en ferian cromita, a menudo con algo de hidróxido de Cr-Fe, asociada a clorita, identificada en serpentinitas altamente carbonatadas que albergan mineralizaciones diseminadas de arseniuros.

Las mineralizaciones de arseniuros de Co-Ni-Fe son posteriores a las rocas regionales neoproterozoicas del inlier de Bou Azzer. Este hecho se ha comprobado utilizando relaciones de campo y dataciones geocronológicas. Los análisis de isótopos de Pb, S, Rb/Sr, Sm/Nd de las mineralizaciones de arseniuros y sulfarseniuros de cinco yacimientos (Filon 7/5, Aghbar, Tamdrost, Ightem y Aït- Ahmane) y de algunas muestras regionales de roca total han mostrado que dichas mineralizaciones se formaron durante eventos hidrotermales multiepisódicos relacionados con la reactivación hercínica de fallas antiguas, durante el Devónico-Carbonífero. Estos datos isotópicos indican también que el complejo ofiolítico del que forman parte las serpentinas mineralizadas actuó como la principal fuente de elementos formadores de mineral, junto con una serie de litologías isotópicamente diferentes tanto del basamento inferido como de la cubierta volcánica y sedimentaria.

Los fluidos mineralizadores se infiltraron a alta temperatura en la serpentinita lixiviando Co, Ni y Fe. Estos fluidos de alta temperatura (>400 ◦C), ligeramente alcalinos, oxidados y ricos en $CaCl_2$ se canalizaron a través de las fallas que separan la serpentinita y el cuarzo diorita (localmente también los gabros y las rocas volcanosedimentarias) depositando arseniuros de Ni

y Ni-Co en los espacios abiertos generados durante el funcionamiento de las fallas (mineralizaciones de tipo contacto). En el trascurso de la precipitación de los arseniuros, los fluidos se empobrecieron progresivamente en Ni, y tendieron a infiltrarse en la serpentinita (lejos de la zona de contacto serpentinita/adyacentes) por percolación intergranular. La interacción, fluido/roca dió lugar a la disolución de la serpentinita infiltrada y a la precipitación de los arseniuros de Co y Fe. La circulación posterior de los fluidos mineralizadores empobrecidos en Ni y Co a través de zonas de falla intra-serpentinitas fueron los responsables de la formación de las mineralizaciones encajadas en serpentinitas. Estos fluidos evolucionaron a baja temperatura (≤200ºC), aumentando la fO_2 (el CO_2 y el CO_3^{2-} aumentaron por encima del HCO_3^-) y produjeron la disolución de la serpentinita acoplada a la precipitación de los arseniuros de Co y Fe. Bajo las condiciones físico-químicas predominantes durante la formación de estas mineralizaciones de baja temperatura encajadas en serpentinitas, los centros homogéneos ricos en Cr y Fe^{2+} de las espinelas cromíferas Tipo 1A asociadas a las mineralizaciones diseminadas de arseniuros se alteraron a hidróxidos de Cr-Fe, dando lugar a las espinelas zonadas Tipo 1B. En el trascurso de la precipitación de los arseniuros de Co-Fe, tanto la ferrian cromita como los hidróxidos de Cr-Fe (tipo 3) tendieron a desestabilizarse provocando su disolución. Solo los granos de ferrian cromita homogénea (Tipo 3) incluidos en calcita y löllingita en mineralizaciones masivas (y en menor medida en mineralizaciones diseminadas) de arseniuros sobrevivieron a este proceso.

Résumé

Découvert par hasard par un géologue français en 1929, le district de Bou Azzer (Anti-Atlas central, Maroc) est devenu le seul producteur mondial de Co à partir de minerais hydrothermaux primaires d'arséniure de Co. Les gisements de Co-Ni-Fe de Bou Azzer se trouvent souvent en association avec de la serpentinite (d'âge cryogénique). Les dépôts se présentent sous la forme de : (1) minéralisations de type contact, réparties principalement le long du contact entre la serpentinite et les roches cryogéniques ou édiacariens adjacentes (diorite quartzique, gabbro et roches volcano-sédimentaires) ; (2) des minéralisations discordantes constituées de veines orientées N-S à NE-SW traversant les différentes lithologies (serpentinites, diorites quartzifères, gabbros et roches volcano-sédimentaires), et (3) des minéralisations encaissées dans la serpentinite constituées de corps lenticulaires à tabulaires logés dans des zones de failles intra-serpentinites. La formation des minéralisations de type contact et des minéralisations encaissées dans la serpentinite a été accompagnée par le développement d'un halo d'altération carbonaté et/ou siliceux. Dans le processus de formation de ces gisements, plusieurs étapes ont été identifiées, dont une étape de pré-minéralisation caractérisée par la précipitation de l'or associé principalement au chlorite et au quartz, une étape de minéralisation principale dans laquelle se forment des associations d'arséniures de Ni et de Co, et une étape épithermale tardive, post-minéralisation, dans laquelle se forment des sulfures associés au quartz et à la calcite. L'étape de formation de l'arséniure peut être subdivisée en trois sous-étapes : (1) le stade IIa, au cours duquel se forment des arséniures de Ni et de Co, parmi lesquels prédominent la nickeline, la rammelsbergite, la skuttérudite riche en Ni, les membres de la série des solutions solides de rammelsbergite-safflorite-löllingite et, en plus faible proportion, les sulfarséniures de la série des solutions solides de gersdorfite-cobaltite ; (2) le stade IIb, dans lequel les arséniures de Co et de Fe, principalement la skuttérudite riche en Co, les diarséniures de la série des solutions solides de rammelsbergite-safflorite-löllingite (leur composition évolue de termes riches en Co et en Ni vers des termes riches en Fe) et de la série des safflorites-löllingites, et de cobaltite, et (3) le stade IIc caractérisé par la formation d'une minéralisation Fe-Co composée de skuttérudite de troisième génération, de safflorite, de löllingite, de cobaltite, d'alloclase, d'arsénopyrite et de molybdénite. Ce sont les minéraux de

ce dernier sous-stade qui caractérisent les minéralisations hébergées par la serpentinite (par exemple F56) et les minéralisations distales et disséminées de certains gisements de type contact (par exemple F7/5, Aghbar). Cependant, l'association minérale du gisement étudié (F55), encaissé dans la serpentinite, est beaucoup plus simple puisqu'elle se compose exclusivement de löllingite avec des quantités mineures de Co et de Ni.

Le spinelle chromifère est un minéral minoritaire dans les minéralisations d'arséniure de Fe-Co incluses dans les serpentinites étudiées. Quatre types de spinelles chromifères avec des relations texturales différentes ont été identifiés : (1) spinelle chromifère zoné formé par un noyau homogène de spinelle riche en Cr- et Fe^{2+} entouré de bordures de chromite ferrique (Type 1A) que l'on trouve généralement dans la serpentinite carbonatisée riche en talc et la minéralisation d'arséniure disséminée ; (2) spinelle chromifère zoné avec des noyaux poreux composés d'hydroxydes de Cr-Fe entourés de chromite ferrique (Type 1B), identifié dans une minéralisation d'arséniure disséminée ; (3) spinelle chromifère homogène (type 2) consistant uniquement en chromite ferrique noyé dans de la löllingite et, dans une moindre mesure, de la calcite, dans une minéralisation massive d'arséniure de fer disséminé ; et (4) spinelle chromifère partiellement dissous (type 3) consistant principalement en chromite ferrique, souvent avec un peu d'hydroxyde de Cr-Fe, associé à de la chlorite, identifié dans des serpentinites fortement carbonatées abritant une minéralisation d'arséniure disséminé.

Les minéralisations d'arséniure de Co-Ni-Fe sont postérieures aux roches néoprotérozoïques régionales de la boutonnière de Bou Azzer. Ceci a été vérifié à l'aide de relations sur le terrain et de datations géochronologiques. Des analyses isotopiques Pb, S, Rb/Sr, Sm/Nd de minéralisations d'arséniure et de sulfarséniure provenant de cinq gisements (Filon 7/5, Aghbar, Tamdrost, Ightem et Aït-Ahmane) et de quelques échantillons régionaux de roches entières ont montré que ces minéralisations se sont formées au cours d'événements hydrothermaux multi-épisodiques liés à la réactivation hercynienne d'anciennes failles au cours du Dévonien-Carbonifère. Ces données isotopiques indiquent également que le complexe ophiolitique dont font partie les serpentines minéralisées a été la principale source d'éléments minéralisateurs, ainsi qu'un certain nombre de lithologies isotopiquement différentes provenant à la fois du socle présumé et de la couverture volcanique et sédimentaire.

Les fluides minéralisateurs ont percolé à haute température dans la serpentinite, lessivant le Co, le Ni et le Fe. Ces fluides à haute température (>400 °C), légèrement alcalins, oxydés et riches en $CaCl_2$ ont été canalisés par des failles séparant les serpentinites des quartz diorites (localement aussi des gabbros et des roches volcanosédimentaires) déposant des

arséniures de Ni et de Ni-Co dans les espaces ouverts générés lors du fonctionnement des failles (minéralisations de type contact). Au cours de la précipitation des arséniures, les fluides sont devenus progressivement appauvris en Ni et ont eu tendance à s'infiltrer dans la serpentinite (loin de la zone de contact serpentinite/roche adjacent) par percolation intergranulaire. L'interaction fluide/roche a entraîné la dissolution de la serpentinite infiltrée et la précipitation d'arséniures de Co et de Fe. La circulation subséquente de fluides minéralisateurs appauvris en Ni- et Co à travers des zones de failles intra-serpentinites est à l'origine de la formation des minéralisations encaissées dans la serpentinite. Ces fluides ont évolué à basse température (≤200ºC), en augmentant la fO_2 (le CO_2 et le CO_3^{2-} ont augmenté au-dessus du HCO_3^-) et ont produit une dissolution de la serpentinite couplée à la précipitation d'arséniures de Co et de Fe. Dans les conditions physico-chimiques prévalant lors de la formation de ces minéralisations à basse température incluses dans les serpentinites, les centres homogènes riches en Cr et Fe^{2+} des spinelles chromifères de type 1A associés aux minéralisations d'arséniure disséminées ont été altérés en hydroxydes de Cr-Fe, donnant naissance aux spinelles zonées de type 1B. Au cours de la précipitation des arséniures de Co-Fe, la chromite ferrique et les hydroxydes de Cr-Fe (type 3) ont tendance à se déstabiliser et à se dissoudre. Seuls les grains de chromite ferrique homogènes (type 3) noyés dans la calcite et la löllingite dans la minéralisation d'arséniure massive (et dans une moindre mesure disséminée) ont survécu à ce processus.

Chapter I: General Introduction

1 Introduction

Cobalt production in the world mainly comes from sediment-hosted, magmatic Ni-Cu and laterite deposits (Alves Dias et al., 2018); an exception is the Bou Azzer district in central Anti Atlas (Morocco) which contributes with more than 2% to the world's cobalt production (U.S. Geological Survey, 2013). This district is the only locality in the world where Co is directly mined from primary Co-Ni arsenide and sulfoarsenide ores. It produces about 150,000 t of ore at an average grade of 1% Co and 1% Ni (Ikenne et al., 2020). In addition to Co and Ni, 3-4 g/t gold and silver are also recovered as by-products (Bouadellah et al., 2016). The Bou Azzer district was discovered for the first time in 1929 by Jean Epinat, a French industrialist, who observed several ore outcrops composed of complex assemblages including oxides, carbonates, arseniates and arsenides (Nataf, 2003). Subsequently, these ores were exploited by artisan methods until the opening of the Bou Azzer mine in 1934 (Maacha et al., 2011).

Co-Ni-Fe arsenide ores in the Bou Azzer district are spatially related to serpentinite forming part of a Neoproterozoic ophiolite complex. This ophiolite obducted during the major Pan-African deformation phase as a consequence of the collision between the West African Craton (WAC) and a hypothetic arc in the North (Leblanc, 1975, 1981; Saquaque et al., 1989; Hefferan et al., 2014; Triantafyllou et al., 2016, 2018; Soulaimani and Hefferan, 2017; Soulaimani et al., 2018; Fig. I. 1). Bou Azzer ores have been extensively studied over the last few decades, resulting in the release of abundant research papers, theses, and unpublished mining company reports, which have provided valuable information on the paragenetic sequence, phase relations, mineral geothermometry and geochronology of the different types of

ores, as well as the physicochemical characteristics of ore-forming fluids. (e.g., Leblanc, 1975; Leblanc and Billaud, 1982; En-Naciri, 1995; Essarraj et al., 2005; El Ghorfi, 2006; Dolansky, 2007; Ahmed et al. 2009a; Oberthür et al., 2009; Gervilla et al. 2012a; Lasobras, 2012; Lázaro, 2012; Maacha, 2013; Fanlo et al., 2015, 2017; Bouabdellah, et al., 2016; Ikenne et al., 2020; Tourneur et al., 2021; Souiri et al., 2021).

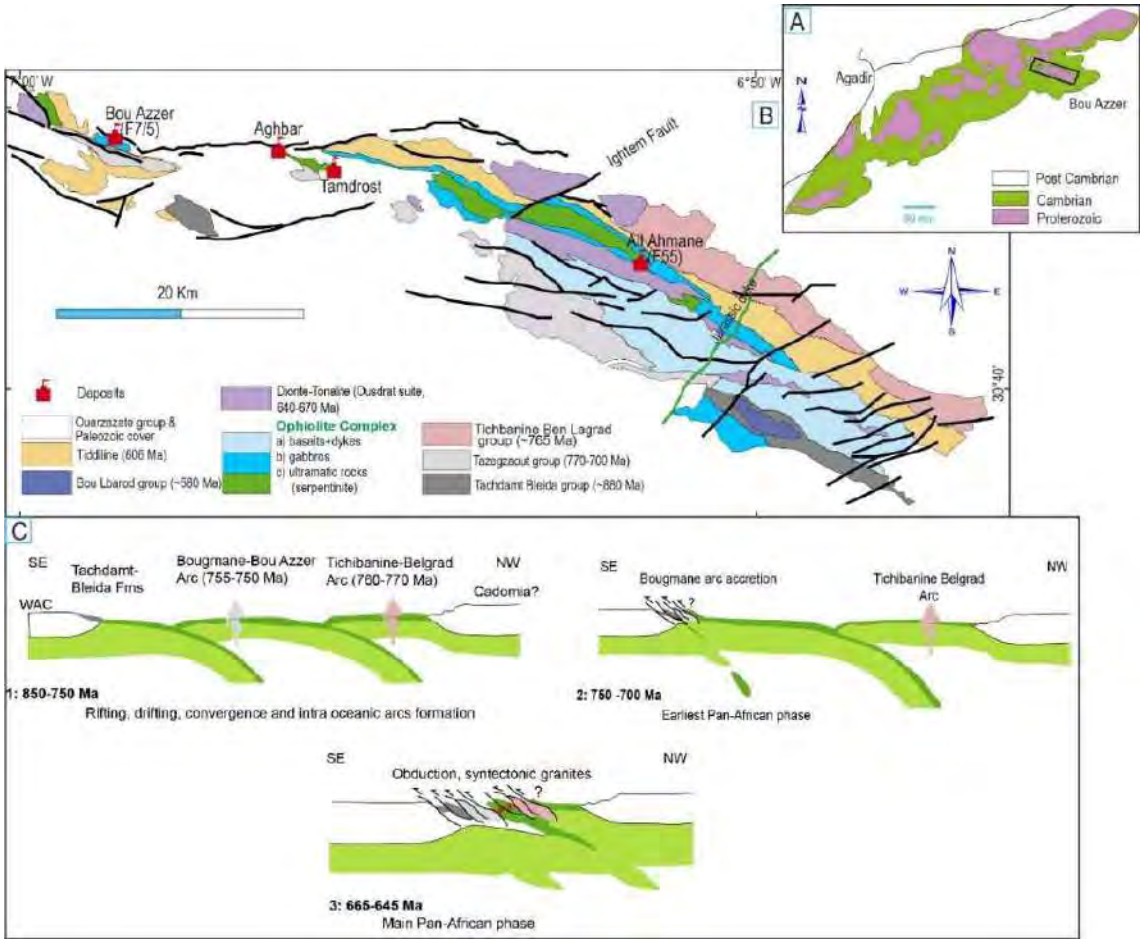

Fig. I. 1: (A). Simplified geological map of the Anti-Atlas belt (Gasquet et al., 2008). (B). Geological map of Bou Azzer inlier (Central Anti Atlas, Morocco) (modified from El Hadi et al., 2010; Soulaimani et al., 2018), showing the studied Co-Fe deposits in the district. (C) Two-arc hypothesis of the Cryogenian evolution of the Anti-Atlas Pan-African belt (after Admou et al., 2013; Soulaimani and Hefferan, 2017).

Most exploited Co-Ni arsenide orebodies in the Bou Azzer district correspond to WNW-ESE flame-shaped bodies, flat lenses and pocket-like masses located at the contacts between serpentinite bodies and quartz diorite or, locally, gabbros, younger volcanic and sedimentary rocks. Those orebodies consist mainly of elongated lenses of massive Ni-Co-Fe arsenide minerals, included in carbonate or siliceous gangue (e.g., Leblanc, 1975; Leblanc and Billaud,

1982; En-Naciri, 1995; El Ghorfi, 2006; Maacha, 2013; Tourneur et al., 2021; Fig. I. 2). This morphological type of ores was recently re-defined as "contact type ores" by Tourneur et al., (2021). Co-Ni-Fe arsenide orebodies also occur as N-S to NE-SW veins, cross-cutting the different lithologies (quartz diorite, gabbro, younger volcanic rocks); ores in these crosscutting veins are present only along segments near the contact with serpentinite and/or massive mineralization (e.g., En-Naciri, 1995; El Ghorifi, 2006; Maacha, 2013; Tourneur et al., 2021; Fig. I. 2). This second morphological type was re-defined by Tourneur et al., (2021) too as "cross-cutting ore type". The two orebody types share a rather similar mineralizing history.

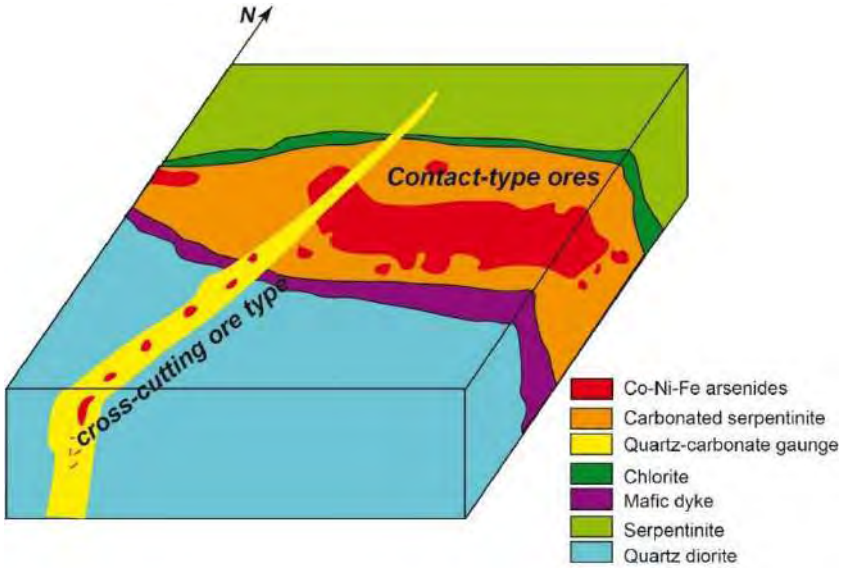

Fig. I. 2: Simplified 3D sketch of mineralised ore-types from Bou Azzer district (modified after Tourneur et al., 2021).

Regardless of the existence of multiple overlapping ore-forming hydrothermal pulses (talcification, silicification, carbonation; Souiri et al., 2021) there is a broad consensus on the existence of three main stages of mineral deposition (Maacha, 2013; Bouabdellah et al., 2016; Fig. I. 3): (1) a pre-arsenide ore (stage I) consisting of gold associated to chlorite. quartz and minor muscovite and calcite, (2) an arsenide stage (stage II) made up of mono-, di- and tri-arsenides, and sulfarsenides, and (3) an epithermal stage (post-ore stage, Stage III) characterized by the precipitation of sulfides associated to late quartz and calcite. The arsenide stage was characterized by the precipitation of Ni-arsenide minerals followed by Co-rich arsenide minerals and Fe-rich arsenide minerals (Leblanc, 1975; En-Naciri, 1995; Ahmed et al., 2009a; Gervilla et al., 2012a; Bouabdellah et al, 2016; Fanlo et, al., 2017; Ikenne et al., 2020;

Tourneur et al., 2021). The early Ni arsenide assemblage is composed of nickelite (NiAs), rammelsbergite ($NiAs_2$), Ni-rich skutterudite ($(Co,Ni)As_3$), members of the rammelsbergite($NiAs_2$)–safflorite($CoAs_2$)–löllingite($FeAs_2$) solid solution series and sulfarsenides [gersdorffite (NiAsS) and minor cobaltite((CoAsS)]. The Co-rich arsenide assemblage is made up of Co-rich skutterudite, Co-Ni-Fe diarsenides evolving from Co- and Ni-rich compositions to that of löllingite in the rammelsbergite–safflorite–löllingite ternary system, and cobaltite. The Fe-rich arsenide assemblage is composed of a third generation of skutterudite, safflorite, löllingite, cobaltite, alloclasite, arsenopyrite and molybdenite. At orebody scale, a zoning was underlined by the presence of Ni di-arsenides in core followed by Co di- and tri-arsenides, Fe di-arsenides and sulfoarsenides toward periphery (En-Naciri, 1995). This type of zoning has also been described in the Aghbar deposit by Leblanc (1975). However, Gervilla et al. (2012a) indicate that nickel ores in the Aghbar deposit mainly crystallize in veins, concentrated in narrow bands within the lode-like body whereas Co-Fe ores occur both in veins associated with calcite and dolomite and mainly replacing the host serpentinite. At district scale a West to East zoning was described by En-Naciri (1995), El Ghorfi (2006), Maacha (2013) and Ikenne et al. (2020). According to these authors, western deposits are richer in Co-arsenides (mainly Co-rich skutterudite and safflorite) than central and eastern ones, which are enriched in Ni, and Fe arsenides, mainly lollingite, nickeline, rammelsbergite, gersdorfite and Ni-Fe rich skutterudite).

Few fluids inclusion studies (En-Naciri, 1995; Dolansky, 2007) and some C, O, and H isotopic data (Dolansky, 2007; Maacha et al., 2015) are available from contact-type and crosscutting-type ores. Results suggest that ore-forming fluids correspond to complex acidic (pH<5) and saline brines (~36-51 wt. % NaCl + $CaCl_2$ eq.) composed of Na, Ca, K, Ba, Cl (En-Naciri, 1995; Dolansky, 2007; Maacha et al., 2015). Raman spectroscopy analysis show the existence of CH_4 and/or N_2 in variable proportions (En-Naciri, 1995; Lebedev et al., 1999; Maacha et al., 1998; Essarraj et al., 2005), with minor amounts of CO_2 present in some samples (Essarraj et al., 2005). En-Naciri (1995) reports fluid inclusions in pre-ore quartz and post-ore calcite containing moderate to highly saline fluids (15-22 wt% NaCl and 16.5-20.5 wt% $CaCl_2$) trapped at low temperatures (120-240ºC) under variable pressures (0.4-1.2 kb). In contrast, Dolansky (2007) shows that fluid inclusion in pre-ore quartz and post ores calcite were trapped at completely different temperature and pressure conditions, stablishing that primary fluid

inclusions in pre-ore quartz contains highly saline brines trapped at relatively high temperature and pressures (T=320-409ºC; P=1.6-2.5 kb) and that secondary fluid inclusions in pre-ore quartz (36-45 wt% NaCl and 13-26 wt.% $CaCl_2$) were trapped at temperature ranging from 164 to 290 °C and pressures from 0.88 to 1.4 kb. According to Dolansky (2007), primary fluid inclusions in post-ore calcite (15.5-19.1 wt% NaCl and 20.9-21.5 wt% $CaCl_2$) represent the ore-forming fluids of the late depositional sequence trapped at very low pressure (~ 0.65 kb) and temperature ≥200 °C.

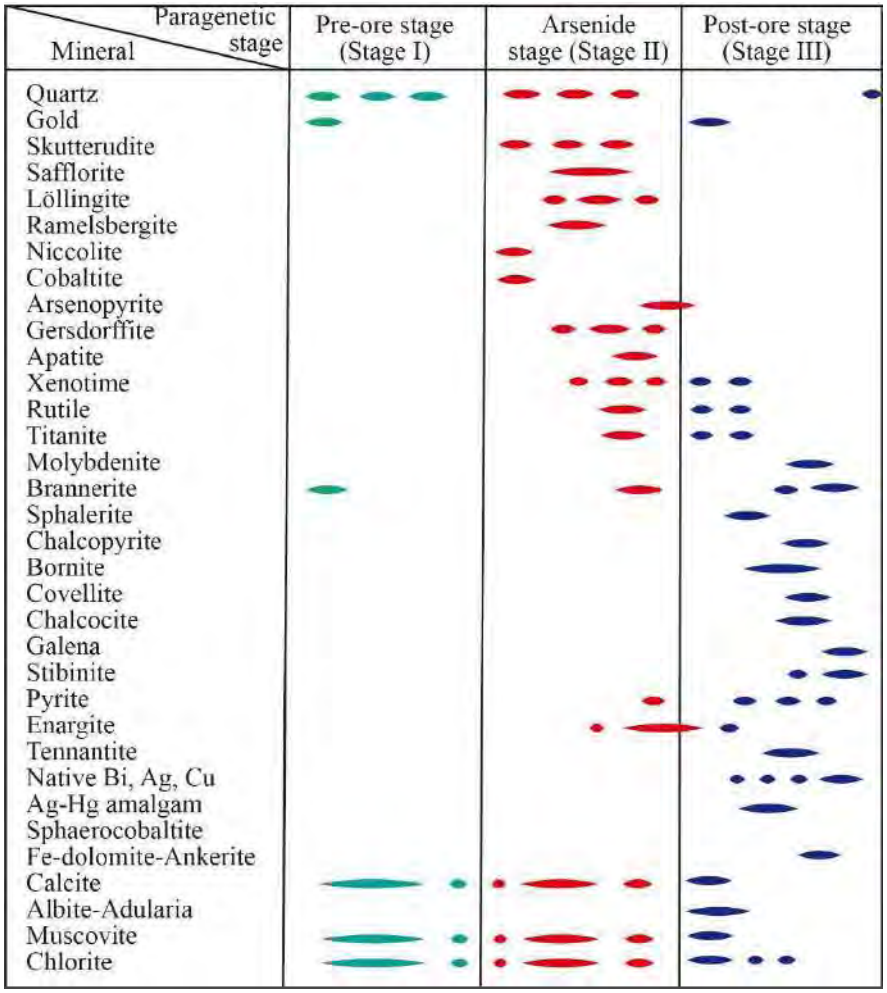

Fig. I. 3 : Idealized paragenetic sequence for polymetallic Bou Azzer Co–As–Fe–Ni (±Ag ± Au) district (modified after Bouabdellah et al., 2016).

δ ^{18}O and δ D isotopes obtained on pre-arsenide chlorite ($\delta^{18}O_{fluid}$= 9.5‰; δD_{fluid}= -42.4‰) and quartz ($\delta^{18}O_{fluid}$= 7.9 - 9.6‰; δD_{fluid}= -62 to -30‰) show that ore forming fluids possess a magmatic water signature (Dolansky, 2007). Conversely, $d^{13}C$ and $d^{18}O_{fluid}$ from

calcite (syn-arsenide stage) range respectively from -3.72 to -6.5‰ and from 14.19 to 20.91‰, comparable to $d^{13}C$ and $d^{18}O_{fluid}$ values obtained for syn-arsenide stage dolomite ($d^{13}C$= -3.72- -4.32‰; $d^{18}O_{fluid}$ =16.09- 20.69‰). These $d^{13}C$ and $d^{18}O_{fluid}$ isotopic data indicate the possible contribution of exogenic water in the formation of the associated arsenide ore (Maacha et al., 2015). No S isotope data have been obtained from sulfur-bearing minerals (e.g., sulfarsanides) from the arsenide assemblage and only few are available from sulfide minerals (galena, chalcopyrite, pyrite, barite) of the post arsenide, epithermal ore assemblage. These latter data show very scattered values ranging from $\delta^{34}S$=-32.3 to $\delta^{34}S$= 9.9‰, and are not representative of the S isotope composition of ore forming fluids (Levresse, 2001; Dolansky, 2007; Maacha et al., 2015).

Many dating methods were performed to determine age of ore formation (Ledent, 1960; En-Naciri et al., 1997; Leveresse, 2001; Gasquet et al., 2005; Dolansky, 2007; Oberthür et al., 2009; Fig. I. 4) showing that: i) mineralization must be younger than trachyte from Ouarzazate group dated between 533 and 531 Ma (Leveresse, 2001; Gasquet et al., 2005); ii) the estimate age of pre-arsenide ores obtained by $^{40}Ar/^{39}Ar$ on muscovite range from 392 to 356 Ma (Leveresse, 2001); iii) U-Pb dating on brannerite yielded a wide spectrum of ages from 550 Ma to 240 ± 10 Ma (Ledent, 1960; En-Naciri et al., 1997; Dolansky, 2007; Oberthür et al., 2009); iv) post-ore carbonate was dated at 308±31 Ma (Sm-Nd, Oberthür et al., 2009), and v) Re-Os dating of molybdenite related also to post-ore stage revealed an age of 350 – 400 Ma (Oberthür et al., 2009); vi) post-ore adularia was dated at 215 ± 8 Ma (Ar-Ar, Leveresse, 2001). The U-Pb results obtained on brannerite cover a wide range of ages since more than one generation of brannerite were analyzed. Early brannerite included in skutterudite, lacking any visible signs of alteration, was dated between 385 and 375 Ma (Dolansky, 2007), whereas brannertite crystals associated to sulfides (epithermal, post-arsenide stage) that may have originally been enclosed by skutterudite but are now associated to chlorite and molydenite partially surrounded by this tri-arsenide yield calculated ages ranging from 257 ± 8 to 32 ± 2 Ma (Dolansky, 2007). While Oberthür et al., (2009) give an age around 310 ±5 Ma for brannerite occurring in in the outer zones of skutterudite.

Most proposed ore-forming models involve mineral deposition at Devonian-Carboniferous times (e.g., Leveresse, 2001; Dolansky, 2007; Oberthür et al., 2009) involving the contribution of high saline brines with high chloride contents (Leblanc and Lbouabi, 1988;

En-Naciri, 1995; En-Naciri et al., 1995; Lebedev et al., 1999; Essarraj et al., 2005; Dolansky, 2007). Those brins interacted with serpentinite (Dolansky, 2007; Maacha, 2013; Ikenne et al., 2020) leaching out Co, Ni and As (e.g., Leblanc, 1974, 1981; Leblanc and Billaud 1982; Leblanc and Fischer, 1990; Azizi Samir et al., 1990; Maacha et al., 1998). Nevertheless, Bouabdellah et al. (2016) argued that the source of all metals and As has to be sought out of the Bou Azzer inlier, probably in the black shales of the Imiter Group.

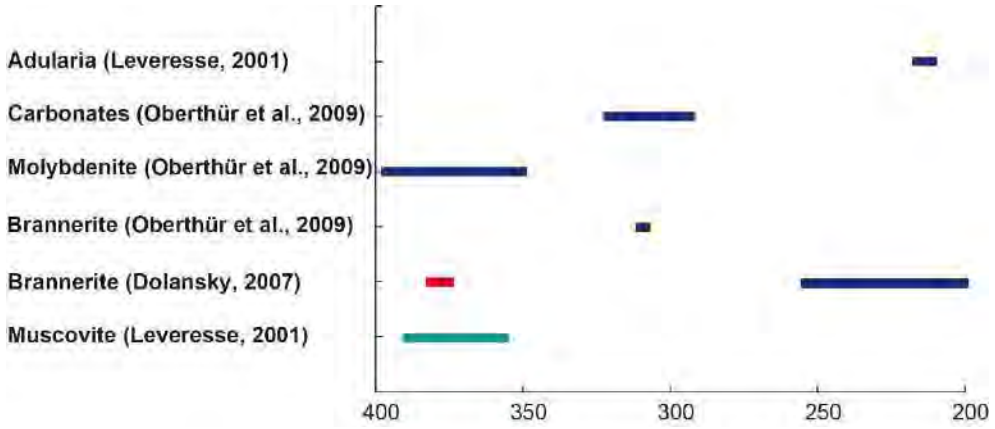

Fig. I. 4: Representative diagram of the dated minerals from stage I (bluish green), stage II (Red) and stage III (blue) of the Bou Azzer district

Maacha (2013), Bouabdellah et al. (2016) and Ikenne et al. (2020) propose that ore forming models involve mixing between As-bearing, NaCl-dominated saline brines derived probably from a felsic magmatic source and meteoric waters which became enriched in Ca and S after interaction with buried evaporite and carbonate horizons (Essarraj et al., 2005; Dolansky, 2007). So, the metals were leached from serpentinites by As-bearing, NaCl-dominated magmatic brines and transported in solution as chloride complexes (Dolansky, 2007). Ore mineral deposition occurred mainly in response to increasing pH and decreasing fO_2 of the fluids, which resulted from increased interaction with the serpentinites, and mixing between the magmatic brines and Ca- and SO_4^{2-}-enriched meteoric waters (Dolansky, 2007; Maacha, 2013; Bouabdellah et al., 2016; Ikenne et al., 2020). Tourneur et al., (2021) propose to call this type of deposits Serpentinite-Hosted Massive Arsenides (SHMA) arguing that the massive part of the deposit forms by circulation of hydrothermal fluids through a serpentinite breccia formed during a tectonic exhumation along a low angle extensional detachment. Gervilla et al. (2012a) and Fanlo et al. (2015) showed evidences of serpentinite replacement by ore-forming fluids identifying Cr-spinel (and its alteration product, ferrian chromite) as the only remnant of the

serpentinite mineral assemblage. This mineral does not change its composition during such replacement process but simply become fractured and dissolved (Fanlo et al., 2015). Both hydrothermal remobilization and serpentinite replacement, involve leaching of metals (Co, Ni, Fe) from serpentinite; thus, complete dissolution of serpentinite during replacement would supply their total amount of Co and Ni to the ore-forming fluids.

2 Justification for the research and aims

All scientific results and genetic interpretations described above have been based on data from contact-type and cross-cutting type ores. Nevertheless, internal reports and maps show the presence of arsenide ores hosted by serpentinite far away from any contact with quartz-diorite, gabbro, volcanic or sedimentary rocks. For example, F55 deposit mined by the Managem Group in the Ait Ahmane area in 2018/2019, produced raw material with up to 2.4% Co and 0.2% Ni on average. This type of ore deposits do not fit with traditional interpretations based on ore precipitation filling fault-related, open spaces created along the contacts between quartz diorite intrusions (or locally gabbros, volcanic or sedimentary rocks), and serpentinites (Leblanc, 1975; En-Naciri, 1995; El Ghorfi, 2006; Maacha, 2013; Bouabdellah, et al., 2016; Ikenne et al., 2020), but concur with the existence of Co-Ni arsennide ores formed at the expenses of serpentinite in the Aghbar deposit rather than by simple filling of open fractures Gervilla et al., (2012a). The identification of these serpentinite-hosted Co-Fe arsenide ores as well as those reported in the Aït Ahmane area (Hajjar, 2011) adds new data that could contribute to complete or modify the existing ore-forming models (Maacha, 2013; Bouabdellah et al., 2016; Ikenne et al., 2020; Tourneur et al. 2021).

Serpentinite replacement by ore-forming fluids can be tracked by the morphological and chemical changes suffered by accessory Cr-spinel grains remaining in the arsenide ore assemblage and in the altered host. Previous studies (Gervilla et al., 2012b; Fanlo et al. 2015) showed that Cr-spinel scattered in arsenide ores exhibits zoning patterns characterized by Cr- and Fe^{2+}-rich cores rimmed by ferrian chromite (rich in Fe^{3+}) with compositions similar to those of Cr-spinels included in barren serpentinite already investigated by Gahlan and Arai, (2007), Fanlo et al. (2015), Hodel et al. (2017). Although these Cr-spinels were interpreted as result of interaction with the hydrothermal system responsible for the formation of the Co-Ni arsenide ores (e.g., El Ghorfi et al., 2008), Fanlo et al. (2015) proved that such Cr-spinel alteration was

much earlier than mineralization, taking place during Pan-African orogenesis by sea floor serpentinization in a metal-rich environment caused by the presence of nearby black smoker-type hydrothermal vents. None of the latter studies paid attention to the dissolution features shown by Cr-spinel grains scattered in Fe-Co ores fully hosted by serpentinites and in their alteration halos.

The identification of serpentinite-hosted ores in the Bou Azzer district and a possible way to track its origin through serpentinite replacement by ore-forming fluids allow to complete the classification of ore-deposit types and supply new data to understand the development of the mineralizing process. Nevertheless, as it was pointed out above, many question marks still exist on the nature and provenance of ore-forming fluids as well as on the age of ore formation. Thus, the aims of this Ph.D. Thesis try to find answers to most questions still remaining on the genesis of the different types of arsenide ores of the Bou Azzer district. To reach such goal, the research plan includes three major objectives:

1. To understand the mechanism by which ores hosted by serpentinite formed and how ore-forming fluids migrate into, and spread out over the host serpentinite. This will be addressed by a complete mineralogical and geochemical study of two orebodies hosted by serpentinite from Ait Ahmane (F55 and F56 orebodies) and their alteration halos. Geochemical results will also include data from barren serpentinites and some contact-type ores (e.g. Filon 7/5 and Aghbar deposits) and will be discussed to shed additional light on the provenance of major ore-forming elements: As, Co, Ni and Fe (Paper 1; Chapter II).
2. To characterize the complete alteration sequence affecting the Cr-spinel grains included serpentinite-hosted Fe-Co ores, assuming that these ores represent precipitates from the latest, more residual arsenide ores-forming fluids. This will allow understanding the interaction between such fluids and serpentinites and will help to stablish morphological and chemical features of Cr-spinel that could be used as indicators of late mineralizing events (Paper 2, Chapter III).
3. To constrain the source and age of ore-forming fluids in the Bou Azzer district by a Pb, Sr, Nd and S isotope survey of a representative set of arsenide minerals from different ore deposits and of barren samples from regional lithological units (Paper 3, Chapter IV). The novelty of the approach proposed in this Ph.D. Thesis

is that isotopic analyses were performed on arsenide and sulfarsenide minerals of the main arsenide ore-forming stage, in contrast to previous studies (e.g., Leveresse, 2001; Dolansky, 2007; Oberthür et al., 2009; Maacha, 2013) which were focused on gangue minerals and sulfides from pre- and post-arsenide stage.

3 Sampling and Analytical methods

This study was mainly established on the basis of samples from Co-Fe arsenide ores hosted (F55, F56) or disseminated in serpentinite (F7/5). So, the samples were cut, mounted on a glass plate and polished at the Department of Mineralogy and Petrology of the University of Granada (Spain) for petrographic observations. They were studied under transmitted- and reflected-light, polarized microscope, as well as by a SUPRA40VP scanning electron microscope at the Centro de Instrumentation Científica (CIC) of the University of Granada, Spain.

The chemical composition of arsenide ore minerals and Cr-spinel was obtained by using two different electron-probe instruments. Arsenides were analyzed in the Centros Científicos y Tecnológicos (CCiT) of the University of Barcelona (Spain) (Chapter II. 3). Electron-probe micro analyses of Cr-spinel from F55, were performed at the Centro de Instrumentación Científica (CIC) of the University of Granada. While those from F7/5 were analysed in the Centros Científicos y Tecnológicos (CCiT) of the University of Barcelona (Spain) (Chapter II. 3; Chapter III. 4).

Whole-rock samples from the F55 and F56 veins and their host altered and unaltered serpentinite as well as arsenide ore samples from the F7/5 and Aghbar orebodies were Analyzed at INTERTEK (Australia) for S, As, Fe, Co, Ni, Os, Ir, Ru, Rh, Pt, Pd and Au (Chapter II. 3).

Many deposits from Bou Azzer district were sampled for microscopic observations, such as Mechoui, Filon 7/5, Tamdrost, Aghbar and Ightem Ambed, Agoudal, and Ait Ahmane. Isotope investigations (Pb, Sr, Nd, S isotopes) were mainly focused on three deposits; Tamdrost, Aghbar and Ait Ahmane which are shortly described at Chapter IV. 3, as well as two other deposits (Filon 7/5 and Ightem) from which several samples were analysed for S isotopes.

Chapter II: Formation of serpentinite-hosted, Fe-rich arsenide ores at the latest stage of mineralization of the Bou-Azzer mining district (Morocco)

This chapter II corresponds to a paper:

Hajjar Z., Gervilla F., Fanlo I., González-Jiménez J.M., Ilmen S., 2021. Formation of serpentinite-hosted, Fe-rich arsenide ores at the latest stage of mineralization of the Bou-Azzer mining district (Morocco). Ore Geology Reviews 128, 103926. (IF. 3.714)

Abstract

The Bou Azzer district in the central Anti-Atlas of Morocco is the world's unique mining district where Co is exploited from serpentinite-hosted hydrothermal Co-Ni-Fe arsenide ores. This paper provides the first-ever mineralogical and geochemical characterization of a suite of Fe-rich arsenide orebodies found during recent mining in the Ait Ahmane area, in central Bou Azzer district. These are lens-like orebodies of massive and disseminated Fe-rich ores fully hosted in serpentinites (hereafter named as serpentinite-hosted ores) that are typically enveloped by arsenide-poor, carbonated serpentinite, evolving irregularly outwards to talc-rich serpentinite. The central part of these orebodies mainly consists of massive ore made up of aggregates of zoned spindle-like crystals of löllingite whereas the outer zone of disseminated ore consists of rosette-like löllingite. These ores often contain accessory grains of chromite that display strong fracturation, zoning and alteration.

We propose a general model for the formation of the Bou-Azzer Co-Ni-Fe arsenide ores[3] associated to the infiltration of high-temperature (>400ºC) slightly alkaline, oxidized and $CaCl_2$-rich fluids through opening fault and fractures. When channeled through faults separating serpentinite and quartz diorite (or other rocks) the fluids deposited Ni- and Ni-Co-rich ores in these fault-related open spaces (here re-defined contact-type ores). Over the course of mineral deposition, the generated Ni- poor fluids tended to migrate into serpentinite, first through networks of thin entwined veins and progressively by intergranular percolation, promoting dissolution of the infiltrated serpentinite and precipitation of Co-Fe ores (the presence of remnants of chromite included in coexisting arsenides and calcite sustains the role played by dissolution/precipitation, ore-forming process). Further circulation of the evolving fluids through weak zones of massive serpentinite away from the serpentinite-quartz diorite (or other rocks) contact (intra serpentinite faults), formed the serpentinite-hosted, Fe-rich ore type represented by the F55 lens. These fluids most probably evolved at low temperature (~200ºC) towards slightly higher pH values and oxidizing conditions increasing the proportions of CO_2 and CO_3^{2-}, promoting the dissolution of serpentine, the increase in the magnetite component of chromite, the formation of Cr and Fe hydroxides, the mobilization of silica out of the reactive zone and the precipitation of calcite+Fe-rich arsenides.

Keywords: Fe-ores, Serpentinite hosted ores, F55 lens Ait Ahmane area, Bou Azzer district.

1 Introduction

Most cobalt's world production is obtained as a by-product from sediment-hosted, magmatic Ni-Cu and laterite deposits and only a small percentage (16% in 2016) is produced as a primary commodity (Alves-Dias et al., 2018). The latter production is mostly extracted from the hydrothermal deposits of the Bou Azzer mining district in Morocco where Co is beneficiated from Co-Ni-Fe arsenide ores. Although the alteration products of these ores (mainly erythrite: $Co_3(AsO_4)_2.8H_2O$) were known for a long time by the inhabitants of the Bou Azzer region who used them as insecticides and in rat poison, the history of this mining district started in 1929 when Jean Epinat, a French industrialist, was taken to the area and discovered several ore outcrops composed of complex assemblages including oxides, carbonates, arseniates and arsenides (Nataf, 2003). Afterwards, these mineralizations were exploited under artisanal mining mode, which was soon followed by the opening of the Bou Azzer mine in 1934 (Maacha et al., 2011). Since then, the Bou Azzer deposits have been an important source of Co and nowadays produce up to 2,500 tons of cobalt, 1,0000 tons of arsenic, 300 tons of nickel and 250 kg of gold (Bouabdellah, et al., 2016).

The Co-Ni-Fe arsenide ores in the Bou Azzer district are WNW-ESE flame-shaped orebodies, flat lenses and pocket-like masses located at the contacts between serpentinite bodies and quartz diorite or, locally, gabbros, younger volcanic rocks and sedimentary rocks (here after contact ores). Arsenide ores also fill NE-SW, N-S cross-cutting veins hosted in all these rocks (here after cross- cutting ores) (Leblanc, 1975; En-Naciri, 1995; El Ghorfi, 2006; Gervilla, 2012; Maacha, 2013; Bouabdellah, et al., 2016; Ikenne et al., 2020). The crystallization sequence of the mineralized bodies was summarized in three stages by Maacha, (2013) and Bouabdellah et al., (2016): (a) a pre-arsenide ore consisting of gold associated to chlorite and quartz, (b) an arsenide stage made up of mono-, di-and tri-arsenides, and sulfarsenides, and (c) an epithermal stage marked by the precipitation of sulfides associated to late quartz and calcite. At deposit scale, contact ores tend to be rich in Ni and Ni-Co arsenides [nickeline, NiAs; rammelsbergite, $NiAs_2$; Ni-rich skutterudite $(Co,Ni)As_3$, members of the rammelsbergite ($NiAs_2$)-safflorite ($CoAs_2$), and the rammelsbergite ($NiAs_2$)-safflorite CoAs)-löllingite ($FeAs_2$) solid solution series] in the center of lodes evolving progressively to Co- and Fe-rich arsenide assemblages (mainly containing skutterrudite, members of the löllingite-

safflorite series and löllingite) towards the disseminated ores found in serpentinite (Leblanc, 1975; En-Naciri, 1995; Gervilla et al., 2012). Fluid inclusions studies on pre- and post-ore quartz, and post-ore calcite show the presence of moderate to highly saline fluids (15-22 wt% NaCl and 16.5-20.5 wt% $CaCl_2$) trapped at low temperatures (120-240ºC) under variable pressures (0.4-1.2 kb) (En-Naciri, 1995). In contrast, primary inclusions in pre-ore quartz identified by Dolansky (2007) yielded information on mineralizing fluids being highly saline brines (31-42 wt% NaCl and 6-13 wt.% $CaCl_2$) that were trapped at relatively higher temperature (298-409ºC) under relatively high pressures (1.6-2.5 kb). This information obtained from fluid inclusion along with phase relations and mineral geothermometry of arsenides (Gervilla et al., 2012), seems to indicate a general trend of decreasing temperature of ore formation within single deposits with Ni-rich ores formed at higher temperatures than Co- and Fe-rich ones. Available C, O and H isotopic data (Dolansky, 2007; Maacha et al., 2015a,b) argue for the presence of both magmatic and exogenic water for the formation the arsenide ores.

Two newly-discovered ore deposits (F53 and F55) were mined by the Managem Group in the Ait Ahmane area in 2018 but since 2019, mining operations only remained active in the F53 deposit, becoming the main ore deposit in the area from the seventies of the past century. Two types of orebodies coexist in the F53 deposit: 1) massive ores found along the contact between serpentinites and quartz diorite (hereafter contact-type ores), and 2) semimassive to disseminated ores in quartz veins cross-cutting quartz diorite (hereafter, cross-cutting-type ores). These two types of ores were exploited in 2019, producing raw material with up to 2.40% Co and 0.20% Ni on average. The F55 deposit is a 95 meters-long and up to 9 meters-thick lens of massive to disseminated ores hosted by serpentinite, having Co and Ni contents similar to those of the F53 deposit (2,03% and 0.75% respectively), which are significantly higher Co and slightly lower Ni than the average grades (~1% Co and 1% Ni) reported for the whole Bou Azzer district (Bouabdellah et al., 2016).

The different contact-type orebodies of the Bou Azzer district have traditionally been interpreted as fillings of fault-related, open spaces created along the contacts between quartz diorite intrusions (or locally gabbros, volcanic or sedimentary rocks), and serpentinites (Leblanc, 1975; En- Naciri, 1995; El Ghorfi, 2006; Maacha, 2013; Bouabdellah, et al.,

2016; Ikenne et al., 2020). However, texture of the arsenide ores in the Aghbar deposit (Gervilla et al., 2012) shows replacement relationships between ores and their host serpentinite suggesting that such ores formed at expenses of serpentinite rather than by simple filling of open fractures. Thus, the identification of serpentinite- hosted orebodies (serpentinite-hosted ores) at Ait Ahmane as well as the presence of volumetrically important disseminated ores in serpentinites in the Aghbar deposit (Gervilla et al., 2012; Fanlo et al., 2015) with high Co/Ni ratios rise two important questions to understand the spatial evolution of the Bou Azzer hydrothermal system at different scales and the local mechanisms of ore formation: 1) how ore-forming fluids migrate into, and extend towards the host serpentinite? and 2) why serpentinite hosted ores are mainly made up of Co- Fe arsenides?

This paper aims to answer these two questions providing new knowledge that may help to explore new ore deposits in this worldwide unique mining district as well as to plan exploitation strategies within single deposits. In order to achieve this goal we provide a very careful updated characterization of the mineralogy and chemistry of the F55 ore lens comparing it with the nearby, already exploited F56 lens and the contact-type ores of the F53 deposit both at Ait Ahmane, as well as with literature and own data from the contact-type ores of the F7/5 orebody in the western part, and the Aghbar deposit in the central part of the Bou Azzer mining district (cross-cutting-type ores are not studied or discussed in this paper). Our results provide unprecedented insights on: 1) the mineralogical and geochemical peculiarities of serpentinite-hosted ore lenses and associated alteration halos with respect to the most frequent contact-type ores; 2) the evolution of ore-forming fluids at the district scale and within single deposits and 3) the extent of interaction between mineralizing fluids and the host serpentinite. Whole-rock geochemical data from the F55 ore lens and its variably altered host rocks, the F56 lens, the contact-type ores of the F5/7 orebody and the Aghbar deposit will also allow discussing the possible provenance of major ore-forming elements (As, Co, Ni and Fe).

2 Geology

The Bou Azzer El Graara inlier is located in the western part of the central Anti-Atlas (Morocco) (Choubert, 1963; Leblanc, 1975; Saquaque et al., 1989; Figure 1) and is mainly composed of Proterozoic terranes, from early Cryogenian to late Ediacarian (D'Lemos

et al., 2006; Blein et al., 2014). The oldest of these terranes is located in the southern part of the Bou Azzer inlier and includes two units: the Tachdamt Bleida unit and the Tazegzaout unit. The Tachdamt Bleida unit is composed of stromatolitic limestone, quartzite, tholeiitic basalts and schists, and represents a passive margin formed during Tonian or Early Cryogenian (Clauer, 1974; Bouougri et al., 2020). The Tazegzaout unit is composed of orthogneiss, metagabbro, schists and pegmatite attributed too to Early Cryogenian (D'Lemos et al., 2006; Blein et al., 2014; Hefferan et al., 2014). These units were previously considered Paleoproterozoic (PI) by Leblanc (1981).

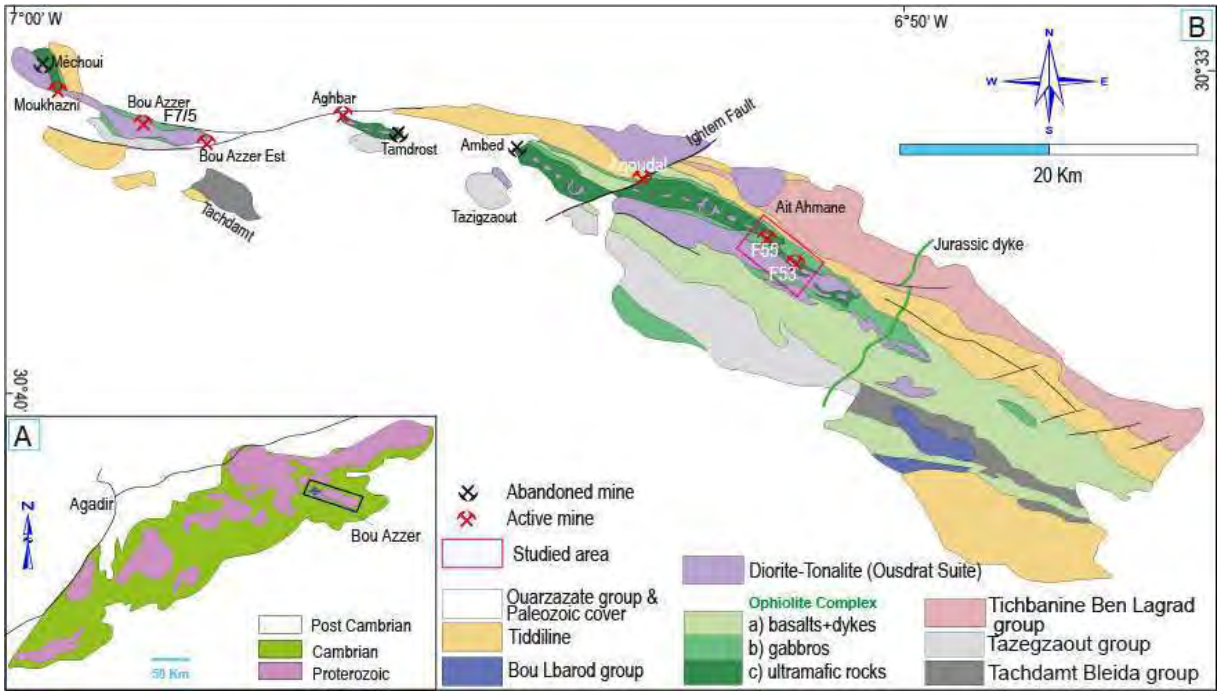

Fig. II. 1. (A). Simplified geological map of the Anti-Atlas belt. (B). Geological map of Bou Azzer inlier (Central Anti Atlas, Morocco) (modified from El Hadi et al., 2010), showing the main Co-Ni deposit in the district.

The late Cryogenian terrane is represented by three units: the Tichibanine Ben Lagrad Group, the ophiolite complex and the Ousdrat suite. The first group consists of a complex tectonic assemblage made up of metagreywackes and arc-related basalts, andesites, rhyolites and tuffs (Tekiout, 1991; Naidoo et al., 1991). This volcanic arc was dated to be active between 761 ± 7 Ma and 767 ± 7 Ma (zircon U-Pb age) from a rhyolite sample by Blein et al., (2014). The ophiolite complex includes, from bottom to top, serpentinized mantle peridotites, gabbros (by zircon U-Pb age: 697 ± 8 Ma (Bodinier et al., 1984; El Hadi et al., 2010); 758.7 ± 2.1 Ma and at 659 ± 7 by apatite U-Pb age (Hodel et al., 2020)), sheeted dykes, submarine

pillow basalts and locally, a varied set of partly metamorphosed sedimentary rocks, including metapelites, sandstones and limestones. The Ousdrat Suite is made up of diorite, quartz-diorite and monzodiorite intruding the ophiolite complex. These intrusions are dated at 640-670 Ma (Mrini, 1993 ; Inglis et al., 2003 ; Samson et al., 2004, Blein et al., 2014; Triantafyllou et al., 2020).

The Ediacaran terranes are also represented by three groups; the Bou Lbarod group, the Tiddiline group, and Ouarzazate group. The Bou Lbarod Group consist of mafic volcanic rocks intruded by post-kinematic stocks such as the Bleida granodiorite dated, using the U-Pb method in zircons, between 630 and 580 Ma ago (Inglis et al., 2004; Blein et al., 2014). The Tiddiline group unconformably overlies the ophiolite series and is composed of terrigenous sediments (siltstone and conglomerate) with local pyroclastic rocks (U-Pb age on zircons of 606 ± 5 Ma; Blein et al., 2014). The Ouarzazate Group gathers a suit of potassic to high-potassic volcanic rocks (ignimbrites and tuffs) made up of andesites, dacites and rhyolites, interstratified with chaotic breccia, polygenic conglomerates and arkosic sandstones. The U-Pb age obtained on 10 zircon grains from a rhyolitic welded tuff of the Ouarzazate bracketed the time of formation of this group between 567 ± 5 Ma and 566 ± 4 Ma (Blein et al., 2014). A Lower Cambrian-Upper Proterozoic, carbonate-dominated sedimentary succession (Adoudou and Lie-de-vin formations; Choubert, 1963), dated at 541 ± 6 Ma by U-Pb on seven zircons (Blein et al., 2014), overlies the Ouarzazate group.

The Ait Ahmane area is located in the central portion of the Bou Azzer-El Graara inlier but includes the easternmost outcrops of Co-Ni arsenide ores of the Bou Azzer mining district (Fig. II. 1). This area also includes the most complete outcrop of the lithological units that constitute the ophiolite sequence (Choubert, 1963; Leblanc, 1975, 1981; Boudinier et al., 1984; El Hadi, 1988; Saquaque, 1992; Hilal 1991; Admou, 2000; Maacha, 2013; Bhilisse, 2018). The serpentinite outcrops are usually bounded to the south by quartz diorite intrusions dated at 650 ±2 Ma using U-Pb on zircons (Inglis et al., 2003). In this area Leblanc, (1981) identified up to ten mineralized veins (from F51 to F61), many of which were mapped (1/1000) by the geological service of CTT mine of Bou Azzer (Fig. II. 2).

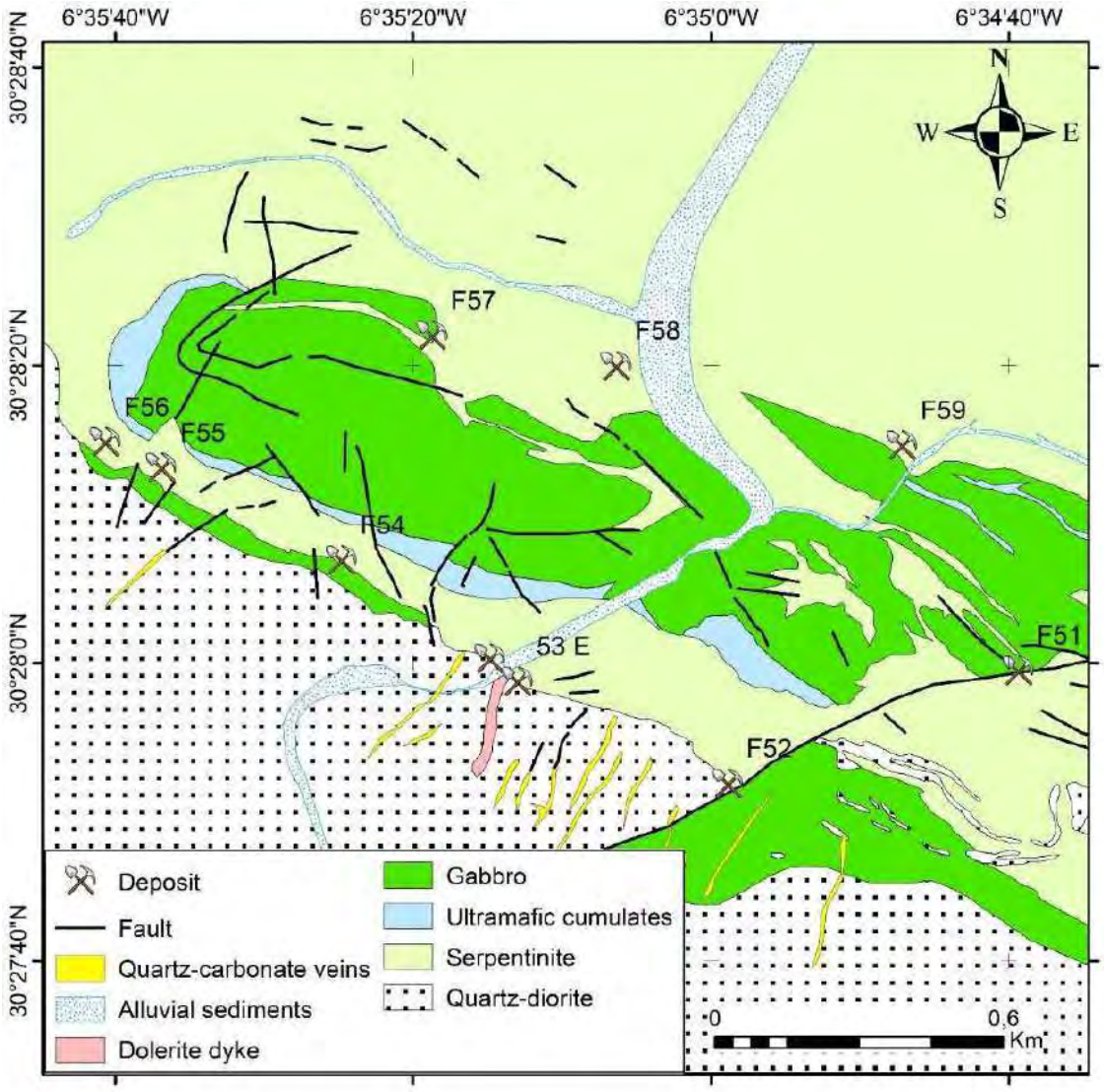

Fig. II. 2. Geological map of Ait Ahmane area (modified from Saquaque, 1992), showing the position of Fe-Co ores.

3 Samples and analytical methods

This study was mainly performed on the basis of eighteen samples collected from the F55 lens and its host rocks and two samples from the F56 lens (Fig. II. 3). The F55 lens was under exploitation in November 2016, at the time of our field campaign, allowing complete sampling along two cross sections intersecting the main lens, as well as the host, variably altered serpentinites. The F56 lens was completely exploited at that time and the few highly weathered ore remains did not provide material enough for representative sampling; thus, only one fresh sample and a partly altered one could be collected for comparison. The

samples were cut, mounted on a glass plate and polished at the Department of Mineralogy and Petrology of the University of Granada (Spain) for petrographic observations. They were studied under transmitted- and reflected-light, polarized microscope, as well as by a SUPRA40VP scanning electron microscope at the Centro de Instrumentation Científica (CIC) of the University of Granada, Spain, using STEM and EDX detectors. Operating conditions were: accelerating voltage of 20 kV, beam current of 20 nA and count times of 20 s.

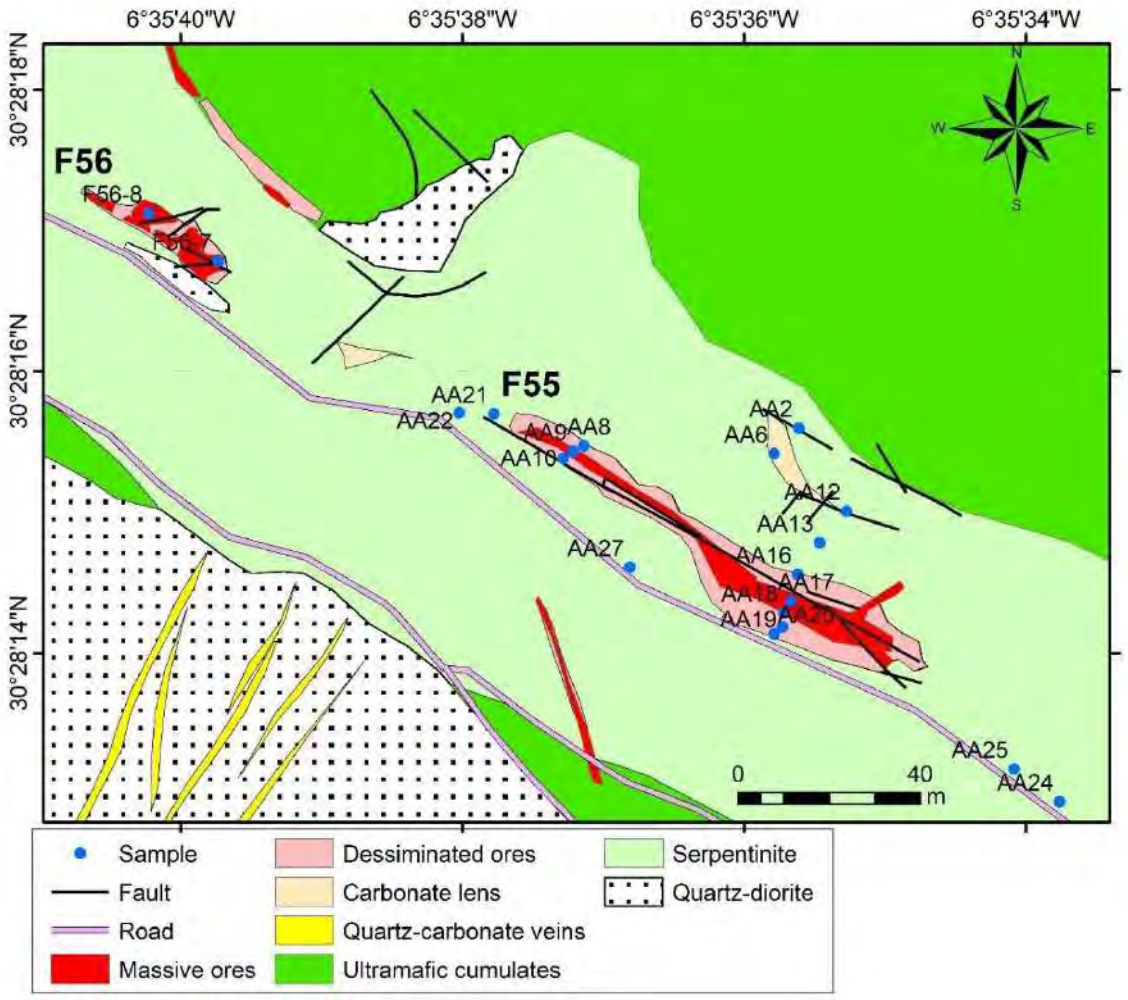

Fig. II. 3. Geological map of F55 and F56 lenses (Ait Ahmane area, Bou Azzer, Anti- Atlas); internal report of CTT mine Bou Azzer).

The chemical composition of arsenide ore minerals (Appendix A) and chromite (Appendix B) was obtained by using two different electron-probe instruments. Arsenides were analyzed in the Centros Científicos y Tecnológicos (CCiT) of the University of Barcelona (Spain) using a JEOL JXA- 8230 instrument equipped with five WDS spectrometers, under an

excitation voltage of 20 kV and a beam current of 20 nA, with a beam 2-3 μm in diameter. Monitored spectral lines were AsLα, SKα, SbKα., FeKα, CoKα, NiKα, and BiLα. Pyrite, GaAs, NiO, as well as pure Co, Cu, Au, Zn, Bi and Pb metal were used as primary standards. Chromite analyses were performed at the Centro Instrumentación Científica (CIC) of the University of Granada by means of a CAMEBAX SX100 instrument under excitation voltage of 20 kV, beam current of 20 nA and beam diameter of 5 μm. Monitored spectral lines were MgKα, FeKα, AlKα, CrKα, SiKα, TiKα, MnKα, NiKα, VKα, and CoKα using MgO, Fe_2O_3, Al_2O_3, Cr_2O_3, SiO_2, TiO_2, $MnTiO_3$, NiO, V_2O_3, ZnS, NiO, and metallic cobalt as standards.

Nineteen whole-rock samples from the F55 and F56 veins and their host altered and unaltered serpentinite as well as ten arsenide ore samples from the F7/5 orebody and four from the Aghbar deposit (located, respectively, in the western and central parts of the Bou Azzer mining district) were Analyzed at INTERTEK (Australia) for S, As, Fe, Co, Ni, Os, Ir, Ru, Rh, Pt, Pd and Au. The method used to determine Cu, Fe, Ni and S concentrations involved sodium peroxide fusion followed by dilution in concentrated hydrochloric acid followed by Inductively Coupled Optical Plasma Emission Spectrometry. The analysis of As, Co, PGE and Au were performed by nickel sulfide fire assay collection prior to Inductively Coupled High Resolution Plasma Mass Spectrometry (ICP-MS). Detection limits were 20 ppm for As, Co, Cu, and Ni, 0,1wt. % for Fe, 0,05 wt. % for S, 1 ppb for PGE and 2 ppb for Au. However, arsenide ore samples with >40 wt. % As were very difficult to fuse forcing to diminish the weight of the charges down to 1 gram, what rose the detection limit of these noble metals up to 25 ppb. These analytical conditions didn't allow measuring Os, Ir and Rh from some arsenide-rich, massive ores.

4 The arsenide ore lenses

4.1 Petrography

The two deposits (F55 and F56) analyzed in this study are of the serpentinite-hosted type, fully hosted in serpentinites whose protolithic rocks were metadunite and metaharzburgite now made up of mesh-textured lizardite and antigorite with minor chrysotile

(Fig. II. 4B) as well as scattered and isolated chromite grains (200-400 µm across). Partly altered (bastitized) orthopyroxene are still preserved in harzburgitic rocks.

The F55 deposit has a flat lens shape striking N120E and dipping 62º to SW (Fig. II. 3; Fig. II. 4A). It shows a zoned structure consisting of a massive core (modal proportions of arsenides vary from ~60% to almost 100%) surrounded by a variably-thick (2.5-7 m) envelope of disseminated ore in carbonated serpentinites. The core-envelope transition is often gradual as well as the external limits of the envelope which evolve outwards to progressively less carbonated rocks and locally to talc-rich serpentinites. The main carbonate mineral in this halo is calcite which is found fillings irregular veinlets in serpentinite (Fig. II. 4C and D), locally with minor talc and chlorite interstitial to calcite grains. Calcite also replaces serpentine at the veinlet walls, especially in zones characterized by tight networks of such veinlets giving rise to rocks almost completely composed of calcite. Chromite remains either in the serpentinite matrix or included in calcite where it becomes partly corroded. Talc-rich serpentinites often show fibrous texture (Fig. II. 4E) and contain scattered small (50-100 µm across) crystals of magnetite and partly altered chromite (200-400 µm across). The latter is usually zoned showing unaltered cores surrounded by variably thick (25-50 µm) rims of ferrian chromite.

Massive arsenide ore forming the central part of the F55 lens (>70 vol.% arsenides) mainly consists of aggregates of spindle-shaped, zoned crystals of Fe-rich diarsenides (mainly löllingite) containing, serpentine, chlorite and chromite inclusions (Fig. II. 5A, F) as well as minor nickeline, chalcopyrite and sphalerite, in a calcite matrix. Chromite grains are often fractured and also occur included in the coexisting calcite.

Likewise, the disseminated ore located in the carbonated halo also consists of löllingite, which forms rosettes and spindle-shaped grains scattered in the calcite-dominated, talc- and serpentine- bearing matrix (Fig. II. 5B and C). Transition between massive and disseminated ores takes place through a zone of semimassive ores where Co-Fe arsenides fill thin entwined veins in a carbonated, partly mineralized serpentinite matrix. Löllingite rosettes often show Co- and at lesser extent Ni-rich growth bands or contain Ni-rich cores (Fig. II. 6A, b and C), which include tiny grains (10-20 µm across) of native bismuth and at lesser extent galena and chalcopyrite. Chromite is also a minor constituent of this assemblage occurring as partly fractured and altered grains included in löllingite and calcite. Chromite

associated to calcite in both massive and disseminated ores frequently shows irregular alteration to a less reflective heterogeneous material, progressing along fractures and replacing the core of chromite crystals, thus giving rise to irregular, partly altered or atoll-shaped grains.

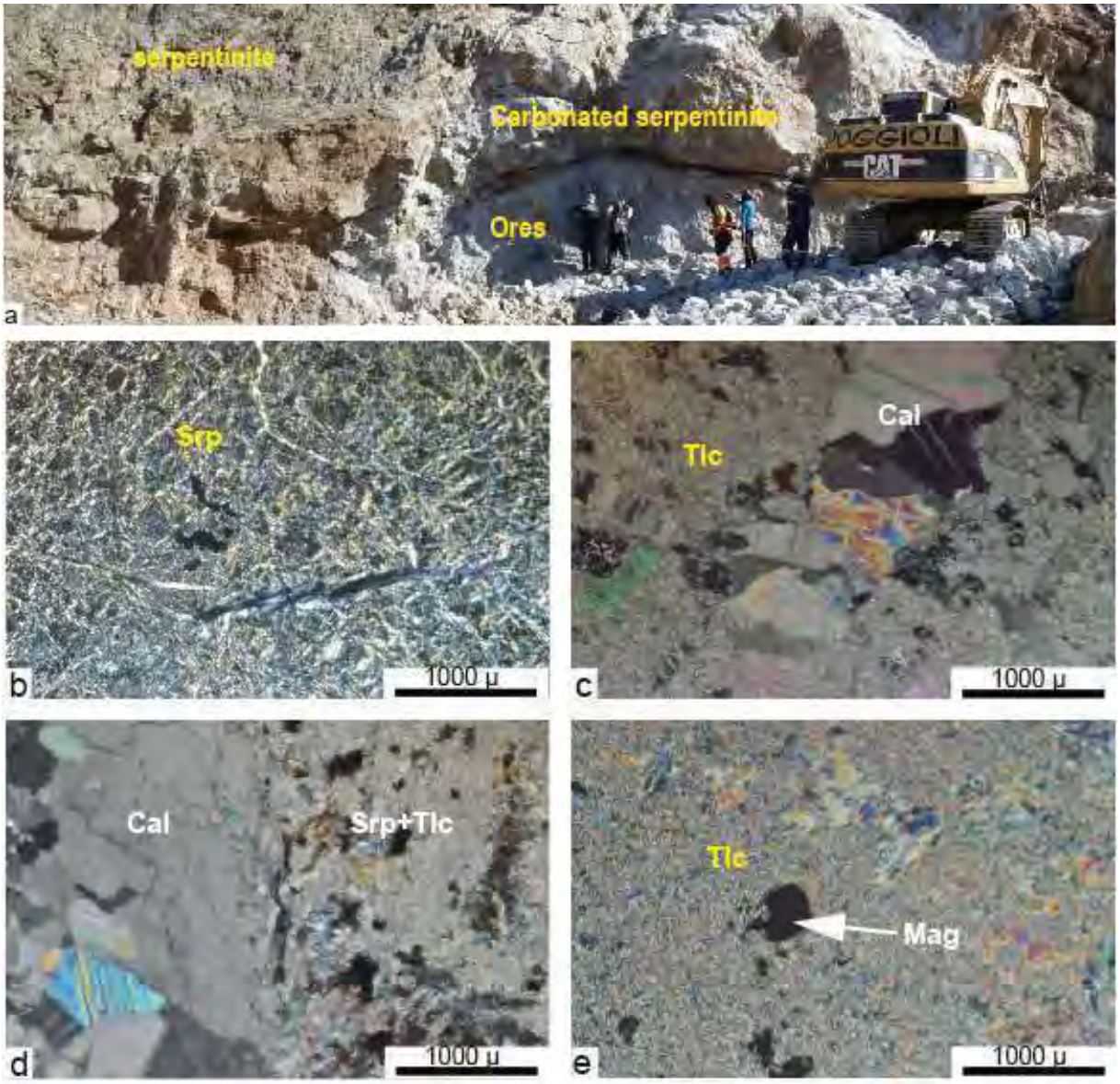

Fig. II. 4. (a). Field observation of the main F55 lens in the Ait Ahmane district. (b to e). Microphotographs of rocks hosted F55 ores observed by LPA. (b). serpentinite rock composed mainly by serpentine (srp). (c & d). calcite (Cal) filling of irregular veinlets affecting serpentine (srp) and talc minerals (tlc). (e). fibrous texture of talc (tlc), containing scattered small magnetite crystals.

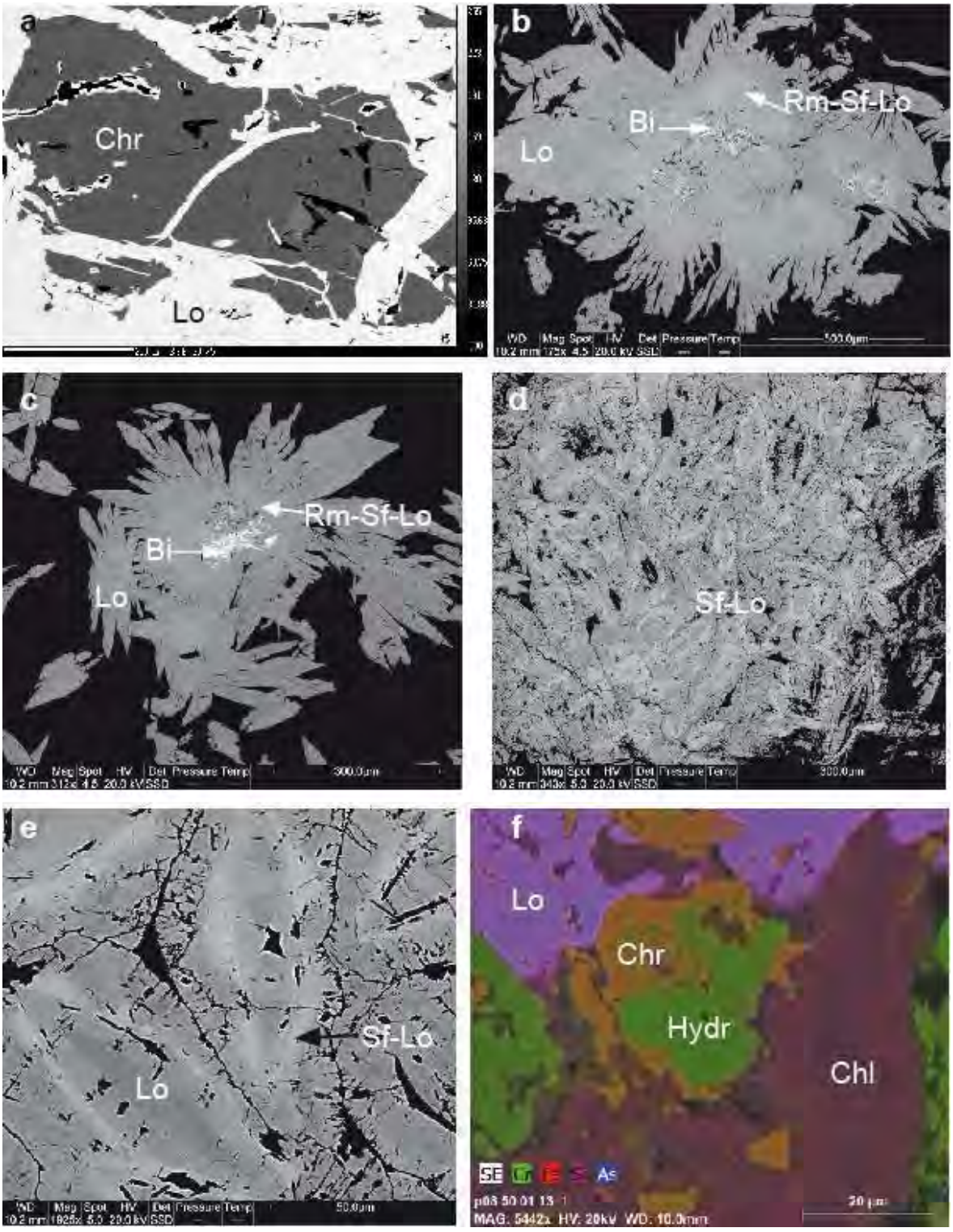

Fig. II. 5. Microphotographs of ore minerals from F55 and F56 ores. (a). Chromite (Chr) replaced by löllingite (Lo). (b & c). löllingite rosettes (Lo) grains containing Co-Ni richdiarsenides bands (Rm-Sf-Lo) and Bi inclusion (Bi); scattered in calcite in disseminated ores from F55 lens. (d & e). aggregates of spindle-shaped, zoned crystals of löllingite-safflorite included in calcite (F56 lens). (e) is zoom of (d) (f). map of chromite (Chr) altered into Fe-Cr- rich hydroxides (hdr); scattered in chlorite (Chl).

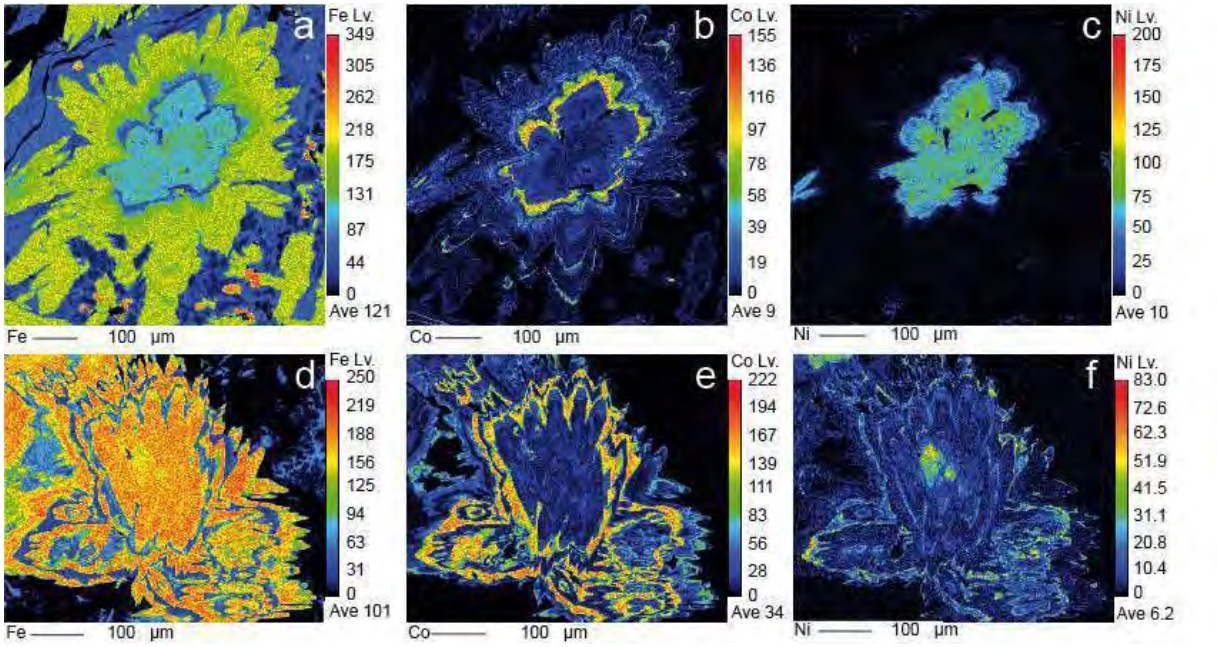

Fig. II. 6. X-ray chemical distribution maps of Fe, Co, and Ni for two characteristic zoned löllingite rosettes from F55 ores (a. b. c) and F56 ores (d. e. f) (Ait Ahmane area, Bou Azzer district).

The F56 deposit is a lens with a flatter-like morphology and smaller in size (maximum thickness of 6 m and 35 m in length) than F55. It is oriented as the F55 within the serpentinite host rock although it is attached to a small intrusion of quartz diorite (Fig. II. 3). It develops a halo of carbonated serpentinite which contains partly weathered, subhedral crystals of skutterudite (~40 mod. %) as well as rosettes and aggregates of spindle-shaped, zoned crystals of löllingite containing bands of löllingite-safflorite, both included in calcite (Fig. II. 5D and E; Fig. II. 6D, e and F). Arsenide minerals contain inclusions of serpentine, some chlorite and corroded grains of chromite. Sulfide minerals are also present as galena grains included in löllingite-safflorite and disseminated crystals of arsenopyrite.

4.2 Mineral chemistry of arsenides

The chemical composition of diarsenides from the F55 lens plots in the Ni-poor region of the $CoAs_2$-$NiAs_2$-$FeAs_2$ (safflorite-rammelsbergite-löllingite) system, most of them (~75% of spot analyses) clustered on the Fe-rich end (löllingite) of the $CoAs_2$-$FeAs_2$ binary (Fig. II. 7A). In massive ores, spindle-shaped crystals consist of Ni-poor löllingite (<0.63 wt.% Ni) with diffuse sector zoning and/or alternate bands characterized by slight enrichments of Co (up to 3.21 wt.%) but often include bands with significantly higher Co contents (12.51-

19.49 wt.% Co) (Fig. II. 6B and Fig. II. 7A, Appendix A). Diarsenides occurring as rosettes show Ni-richer cores with compositions plotting along the rammelsbergite-löllingite joint (6.16-12.92 wt.% Ni, 7.79-13.33 wt.% Fe and 0.47-2.26 wt.% Co) evolving outwards through narrow bands of rammelsbergite-safflorite-löllingite (6.71-8.22 wt.% Ni, 9.40-14.52 wt.% Co and 7.79-13.33 wt.% Fe) to compositions close to the löllingite corner (27.12- 28.83 wt.% Fe, 0-0.11 wt.% Ni and 0.05-1.38 wt.% Co) (Fig. II. 7A; Appendix A).

Diarsenide rosettes from the F56 lens show the same pattern of zoning of löllingite rosettes from F55, having cores slightly enriched in Ni (2.19-4.83 wt.% Ni) surrounded by rims of almost pure löllingite often containing bands enriched in up to 5.4 wt.% Co (Fig. II. 7A). The composition of the different zones and bands of spindle-shaped crystals, both disseminated and forming aggregates, extend along the löllingite-safflorite joint, from nearly pure löllingite to safflorite containing up to 1.34 wt.% Fe and 3.24 wt.% Ni.

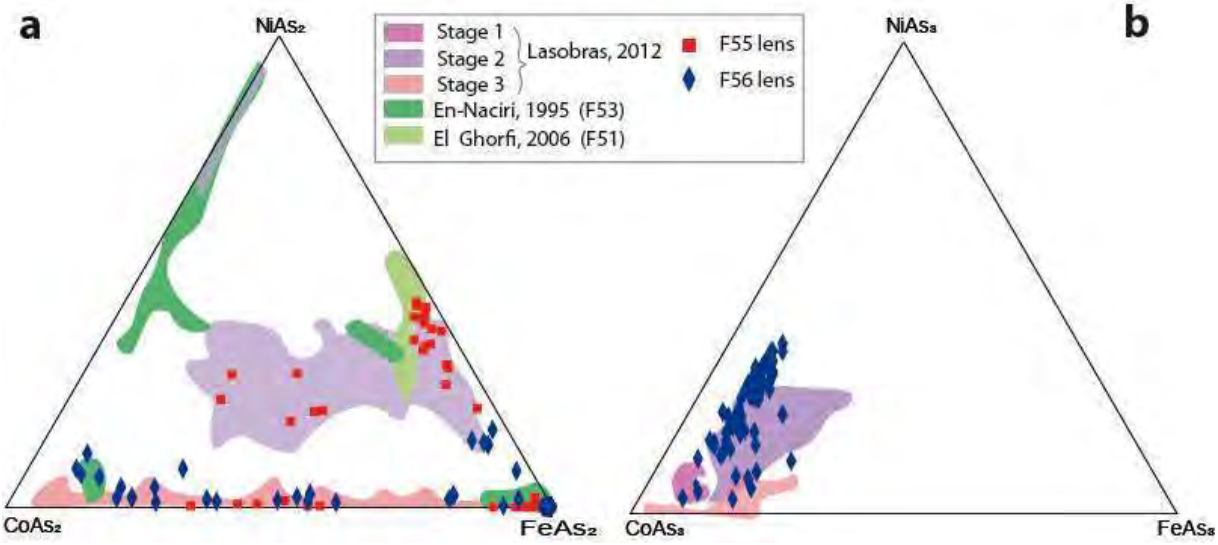

Fig. II. 7. (a). Plot of diarsenides composition from F55 and F56 ores from Ait Ahmane area in the system CoAs2–NiAs2–FeAs2. (b). Plot of skutterudite composition from F56 ores from Ait Ahmane area in the system CoAs3–NiAs3–FeAs3. The compositional fields of di- and tri-arsenides analyzed by others authors from ores of the Ait Ahmane Area (Bou Azzer district; (En-Naciri, 995; El Ghorfi, 2006; Lasobras, 2012)) are also shown for comparison.

The compositions of diarsenides from F55 and F56 ore lenses partly overlaps those reported by El Ghorfi, (2006) for the F51 lens and mainly by En-Naciri, (1995) and Lasobras, (2012) for the F53 lens, highlighting the Ni-poor and extremely Fe-rich nature of these minerals in the studied serpentinite-hosted ores.

Electron-probe micro-analyses of skutterudite reveals a diffused zoned structure with alternating Co-rich (up to 19.24 wt.% Co, 1.38 wt.% Fe and 0.62 wt.% Ni) and Ni-rich (up to 7.33 wt.% Ni, 11.66 wt.%Co and 4.7 wt.%Fe) bands. Taken as a whole, the compositional field of skutterudite from F56 ore lens partly overlaps the fields reported by Lasobras (2012) for differenttextural types of skutterudite from the F53 deposit but extends toward Ni-rich compositions (Figure7B).

4.3 Mineral chemistry of Chromite

The studied talc-rich serpentinite sample from the outer part of the carbonated halo contains chromite with cores slightly enriched in Fe_2O_3 (11.44-17.96 wt.%) but with similar low Mn and Zn contents (<0.8 wt.% MnO and <0.5 wt.% ZnO) to chromite cores in noncarbonated, barren serpentinites (Fig. II. 8). It also shows rims with higher Fe_2O_3 (27.13-33.74 wt.%) and slightly higher Mn (0.68-1.10 wt.% MnO) and Zn (0.23-0.70 wt.% ZnO) contents than cores (Appendix B). Chromite in carbonated serpentinite containing minor arsenides shows small core-to-rim variations in the proportion of trivalent cations both in grains associated to serpentine minerals and in those included in calcite and, as a whole, overlap the composition of chromite from the talc-rich serpentinite (Fig. II. 8). It also shows small differences in Mn and Zn contents between grains included in calcite (0.58-0.96 wt.% and 0.24-0.47 wt.% respectively) and grains included in serpentine (0.44-0.84 wt.% MnO and 0.16-0.40 wt.% ZnO); these values are slightly lower than those of altered rims of chromite from talc- rich serpentinite. In contrast, accessory chromite in disseminated and massive ores exhibit a distinct composition mostly plotting in the Al-poor region of the Cr-Fe^{3+}-Al ternary (Figure 8). Although some few cores of chromite grains have compositions comparable to those described from talc-rich serpentinites and poorly mineralized carbonated serpentinites (Fe_2O_3=10.09-16.65 wt.%, MnO=1.07- 1.18 wt.%, ZnO=0.50-0.58 wt.%), the composition of most chromite grains in disseminated and massive arsenide ores (both included in calcite and in löllingite) plot in a field that overlaps and extends beyond the field of rims of highly altered chromite grains described by Gahlan and Arai, (2007) and Hodel et al., (2017), approaching the composition of magnetite (Fig. II. 8): Fe_2O_3 varies from 28.00 to 65.95 wt.%, MnO from 0.28 to 3.73 wt.% and ZnO from 0.05 to 0.57 wt.%. These chromite grains

do not show a general pattern of core-to-rim chemical variation but rims (where present) frequently have 1 to 2 wt.% Fe_2O_3 higher than cores and locally are slightly richer in Mn and Zn than cores (Appendix B). The Mn and Zn contents of accessory chromite in massive and disseminated arsenide ores of the F55 lens are comparable to those reported by Fanlo et al., (2015) from the Tamdrost arsenide ores and the F53 lens of the Aït Ahmane district, but are much smaller than the contents reported by these authors for accessory chromite from Co- and Fe-rich arsenide ores of the Aghbar deposit where MnO reaches up to 18.5 wt.% and ZnO up to 19.7 wt.%. Taken as a whole, chromite from mineralized rocks has much smaller Mg# (from 0.02-0.33) than barren serpentinite, talc-rich serpentinite and carbonated serpentinite (Mg#=0.20-0.44).

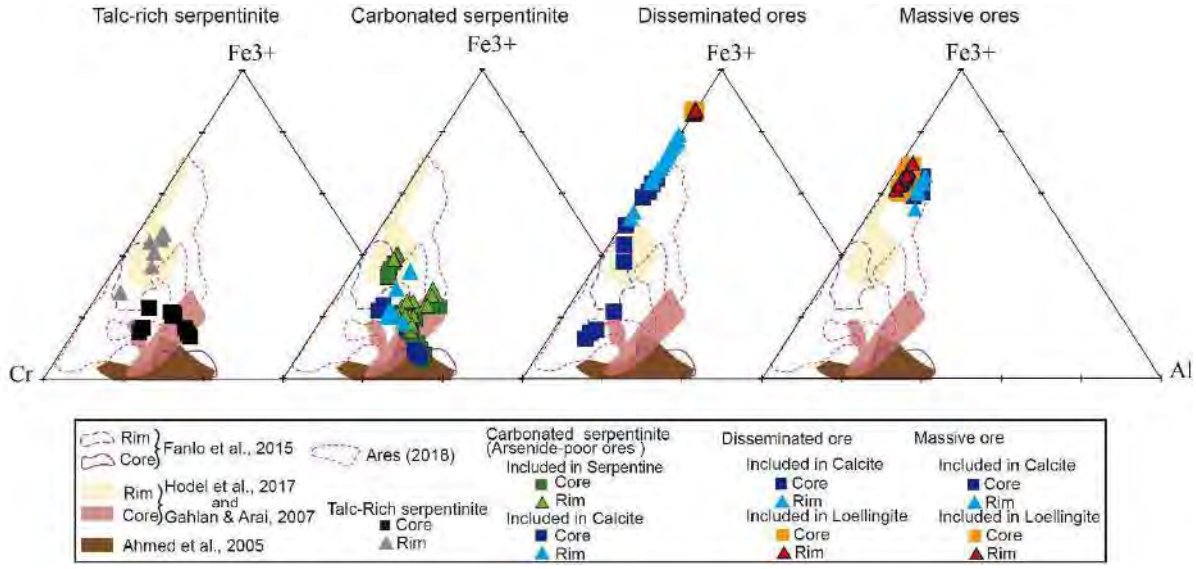

Fig. II. 8. Compositional variations in terms of Cr–Fe3+–Al of accessory chromite grains associated to Fe-arsenide ores in F55 lens from Ait Ahmane area. The omposition of chromite analyzed by others authors from Bou Azzer (peridotite mantle: Ahmed et al., (2005), serpentinite from Ait Ahmane area: Hodel et al., (2017); Ait Ahmane ores hosted in serpentinite: Fanlo et al., (2015); F7/5 deposit: Ares, (2018)) are also shown for comparison.

EPMA data of the less reflective material observed in some altered chromite grains showing irregular to atoll-shaped morphology (Fig. II. 5F) reveal similar proportions of Cr_2O_3 and Fe_2O_3, with minor Al_2O_3, MgO, MnO and ZnO. They also contain traces of TiO_2, V_2O_3, NiO and CoO, and show low totals, ranging from 72.19 to 75.81 wt.%, thus indicating the presence of 24.19-27.81 wt.% light elements. The heterogeneous nature of this material as well as its major composition, mainly consisting of Cr_2O_3 and Fe_2O_3 with totals around 74 wt.% suggest it consists of, probably amorphous Cr and Fe hydroxides [$Cr(OH)_3$+$Fe(OH)_3$]

including variable amounts of tiny chromite remains. The fact that water represents 26.18 wt.% and 25.29 wt.% of the molecular weight of $Cr(OH)_3$ and $Fe(OH)_3$ respectively, support this interpretation.

4.4 Whole rock analyses

Major ore-forming element (As, Co, Ni and Fe) contents broadly increase from serpentinite, talc-rich serpentinite and barren carbonated to partly mineralized, carbonated serpentinite and mainly in massive arsenide ores of the F55 lens (

Table II. 1). Such enrichment trend is very clear for As and, at lesser extend Co but is poorly defined for Fe and is almost absent for Ni.

All analyzed samples (

Table II. 1) show unusually high As contents, varying from 196.5 ppm (average) in talc-rich serpentinites to 49.03 wt.% (average) in massive arsenide ores of the F55 lens. These values are $\sim 10^3$ to $\sim 10^7$ times higher than the primitive mantle values reported by Lyubetskaya and Korenaga, (2007) (Fig. II. 9). Co contents are quite low in barren, uncarbonated serpentinites and talc-rich serpentinites (from 13 to 169 ppm;

Table II. 1) having primitive mantle-normalized (Co_N) values usually below 1 (in two samples Co_N reaches 1.33 and 1.61; Fig. II. 9). The carbonated serpentinite sample AA-6 has $Co_N > 1$ (1.26) correlated with a significant increase in As content (3.88 wt.%;

Table II. 1). As expected, Co contents in ore samples increase up to 665 ppm Co (ave.) in disseminated ores and to 11840 ppm Co (ave.) in massive ores, representing Co enrichments 5 to 240 times the primitive mantle values (Fig. II. 9). Ni does not show a distribution pattern comparable to that of Co since Ni contents of barren serpentinites (1050-2445 ppm) overlap those of massive arsenide ore samples (870- 7093 ppm) (

Table II. 1). As a whole, Ni_N values range from slightly below 1 (down to 0.47) to slightly above 1 (up to 1.50). Only three samples surpass these values: ore samples AA-19A (Ni_N=2.37) and AA-20 (Ni_N=3.57) from the F55 lens and the sample AA-8 (Ni_N=2.26) from the F56 lens (Fig. II. 9). The distribution pattern of Fe is somewhat similar to that of Ni since all barren samples but one, as well as the poorly mineralized samples from the western end of

the F55 vein show Fe_N values below 1 (Fig. II. 9), corresponding to Fe contents ranging from 2.18 to 6.14 wt.% (

Table II. 1); only the sample AA-27 has 6.57 wt.% and Fe_N=1.06. Ore samples are significantly enriched in Fe (from 14.05 to 22.56 wt.%; 19.98 wt.% on average) representing primitive mantle-normalized values between 2.26 and 3.63. S does not correlate with any of the other elements.

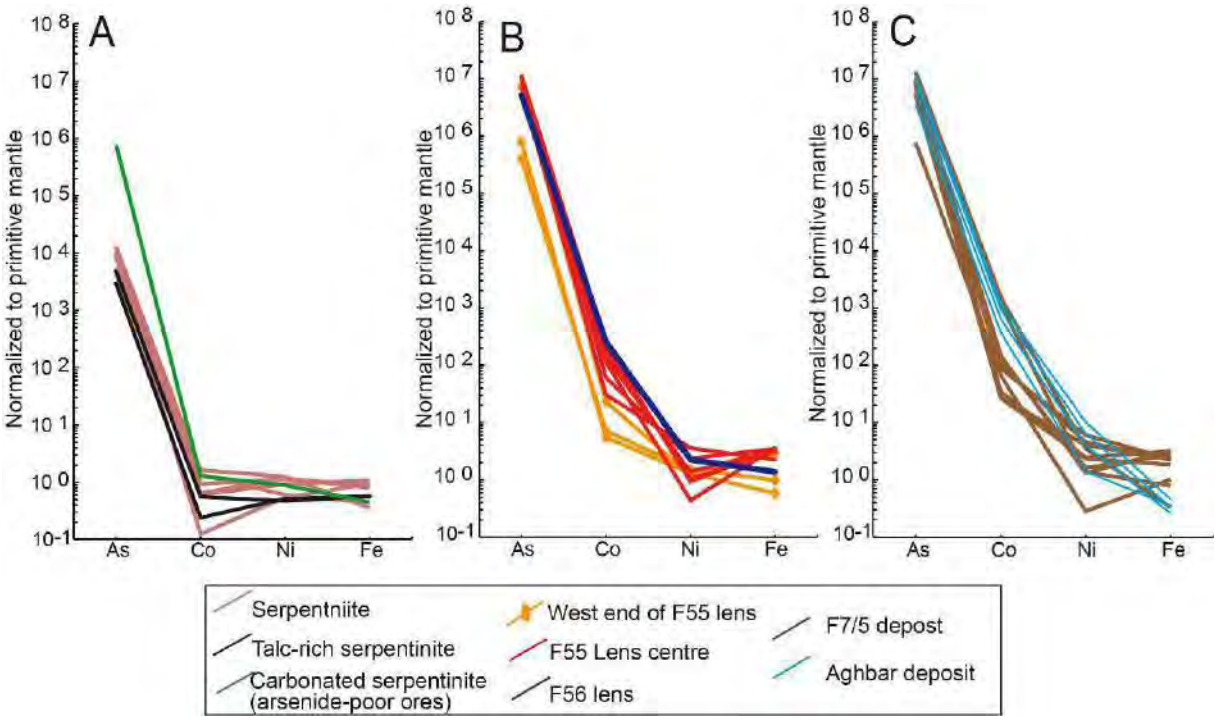

Fig. II. 9. Primitive mantle-normalized As-Co-Ni-Fe spidergrams of ores from Ait Ahmane area (F56, F55 ores, and its host rocks), F7/5 and Aghbar deposits (Bou Azzer district, Morocco). Normalizing values are taken from Lyubetskaya and Korenaga, (2007).

The analyzed samples from the F7/5 and Aghbar contact-type deposits have lower As (38.94% As and 38.49% As on average, respectively) and Fe (12.63 wt.% Fe and 2.21 wt.% Fe on average, respectively) contents, but are much richer in Co (35524 ppm Co and 84125 ppm Co on average) and Ni (5533 ppm Ni and 11022 ppm Ni on average, respectively) than those from the F55 lens. These data question the suggested west to east enrichment in Ni and Fe suggested by En-Naciri (1995) because the Co- and Ni-richest ore is that from Aghbar, located in the center of the Bou Azzer district.

Whole-rock Co contents in the F55 lens are poorly correlated with those of As, which in turn shows a good positive correlation with Fe (Fig. II. 10A and C). Ni and As are

uncorrelated (Fig. II. 10B). However, the comparison of these data with those of arsenide ores from the F56 lens, the F7/5 orebody and the Aghbar deposit split the plotted results in two well differentiated groups (Figures 10D, E and F): a group with a Co-Ni trend and a group with a Fe trend. The Co-Ni trend includes the samples from Aghbar and some from F7/5 and is defined by a positive correlation between Co and Ni with As, but Fe contents unrelated with those of As. In contrast, the Fe trend is mainly defined by th samples from F55 and most but two samples (the Co and Ni richest ones) from F7/5 and shows a good correlation between Fe and As but no correlation of Co and Ni with As. The only sample analyzed from F56 could be ascribed both to the Ni-Co trend and the Fe trend (Figures 10D, E and F).

Table II. 1. Whole-rock major ore-forming elements and noble metal contents.

	As (ppm)	Co (ppm)	Ni (ppm)	Fe (%)	S (%)	Os (ppb)	Ir (ppb)	Ru (ppb)	Rh (ppb)	Pt (ppb)	Pd (ppb)	Au (ppb)
F55 Lens												
Serpentinite												
AA 13	462	13	1058	5,8	X	5	5	7	X	5	4	4
AA 21	414	67	2302	4,9	0,10	7	7	8	2	13	5	4
AA 22	546	97	2242	5,5	X	6	5	7	X	8	5	4
AA 24	644	169	2445	2,2	X	3	6	6	X	7	2	3
AA 25	505	140	1180	2,7	X	4	5	6	2	6	9	4
AA 27	220	63	1814	6,6	X	4	6	7	X	6	5	5
Talc-rich spentiinite												
AA 2	246	58	931	4	X	X	2	X	X	2	17	3
AA 12	147	25	1011	4	X	X	2	X	X	2	3	X
Carbonated serpentinite (arsenide-poor ores)												
AA 6	38800	132	1735	2,76	0,07	5	6	9	X	4	6	4
West end of lens												
AA 8	19600	754	2978	6	0,24	5	6	8	X	7	7	X
AA 9	355600	2451	2366	18	0,76	9	18	6	3	17	25	34
AA 10	39600	576	2572	4	0,11	3	5	7	2	8	14	3
Lens center												
AA-16	504400	14200	2732	20,6	0,83	X	X	55	X	158	112	491
AA-17	473600	19600	2035	19,6	0,58	X	X	53	X	134	117	341
AA-18	566200	25300	1834	21,5	0,78	X	X	45	X	117	93	358
AA-19A	511600	6345	4701	21,6	0,74	X	X	62	X	93	83	233
AA-19B	540900	11800	870	22,6	0,75	X	X	49	X	139	92	289
AA-20	345000	3183	7093	14,1	0,63	X	X	46	X	90	74	99
F56 ores												
F56-8	257100	26800	4493	8,51	0,48	X	X	48	X	114	87	49
F7/5 deposit												
F7/5-1	264100	2846	4723	11,68	0,42	X	X	59	X	129	79	150
F7/5-2	675900	165500	7103	2,05	1,46	X	X	53	X	129	96	2197
F7/5-3A	367400	9389	12100	14,54	0,66	47	40	118	33	197	133	250
F7/5-3B	410900	10700	9119	14,29	0,73	X	26	77	X	134	92	77
F7/5-4	488200	122900	2737	4,98	1,16	X	X	49	X	101	66	370
F7/5-5A	521200	15800	2630	20,74	0,82	X	X	51	X	105	82	346
F7/5-5B	411500	14400	3242	17,32	0,62	X	X	44	X	82	68	201
F7/5-6	39000	7147	571	6,45	0,54	X	X	63	31	144	98	93
F7/5-7	272000	2878	8126	14,31	0,53	37	31	95	X	142	115	X
F7/5-8	443600	3680	4976	19,96	0,81	X	X	71	X	116	103	964

Aghbar deposit												
AGE-2	563200	126300	20400	2,86	0,72	X	X	54	X	116	97	4766
AGE-5	176600	40200	2793	2,25	0,34	X	X	48	X	99	74	225
AGE-6A	499300	101100	12900	2,09	0,60	X	X	53	X	162	128	2782
AGE-6B	300600	68900	7994	1,62	0,38	X	X	54	X	122	89	942

X: under detection limit caused by high As contents

Platinum-group element contents in barren, noncarbonated serpentinites vary from 22 to 42 ppb (

Table II. 1) and their most frequent chondrite-normalized pattern shows a nearly flat segment from Os to Ru around 10^{-2} times the chondritic values (Naldrett and Duke, 1980) followed by a negative slope from Ru to Rh and a positive-sloped, variably-tilted segment from Rh to Pd (Fig. II. 11A). Some few samples show either Ru and Pt positive anomalies or Pd negative anomalies. The talc-rich serpentinite is extremely depleted in PGE but one of the samples (AA-2) shows a significant enrichment in Pd (17 ppb). In contrast, the chondrite-normalized PGE pattern of carbonated serpentinite mostly mimic that of serpentinites. In ore samples from F55 and F56, bulk Ru, Pt and Pd contents increase above 10 times the chondritic values, as the proportion of arsenide minerals increases always showing chondrite-normalized PGE patterns with positive slopes from Ru to Pd (note that Rh could not be analyzed), plotting within the field of Co-rich ores, above that of Fe-rich ores, as defined by Leblanc and Fischer, (1990) (Fig. II. 11B). PGE values of the F55 ores overlap those of the F5/7 orebody and the Aghbar deposit, showing comparable morphologies of their chondrite- normalized patterns (Fig. II. 11) but plot 10 times above the values reported by Ahmed et al., (2009a) which mostly overlap the field of barren serpentinites.

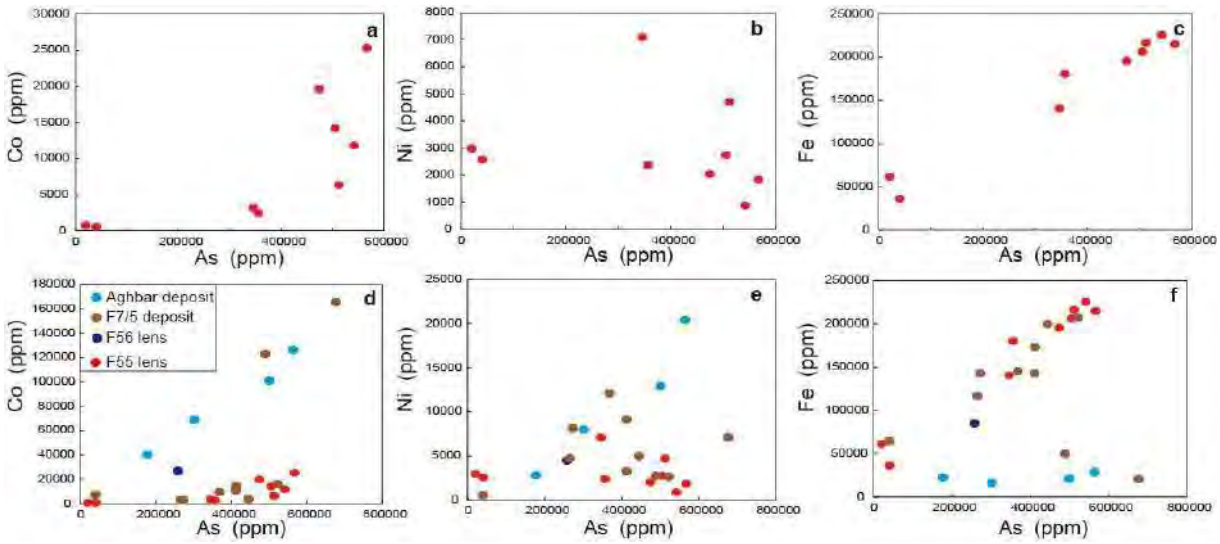

Fig. II. 10. As-Co, As-Ni, and As-Fe diagrams of ores from Ait Ahmane area (F55 and F56), F7/5 and Aghbar deposits (Bou Azzer district, Morocco).

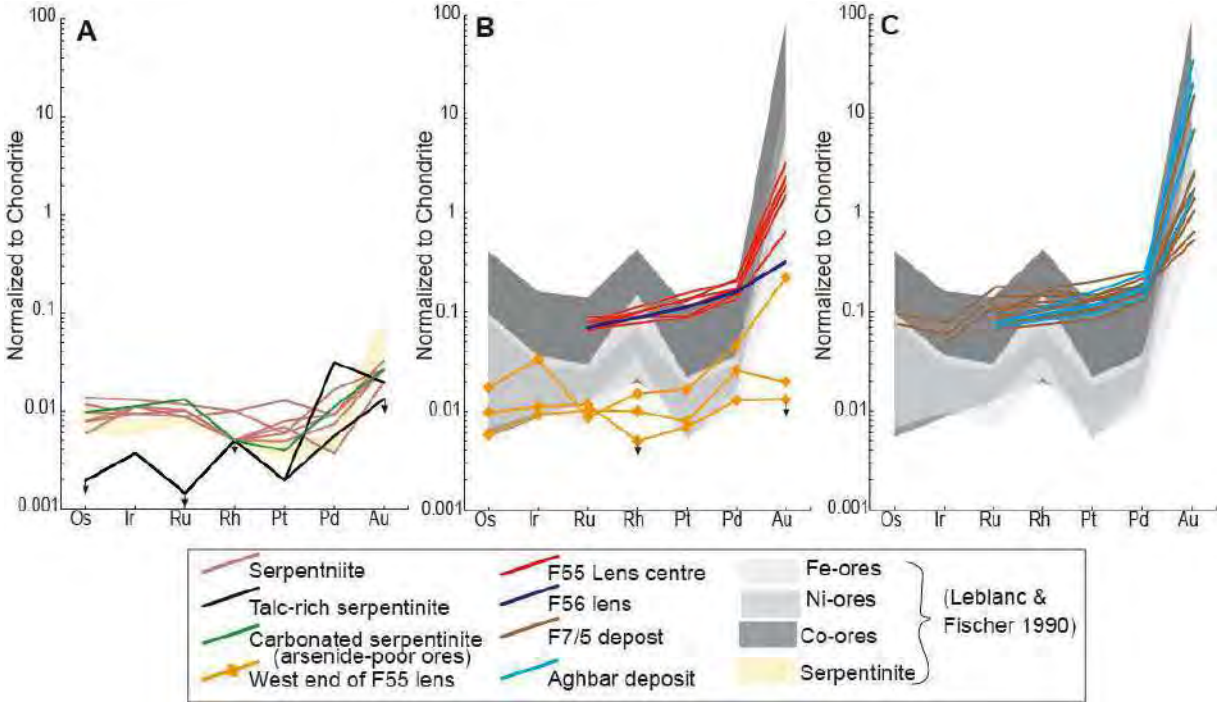

Fig. II. 11. Chondrite-normalized PGE spidergrams of ores from Ait Ahmane area (F56, F55 ores, and its host rocks), F7/5 and Aghbar deposit (Bou Azzer district, Morocco). Normalizing values are taken from Naldrett and Duke (1980).

Taken as a whole, gold contents increase from barren, noncarbonated serpentinites (3-5 ppb Au) to massive ores (34-4766 ppb Au) although in some few samples (both mineralized and barren) they are below detection limit (

Table II. 1). In spite of this trend, gold contents show no correlation with As, excepting for the four samples from the Aghbar deposit. Most samples show positive-sloped segments from Pd to Au in the chondrite-normalized patterns (Fig. II. 11) and as expected, Au contents tend to increase from the F55 lens (99-491 ppm Au) to the F5/7 (0-2197 ppm Au) and mainly the Aghbar (225-4766 ppm Au) deposits as the relative abundance of the high-temperature, Ni-rich ores does (native Au mainly occur included in early formed nickelite and rammelsbergite; Ahmed et al., 2009b; Gervilla et al., 2012).

5 Discussion

5.1 Serpentinite-hosted versus contact ores at Bou Azzer

The studied F55 lens shows some mineralogical and structural features somehow characteristic of serpentinite-hosted ores in the Bou Azzer mining district. The most striking one is the mineralogical composition of the arsenide ore assemblage which is mainly composed of nearly stoichiometric löllingite arranged in aggregates of zoned spindle-like crystals or rosettes. The latter aggregates often contain thin growth bands composed of intermediate members of the rammelsbergite- safflorite-löllingite, rammelsbergite-löllingite and löllingite-safflorite solid solution series (Fig. II. 6; Fig. II. 7A). The mineral chemistry of this assemblage as a whole reveals its characteristic low Ni and relatively low Co nature, allowing a definition for this type of ores as Fe-rich. The second characteristic feature of the F55 serpentinite-hosted orebody is its zoned structure (Fig. II. 3) consisting of massive arsenide ore enveloped by disseminated ore hosted by carbonated serpentinites (Fig. II. 12A).

The comparison of these mineralogical and structural features with those of the other orebodies of the Ait Ahmane district reveals that F56 (a serpentinite-hosted lens but close to a small stock of quartz-diorite) has a similar envelope of carbonated serpentinite (Fig. II. 3), although its mineralogical assemblage is not only dominated by löllingite but contains up to 40 mod. % skutterudite (Co-Fe ore). In other deposits (F1 and F53) of the Bou Azzer district, this Co-Fe ore assemblage is preceded by an earlier Ni-rich one (Ni-Co ore), mainly composed of variable proportions of nickeline, rammelsbergite-safflorite, rammelsbergite-safflorite-löllingite and skutterudite (En-Naciri,1995; En-Naciri et al., 1997; El Ghorfi, 2006, Lasobras, 2012; Maacha, 2013). Interestingly, Gervilla et al.,

(2012) reported a similar two-stage deposition at Aghbar where the early crystallization of Ni-rich arsenide ores was overlapped (and partly replaced) by a later event of ore formation characterized by the development of Co-Fe arsenide ores disseminated in serpentinite (Fig. II. 12B). Furthermore, results on old samples collected by M. Leblanc for his Ph.D. Thesis from the F7/5 orebody show a similar depositional sequence characterized by an early stage of nickeline partly replaced by Ni-rich skutterudite (up to 17 wt.% Ni) followed by the crystallization of diarsenides (rammelsbergite-safflorite, rammelsbergite-safflorite-löllingite and löllingite-safflorite) (Ni-Co ore) and ending with the formation of members of the gersdorffite-cobaltite series (Fanlo et al., 2017). Nevertheless, some samples collected recently from an area currently being mined at the F7/5 orebody (their major ore-forming elements and noble metals contents are listed in

Table II. 1) mainly consist of löllingite-dominated, arsenide ore assemblages (Co-Fe ore) disseminated in serpentine, locally with skutterudite and remnants of Ni-Co arsenides in the massive samples. These sequences of ore-forming events agree with the sequence of deposition for arsenide minerals proposed by Leblanc, (1975) and with those suggested by En-Naciri, (1995); En-Naciri et al., (1997) and Ahmed et al., (2009b) for the whole Bou Azzer district. Therefore, it can be concluded that formation of arsenide ores at Bou Azzer started with the crystallization of massive Ni arsenides followed by Ni-Co arsenides (and sulfarsenides), both filling veins mainly along the quartz diorite-serpentinite contacts, but evolved to the subsequent crystallization of Co-Fe and Fe arsenides disseminated in serpentinite, which show increasing Fe/Co ratio with increasing the distance from the contact with the quartz diorite intrusion. Thus, the ores studied in the F55 lens would represent the crystallization products of residual fluids, formed at the end of the mineralizing events of the Ait Ahmane district.

Whole-rock As, Co, Ni and Fe contents further confirm the existence of two groups of arsenide ores since massive ores from Aghbar and F7/5 deposits show high Ni and Co contents positively correlated with As (the Ni-Co trend). In contrast, massive ores from F55 and those occurring disseminated in serpentinite both in the carbonated halo of F55 and in the new samples from the F7/5 orebody are rich in Fe positively correlated with As (the Fe trend) (Fig. II. 10).

Unlike the relatively homogeneous carbonated nature of the hydrothermal alteration halo around the F55 and F56 lenses, the alteration patterns of all other deposits vary with the lithology of the host rock. The wideness of alteration halos in contact ores from the whole Bou Azzer district ranges from centimeter- to meter-scale consisting of intense chloritization (locally with epidote), silicification and less commonly carbonatization in quartz-diorite, and of carbonatization (mainly calcite) with variable but minor chlorite and talc in the serpentinite (Leblanc, 1975; En-Naciri, 1995; Dolansky, 2007; Maacha, 2013). Ignimbrites from Aghbar become altered to chlorite and various clay mineral assemblages and carbonatization mainly forms dolomite (Dolansky, 2007). This zoning pattern of alteration halos allow correlate the deposition of Ni-rich and Ni-Co, vein-type arsenide ores with the early silicification and chloritization event [e.g. gold occurs associated to chlorite and quartz (Maacha, 2013; Bouabdellah et al., 2016) and mainly included in nickeline and rammelsbergite (Ahmed et al., 2009b; Gervilla et al., 2012)]. With the progressive decrease of pressure and temperature, the mineralizing fluids became less saline but with higher $CaCl_2$/NaCl ratio (Dolansky, 2007) giving rise to the development of the Co-Fe and later Fe arsenide ores associated with calcite alteration in serpentinites. Although fluid inclusion data are scarce and rather controversial (see En-Naciri, 1995; En-Naciri et al., 1997; Dolansky, 2007), the results obtained by Dolansky, (2007) partially agree with the conclusions obtained by Gervilla et al., (2012) from phase relations in the sense that temperature should decrease over the course of ore mineral deposition from >400ºC to >200ºC (these values correspond to trapping temperatures and represent minimum crystallization values; Dolansky, 2007). Unpublished data on chlorite geothermometry obtained from chlorite crystals associated to calcite in Co-Fe ores disseminated in serpentinites in the F7/5 orebody yielded temperatures between 187º and 269ºC (Ares, 2018). These data support the proposed timing of ore formation and carbonate alteration in the F55 lens, at the end of the Co-Ni-Fe arsenide mineralization process, at low temperature.

5.2 *Mechanisms of ore formation: vein filling versus replacement*

The presence of inclusions of serpentine, chlorite and partly corroded crystals and fragments of fractured chromite in arsenide minerals of the F55 lens and in the mineralized serpentinites of the F53, F7/5, Aghbar and Tamdrost contact-type deposits (Gervilla et al.,

2012; Fanlo et al., 2015; Ares, 2018) show that formation of Co-Fe and Fe ores in serpentinites should take place by dissolution/precipitation processes which gave rise to the replacement of serpentinite by skutterudite, löllingite-safflorite and löllingite with variable amounts of calcite. The degree of replacement should be maximum near the main zone of supply of ore-forming fluids (usually the quartz diorite- serpentinite contact) becoming progressively less important away from such zone. Since chromite is ubiquitous in serpentinites and exhibits low solubility under most geological conditions (Oze et al., 2007), it can be used as indicator of the degree of serpentinite replacement (chromite is a high-temperature magmatic mineral and cannot be formed by hydrothermal ore-forming fluids). Thus, chromite relicts shouldn't be expected in massive, Ni-rich arsenide ores but are frequently abundant in mineralized serpentinites with ~10 to 50 mod. % arsenides as occur in Aghbar, Tamdrost and the F53 orebody in Ait Ahmane (Gervilla et al., 2012; Fanlo et al., 2015). In the latter ores, the chemical composition of chromite is not modified during ore-forming processes (except for some slight Co enrichments) preserving a zoning pattern originated during early sea-floor serpentinization and/or Pan- African orogenesis (Fanlo et al., 2015). In contrast, the chromite grains studied in the F55 lens as well as those from some recent samples of the F7/5 orebody (Ares, 2018) show compositions depleted in Al and enriched in both Fe^{2+} and Fe^{3+}, evolving towards the composition of magnetite, and locally become highly altered up to the formation of Cr and Fe hydroxides (Fig. II. 8). This strong alteration degree of chromite took place during the mineralization process and could be associated with small changes in pH and redox conditions of the mineralizing fluids. Although the nature of ore-forming fluids is not well constrained, Dolansky, (2007) argue that they should be slightly acid (pH ~5) and reduced (CH_4 and N_2 predominate over CO_2 in the vapor phase and H_2S in solution) containing Cl^- andHCO_3^- (Fig. II. 12). Assuming that the F55 lens formed at low temperature (~200ºC), from the latest mineralizing fluids in the Ait Ahmane district it would be possible that fluids evolved towards slightly higher pH values and oxidizing conditions, increasing the proportions of CO_2 and CO_3^{2-} (over HCO_3^-), promoting the dissolution of serpentine, the increase in the magnetite component of chromite, the formation of Cr and Fe hydroxides at fO_2 maxima, the mobilization of silica out of the reactive zone (Ulrich et al., 2014) and the precipitation of

calcite-rich Fe arsenides. The mobilization out of silica can control the local formation of talc-rich serpentinites.

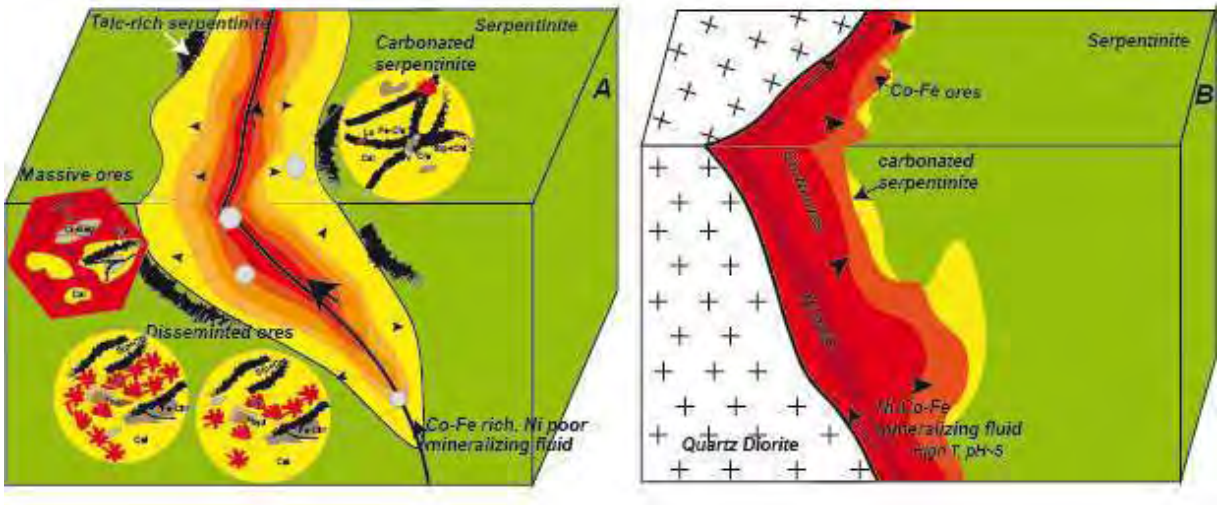

Fig. II. 12. Schematic bloc diagram of ores zoning in the serpentinite hosted ores (F55 lens, A), and in contact-type ores (B).

The zoned structure of the F55 lens suggest that the core of massive ore could represent the reactive zone with higher fluid/rock ratio and that the disseminated envelope should generate under decreasing fluid/rock ratios forming dense networks of thin stockwork-ore veins in a poorly disseminated serpentine matrix near the contact with the massive core, evolving outwards to less and less volume of veins up to the formation of vein-free, disseminated ores in serpentine (Fig. II. 12A). This model could also apply to the more frequent contact ore bodies in Bou Azzer. In this scenario, it could be expected that massive Ni-Co arsenide ores form first at high temperature, filling fault-related, open spaces generated along the contacts between serpentinite and quartz diorite (gabbros, volcanic or sedimentary rocks) (Fig. II. 12B). This type of ore should exhibit sharp contacts with the quartz diorite intrusion such as observed in F7/5. Upon the events of mineral deposition, evolving fluids were very likely first channeled along the contact between the early formed Ni-Co ores promoting their partial replacement and subsequently flooded over the serpentinite giving rise to the development of semimassive and disseminated Co-Fe ores (Fig. II. 12B).

5.3 *Sources for major ore-forming metals*

Regardless of the magmatic or meteoric origin (or a mixture of both provenances) of the ore- forming fluids, there is a general consensus on the role played by serpentinites as source of Co and Ni; in contrast, the origin of As remains controversial (see Leblanc, 1975; Leblanc and Billaud, 1982; Leblanc and Fischer, 1990; En-Naciri, 1995; En-Naciri et al., 1997; Dolansky, 2007; Ahmed et al., 2009b; Maacha, 2013; and Bouabdellah et al., 2017). Although the whole-rock data presented here (

Table II. 1) are still scarce, they provide valuable information on barren, variably carbonated serpentinites (from noncarbonated to serpentinites almost completely replaced by carbonates) as well as on four deposits containing Ni-Co ores (Aghbar), Co-Fe ores (F7/5 and F56) and Fe ores (F55), thus allowing debate on the possible fluid-mediated exchange of As, Co, Ni and Fe between serpentinite and ores.

The high As content of serpentinites (up to 644 ppm) in the Ait Ahmane area (

Table II. 1) indeed suggest a role of this rock type as source for this element. However, the extremely high As concentrations of the hosted arsenide ores of its nearby F55 lens (~10^3 times higher) should require extensive leaching of these serpentinites. In contrast, the analyzed samples are far to be depleted in Asbut still contain ~10^4 times the primitive mantle values (Fig. II. 8). These values are also higher than those of other As-rich serpentinites described in literature (e.g. 6-275 ppm As, Hattori et al., 2005).

A different scenario can be envisaged for Co, Ni and Fe if one assumes that their budget in peridotites shouldn't be substantially affected by serpentinization. The contents of Co in six of the eight barren serpentinites and talc-rich serpentinites analyzed ranges from 13 to 97 ppm (

Table II. 1), well below the values expected for serpentinites derived from depleted mantle peridotites [e.g. Marchesi et al., (2016) reports ~142 ppm Co in harzburgite and ~152 ppm Co in dunite]. Similarly, five of the eight barren serpentinites and talc-rich serpentinites, as well as the carbonated serpentinite, are depleted in Ni (931-1814 ppm Ni;

Table II. 1) with respect to mantle harzburgite (~2106 ppm Ni) and dunite (~2905 ppm Ni) (Marchesi et al., 2016). The Fe-depleted nature of the studied Ait Ahmane serpentinites relative to the expected harzburgite and dunite protoliths is not so evident as for Co and Ni

since only two of the six serpentinites, as well as the talc-rich serpentinites and the carbonated serpentinite have Fe contents (2.18-3.51 wt.%) well below those expected in dunite and harzburgite [4.77 and 5.46 wt.% Fe; calculated from Marchesi et al., (2016)]. Nevertheless, the presence of magnetite veins with bleached serpentinite walls (Hodel et al., 2017) evidence that Fe was extensively mobilized during hydrothermal alteration of serpentinites.

PGE contents in arsenide ores are 10 times above those reported for serpentinites but the morphology of the chondrite-normalized PGE patterns of the latter rocks, similar to depleted-mantle rocks but with Pd positive anomalies, suggest a more complex process of leaching. PGE leaching from serpentinites could be associated with silica alteration since the lowest values were found in the talc- rich serpentinites. Au contents are anomalously high in all analyzed rock-types; in fact, serpentinites show Au values slightly above 3 to 5 times the primitive mantle values (0.88 ppb Au; Lyubetskaya and Korenaga, 2007), in spite of the depleted nature of the mantle protoliths.

The reported contents of major ore-forming elements and noble metals allow linking the origin of Co, Ni, Fe and PGE with the Bou Azzer serpentinite but do not support any connection between As and Au with such rocks. The infiltration of high-temperature hydrothermal fluids (most probably well above 400ºC) though serpentinites during the Hercynian orogeny [most geological and geochronological data support that the mineralization event took place between 380 and 310 Ma; e.g. Levresse, 2001; Gasquet et al., 2005; Dolansky, 2007; Oberthür et al., 2009; Bouahdellah et al., 2016)] leached Co, Ni, Fe and PGE from these ultramafic rocks and became channeled mainly along the quartz-diorite-serpentinite contacts promoting the crystallization of Ni and Ni-Co ores under extremely high fluid/rock ratios. The resulting Ni-impoverished fluids shifted their flow paths to the contacts between the early formed Ni-Co ores and serpentinites maintaining high fluid/rock ratios nearby the contacts but diminishing such rations away from them. With the evolution of the hydrothermal system towards lower pressures and temperatures, fluids should have precipitated those Co-Fe ores that now are partly replacing Ni-Co ores, filling thin entwined veins and/or disseminated in serpentinite. Under the lower temperature estimated (~200ºC) for the formation of the F55 lens, the residual fluids could locally concentrate along weak zones (e.g. faults) within serpentinites forming Fe ores. This mechanism of fractionation of the infiltrating

(metasomatic) fluids partly explains the anomalously high Co/Ni ratio of arsenide ores relative to the same ratio in serpentinites, although more precise mass balance calculations would be necessary to assure that serpentinites are the only source of Co. Since the origin of As and Au seems unrelated with the serpentinites, they should be supplied to the mineralizing hydrothermal fluids after leaching country-rocks from older geological units. The latter may include organic-rich black shales of the Imiter Group, which could be good candidates as source of As and as additional source of Co (they contain up to 6180 ppm As and 36,8 ppm Co on average; Pasava, 1994), thus justifying the anomalously high concentration of Co (and the high Co/Ni ratio) in the Bou Azzer ores well above that expected from lixiviation of only serpentinites. The origin of Au is more enigmatic but could be linked with some of the acid/intermediate igneous rocks (granodiorite, monzonite, pegmatite…) of Lower Cryogenian age present in the Bou Azzer inlier. This is clearly a fertile field for further investigation.

6 Conclusions

Fe-rich, serpentinite-hosted ores in the Ait Ahmane area (e.g. the F55 lens) show lens-like morphology and a zoned structure with core of massive ore evolving progressively to disseminated ore in carbonated serpentinite, arsenide-poor, carbonated serpentinite, and talc-rich serpentinite, away from the ore lens. Ore assemblage consists of löllingite in calcite-dominated gangue (± serpentine ± chlorite) containing scattered zoned grains or fragments of fractured grains of chromite. Löllingite occurs as massive aggregates of spindle-shaped, zoned crystal containing Co-rich bands or arranged in rosette-like aggregates, showing Ni-rich cores and Co- and Ni-rich growth bands. The F56 lens, occurring close to a quartz-diorite intrusion are also mainly made up of loelllingite but contain around 40 mod. % skutterudite in the arsenide ore assemblage.

In contrast to the Fe-rich, serpentinite-hosted ores, the more frequent contact-type ores in the Bou Azzer district consist of Ni-rich ores (mainly nickeline and rammelsbergite) evolving to, and partly replaced by Ni-Co (rammelsbergite-saffloritea, rammelsbergite-safflorite-löllingite, skutterrudite and safflorite) and Co-Fe ores (rammelsbergite-safflorite-löllingite, löllingite-safflorite, skutterudite, löllingite and cobaltite). Whereas Ni and Ni-Co ores tend to be massive and locate along the fault-zone that put together

serpentinites and other rocks (quartz diorite, gabbros, volcanic rocks, sedimentary rocks), Co-Fe ores are preferentially found as disseminations in serpentinites. Whole- rock, major element contents further contribute to differentiate contact-type and serpentinite-hosted ores since the former show characteristic positive correlation between Ni and Co with As, whereas in the serpentinite-hosted ores As correlates only with Fe.

Accessory chromite associates only with Co-Fe- and Fe-rich ores, occurring as partly dissolved zoned grains and fragments of fractured grains included in arsenide minerals, calcite and serpentine. Its composition reveals increasing depletion in Al and Cr coupled with enrichment in Fe^{3+} and Fe^{2+} up to the formation of Fe^{3+} and Cr hydroxides from barren carbonated serpentinites to massive ores. These textural and chemical features support a genetic model of Co-Fe- and Fe-rich ores based on dissolution/precipitation reactions of low-temperature, ore-forming fluids while migrate through serpentinite under slightly alkaline and oxidizing conditions, with increasing $CaCl_2$/NaCl ratio. In this scenario, partly fractured and altered chromite grains constitute residues of the serpentinite replacement.

The studied serpentinite-hosted ores formed by the infiltration of low-temperature (~200ºC) hydrothermal fluids in serpentinites at the end of the Hercynian orogeny. Ore-forming fluids channeled along intra serpentinite fault zones, promoting the formation of massive ores under high fluid/rock ratio, and subsequently infiltrated into the host serpentinite through a network of thin entwined veins and intergranularly, giving rise to semimassive and disseminated ores. This model can be applied too, to the formation of contact-type ores where high-temperature fluids channeled along the fault separating serpentinite and quartz diorite (or other rocks) promoting the sequential crystallization of Ni- and Ni-Co-rich ores in fault-related open spaces followed by Co-Fe ores in serpentinites under progressively less temperature (from >400º to <200ºC). The formation of the latter ores in serpentinites took place by the same dissolution/precipitation processes as described for serpentinite-hosted ores.

Whole-rock data suggest that Ni, Co, Fe and platinum-group elements were leached out from serpentinites by the ore-forming fluids whereas As and Au should come from different lithological units in the Bou Azzer inlier. A good candidate for As could be the organic-rich black shales of the Imiter Group which could also supply additional Co. The

source of Au could be related with the Lower Cryogenian acid/intermediate magmatism reported in Bou Azzer.

Declaration of Competing Interest

The authors declare the following financial interests/personal relationships which may be considered as potential competing interests: This study was supported by the Spanish project RTI2018-099157-A-I00 granted by the "Ministerio de Ciencia, Innovaci´on y Universidades" as well as the Ram´on y Cajal Fellowship RYC-2015-17596 granted to JMGJ by the "Ministerio de Economía y Competitividad" (MINECO).

Acknowledgements

This research was supported by the Spanish project RTI2018-099157-A-I00 granted by the "Ministerio de Ciencia, Innovación y Universidades" as well as the Ramón y Cajal Fellowship RYC- 2015-17596 granted to JMGJ by the "Ministerio de Economía y Competitividad" (MINECO). We wish thank Dr. Moha Ikenne and Dr. Ilya Prokopyev for their constructive review, which helped to improve the presentation of the data and the discussion.

Appendix 1. Supplementary data

Supplementary data to this article can be found in Appendix 1

References

Admou, H., 2000. Structuration de la paléosuture ophiolitique panafricaine de Bou Azzer- Siroua. Anti-Atlas central, Maroc. PhD thesis, Cadi Ayyad University, Marrakech, Morocco, 201p.

Ahmed, A.H., Arai, S., Abdel-Aziz, Y.M., Rahimi, A., 2005. Spinel composition as a petrogenetic indicator of the mantle section in the Neoproterozoic Bou Azzer ophiolite, Anti-Atlas, Morocco. Precamb. Res. 138, 225–234.

Ahmed, A.H., Arai, S., Abdel-Aziz, Y.M., Ikenne, M., Rahimi, A., 2009a. Platinum-group elements distribution and spinel composition in podiform chromitites and associated rocks from the upper mantle section of the Neoproterozoic Bou Azzer ophiolite, Anti- Atlas, Morocco. J. Afr. Earth Sci. 55, 92–104.

Ahmed, A.H., Arai, S., Ikenne, M., 2009b. Mineralogy and Paragenesis of the Co-Ni Arsenide Ores of Bou Azzer, Anti-Atlas, Morocco. Econ Geol, 104, 249–266.

Alves-Dias, P., Blagoeva, D., Pavel, C., Arvanitidis, N., 2018. Cobalt: demand-supply balances in the transition to electric mobility. JRC Science for Policy Report. European Commision.https://publications.jrc.ec.europa.eu/repository/bitstream/JRC112285/jrc112285_cobalt.pdf

Ares A., 2018. Las espinelas cromíferas del filón 7/5 del distrito minero de Bou Azzer (Marruecos): residuos del reemplazamiento de serpentinitas. TFM. Universidad de Huelva-Universidad Internacional de Andalucía. 54p.

Bhlisse, M., 2018. Etude structurale, minéralogique et géochimique des serpentinites associées aux minéralisations polymétalliques du district de Bou Azzer-El Graara (Anti- Atlas central). Ph.D. thesis, Cadi Ayyad University, Marrakech, Morocco, 274p.

Blein, O., Baudin, T., Chèvremont, P., Soulaimani, A., Admou, H., Gasquet, P., Cocherie, A., Egal, E., Youbi, N., Rzin, P., Bouabdelli, M., Gombert, P., 2014. Geochronological constraints on the polycyclic magmatism in the Bou Azzer-El Graara inlier (Central Anti-Atlas Morocco). J. Afr. Earth Sci. 99, 287–306.

Bouabdellah, M., Maacha, L., Levresse, G., Saddiqi, O., 2016. The Bou Azzer Co–Ni–Fe–As (– Au – Ag) District of Central Anti-Atlas (Morocco): A Long-Lived Late Hercynian to Triassic Magmatic-Hydrothermal to Low-Sulphidation Epithermal System, Mineral Deposits of North Africa, (eds.), Mineral Deposits of North Africa, Mineral Resource Reviews, 229-247

Bodinier, J. L., Dupuy, C., Dostal, J., 1984. Geochemistry of Precambrian ophiolites from Bou Azzer, Morocco. Contrib. Mineral. Petrol., 87, 43-50

Bouchador, A., 2012. Etude géologique et métallogénique des gîtes arséniés de Co-Ni dans le filon 57 ; Champs filonien d'Aït Ahmane, District minier de Bou Azzer, ophiolite de Bou Azzer, Anti Atlas Central, Maroc. Master, Cadi Ayyad University, Marrakech, Morocco, 102p.

Bouougri, E., Ait Lahna, A., Tassinari, C.C.G., Basei, M. A.S., Youbi, N., Admou, H., Saquaque, A., Boumehdi, A., Maacha, L., 2020. Time constraints on early Tonian Rifting and Cryogenian Arc terrane-continent convergence along the northern margin of the West African craton: Insights from SHRIMP and LA-ICP-MS zircon geochronology in the Pan-African Anti-Atlas belt (Morocco). Gondwana Res. 85, 169-188

Choubert, G., 1963. Histoire géologique du précambrien de l'Anti-Atlas. Notes et mém. Serv. Géol. Maroc, 162, 352p

Clauer, N., 1974. Utilisation de la méthode Rb–Sr pour la datation d'une schistosité de sédiments peu métamorphisés : application au Pré - cambrien II de la boutonnière de Bou–Azzer–El Graara (Anti-Atlas, Maroc). Earth Planet. Sci. Lett. 22, 404–412.

D'Lemos, R.S., Inglis, J.D., Samson, S.D., 2006. A newly discovered orogenic event in Morocco: Neoproterozoic ages for supposed Eburnean basement of the Bou Azzer inlier, Anti-Atlas Mountains. Precamb. Res. 147, 65–78.

Dolansky, LM., 2007. Controls on the genesis of hydrothermal cobalt mineralization: insights from the mineralogy and geochemistry of the Bou Azzer deposits, Morocco. Master, McGill University, Montréal, Canada, 162p

EL Ghorfi, M., 2006. Etude géochimique et métallogenique des métaux précieux (or, argent et platinoïdes) associes aux minéralisations à Co, Ni, Cr de Bou Azzer-El Graara, et dans la série de Bleida Far West, Anti-Atlas, Maroc. PhD thesis, Cadi Ayyad University, Marrakech, Morocco, 256 p.

El Hadi, H.F., 1988. Etude pétrographique et géochimique des cumulats ultramafiques et mafiques

du complexe ophiolitique de Bou Azzer El Graara (Anti-Atlas, Maroc). Thèse 3ème cycle, Cadi Ayyad University, Marrakech, Morocco, 173p.

EL Hadi, H.E., Simancas, J.F., Martinez-Poyatos, D., Azor, A., Tahiri, A., Montero, P., Bea, C.M., Gonzalez-lodeiro, F., 2010. Structural and geochronological constraints on the evolution of the Bou Azzer Neoproterozoic ophiolite (Anti-Atlas, Morocco). Precamb. Res. 182, 1–14.

En-Naciri, A., 1995. Contribution à l'étude du district à Co. As (Ni, Au, Ag) de Bou Azzer. Anti-Atlas (Maroc) Données minéralogiques et géochimiques. PhD thesis, Université d'Orléans. France 245 p.

En-Naciri, A., Barbanson, L., Touray, J.C., 1997. Brine inclusions from the Co-As (Au) Bou Azzer district, Anti-Atlas, Morocco. Econ Geol, 92, 360-367.

Fanlo, I., Gervilla, F., Colás, V., Subías, I., 2015. Zn-, Mn- and Co-rich chromian spinels from the Bou-Azzer mining district (Morocco): Constraints on their relationship with the mineralizing process. Ore Geol. Rev. 71, 82–98.

Fanlo, I., Arranz, E., Subías, I., Gervilla, F., 2017. The Filon 7/5 (Bou Azzer district, Morocco): an example of Co-Ni ores formation under disequilibrium conditions. In: Mineral Resources to Discover. Proceedings of the 14th Biennial SGA Meeting, v. 1, pp. 1531-1534.

Gahlan, H., Arai, S., 2007. Genesis of peculiarly zoned Co, Zn and Mn-rich chromian spinel in serpentinite of Bou Azzer ophiolite, Anti Atlas, Morocco. J. Miner. Petrol. Sci, 102, 69-85.

Gasquet, D., Levresse, G., Cheilletz, A., Azizi-Samir, M.R., Mouttaqi, A., 2005. Contribution to a geodynamic reconstruction of the Anti-Atlas (Morocco) during Pan-African times with the emphasis on inversion tectonics and metallogenic activity at the Precambrian- Cambrian transition. Precamb. Res.140, 157–182.

Gervilla, F., Fanlo, I., Colás, V., Subías, I., 2012. Mineral compositions and phase relations of Ni–Co–Fe arsenide ores from the Aghbar mine, Bou Azzer, Morocco. Can. Mineral. 50,2, 447–470.

Hajjar, Z. 2011. Contribution à l'étude des Filons F53, F54, F55, champs minier d'Aït Ahmane (Bou Azzer, Anti Atlas, Maroc). Master, Cadi Ayyad University, Marrakech, Morocco, 105p.

Hattori, K., Takahashi, Y., Guillot, S., Johanson, B., 2005. Occurrence of arsenic (V) in forearc mantle serpentinites based on X-ray absorption spectroscopy study. Geochim. Cosmochim. Acta, 69, 23, 5585–5596.

Hefferan, K., Soulaimani, A., Samson, S.D., Admou, H., Inglis, J., Saquaque, A., Chaib, L., Heywood, N., 2014. A reconsideration of Pan African orogenic cycle in the Anti-Atlas Mountains, Morocco. J. Afr. Earth Sc. 98, 34-46

Hilal, R., 1991. L'ophiolite de Bou Azzer (Anti-Atlas, Maroc) structure, perographie, géochimie, et contexte de mise en place. Thèse 3ème cycle, Cadi Ayyad university, Marrakech, Morocco, 175p

Hodel, F., Macouin, M., Triantafyllou, A., Carlut, J., Berger, J., Rousse, S., Ennih, N., Trindade, R.I.F., 2017. Unusual massive magnetite veins and highly altered Cr-spinels as relics of a Clrich acidic hydrothermal event in Neoproterozoic serpentinites (Bou Azzer ophiolite, Anti-Atlas, Morocco). Precamb. Res. 300, 151-167

Hodel, F., Triantafyllou, A., Berger, J., et al., 2020. The Moroccan Anti-Atlas ophiolites: Timing and melting processes in an intra-oceanic arc-back-arc environment, Gondwana Res. 86, 182-202

Ikenne, M., Souhassou, M., Saintilan, N.J., Karfal, A., El Hassani, A., Moundi, Y., Ousbih, M., Ezzghoudi, M., Zouhir, M., Maacha, L., 2020. Cobalt-Nickel-Copper arsenide, sulpharsenide

and sulphide mineralisation in the Bou Azzer window, Anti-Atlas, Morocco: One century of multi-disciplinary and geological investigations, mineral exploration and mining. Geological Society, London, Special Publications, 502, https://doi.org/10.1144/SP502-2019-132

Inglis, J.D., Samson, S., D'Lemos, R.S., Admou, H., 2003. Timing of regional greenschist facies deformation in the Bou Azzer Inlier, Anti-Atlas: U–Pb constraints from syntectonic intrusions. First meeting of IGCP 485, El Jadida, Morocco, 40–42pp.

Inglis, J.D., MacLean, J.S., Samson, S.D., D'Lemos, R.S., Admou, H., Hefferan, K., 2004. A precise U– Pb zircon age for the Bleida granodiorite, Anti-Atlas, Morocco: implications for the timing of deformation and terrane assembly in the eastern Anti-Atlas. J. Afr. Earth Sc, 39, 277–283.

Lasobras, E., 2012. Composición mineral y relaciones de fase de los arseniuros de Co-Fe-Ni del yacimiento de Aït-Ahmane (Bou-Azzer, Marruecos). Diferencias con otros depósitos. TFM., Universidad de Zaragoza. Spain, 53p.

Leblanc, M., 1975. Ophiolites précambriennes et gîtes arséniés de Cobalt (Bon Azzer. Maroc). PhD thesis, Univ. Paris VI, France, 329p.

Leblanc, M., 1981. Ophiolites précambriennes et gîtes arséniés de cobalt (Bou Azzer-Maroc). Notes et mém. Serv. Géol. Maroc, 280, 311p.

Leblanc, M., Billaud, P., 1982. Cobalt arsenide orebodies related to an Upper Proterozoic ophiolite: Bou Azzer (Morocco). Econ Geol. 77, 162-175.

Leblanc, M., Fischer, W., 1990. Gold and platinum group elements in cobalt-arsenide ores: Hydrothermal concentration from a serpentinite source-rock (Bou Azzer, Morocco). Miner. Petrol., 42, 197-209.

Levresse, G., 2001. Contribution à l'établissement d'un modèle génétique des gisements d'Imiter (Ag-Hg), Bou Madine (Pb-Zn-Cu-Ag-Au) et Bou Azzer (Co-Ni-As-Ag-Au) dans l'Anti-Atlas marocain. Ph.D. thesis, CRPG-CNRS, Nancy, France, 191p.

Lyubetskaya, T., Korenag, J., 2007. Chemical composition of Earth's primitive mantle and its variance. J. Geophys. Res., 112, B03211. 21p

Maacha, L., 2013. Etude méallogéniques et géophysiques des minéralisations cobaltifères et cuprifères de Bou-Azzer El Graara Anti Atlas Maroc (Tome 1). PhD thesis, Cadi Ayyad University, Marrakech, Morocco, 344p.

Maacha, L., En-Naciri, O., El Ghorfi, M., Saquaque, A., Alansari, A., Soulaimani, A., 2011. Le district à cobalt, nickel et arsenic de Bou Azzer (Anti-Atlas central). Notes et mém. Serv. Géol. Maroc, 9, 91-97.

Maacha, L., Lebedev, V.I., Saddiqi, O., Zouhair, M., El Ghorfi, M., Borissenko, A.S., Pavlova, G.G., 2015a. Arsenide deposits of the Bou Azzer ore district (anti-atlas metallogenic province) and their economic outlook. editor acad. RAS, doctor of geology V.V. Yarmolyuk – Kyzyl: TuvIENR SB RAS, 66 p.

Maacha, L., El Ghorfi, M., En-Naciri, A., Sadiqqi, O., Soulaimani, A., Alansari, A., Bhilisse, M., 2015b. Nouvelles données isotopiques et d'inclusions fluides des minéralisations cobaltifères de Bou Azzer. Apport à la géologie économique de la boutonnière. (Anti- Atlas central, Maroc). Notes et mém. Serv. Géol. Maroc, 579, 133-139.

Marchesi, C., Garrido, C. J., Proenza, J.A., Hidas, K., Varas-Reus, M. I., Butjosa, L., Lewis J.F., 2016. Geochemical record of subduction initiation in the sub-arc mantle: Insights from the Loma

Caribe peridotite (Dominican Republic). Lithos 252–253, 1–15.

Mrini, Z., 1993. Chronologie (Rb–Sr, U–Pb), traçage isotopique (Sr–Nd-Pb) des sources des roches Magmatiques éburnéennes, panafricaines et hercyniennes du Maroc PhD thesis, Cadi Ayad University, Marrakech, 227p.

Naïdoo, D.D., Bloomer, S.H., Saquaque, A., Hefferan, K., 1991. Geochemistry and significance of metavolcanic rocks from the Bou-Azzer-El Graara ophiolite (Morocco). Precamb. Res. 53, 79-97.

Naldrett, A.J., Duke, J.M., 1980. Platinum metals in magmatic sulfide ores. Science, 208, 811 1417-1424

Nataf, F., 2003. Jean epinat. Un homme, une aventure au Maroc. Souffles, 160 pp.

Oberthür, T., Melcher, F., Henjes-Kunst, F., Gerdes, A., Stein, H., Zimmerman, A., El Ghorfi, M., 2009. Hercynian age of the cobalt-nickel-arsenide-(gold) ores, Bou Azzer, Anti-Atlas, Morocco: Re-Os, Sm-Nd, and U-Pb age determinations. Econ Geol. 104, 1065–1079.

Oze, C., Bird, D.K., Fendorf, S., 2007. Genesis of hexavalent chromium from natural sources in soil and groundwater. PNAS, 104, 16, 6544 – 6549.

Pasava, J., 1994. Geochemistry and role of anoxic sediments in the origin of the Imiter silver deposit in Morocco. Czech Geol. Surv. Bull., 69, 1-11.

Samson, S.D., Inglis, J.D., D'Lemos, R.S., Admou, H., Blichert-Toft, J., Hefferan, K. 2004. Geochronological, geochemical, and Nd-Hf isotopic constraints on the origin of Neoproterozoic plagiogranites in the Tasriwine ophiolite, Anti-Atlas orogen, Morocco. Precamb. Res. 135, 133–147.

Saquaque, A., 1992. Un exemple de suture-arc de Précambrien de l'Anti-Atlas Centro- Oriental (Maroc). PhD thesis, Cadi Ayyad University, Marrakech, Morocco, 338.

Saquaque, A., Admou, H., Karson, J.A., Hefferan, K., & Reuber, I., 1989. Precambrian accretionary tectonics in the Bou Azzer-El Graara region. Geology, 17, 1107–1110.

Talha, M., 2011. Cartographie et métallogénie de la minéralisation arséniée à Co-Ni du filon 52, secteur d'Aït Ahmane, ophiolite de Bou Azzer, Anti-Atlas central, Maroc. Master, Cadi Ayyad University, Marrakech, Morocco, 91p.

Tekiout, B., 1991. Stratigraphie, pétrographie, géochimie et structure de l'ensemble arc/avant arc de la Boutonnière de Bou Azzer-El Graara (unité nord) Anti-Atlas Maroc. Thèse 3ème Cycle, Cadi Ayyad University, Marrakech, Morocco, 151p.

Triantafyllou, A., Berger, J., Baele, J.M., Mattielli, N., Ducea, M.N., Sterckx S., Samson S., Hodel, F., Ennih, N., 2020. Episodic magmatism during the growth of a Neoproterozoic oceanic arc (Anti-Atlas, Morocco). Precamb. Res. 339, April 2020, 105610

Ulrich, M., Munöz, M., Guillot, S., Cathelineau, M., Picard, C., Quesnel, B., Boulvais, P., Couteau, C., 2014. Dissolution–precipitation processes governing the carbonation and silicification of the serpentinite sole of the New Caledonia ophiolite. Contrib Mineral Petrol. 167: 952, 1-19.

Chapter III: Cr-spinel tracks genesis of Co-Fe ores by serpentinite replacement at Bou Azzer, Morocco

This chapter III corresponds to a paper:

Hajjar, Z., Ares, G., Fanlo, I., Gervilla, F., González-Jiménez, J.M., 2022. Cr-spinel tracks genesis of Co-Fe ores by serpentinite replacement at Bou Azzer, Morocco. Journal of African Earth Science, 188, 104471. (IF. 2.468)

Abstract

Co-Fe arsenide ores are associated to serpentinite with alteration haloes of carbonation and talcification in the Bou Azzer inlier (Central Anti Atlas, Morocco). These Co-Fe rich ores consist mainly of skutterudite and members of the löllingite-safflorite series, associated to accessory Cr-spinel grains. Cr-spinel grains exhibit modal abundance and texture-typology inversely correlated with the proportion of Co-Fe arsenide in both Co-Fe arsenide ores and their hosting alteration haloes in serpentinite. So, Cr-spinel grains exhibit distinct textures depending on their relation with the Fe-Co ore: (1) Type 1A zoned grains, consist of homogenous cores of Cr- and Fe^{2+}-rich Cr-spinel surrounded by ferrian chromite rims, which are usually found in carbonatized and talc-rich serpentinite, and in disseminated Co-Fe arsenide ores. (2) Type 1B zoned grains, consist of porous cores of Cr-Fe hydroxides rimmed by ferrian chromite with rare irregular bands of Cr- and Fe^{2+}-rich spinel. They are exclusively hosted by disseminated arsenide ores from F55 and F7/5 orebody. (3) Type 2 grains, consist of homogenous ferrian chromite hosted in löllingite and, at a lesser extent in calcite, in serpentinite hosted massive and disseminated arsenide ores. (4) Type 3 grains, correspond to partly dissolved ferrian chromite, and Cr-Fe hydroxide, associated to chlorite from disseminated Co-Fe arsenide ores.

Type 1A zoned Cr-spinel was produced by an event of ocean-floor serpentinization that affected these mantle rocks during Neoproterozoic times. In contrast, the others three types of Cr-spinel crystals (Type 1B, Type 2 and Type 3) associated to Co-Fe arsenide ores from F/5 and F55 orebody, were produced during the Co-Fe arsenide ore-forming event(s). So, the

infiltration of low temperature, highly oxidizing $CaCl_2$-rich hydrothermal fluids through fractures dissolved partially pre-existing serpentinite, while precipitating Co-Fe arsenides ± calcite assemblage. The first sign of mineralizing fluid infiltration is recorded in the zoned Cr-spinel grains by the replacement of homogenous cores (in Type 1A) by Cr-Fe hydroxide, giving rise to zoned Cr-spinel with porous core (i.e., Type 1B). The increase of Co-Fe arsenides precipitation further promoted dissolution of ferrian chromite and Cr-Fe hydroxide (i.e., Type 3) erasing relicts of former grains, nevertheless some homogenous Cr-spinel grains (i.e., Type 2) persist included in calcite and löllingite in disseminated and massive arsenide ores hosted in serpentinite.

Key words: Cr-spinel, Co-Fe ores, serpentinite, Bou Azzer

1. Introduction

Cr-spinel $(Mg,Fe^{2+})(Cr,Al,Fe^{3+})_2O_4$, is an omnipresent accessory phase in mafic and ultramafic rocks, which showcase a full record of the post-magmatic alteration processes such metamorphism that usually affect these rocks during or after their emplacement into the crust (e.g., Evans and Frost 1975; Bliss and MacLean 1975; Frost 1991; Abzalov 1998; Burkhard 1993; Barnes 2000; Barnes and Roeder, 2001; Proenza et al. 2004; González-Jiménez et al. 2009; Mukherjee et al. 2010; Arai and Ishimaru, 2011; Gervilla et al., 2012a; Prabhakar and Bhattacharya 2013; Barra et al., 2014; Talukdar et al., 2017; Colás et al., 2018). There is a general agreement that the final alteration product of Cr-spinel is usually the so-called ferrian chromite, i.e., a Cr-spinel with high Fe^{3+} contents as well as high Cr/Al and low Mg/Fe^{2+}ratios in a partially inverse, magnesioferrite-type structure (Sergeeva et al., 2017). The replacement of magmatic chromite by ferrian chromite is thought to take place in two separated stages (Gervilla et al., 2012a, 2019): an early one under reduced conditions during which Cr-spinel reacts with host olivine giving rise to porous, ferrous chromite (depleted in Al and Mg) and chlorite, and a second oxidizing stage that often obliterates the former, characterized by significant addition of Fe^{3+} migrating from grain boundaries and fracture walls towards the interior of grains. The extent of alteration in single grains depends on the original composition of Cr-spinel as well as the temperature, fluid/rock ratio and Cr-spinel/silicate ratio being increasingly effective in Al-rich Cr-spinel, at high temperature, increasing fluid pressure and decreasing modal proportions of Cr-spinel (Candia and Gaspar, 1997; Proenza et al., 2004; González-Jiménez et al., 2009; Gervilla et al., 2012a, 2019; Satsukawa et al., 2015). This process may also involve significant enrichment in Mn, Zn and, to a lesser extent Co in ferrian chromite (e.g., Sing and Sing, 2013; Colás et al., 2014; González-Jiménez et al., 2015, 2016), which in some cases as in Bou Azzer may be related to the interaction of Cr-spinel-alteration fluids with nearby Zn-Cu-Co-Ni ores or ore-forming environments (Groves et al., 1977, 1983; Wylie et al., 1987; Gahlan and Arai, 2007).

The Bou Azzer district (Anti Atlas, Morocco) was recognized by Co exploitation from Co-Ni-Fe arsenide and sulfoarsenide minerals (e.g., Maacha, 2013; Bouabdellah et al., 2016; Ikenne et al., 2020). A minor content of Cr-spinel was associated to this Co-Ni-Fe arsenides orebody (Gervilla et al., 2012; Fanlo et al., 2015; Hajjar et al., 2021). Alteration of Cr-spinel

may become more complicated in the serpentinites from the Bou Azzer ophiolite where several stages of hydrothermal alteration (talcification, carbonation, silicification, Souiri et al., 2021) linked with the formation of Co-Ni arsenide ores and later epithermal sulphides overprinted previous serpentinization processes (Ahmed et al., 2005, 2009; Gahlan and Arai, 2007; Fanlo et al., 2015; Hodel et al., 2017; Pujol-Solà et al., 2021). These aforementioned studies showed that the less altered compositions are preserved in the nuclei of Cr-spinel grains from partially serpentinized peridotites. These compositions evolve towards the rims of Cr-spinel grains showing increasingly higher Cr# and Fe^{3+}#, as well as lower Mg# as the serpentinization degree of the peridotite progress (Gahlan and Arai, 2007; Hodel et al., 2017). Accessory Cr-spinels from the Bou Azzer serpentinites are also characterized by their unusually high, although heterogeneous contents of MnO, ZnO and CoO (Ahmed et al., 2005, 2009; Gahlan et al., 2006; Gahlan and Arai, 2007; El Ghorfi et al., 2008; Fanlo et al., 2015; Hodel et al., 2017). These authors interpreted such unusual MnO, ZnO and CoO contents in terms of Cr-spinel-fluid interactions either linked with the continental hydrothermal system responsible for the formation of the Co-Ni arsenide ores (e.g., El Ghorfi et al., 2008) or with early, sea floor serpentinization in a metal-rich environment caused by the presence of nearby black smoker type hydrothermal vents (e.g., Fanlo et al., 2015).

Fanlo et al (2015) showed that alteration zoning of Cr-spinel grains scattered in mineralized serpentinites of the Aghbar, Tamdrost and Aït Ahmane Ni-Co arsenide deposits clearly predated the mineralization event, during which zoned Cr-spinel only became fractured and partly dissolved. More recent studies on serpentinite-hosted, Ni- and Co-poor Fe arsenide ores by Hajjar et al., (2021) have revealed that alkaline and low temperature fluids responsible for the precipitation of the ores may have also produced zoning in some Cr-spinels, although it has been little explored. This paper aims to identifying the complete alteration sequence affecting the Cr-spinel grains associated with the ores in the Bou Azzer serpentinites paying special attention to the effects caused by these oxidized, alkaline, low temperature ore-forming fluids trying to enlarge the knowledge on the varied set of conditions at which Cr-spinel and/or ferrian chromite can be altered.

2. Geology

The Bou Azzer serpentinites is a portion of a dismembered Neoproterozoic ophiolite complex cropping out in the Bou Azzer inlier, in the central Anti-Atlas Mountains, in south Morocco (Fig. III. 1). This ophiolite was obducted during the major Pan-African deformation phase as a consequence of the collision between the west African craton (WAC) and a hypothetic arc in the North (Leblanc, 1975, 1981; Saquaque et al., 1989; Gasquet et al., 2008; El Hadi et al., 2010; Hefferan et al., 2014; Triantafyllou et al., 2016, 2018; Soulaimani et al., 2018). The passive margin in the South west part of the Bou Azzer inlier corresponds to the Tachedamt Bleida group, and is composed of stromatolitic limestone, quartzite, tholeiitic basalts and schists (Clauer, 1974; Bouougri et al., 2020). Two active arcs dated at the Cryogenian (Blein et al., 2014; Triantafyllou et al., 2020) are described in the inlier. The first one in the south, named the Bougmane Bou Azzer group (Tazzegzout group), is made up of orthogneiss, metagabbro, schists and pegmatite (D'Lemos et al., 2006; Blein et al., 2014; Hefferan et al., 2014). The second arc locates at the northeast part of the inlier, is named the Tichibanine Ben Lagrad Group and consists of a complex tectonic assemblage made up of metagreywackes and arc-related basalts, andesites, rhyolites and tuffs (Tekiout, 1991; Naidoo et al., 1991).

The ophiolite complex is composed, from bottom to top, by serpentinized mantle peridotites, to which chromitites pods are associated (Pujol-Sola et al., 2021), gabbros, sheeted dykes, submarine pillow basalts and locally, a varied set of partly metamorphosed sedimentary rocks, including metapelites, sandstones and limestones, and was dated at the Cryogenian (Bodinier et al., 1984; El Hadi et al., 2010). During the subduction-initiation of geodynamic setting two chromitite were formed. The first one corresponds to an intermediate-Cr chromitites (Cr# = 0.60 – 0.74) formed from fore-arc basalts (FAB) in the early stage; while the second one was high-Cr chromitite (Cr# = 0.79 – 0.84) formed from boninitic melts in the ensuing stage (Pujol-Solà et al., 2021).

Granitoid intrusions in the Bou Azzer inlier were regrouped into two suites: the syn-kinematic intrusions grouped under the name of Ousdrat suite, and the post kinematic intrusion grouped under the name Bleida Granitoid. The Oustdrat suite was represented by diorite, quartz-diorite and monzodiorite, and the post kinematic granodiorite stocks, such as the Bleida

granodiorite. U-Pb zircon from the Ousdrat suite confirmed their emplacement/intrusion age between 640 and 670 Ma (Mrini, 1993; Inglis et al., 2003; Samson et al., 2004, Blein et al., 2014; Triantafyllou et al., 2020), while the Bleida granodiotite were intruded at 630 and 580 Ma (Inglis et al., 2004; Blein et al., 2014).

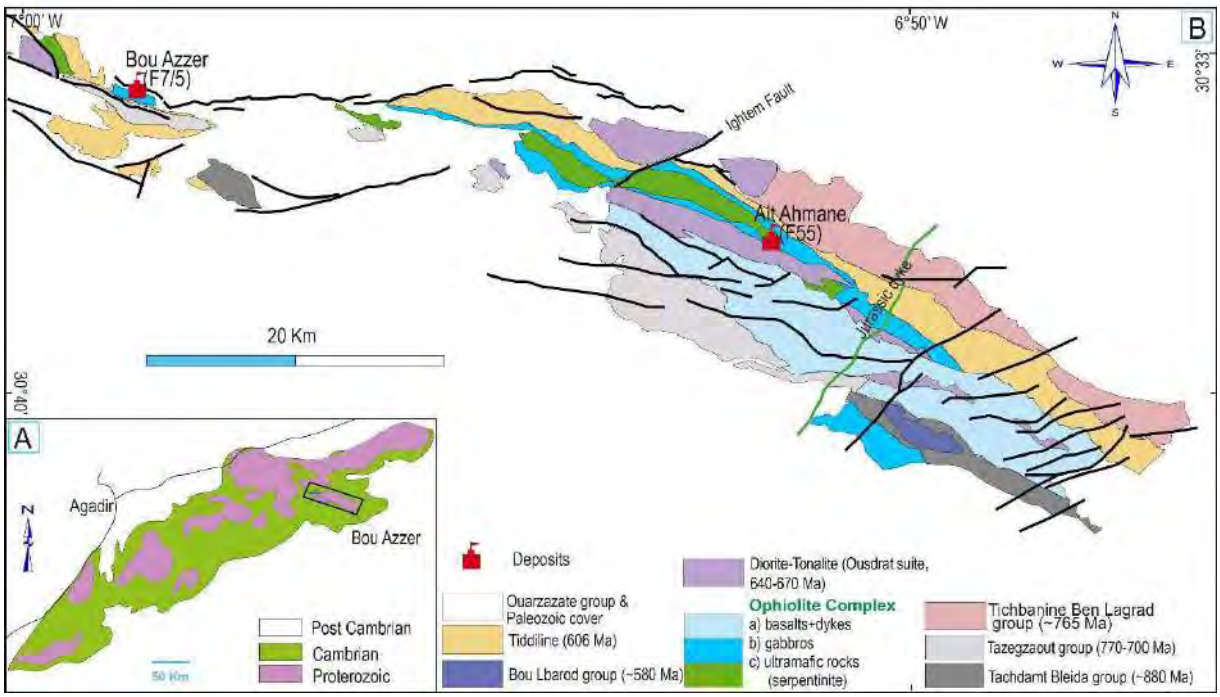

Fig. III. 1. (A). Simplified geological map of the Anti-Atlas belt (Gasquet et al., 2008). (B). Geological map of Bou Azzer inlier (Central Anti Atlas, Morocco) (modified from El Hadi et al., 2010; Soulaimani et al., 2018), showing the studied Co-Fe deposit in the district.

The post orogenic Ediacarian terranes in the Bou Azzer inlier include the Tiddiline and the Ouarzazate groups. The Tiddiline Group is composed of terrigenous sediments (siltstone and conglomerate) with local pyroclastic rocks overlying unconformably the Cryogenian terranes (606 ± 5 Ma; Blein et al., 2014) and the Ouarzazate Group gathers a suit of potassic to high-potassic volcanic rocks (ignimbrites and tuffs) made up of andesites, dacites and rhyolites, interstratified with chaotic breccia, polygenic conglomerates and arkosic sandstones. The age of the Ouarzazate group was bracketed between 567 ± 5 Ma and 566 ± 4 Ma, from a rhyolitic welded tuff (Blein et al., 2014). A carbonate-dominated sedimentary succession dated at 541 ± 6 Ma (Blein et al., 2014) overlies the Ouarzazate group.

The Bou Azzer serpentinites crop out along the WNW-ESE Anti-Atlas Major Fault (AAMF) and frequently host Co-Ni-Fe arsenide ore deposits and more than hundred deposits

have been recognized (Leblanc, 1975, 1981). According to Leblanc (1975, 1981), En-Naciri (1995), El Ghorfi (2006), Gervilla et al. (2012b), Maacha (2013), Bouabdellah et al. (2016), Ikenne et al. (2020) and Hajjar et al. (2021), the Co-Ni-Fe ores occur as: (1) WNW-ESE flame-shaped orebodies, lenses and pocket-like masses located at the contacts between serpentinite bodies and quartz diorite, gabbros or younger volcanic and sedimentary rocks from the Ouarzazate Group (Contact-type ores); (2) NE-SW to N-S cross-cutting veins hosted in all these rocks (Vein-type ores); (3) NW-SE flat lenses hosted in serpentinite (Serpentinite-hosted ores; Hajjar et al., 2021). The Co-Ni orebody mineral assemblages was summarized into three-stages depositional sequence (Maacha, 2013; Bouabdellah et al., 2016): (1) a pre arsenide, silicification stage characterized by the precipitation of some gold and chlorite; (2) the main arsenide ore-forming stage which can be subdivided into three sub stages according to their mineralogy and micro-texture (2a: Ni-Co ores; 2b: Co-Fe ores and 2c: Fe-Co ores evolving to Fe ores; Subías et al., 2022; Hajjar et al., 2021), and (3) an epithermal stage marked by the precipitation of sulfide minerals associated to late calcite.

3. Serpentinite-hosted arsenide ores

This study was performed on disseminated and massive ores hosted in serpentinites from the Filon 55 (F55) from the Aït Ahmane area, located at the eastern end of the Bou Azzer mining district, and the Filon 7/5 (F7/5), nearby the Bou Azzer village, close to the western end of the district (Fig. III. 1). The F55 orebody consists of a flat lens striking N120E, dipping 62º to SW, and is hosted by serpentinite (Fig. III. 2A). Its thickness ranges from 3 to 9 m and extends up to 80 m. The nature of the occurrence gradationally changes from massive to disseminated nature (Fig. III. 2B, C). The arsenide lens is surrounded by an irregular, patched alteration halo, constituted by barren carbonated serpentinite and talc-rich serpentinite (Fig. III. 2A-C; Hajjar et al., 2021). The mineral assemblage of the F55 lens is mainly composed of spindle-shaped, zoned löllingite crystals arranged in massive or rosette-like aggregates. These aggregates include and/or occur in association with serpentine, chlorite and Cr-spinel in a calcite-dominant matrix.

The studied ores in the Filon 7/5 constitute the intra-serpentinite extension of two intersecting contact-type, Co-Ni orebodies (Filon 7, striking N30ºE, and Filon 5, striking N70ºE) developed at the contact between quartz diorite and serpentinite (Fig. III. 2D; Leblanc,

1975, 1981; En-Naciri, 1995; El Ghorfi, 2006). The thickness of the whole orebody is variable and ranges from 1 to 20 m, with a lateral extension ranging from 2 to 3km. Ore-bearing serpentinites are surrounded by a relatively thin (0.5 to 1.5m thick) alteration halo made up of talc-rich, chlorite-bearing serpentinite cut by a network of calcite veinlets (<1cm thick) which becomes tighter towards the ore zone (En-Naciri, 1995; El Ghorfi, 2006). Ores textures and mineralogy of the F7/5 deposit evolve from massive and banded Co-Ni arsenide ores at the contact between quartz diorite and serpentinite to disseminated Fe-rich arsenide ores replacing serpentinites. The latter ores contain variable amounts of newly formed chlorite and relicts of variably altered, accessory Cr-spinel grains.

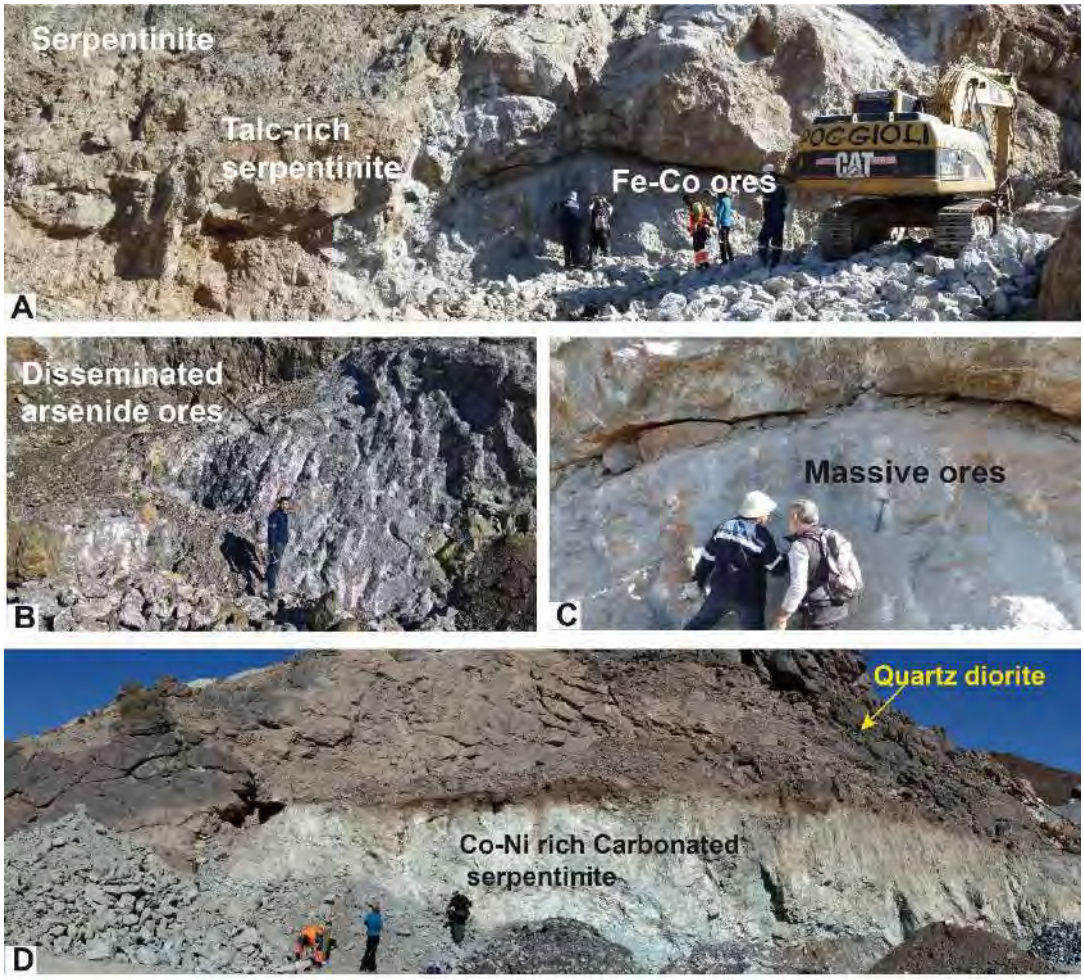

Fig. III. 2. A: Panoramic view of F55 orebody (Ait Ahmane area) hosted in serpentinite. B: western edge of F55 orebody, composed by disseminated Fe arsenide ores. C: massive Fe arsenide ores from central part of F55 orebody. D: Panoramic view of F7/5 orebody in the contact with quartz diorite. F7/5 orebody correspond formed by Co-Ni rich carbonated serpentinite.

Arsenide ores of the main ore mass located at the quartz diorite-serpentinite contact show a complex assemblage of Co-Ni-Fe arsenides and sulfarsenides which roughly precipitate according to the following depositional sequence (En-Naciri, 1995; El Ghorfi, 2006; Maacha, 2013; Fanlo et al., 2015): 1) Ni-Co arsenide ores made up of Ni-rich skutterudite, nickeline and Ni-rich, ternary diarsenides of the rammelsbergite-safflorite-löllingite series followed by sulfarsenides of the gersdorffite-cobaltite series; 2) Co-Fe arsenide ores composed of skutterudite and members of the safflorite-löllingite series with some late alloclasite; 3) Fe-Co arsenide ores consisting of a third generation of skutterudite and Fe-rich members of the löllingite-safflorite series. This sequence ends with the formation of arsenopyrite, molybdenite, pyrite, chalcopyrite, galena and realgar-orpiment filling voids, cracks and open spaces in any of the main ore assemblage. Serpentinite-hosted ores mainly record the latest arsenide mineralization event, characterized by the predominance of löllingite in the mineral assemblage with variable but minor amounts of skutterudite (Hajjar et al., 2021). Zoned löllingite often shows Co- and Ni-rich bands with a mineral composition corresponding to ternary diarsenides of the löllingite ($FeAs_2$)-safflorite ($CoAs_2$)-rammelsbergite ($NiAs_2$) system, and may contain inclusions of native bismuth, nickeline, chalcopyrite and sphalerite (Hajjar et al., 2021).

4. Samples and methods

Six samples from F55 and seven samples from F7/5 were selected to study the alteration zoning patterns of accessory Cr-spinel grains and their possible connection with the ore-forming process. Samples from F55 deposit represents the massive core and the disseminated rim of the orebody, as well as, the barren carbonated serpentinites and the talc-rich serpentinites from the alteration halo. The selected samples from F7/5 correspond to serpentinites with variable proportions of arsenide ore. The samples were cut, thinned and polished at the department of Mineralogy and Petrology of the University of Granada (Spain) for petrographic observations under transmitted- and reflected-light, polarized microscopy. Additional petrographic observations were made by a SUPRA40VP scanning electron microscope at the Centro de Instrumentación Científica (CIC) of the University of Granada, Spain, using STEM and EDX detectors. Operating conditions were: accelerating voltage of 20 kV, beam current of 20 nA and count times of 20 s.

Electron-probe micro analyses of Cr-spinel from F55, were performed at the Centro de Instrumentación Científica (CIC) of the University of Granada using a CAMEBAX SX100 instrument under excitation voltage of 20 kV, beam current of 20 nA and beam diameter of 5 μm. Monitored spectral lines were MgKα, FeKα, AlKα, CrKα, SiKα, TiKα, MnKα, ZnKα, NiKα, VKα, and CoKα using Periclase, Fe_2O_3, Al_2O_3, Cr_2O_3, SiO_2, TiO_2, $MnTiO_3$, NiO, V_2O_3, ZnS, NiO, and metallic cobalt as standards. While those from F7/5 were analysed in the Centros Científicos y Tecnológicos (CCiT) of the University of Barcelona (Spain) using a JEOL JXA-8230 instrument equipped with five WDS spectrometers, under an excitation voltage of 20 kV and a beam current of 20 nA, with a beam 2 μm in diameter. Monitored spectral lines were MgKα, FeKα, AlKα, CrKα, SiKα, TiKα, MnKα, ZnKα, NiKα, VKα, and CoKα using periclase, Fe_2O_3, corundum, Cr_2O_3, diopside, rutile, rhodonite, sphalerite, nickel, vanadium, and Cobalt as standards. The Fe speciation was recalculated from microprobe data based on Cr-spinel formula of 4 oxygen and charge balance.

5. Cr-spinels in the Co-Fe ores and hosting serpentinites

5.1. Textural types

Cr-spinel is a ubiquitous accessory mineral in the studied Fe-(Co) arsenide ores from the F55 and F7/5 deposits, which abundance tends to decrease as the modal proportion of Fe arsenides increase. Four different textural types of Cr-spinels can be recognized in the studied samples (Figs. 3-4): (1) zoned Cr-spinel with homogenous core (Type 1A), (2) zoned grains with porous core (Type 1B), (3) homogenous Cr-spinel (Type 2) and (4) partly dissolved Cr-spinel (Type 3).

Zoned grains of Type 1A consist of dark-grey homogenous Cr-spinel core surrounded by lighter rim of ferrian chromite (Fig. III. 3a-b) of irregular morphology and variable thickness (25-100 μm). Occasionally, the homogenous cores of grains (ferrian chromite composition) evolve outward to an irregular, darker porous envelope and to a discontinuous, homogeneous rim with well-formed crystal face (Fig. III. 3c). Type 1A grains are mainly found in the alteration halo of F55 orebody (talc-rich serpentinite and carbonated serpentinite) and scattered in disseminated arsenide ores from both F7/5 and F55 orebody.

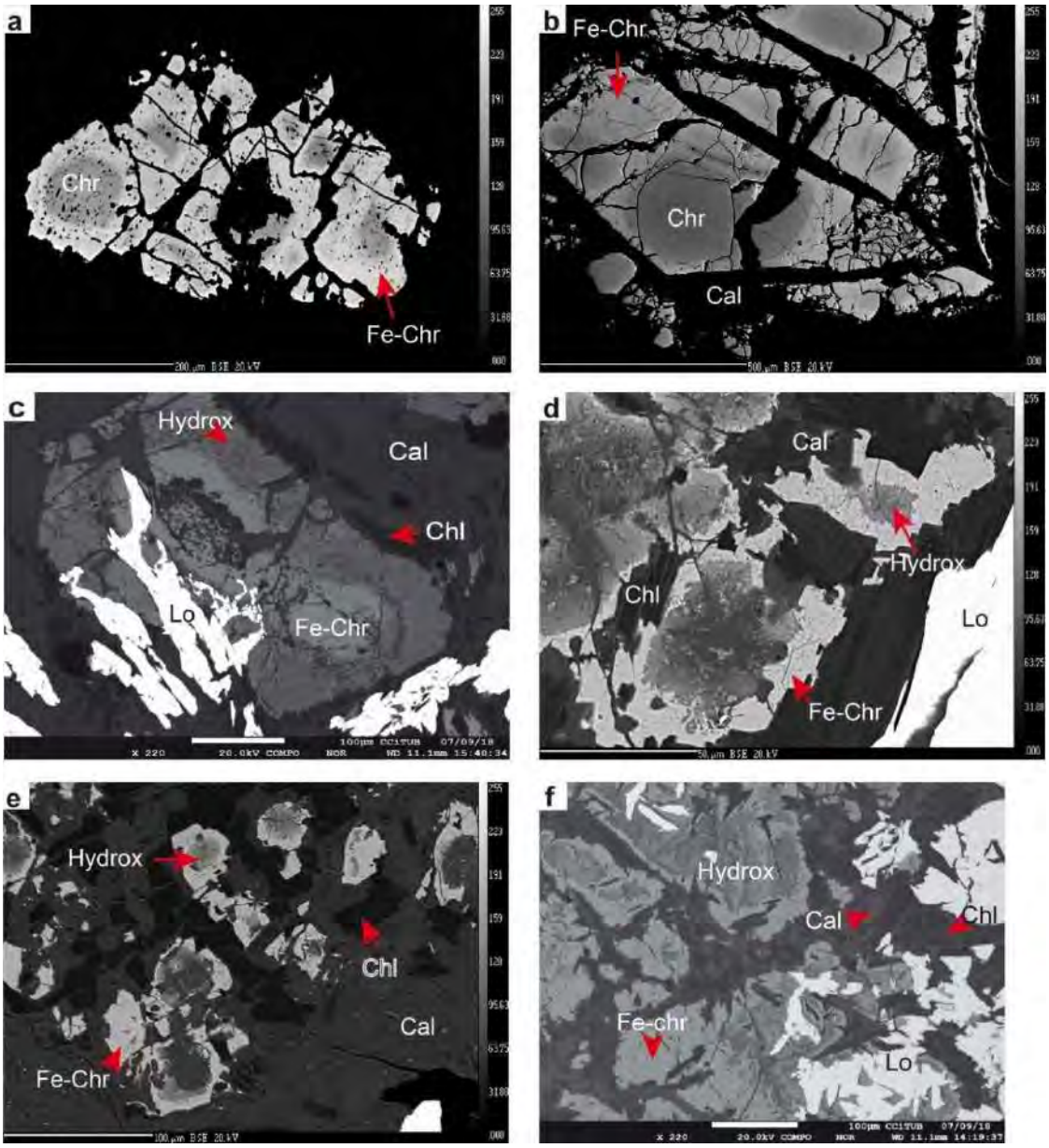

Fig. III. 3. Back scattered electron image of the different textural types of zoned Cr-spinel. a. Type 1A Cr-spinel crystal from talc rich serpentinite (F55 deposit). b. Type 1A Cr-spinel crystal associated to calcite from carbonated serpentinite (F55 deposit). c. Zoned Cr-crystal from F7/5 deposit with porrous homogenous core (Chr) evelving into a porrous rims constitued by Fe-Cr hydrxide (Hydrox); associated to calcite (Cal) and lollingite (Lo) with minor chlorite (Chl). d. e. Type 1B Cr-spinel crystals with porous core composed by Fe-Cr hydroxide, associatd to a chlroite (Chl) rich calcite matrix (Cal) (F55 deposit). f. Type 1B Cr-spinel crystals composed by Fe-Cr hydroxides core surrounded by ferrian chromite (Fe-Chr), partially replaced by lollingite (Lo).

Zoned grains of Type 1B consist of dark porous (Type 1B; Fig. III. 3d-f, Fig. III. 4a-b) cores surrounded by lighter rims of ferrian chromite or fine bands of Cr-spinel of irregular morphology and variable thickness (10-100 µm; Fig. III. 3d-f, Fig. III. 4a-b). Type 1B grains predominates in disseminated arsenide ores associated to chlorite-rich, calcite matrices (Fig. III.

3d-e) or included in löllingite (Fig. III. 3f, Fig. III. 4a-b) in hosted serpentinites ores from both deposits. Often this latter type of zoned Cr-spinel grains exhibits a well-developed crack-seal filled by calcite (Fig. III. 3e).

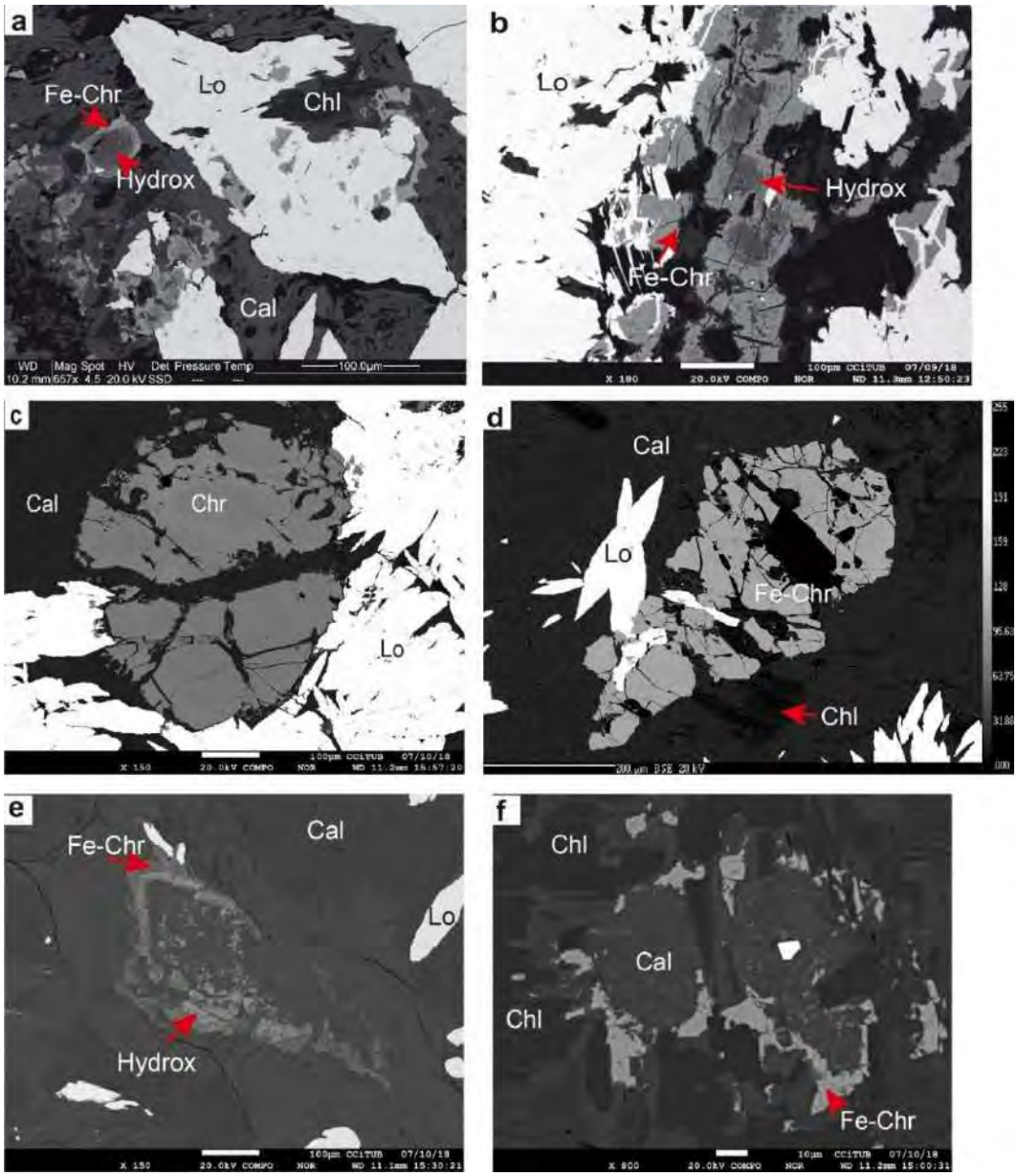

Fig. III. 4. Back scattered electron image of Cr-spinel. a. Type 1B Cr-spinel crystals composed by Fe-Cr hydroxides core surrounded by ferrian chromite (Fe-Chr), partially replaced by lollingite (Lo).. b. Type 1B Cr-spinel with porrous core composed by Cr-Fe hydroxide surrinded by Ferrian chromite (Fe-Chr) associated to lollingite (Lo). c. Ferrian chromite (Fe-Chr) (Type 2) included in calcite (Cal) and chlorite (Chl), being replaced by löllingite (Lo) (F7/5 deposit). d. Type 2 Cr-spnel corresponding to Ferrian chromite (Fe-Chr) included in calcite (Cal) with minor chlorite (Chl), associated to löllingite (Lo) (F55 deposit). e. f. Type 3: disolved Cr-spinel (Fe-chr) with Fe-Cr hydroxide relics (Hydrox) associatd to calcite (Cal).

The Type 2 homogenous grains are hosted in calcite and löllingite from both disseminated and massive Co-Fe ores of F7/5 and F55 deposits. They exhibit corroded grain boundaries (Fig. III. 4c-d). Cr-spinel as inclusion within calcite (± chlorite) are fractured and exhibit variable grain size (200-600 µm), showing lobate grain boundaries (Fig. III. 4c-d). In turn, those within löllingite occur as large, subrounded fractured grains (200-400 µm), or isolated small (20-100 µm) fragments of previous fractured grains (Fig. III. 4d).

The partly dissolved grains of Type 3 groups a varied set of irregulars, usually minute (<100 µm) grains included in calcite + chlorite matrices (Fig. III. 4e-f). They mainly show homogeneous texture locally evolving to porous. In fact, it is possible to observe dissolved grains preserving remnant of pieces of fractured zoned crystals with porous cores.

5.2. Mineral chemistry

As shown in Figure 5, in the Cr# versus Mg# diagram the grains of Cr-spinel analysed in this study overlap, as a whole, most of the Cr- and Fe^{2+}-rich compositional field reported by Hodel et al. (2017); Fanlo et al. (2015) and, at much lesser extent, Ahmed et al. (2005 and 2009) for Cr-spinel from barren serpentinites from the Bou Azzer ophiolite (Fig. III. 5). They also have comparable Fe^{3+} contents as illustrated their similar Fe^{3+}# [Fe^{3+}#=Fe^{3+}/(Cr+Al+Fe^{3+})] ratio (Fig. III. 5) and molar proportions of trivalent cations (Cr-Fe^{3+}-Al) (Fig. III. 6).

The Type 1A zoned Cr-spinel with homogenous cores have cores with relatively lower Cr# (0.64-0.98), and Fe^{3+}# (0.05-0.43), Mg# (0.25-0.47), and rims with similar Cr# (0.65-0.99) but higher Fe^{3+}# (0.10-0.72), and overall lower Mg# (0.03-0.43) (Fig. III. 5, Table III. 1).

However, Figure 5 further shows an overall enrichment in Cr and Fe^{3+}, and depletion in Mg from Cr-spinel in barren talc-rich and carbonated serpentinites (Cr#=0.64-0.89; Fe^{3+}=0.05-0.47; Mg#=0.20-0.47) to disseminated arsenide ores hosted in serpentinite (Cr#=0.80-0.99; Fe^{3+}=0.06-0.72; Mg#=0.03-0.35) (Table III. 1; Fig. III. 5; Fig. III. 6A). At the detail, Cr-spinel from carbonated serpentinite show a very small core-to-rim variation (Cr#=0.64-0.84; Fe^{3+}=0.05-0.24; Mg#=0.31-0.47 in core; Cr#=0.65-0.80; Fe^{3+}=0.10-0.35; Mg#=0.25-0.43 in rim), those value were similar to those from Cr-spinel core in talc rich serpentinite (Cr#=0.65-0.81; Fe^{3+}=0.14-0.24; Mg#=0.27-0.36). Cr#, Fe^{3+}#, and Mg# value of Cr-spinel from talc-rich serpentinite demonstrates a pronounced core-to-rim variation (Cr#=0.86-0.89; Fe^{3+}=0.37-0.47; Mg#=0.20-0.27 in rim). It indicates that Cr-spinel grains from talc-rich serpentinite recorded a

higher alteration degree leading to the formation of ferrian chromite in rim crystal. Cr-spinel from disseminated arsenide ores from both F55 and F7/5 orebody show an increase of Cr# and Fe^{3+}# value from core-to-rim accompanied by a decrease of Mg# value (Cr#=0.80-0.98; Fe^{3+}=0.06-0.42; Mg#=0.25-0.35 in core, and Cr#=0.84-0.99; Fe^{3+}=0.23-0.72; Mg#=0.03-0.32 in rim). Cr-spinel rims from Type 1A are aligned on a trend (Cr# and Fe^{3+}# increase while Mg# decrease), which can be interpreted as the chemical evolution of the rims of the Cr-spinel with changing of the geological settings (within the F55 deposit) (Fig. III. 5).

Some minor elements also tend to vary according to this trend since zoned Cr-spinel with homogeneous core (Type 1A) scattered in disseminated arsenide ores from F7/5 and F55 orebody has higher MnO (0.36-3.13 wt.%), ZnO (0.11-0.79 wt.%), NiO (0.0-0.61 wt.%) and Co (0.03-0.23 wt.%) than that in talc-rich and carbonated serpentinites (0.44-1.1 wt.% MnO, 0.09-0.16 wt.% CoO, 0.06-0.43 wt.% NiO and 0.16-0.7 wt.% ZnO) (Fig. III. 7). This figure shows core-to-rim enrichment in MnO and NiO, an opposite trend in ZnO if outliers are not taken into account (outliers denote anomalous maximum values in rims). CoO and V_2O_3 contents do not reveal appreciable differences between barren and mineralized serpentinites; although V_2O_3 exhibits a subtle core (0-0.23 wt.% V_2O_3)-to-rim (0.04-0.3 4 wt.% V_2O_3) enrichment. TiO_2 uses to be around or below the detection limit.

The light rims surrounding the porous cores of Type 1B zoned Cr-spinel, from both F7/5 and F55 deposit exhibit chemical composition in terms of Cr# (0.82-0.99) and Mg# (0.03-0.32) (Fig. III. 5) similar to the homogeneous Cr-spinel of Type 2 (Cr#=0.74-1.00; and Mg#=0.01-0.37; Fig. III. 5) and Type 3 partly dissolved Cr-spinel (Cr#=0.58-1.00 and Mg#=0.0-0.28; Fig. III. 5), all of them overlapping the compositional field of the ferrian chromite rims surrounding the cores of Type 1A zoned Cr-spinel with homogenous cores (Table III. 2; Fig. III. 5). Most Fe^{3+} contents of Cr-spinel (Type 1B, Type 2, Type 3) from F55 and F7/5 orebody are also indistinguishable (Fe^{3+}#= 0.40-0.87; Fig. III. 5; Fig. III. 6 B-D), except for a set of analyses (Type 2 homogeneous Cr-spinels) from F7/5 which show very low Fe^{3+}# values (0.04-0.11), comparable to type 1A core composition (Fe^{3+}#=0.06-0.42, Cr#=0.8-0.98, Mg#=0.26-0.35) of zoned Cr-spinel in F7/5 orebody (Fig. III. 5; Fig. III. 6C). Minor element contents do not show a well-defined trend (Fig. III. 7), although maximum values (outliers) of MnO (5.12 wt.%) and NiO (1.17 wt.%) were measured in partly dissolved Cr-spinel (Type 3) from the F7/5 orebody and those of ZnO (2.36 wt.%) and CoO (0.68 wt.%) occur in rims of zoned Cr-spinel with

porous rims (Type 1B) from F7/5 and homogeneous Cr-spinel from F55, respectively (Table III. 2).

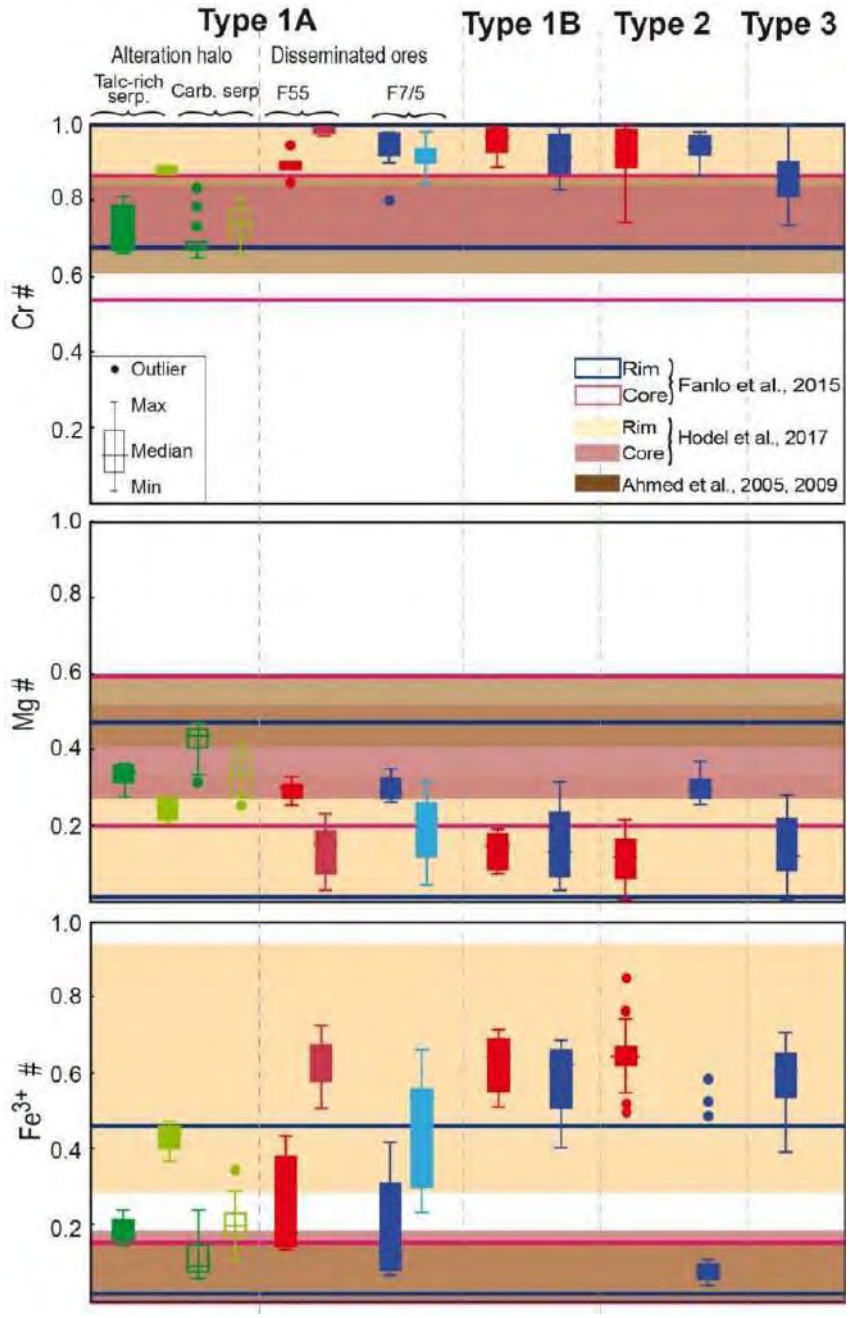

Fig. III. 5. Distribution of Cr# [=Cr/(Cr+Al)], Mg# [=Mg/(Mg=Fe^{2+})], and Fe^{3+}# [=Fe^{3+}/(Fe^{3+}+Cr+Al)] values in Cr-spinel grains associated to Co-Fe arsenide ores in F7/5 and F55 deposit (Bou Azzer district). Dark colors correspond to core composition, while ligh colors correspond to rim composition. The composition of Cr-spinel analyzed by others authors from Bou Azzer (peridotite mantle: Ahmed et al. (2005), serpentinite from Ait Ahmane area: Hodel et al. (2017). Serpentinite and ore assemblages from Aghbar, Tamdrost and Ait Ahmane: Fanlo et al., (2015)).

Table III. 1. Compositional ranges of Cr-spinel with homogeneous core

	SiO_2	TiO_2	V_2O_3	Al_2O_3	Cr_2O_3	FeO	Fe_2O_3	MnO	MgO	CoO	NiO	ZnO	Mg#	Cr#	Fe^{3+}#
Zoned chromian spinel with homogenous core (Type 1A)															
F55 deposit															
Talc -rich serpentinite															
Rim (Nbr. 6)															
Min	0,06	0,08	0,24	2,84	31,72	22,92	27,13	0,68	3,55	0,11	0,09	0,23	0,20	0,86	0,37
Max	1,82	0,15	0,34	4,09	38,66	24,97	33,74	1,10	4,91	0,15	0,37	0,70	0,27	0,89	0,47
Core (Nbr. 12)															
Min	0,03	0,01	0,10	7,09	41,63	22,29	11,44	0,60	5,10	0,13	0,06	0,32	0,27	0,65	0,14
Max	0,27	0,07	0,22	15,25	49,73	24,19	17,96	0,81	7,18	0,16	0,20	0,50	0,36	0,81	0,24
Carbonated serpentinite															
Rim (Nbr. 37)															
Min	0,03	0,03	0,11	6,79	35,93	19,83	8,03	0,47	4,64	0,10	0,10	0,16	0,25	0,65	0,10
Max	1,28	0,16	0,31	14,74	47,24	24,30	25,89	0,96	8,41	0,16	0,43	0,47	0,43	0,80	0,35
Core (Nbr. 21)															
Min	0,03	0,05	0,17	6,17	37,53	19,29	4,32	0,44	5,79	0,09	0,06	0,21	0,31	0,64	0,05
Max	1,07	0,13	0,23	16,82	48,53	22,81	18,72	0,67	9,58	0,15	0,24	0,47	0,47	0,84	0,24
Disseminated ores															
Rim (Nbr. 14)															
Min	0,03	0,00	0,18	0,11	18,24	23,76	36,13	0,73	0,44	0,12	0,17	0,11	0,03	0,96	0,50
Max	0,31	0,03	0,29	0,80	33,48	28,93	50,82	1,54	4,03	0,18	0,33	0,27	0,23	0,99	0,72
Core (Nbr. 7)															
Min	0,03	0,00	0,02	1,59	37,06	21,53	10,09	1,07	4,43	0,11	0,01	0,33	0,25	0,84	0,13
Max	0,08	0,01	0,20	5,96	55,96	23,54	31,77	1,18	5,97	0,17	0,17	0,58	0,33	0,94	0,43
F7/5 deposit															
Disseminated ores															
Rim (Nbr. 11)															
Min	0,00	0,00	0,04	0,32	20,62	22,04	21,88	0,42	0,65	0,03	0,20	0,14	0,04	0,84	0,23
Max	0,70	0,03	0,26	3,48	44,51	28,69	46,88	3,13	5,69	0,19	0,61	0,79	0,32	0,98	0,66
Core (Nbr. 14)															
Min	0,00	0,00	0,00	0,95	36,38	21,00	4,55	0,36	4,63	0,04	0,00	0,17	0,26	0,80	0,06
Max	0,07	0,04	0,14	8,72	64,40	23,78	30,93	0,89	6,32	0,23	0,41	0,51	0,35	0,98	0,42

Table III. 2. Compositional ranges of Cr-spinel with porous core, homogeneous and partly dissolved

	SiO_2	TiO_2	V_2O_3	Al_2O_3	Cr_2O_3	FeO	Fe_2O_3	MnO	MgO	CoO	NiO	ZnO	Mg#	Cr#	Fe^{3+}#
Zoned chromian spinel with porous core (Type 1B)															
F55 deposit															
Disseminated ores				Nbr. 15											
Min	0,04	0,00	0,15	0,11	19,34	24,90	36,06	0,67	1,07	0,10	0,21	0,11	0,07	0,88	0,51
Max	0,42	0,05	0,39	2,37	31,00	27,09	50,90	2,45	3,34	0,16	0,55	0,51	0,19	0,99	0,71
F7/5 deposit															
Disseminated ores				Nbr. 17											
Min	0,00	0,00	0,03	0,11	19,28	21,78	29,13	0,49	0,48	0,00	0,17	0,10	0,03	0,82	0,40
Max	1,93	0,12	0,33	3,93	37,34	28,21	47,79	4,87	5,67	0,18	0,92	2,36	0,32	0,99	0,69
Homogenous chromian spinel (Type 2)															
F55 deposit															
Disseminated ores				Nbr. 37											
Min	0,03	0,00	0,07	0,02	8,80	22,69	35,85	0,28	0,13	0,09	0,09	0,00	0,01	0,88	0,50
Max	0,10	0,05	0,37	2,81	31,40	29,57	63,95	3,23	3,34	0,21	0,77	0,66	0,19	1,00	0,87
Massive ores			Nbr. 61												
Min	0,05	0,03	0,17	1,32	17,35	24,04	38,86	0,38	0,24	0,11	0,40	0,05	0,02	0,74	0,55
Max	0,30	0,06	0,30	5,08	23,10	27,30	48,71	3,73	3,87	0,68	0,87	0,57	0,22	0,92	0,70
F7/5 deposit															
Disseminated ores				Nbr. 34											
Min	0,00	0,00	0,00	0,92	24,88	21,08	2,77	0,27	4,53	0,00	0,00	0,13	0,25	0,86	0,04
Max	0,15	0,04	0,28	6,20	66,38	24,16	42,81	0,63	6,98	0,16	0,77	0,53	0,37	0,98	0,59
Partly dissolved chromian spinel (Type 3)															
F7/5 deposit				Nbr. 27											
Min	0,00	0,00	0,06	0,06	18,81	23,68	33,24	0,34	0,00	0,00	0,13	0,10	0,00	0,58	0,06
Max	1,82	0,06	0,34	7,32	29,66	29,06	48,64	5,12	5,22	0,16	1,17	0,60	0,28	1,00	0,70

Table III. 3: Representative EPMA analysis on Fe-Cr hydroxides associated to Co-Fe ores in Bou Azzer district

	SiO_2	TiO_2	V_2O_3	Al_2O_3	Cr_2O_3	Fe_2O_3	MnO	MgO	CoO	NiO	ZnO	CaO	Na_2O	Total	Al	Cr	Fe^{3+}
F7-5-7-112	1,84	0,11	0,40	1,85	34,21	28,34	4,36	1,04	0,02	0,14	2,67	2,72	0,24	77,93	0,02	0,40	0,30
F7-5-7-128	1,84	0,18	0,33	3,74	34,14	24,76	3,45	4,08	0,04	0,11	3,54	0,58	0,31	77,10	0,04	0,40	0,27
AA8-3-10	2,63	0,08	0,39	0,80	34,28	28,08	3,50	2,05	0,07	0,05	2,35	-	-	74,26	0,01	0,43	0,32
AA8-3-11	2,88	0,09	0,40	0,62	35,57	26,70	3,61	2,50	0,06	0,03	2,43	-	-	74,86	0,01	0,44	0,30
AA17-3-8	0,77	0,18	0,48	3,45	28,84	36,20	3,31	1,09	0,11	0,19	2,09	-	-	76,70	0,04	0,36	0,41
AA17-4-18	0,66	0,21	0,52	5,13	32,66	29,07	2,89	2,43	0,09	0,14	2,72	-	-	76,53	0,05	0,40	0,33
AA17-4-13	0,86	0,18	0,62	4,58	34,78	28,95	3,17	1,97	0,09	0,26	2,66	-	-	78,12	0,05	0,42	0,32
F7-5-5A-26	1,25	0,25	0,38	2,63	29,13	24,99	2,95	1,19	0,03	0,04	3,15	9,86	0,23	76,09	0,02	0,32	0,25
F7-5-5A-28	1,41	0,33	0,44	3,19	35,15	27,37	3,30	2,81	0,09	0,05	3,84	0,70	0,36	79,05	0,03	0,41	0,29
F7-5-8-151	1,62	0,05	0,45	1,29	35,26	32,04	3,86	1,56	0,00	0,09	2,40	0,83	0,24	79,69	0,01	0,41	0,34
F7-5-1-56	1,51	0,17	0,37	3,72	29,59	25,23	3,65	0,44	0,04	0,35	3,41	5,04	0,39	73,92	0,04	0,35	0,27
F7-5-1-60	2,36	0,17	0,43	3,22	31,61	25,17	4,13	0,60	0,06	0,33	4,00	4,76	0,42	77,26	0,03	0,36	0,26
F7-5-1-63	2,38	0,28	0,44	0,72	35,56	27,48	6,39	0,06	0,06	0,12	3,60	0,60	0,43	78,10	0,01	0,41	0,29
F7-5-5b-229	1,95	0,07	0,30	3,66	35,13	27,00	3,24	3,57	0,04	0,13	3,24	0,32	0,29	78,95	0,04	0,41	0,29
F7-5-5b-255	1,41	0,13	0,75	5,21	33,95	28,82	3,71	1,01	0,03	0,23	3,09	0,84	0,33	79,49	0,05	0,40	0,31
F7-5-7-50	1,40	0,19	0,38	5,05	34,15	25,27	3,22	3,49	0,10	0,13	3,80	0,38	0,39	77,94	0,05	0,40	0,27
F7-5-7-51	1,17	0,09	0,36	4,90	33,96	27,22	3,16	3,17	0,10	0,13	3,69	1,10	0,33	79,39	0,05	0,39	0,29
F7-5-7-63	1,37	0,17	0,39	6,02	30,23	23,87	2,57	3,60	0,07	0,16	3,16	0,84	0,25	72,70	0,06	0,38	0,28
F7-5-7-78	1,06	0,18	0,41	5,63	30,41	26,64	3,37	1,83	0,12	0,25	2,52	6,86	0,26	79,53	0,05	0,34	0,27
F7-5-7-79	1,21	0,20	0,47	6,40	33,15	24,93	3,06	2,89	0,08	0,20	3,16	3,56	0,31	79,63	0,06	0,37	0,26
F7-5-7-80	1,10	0,11	0,41	5,35	31,21	26,67	3,03	1,29	0,08	0,37	2,39	6,51	0,35	78,86	0,05	0,35	0,28

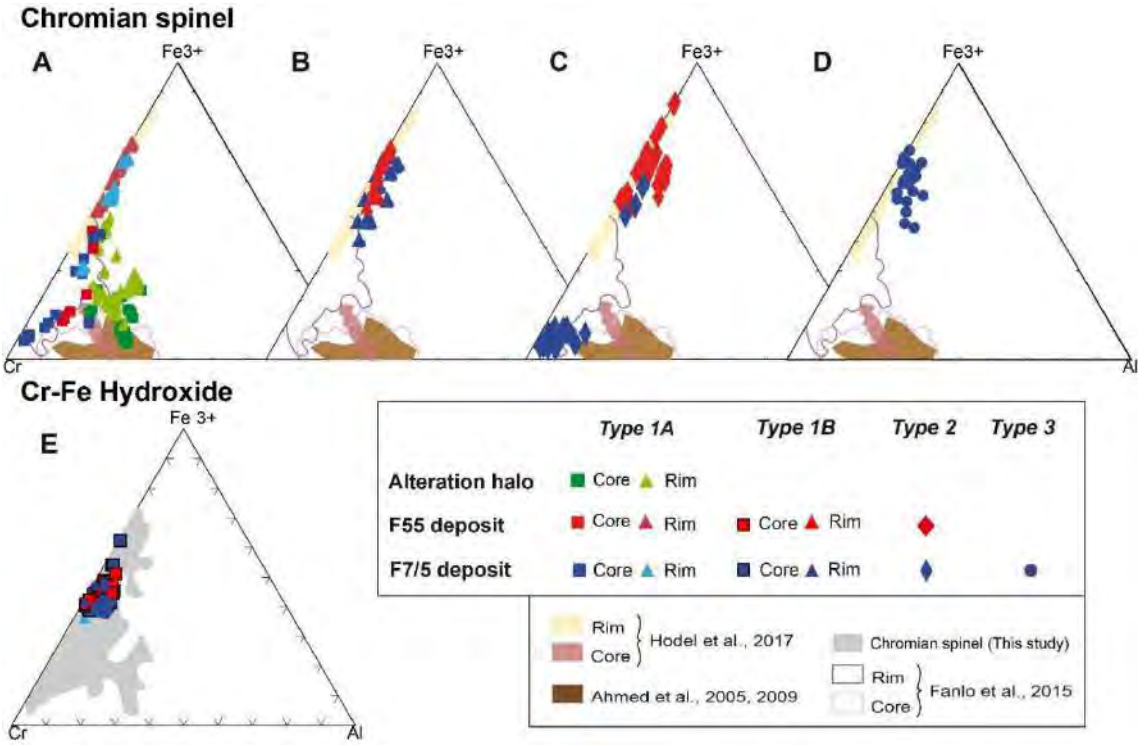

Fig. III. 6. Compositional variations in terms of Cr–Fe^{3+} –Al of Cr-spinel grains (A.B.C.D) and Cr-Fe-hydroxide (E) in F55 and F7/5 deposit. A. Type 1A Cr-spinel with homogenous core. B. Type 1B Cr-spinel with porous core. C. Type 2 homogenous Cr-spinel. D. Type 3 dissolved Cr-spinel. The composition of Cr-spinel analyzed by others authors from Bou Azzer (peridotite mantle: Ahmed et al. (2005), serpentinite from Ait Ahmane area: Hodel et al. (2017). Serpentinite and ore assemblages from Aghbar, Tamdrost and Ait Ahmane: Fanlo et al., (2015)).

The porous material occupying cores and, locally rims, of Type 1B zoned Cr-spinel (Fig. III. 8A-B), or isolated grains partially dissolved (Type 3; Fig. III. 8C, D) is very heterogeneous, consisting of variably-sized Cr-spinel remains embedded in a probably amorphous material which contains micrometric inclusions of phyllosilicates (probably chlorite) and variable proportions of calcite. This latter mineral becomes predominant in some grains and fills crosscutting fractures (Fig. III. 8). The fine-grained mixture of different minerals characterizing this alteration product do not allow obtaining precise electron probe micro-analyses of the amorphous material. However, X-ray chemical distribution maps of Type 1B zoned grains demonstrate that this material shows a high Cr, Mn, and Zn contents compared to ferrian chromite in rim (Fig. III. 8). Nevertheless, careful selection of the spots to be analysed produced results characterized by similar proportions of Cr_2O_3 and Fe_2O_3 (Fig. III. 6E), with minor Al_2O_3, MgO, MnO and ZnO, as well as some SiO_2 and CaO (Table III. 3). Totals do not approach 100% but remain in the range between 74 and 77 wt.%, therefore water represents 26.18 and 25.29 wt.% of the weight percentage of this mineral. As the proportion of Cr_2O_3 increase, the totals

of the electron-probe micro-analyses increase, and decrease of water content. It is worth to note that the high and relatively homogeneous contents of MnO (2-01-4.91 wt.%) and ZnO (2.09-3.84 wt.%) in this material (Table III. 3; Fig. III. 8), exceeding the contents measured in the different Cr-spinel types. The amounts of SiO_2 and CaO obtained in the different spot analyses are caused by the ubiquitous presence of tiny inclusions of chlorite and calcite. Where zoned Cr-spinel with porous core becomes enclosed in calcite, their porous cores tend to be completely replaced by calcite (Fig. III. 8).

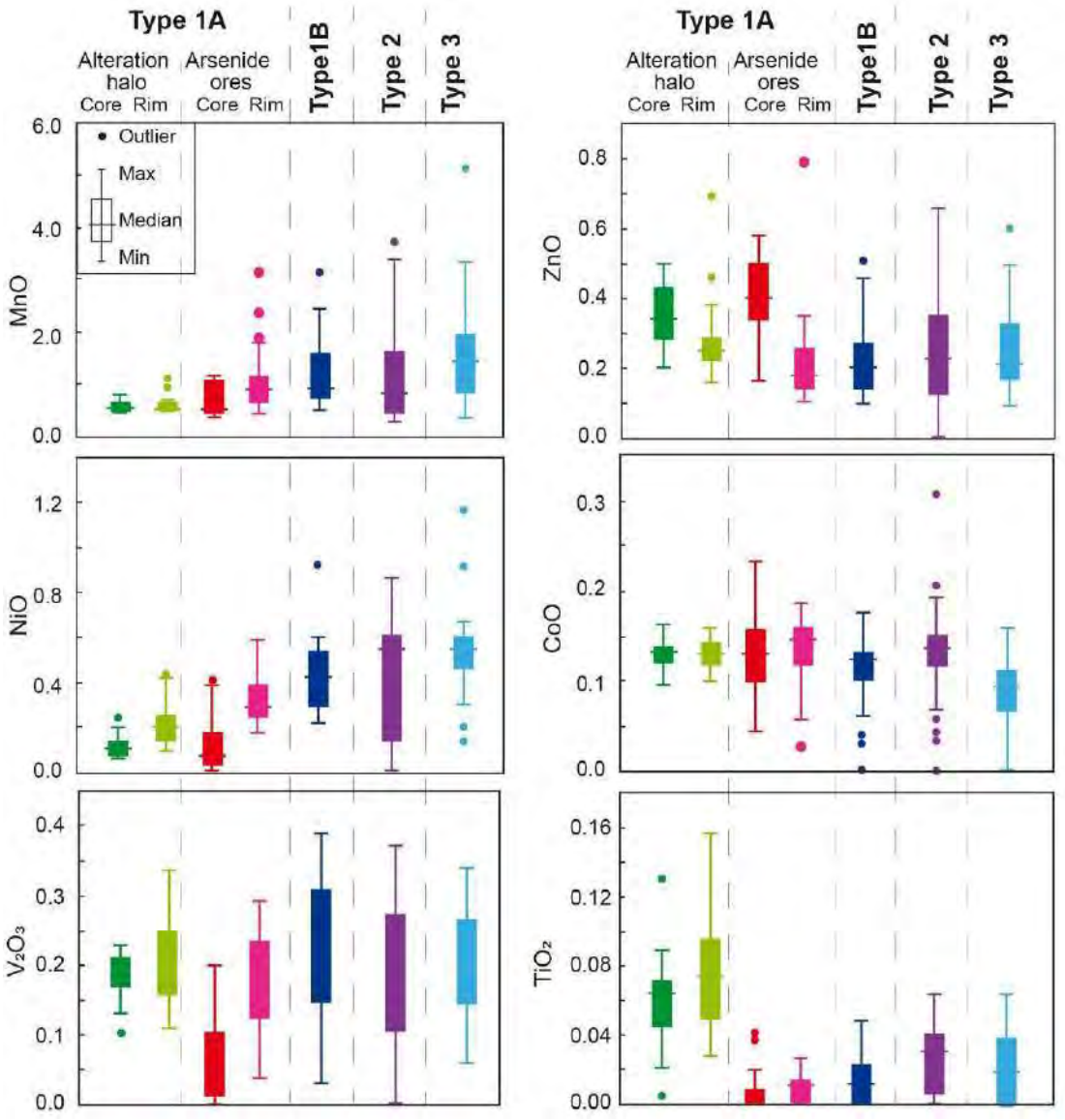

Fig. III. 7. Distribution of traces elements (MnO, ZnO, CoO, NiO, TiO_2, V_2O_3) in Cr-spinel grains associated to Co-Fe arsenide ores in F7/5 and F55 deposit (Bou Azzer district).

The complex geochemical composition of this alteration material, leaves us to suggest that it correspond to Cr-Fe hydroxide, since the proportions of Fe and Cr of these hydroxides are similar. We suppose that it corresponds to one phase solid solution (Goethite- Bracewellite solid solution), intergrow with calcite and chlorite (Fig.8D); which justify the high Si, Al, and Ca contents in electron-probe micro-analysis. The Cr-spinel alteration into hydroxide was described in two alluvial sites. The first one in Guyana with the formation of merumite already described as a complex assemblage of Cr minerals (including CrOOH of different crystallographic structures: Guyanaite, Bracewellite, and Grimaldiite); Milton et al., 1976). The second one has been described in New Caledonia where Cr-spinel was altered into Fe-hydroxide (Goethite; Traore, 2005). This is the first time that the alteration of Cr-spinel to Cr-Fe hydroxide has been described.

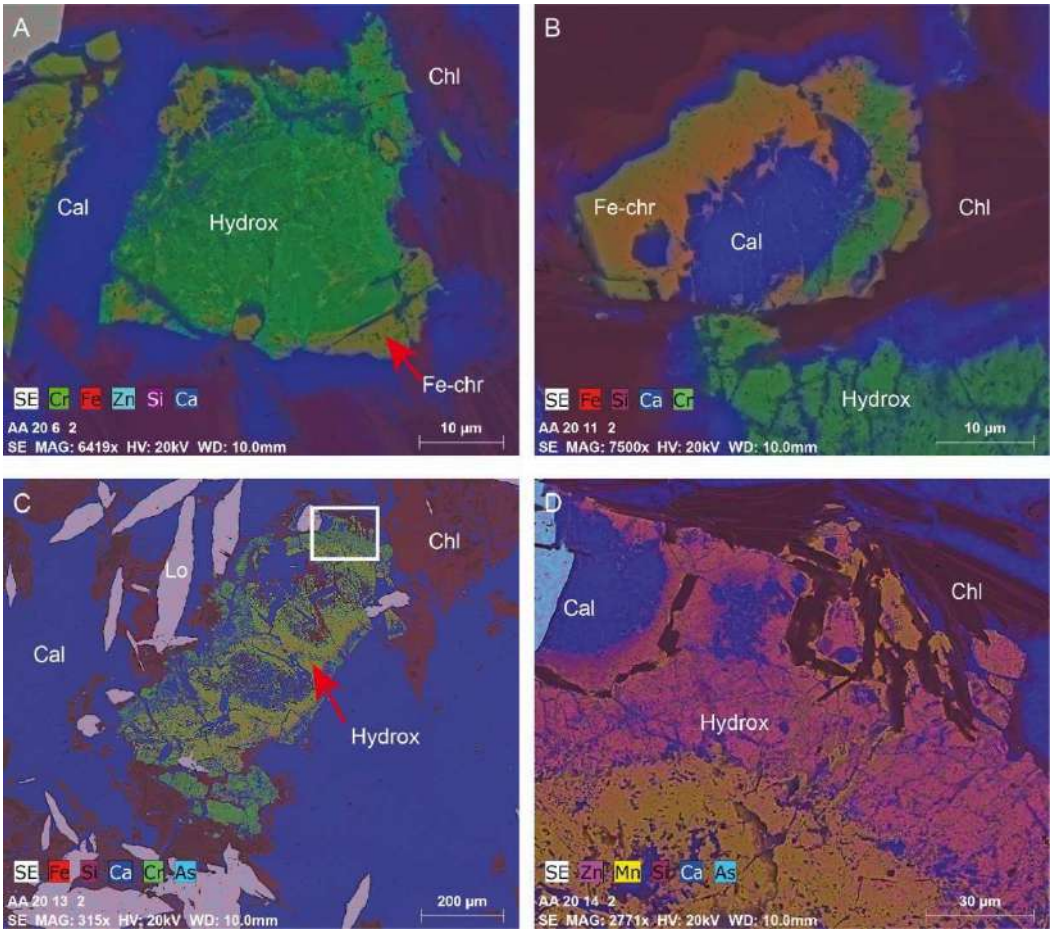

Fig. III. 8. X-ray chemical distribution maps of Fe, Cr, Ca, Mn, and Zn for Type 1B zoned Cr-spinel (A,B) and Type 3 partially dissolved Cr-Fe hydroxide (C, D) from F55 deposit (Ait Ahmane area, Bou Azzer district).

Electron-probe micro-analyses of gangue minerals show that chlorite composition correspond to penninite and clinochlore ($(Mg_{4.51}Fe_{0.20}Al_{0.15}Cr_{0.12}Ca_{0.02}Mn_{0.01}Na_{0.01})_{\Sigma=4.84}Al_2(Si_{2.79}Al_{1.21})_{\Sigma=4}O_{10}(OH)_8$; which is gradually enriched with Cr near type 1B zoned Cr-spinel forming a Cr-rich chlorite $(Mg_{3.57}Fe_{0.86}Cr_{0.32}Mn_{0.03}Ca_{0.02})_{\Sigma=4.80}(Al_{1.58}Cr_{0.42})_{\Sigma=2}(Si_{3.14}Al_{0.86})_{\Sigma=4}O_{10}(OH)_8$. Calcite contains minor amounts of Fe^{2+}(<0.28 pfu) and Mn^{2+} (<0.04 pfu).

6. Discussion

6.1. Pre-ore Cr-spinel

The Type 1A zoning consisting of a homogenous core of Cr-Fe^{2+} spinel surrounded by ferrian chromite rims from the serpentinite-hosted, F55 and F7/5 Fe-Co arsenide ores have zoning pattern and chemical composition almost identical to most accessory Cr-spinel described in barren (Ahmed et al., 2005, 2009; Gahlan and Arai, 2007; Hodel et al., 2017; Fig. III. 9) and mineralized (Fanlo et al., 2015) serpentinites of the Bou Azzer area. These have been interpreted as magmatic Cr-spinel exclusively affected by ocean-floor serpentinization during Neoproterozoic times, probably associated with the Pan-African orogeny (Fanlo et al., 2015; Hodel et al., 2017), and not by talc or carbonate alteration that affected the host serpentinization during the mineralization processes that led to the formation of the Co-Fe ores. This serpentinization event took place in a metal-rich environment characterized by the nearby presence of hydrothermal vent fields (Fanlo et al., 2015) which supplied chlorine-rich, hydrothermal fluids (<350ºC; Hodel et al., 2017) to the environment. The high concentration of metals in these serpentinizing fluids promoted partitioning of Mn and Zn in Cr-spinel up to the anomalously high concentrations (up to 21.4 wt.% MnO and 19.7 wt.% ZnO) as those reported by Gahlan and Arai (2007) and Fanlo et al., (2015). Although some enrichment (often subtle) in MnO, ZnO, CoO and NiO was observed in zoned Cr-spinel from talc-rich and carbonated serpentinites to mineralized serpentinites, its relationship with the mineralizing process remains questionable. The random distribution of MnO-, ZnO-, CoO- and NiO-rich Cr-spinel in barren and mineralized serpentinites from Bou Azzer (Fanlo et al., 2015) suggest that the higher minor element concentrations measured in those Cr-spinel disseminated in Fe-Co arsenide ores could simply be a local feature inherited from the early, Neoproterozoic

serpentinization event not erased or modified during the mineralizing process. The similarity between core-to-rim chemical pattern in Cr-spinel in barren and mineralized serpentinites support this interpretation. Cr-spinel with patterns of zoning similar to reported here for the Type 1A were reported in ophiolites worldwide and interpreted to reflect a two-stage process of alteration of chromite during serpentinization and/or metamorphism. Such alteration mechanism involves fluid-rock interaction promoting a coupled substitution of Al by Fe^{3+} and Mg by Fe^{2+} to form ferrian chromite (Kimball, 1990; Barnes 2000; Proenza et al. 2004; Mellini et al., 2005; González-Jiménez et al., 2009; Merlini et al., 2009; Mukherjee et al. 2010; Gervilla et al., 2012; Barra et al., 2014; Talukdar et al., 2017). As fluid-rock interaction proceed, Cr also became progressively substituted by Fe^{3+} giving rise to ferrian chromite compositions evolving toward the magnetite end-member. Since iron supply to the Cr-spinel grains takes place from the grain boundaries and fracture walls (if present) inward (Gervilla et al., 2019), altered grains develop a typical zoning pattern characterized by an almost unaltered core surrounded a variably thick rim of ferrian chromite rims of variable thickness.

6.2. Cr-spinel dissolution and serpentinite replacement during ore precipitation

Fanlo et al., (2015) reported an event of fracturation in Cr-spinel of the Bou Azzer, which disrupted the zoning pattern of Type 1A Cr-spinel and split the altered grains in fragments. This fracturing event was very likely related to the Variscan orogeny. During this event, deformation of serpentinites led to extensive disruption of the zoning pattern, splitting the altered grains in fragments. This paper, together with that by Gervilla et al. (2012b), illustrate textural relations (Fig. 2 in Gervilla et al. 2012b, and Figs. 3D, I, J, L, M, N, O & P in Fanlo et al., 2015) indicating that precipitation of arsenide ores (and the late epithermal sulfides) overprinting this fracturation event that promoted partial dissolution of Cr-spinel fragments; whereas the small fragments were completely dissolved, the larger fragments tend to acquire rounded outlines becoming included in Co and Fe arsenides (Fig. III. 9).

The alteration process of Cr-spinel from the F55 and F7/5 mineralized serpentinites thus involved new replacement mechanisms not described previously. The textural relations described above show that the replacement reactions that led to the formation of Fe and Cr hydroxides (in Type 1B) mainly took place once the crack was already formed in Cr-spinel

crystals, very likely during an event coeval with the early stages of Fe-Co ore and calcite precipitation. Based on the results obtained by Dolansky (2007) and Hajjar et al., (2021), and on the chlorite geothermometry data from the F7/5 serpentinite-hosted ore by Ares (2018), it is possible to characterize these Fe-Co ore-forming fluids as low-temperature (187-269ºC), $CaCl_2$-rich hydrothermal solutions. Although to our current knowledge, no experimental data are published on the stability of Cr-spinel coexisting with such solutions, the textural distribution of Fe-Cr hydroxides suggest that hydrothermal solutions infiltrated through fractures and preferentially reacted with the less altered nuclei of the zoned grains (Fig. III. 3c-d; Fig. III. 4d-f). The low Fe^{3+}-content of the homogeneous core of such zoned Cr-spinel as well as its bulk chemical composition closer to the primary magmatic one, probably made cores more reactive to these low-temperature, oxidizing hydrothermal solutions. Especially that, the evolving redox conditions of ore fluids is from reduced brines at early stages to more oxidized at later stages (En-Naciri, 1995; En-Naciri et al., 1997; Dolansky, 2007). In contrast, the ferrian chromite rims tend to remain almost unaffected by the replacement, Fe-Cr hydroxides-forming reactions. Nevertheless, they locally became partly dissolved too (Fig. III. 3d), or replaced by Fe-Cr hydroxides (Fig. III. 3f). As expected from the chemical evolution of the ore-forming solutions on cooling (Dolansky, 2007; Hajjar et al., 2021), the rise of the $CaCl_2$/NaCl ratio over the course of these replacement reactions would tend to destabilize the newly formed Fe-Cr hydroxides promoting their dissolution and the precipitation of calcite (Fig. III. 4e-f; Fig. III. 8; and Fig. III. 9).

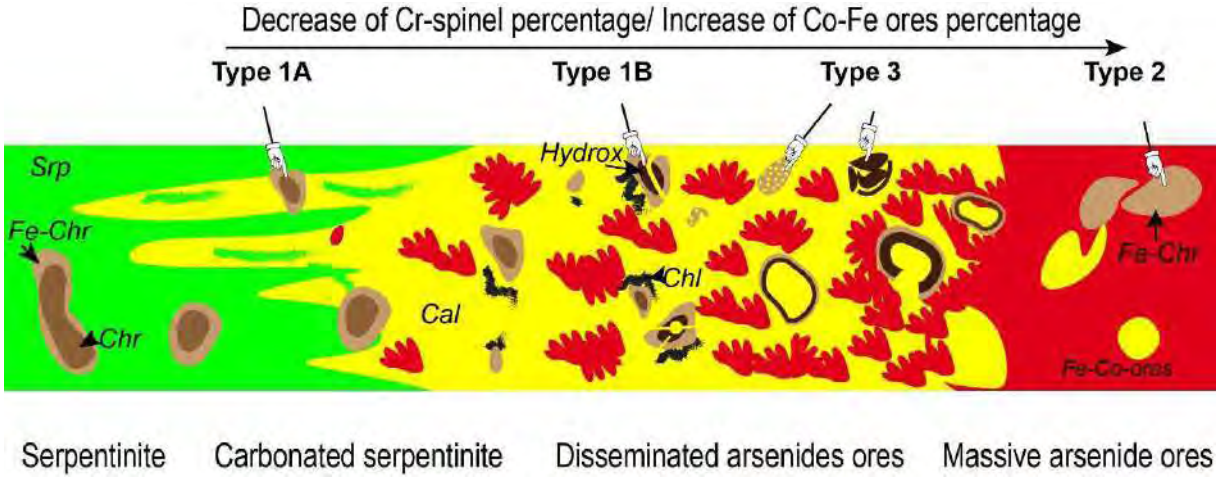

Fig. III. 9. Schematic diagram of ores zoning in the serpentinite hosted ores, showing the distribution of different Cr-spinel texture over this cross section.

This stage of maximum dissolution of Cr-spinel and Co-Fe-hydroxides coincided with the development of massive Fe-Co arsenide ores (i.e., formation of aggregates of spindle-shaped, zoned crystals of Fe-rich diarsenides (mainly löllingite); Fig. III. 4a-c); affected not only the zoned Cr-spinel with Fe-Cr hydroxide cores (Type 1B) but also to all types of highly fractured grains dissolving most of the fragments and leaving remnants of the larger fragments, usually with ferrian chromite composition (Fig. III. 9). So, the Type 2 homogeneous Cr-spinel fragments and their systematic location in calcite + chlorite matrices and löllingite aggregates allow interpreting them as remnants of highly fractured grains in which those fragments with the most reactive composition (e.g., those consisting of Fe-Cr hydroxides) were almost dissolved (Fig. III. 9). Although this interpretation matches well with the fact that most type 2 Cr-spinel grains analysed have ferrian chromite-rich composition (assuming that ferrian chromite is the less reactive composition to the low temperature hydrothermal fluids), it also explains the less frequent occurrence of Al-poor compositions with very high Cr/Fe^{3+} ratio as well as partly dissolved grains containing remains of Fe-Cr hydroxides (Type 3; Fig. III. 9). The former Cr-rich grains would come from fragments of some few less altered grains in which the Al loss took place under reducing conditions (e.g., step one of Gervilla et al., 2012), preventing the oxidation of iron (Fe) and its supply to the Cr-spinel lattice. The occasional presence of Fe-Cr hydroxides coexisting with ferrian chromite remains simply denotes the non-completion of the dissolution reaction.

7. Conclusion

Co-Fe arsenide ores in the Bou Azzer district, mostly composed by skutterudite and members of the löllingite ($FeAs_2$)-safflorite ($(Co, Fe) As_2$) series, are related to serpentinite which has experienced carbonation and talcification alteration. In this alteration halo calcite veins contains relicts of serpentinite, secondary chlorite and Cr-spinel. This latter is also present as accessory grains scattered in disseminated and massive arsenide ores. So, study of Cr-spinel texture involve the presence of four texture type: (1) Type 1A zoned Cr-spinel consisting of a homogenous core of $Cr\text{-}Fe^{2+}$ spinel surrounded by ferrian chromite rims; (2) Type 1B zoned Cr-spinel with porous cores of Cr-Fe hydroxides [$(Cr,Fe)(OH)_3$] rimmed by ferrian chromite with rare irregular bands of Cr- and Fe^{2+}-rich spinel; (3) Type 2 Cr-spinel corresponding to ferrian chromite hosted in löllingite and, at a lesser extent in calcite, in serpentinite hosted

massive and disseminated arsenide ores; and (4) Type 3 Cr-spinel, mainly consisting of partly dissolved ferrian chromite, commonly with Cr-Fe hydroxide,.

Type 1A of Cr-spinel with homogenous core corresponds to most accessories Cr-spinel described in barren and mineralized serpentinites of the Bou Azzer area. Textural and chemical characteristic of those Cr-spinel demonstrate that they were caused by ocean-floor serpentinization during Neoproterozoic times. High Mn and Zn content in Type 1A Cr-spinel was due to their concentration in these serpentinization fluids.

Infiltration of low temperature and high oxidizing hydrothermal fluid through fracture at the Hercynian age tend to replace the homogenous Cr-Fe^{2+} rich spinel in core by Cr-Fe hydroxide, leading to the formation of Type 1B Cr-spinel. Because at such condition Cr-spinel in homogenous core with composition closer to the primary magmatic one, became instable. Ferrian chromite rims remain unaffected by the Cr-Fe hydroxide replacement. Progressive precipitation of Co-Fe arsenide ores partially dissolves Cr-Fe hydroxide and ferrian chromite, giving rise to Type 3 of Cr-spinel; promoting their replacement by löllingite or calcite; and leaving larger homogenous ferrian chromite fragments (Type 2) mainly included in löllingite from massive arsenide ores.

Declaration of competing interest

The authors declare the following financial interests/personal relationships which may be considered as potential competing interests: This study was supported by the Spanish project RTI2018-099157-A-I00 granted by the "Ministerio de Ciencia, Innovaci´on y Universidades" as well as the Ram´on y Cajal Fellowship RYC-2015-17596 granted to JMGJ by the "Ministerio de Economía y Competitividad" (MINECO).

Acknowledgement

We would like to thank associated Editor for handling this paper, as well as Nail Zagrtdenov and Dr. Harald G. Dill for their constructive review and criticism, which helped to improve this work. This research was supported by the Spanish project RTI2018-099157-A-I00 granted by the "Ministerio de Ciencia, Innovación y Universidades" as well as the Ramón

y Cajal Fellowship RYC-2015-17596 granted to JMGJ by the "Ministerio de Economía y Competitividad" (MINECO).

References

Abzalov, A.Z., 1998. Chrome-spinel in gabbro–wehrlite intrusions of Pechenga area, Kola peninsula, Russia: emphasis on alteration features. Lithos 43, 109–134.

Ahmed , A.H., Arai, S., Abdel-Aziz, Y.M., Rahimi, A., 2005. Spinel composition as a petrogenetic indicator of the mantle section in the Neoproterozoic Bou Azzer ophiolite, Anti-Atlas, Morocco. Precamb. Res. 138, 225–234.

Ahmed, A.H., Arai, S., Abdel-Aziz, Y.M., Ikenne, M., Rahimi, A., 2009. Platinum-group elements distribution and spinel composition in podiform chromitites and associated rocks from the upper mantle section of the Neoproterozoic Bou Azzer ophiolite, Anti-Atlas, Morocco. J. Afr. Earth Sci. 55, 92–104.

Arai, S., Ishimaru, S., 2011. Zincian chromite inclusions in diamonds: possibility of deep recycling origin. J. Mineral. Petrol. Sci. 106 (2), 85– 90.

Ares A., 2018. Las espinelas cromíferas del filón 7/5 del distrito minero de Bou Azzer (Marruecos): residuos del reemplazamiento de serpentinitas. TFM. Universidad de Huelva-Universidad Internacional de Andalucía. 54p.

Barnes, S.J., 2000. Chromite in Komatiites, II. Modification during greenschist to mid-amphibolite facies metamorphism. J. Petrol. 41, 387–409.

Barnes, S.J., Roeder, P.L., 2001. The range of spinel compositions in terrestrial mafic and ultramafic rocks. J. Petrol. 42 (12), 2279–2302.

Barra, F., Gervilla, F., Hernández, E., Reich, M., Padrón-Navarta, J.A., González-Jiménez, J.M.,2014. Alteration patterns of chromian spinels from La Cabaña peridotite, southcentral Chile. Mineral. Petrol. 108 (6), 819–836.

Blein, O., Baudin, T., Chèvremont, P., Soulaimani, A., Admou, H., Gasquet, P., Cocherie, A., Egal, E., Youbi, N., Rzin, P., Bouabdelli, M., Gombert, P., 2014. Geochronological constraints on the polycyclic magmatism in the Bou Azzer-El Graara inlier (Central Anti-Atlas Morocco). J. Afr. Earth Sci. 99, 287–306.

Bliss, N.W., MacLean, W.H., 1975. The paragenesis of zoned chromite from central Manitoba. Geochim. Cosmochim. Acta 39 (6), 973–990.

Bouabdellah, M., Maacha, L., Levresse, G., Saddiqi, O., 2016. The Bou Azzer Co–Ni–Fe–As (– Au – Ag) District of Central Anti-Atlas (Morocco): A Long-Lived Late Hercynian to Triassic Magmatic-Hydrothermal to Low-Sulphidation Epithermal System, Mineral Deposits of North Africa, (eds.), Mineral Deposits of North Africa, Mineral Resource Reviews, DOI: 10.1007/978-3-319-31733-5_8

Bodinier, J. L., Dupuy, C., Dostal, J., 1984. Geochemistry of Precambrian ophiolites from Bou Azzer, Morocco. Contrib. Mineral. Petrol., 87, 43-50

Bouougri, E., Ait Lahna, A., Tassinari, C.C.G., Basei, M. A.S., Youbi, N., Admou, H., Saquaque, A., Boumehdi, A., Maacha, L., 2020. Time constraints on early Tonian Rifting and Cryogenian Arc terrane-continent convergence along the northern margin of the West African craton: Insights

from SHRIMP and LA-ICP-MS zircon geochronology in the Pan-African Anti-Atlas belt (Morocco). Gondwana Res.85, 169-188.

Burkhard, D.J., 1993. Accessory chromium spinels: their coexistence and alteration in serpentinites. Geochim. Cosmochim. Acta 57 (6), 1297–1306.

Candia, M.A.F., Gaspar, J.C., 1997.Chromian spinels in metamorphosed ultramafic rocks from Mangabal I and II complexes, Goias, Brazil. Mineral Petrol, 60, 27–40

Clauer, N., 1974. Utilisation de la méthode Rb–Sr pour la datation d'une schistosité de sédiments peu métamorphisés : application au Pré - cambrien II de la boutonnière de Bou–Azzer–El Graara (Anti-Atlas, Maroc). Earth Planet. Sci. Lett. 22, 404–412.

Colás, V., González-Jiménez, J. M., Griffin, W. L., Fanlo, I., Gervilla, F., O'Reilly, S. Y., Pearson, N. J., Kerestedjian, T., Proenza, J. A., 2014. Fingerprints of metamorphism in chromite: new insights from minor and trace elements. Chem. Geol 389, 137–152

Colás, V., González-Jiménez, J.M., Camprubi. A., Proenza, J.A., Griffn, W.L., Fanlo, I., O'Reilly, S.Y., Gervilla, F., González-Partida, E., 2018. A reappraisal of the metamorphic history of the Tehuitzingo chromitite, Puebla state, Mexico. Int Geol Rev. https://doi. org/10.1080/00206814.2018.1542633

D'Lemos, R.S., Inglis, J.D., Samson, S.D., 2006. A newly discovered orogenic event in Morocco: Neoproterozoic ages for supposed Eburnean basement of the Bou Azzer inlier, Anti-Atlas Mountains. Precamb. Res. 147, 65–78.

Dolansky, LM., 2007. Controls on the genesis of hydrothermal cobalt mineralization: insights from the mineralogy and geochemistry of the Bou Azzer deposits, Morocco. Master, McGill University, Montréal, Canada, 162p

El Ghorfi, M., 2006. Etude géochimique et métallogenique des métaux précieux (or, argent et platinoïdes) associes aux minéralisations à Co, Ni, Cr de Bou Azzer-El Graara, et dans la série de Bleida Far West, Anti-Atlas, Maroc. PhD thésis, Cadi Ayyad University, Marrakech, Morocco, 256 p.

El Ghorfi, M., Melcher, F., Oberth€ur, T., Boukhari, A. E., Maacha, L., Maddi, A., Mhaili, M., 2008. Platinum group minerals in podiform chromitites of the Bou Azzer ophiolite, Anti Atlas, Central Morocco. Mineral. Petrol. 92, 59–80.

El Hadi, H.E., Simancas, J.F., Martinez-Poyatos, D., Azor, A., Tahiri, A., Montero, P., Bea, C.M., Gonzalez-lodeiro, F., 2010. Structural and geochronological constraints on the evolution of the Bou Azzer Neoproterozoic ophiolite (Anti-Atlas, Morocco). Precamb. Res. 182, 1–14.

En-Naciri, A., 1995. Contribution à l'étude du district à Co. As (Ni, Au, Ag) de Bou Azzer. Anti- Atlas (Maroc) Données minéralogiques et géochimiques. PhD thésis, Université d'Orléans. France 245 p.

En-Naciri, A., Barbanson, L., Touray, J.C., 1997. Brine inclusions from the Co-As (Au) Bou Azzer district, Anti-Atlas, Morocco. Econ Geol, 92, 360-367.

Evans, B.W., Frost, B.R., 1975. Chrome-spinel in progressive metamorphism – a preliminary analysis. Geochim. Cosmochim. Acta, 39, 959–972.

Fanlo, I., Gervilla, F., Colás, V., Subías, I., 2015. Zn-, Mn- and Co-rich chromian spinels from the Bou-Azzer mining district (Morocco): Constraints on their relationship with the mineralizing process. Ore Geol. Rev. 71, 82–98.

Frost, BR., 1991. Stability of oxide minerals in metamorphic rocks. In: Lindsley RH (ed) Oxide minerals: petrologic and magnetic significance. Mineral Soc Am Rev Mineral 25:469–487

Gahlan, H. A., Arai, S., Ahmed, A. H., Ishida, Y., Abdel-Aziz, Y. M., Rahimi, A., 2006. Origin of magnetite veins in serpentinite from the Late Proterozoic Bou-Azzer ophiolite, Anti-Atlas, Morocco: An implication for mobility of iron during serpentinization. JAES, 46. 318–330.

Gahlan, H., Arai, S., 2007. Genesis of peculiarly zoned Co, Zn and Mn-rich chromian spinel in serpentinite of Bou Azzer ophiolite, Anti Atlas, Morocco. J. Miner. Petrol. Sci, 102, 69-85.

Gasquet, D., Ennih, N., Liégeois, J.-P., Soulaimani, A., Michard, A., 2008. The Pan-African Belt. In A. Michard et al., Continental Evolution: The Geology of Morocco. Lecture Notes in Earth Sciences 116, c_ Springer-Verlag Berlin Heidelberg.

Gervilla, F., Fanlo, I., Colás, V., Subías, I., 2012b. Mineral compositions and phase relations of Ni–Co–Fe arsenide ores from the Aghbar mine, Bou Azzer, Morocco. Can. Mineral. 50, 2, 447–470.

Gervilla, F., Padrón-Navarta, J.A., Kerestedjian, T., Sergeeva, I., González-Jiménez, J.M., Fanlo, I., 2012a. Formation of ferrian chromite in podiform chromitites from the Golyamo Kamenyane serpentinite, Eastern Rhodopes, SE Bulgaria: a two-stage process. Contrib. Mineral. Petrol. 164 (4), 643–657.

Gervilla, F., Asta, M. P., Fanlo, I., Grolimund, D., Ferreira-Sánchez, D., Samson, V. A., Hunziker D., Colas V., González-Jiménez, J. M., Kerestedjian, T. N., Sergeeva, I., 2019. Difusion pathways of Fe^{2+} and Fe^{3+} during the formation of ferrian chromite: a μXANES study. Contrib. Mineral. Petrol, 174, 65 .

González-Jiménez, J.M., Kerestedjian, T., Proenza Fernández, J.A., Gervilla, F., 2009. Metamorphism on chromite ores from the Dobromirtsi ultramafic massif, Rhodope Mountains (SE Bulgaria). Geol. Acta 7 (4), 413–429.

González-Jiménez, J. M., Locmelis, M., Belousova E., Griffin, W. L., Gervilla, F., Kerestedjian, T. N., O'Reilly, S. Y., Pearson, N. J., Sergeeva, I.,2015. Genesis and tectonic implications of podiform chromitites in the metamorphosed ultramafic massif of Dobromirtsi (Bulgaria). Gondwana Res., 27, 2, 555-574.

González-Jiménez, J.M., Barra, F., Garrido, L. N.F., Reich, M., Satsukawa, T., Romero, R., Salazar, E., Colás, V., Orellana, F., Rabbia, O., Plissartf, G., Morata, D., 2016. A secondary precious and base metal mineralization in chromitites linked to the development of a Paleozoic accretionary complex in Central Chile. Ore Geol. Rev., 78, 14-40.

Groves, D.I., Barrett, F.M., Binns, R.A., McQueen, K.G., 1977. Spinel phases associated with metamorphosed volcanic-type iron-nickel sulfide ores from Western Australia. Econ. Geol. 72, 1224–1244.

Groves, D.I., Barrett, F.M., Brotherton, R.H., 1983. Exploration significance of chrome spinels in mineralized ultramafic rocks and nickel-copper ores. Geol. Soc. S. Afr. Spec. Publ. 7, 21–30.

Hajjar Z., Gervilla F., Fanlo I., González Jiménez J.M., Ilmen S., 2021. Formation of serpentinite-hosted, Fe-rich arsenide ores at the latest stage of mineralization of the Bou-Azzer mining district (Morocco). Ore Geol. Rev. 128, 103926.

Hefferan, K., Soulaimani, A., Samson, S.D., Admou, H., Inglis, J., Saquaque, A., Chaib, L., Heywood, N., 2014. A reconsideration of Pan African orogenic cycle in the Anti-Atlas Mountains, Morocco. J. Afr. Earth Sc. 98, 34-46.

Hodel, F., Macouin, M., Triantafyllou, A., Carlut, J., Berger, J., Rousse, S., Ennih, N., Trindade, R.I.F., 2017. Unusual massive magnetite veins and highly altered Cr-spinels as relics of a Cl rich acidic hydrothermal event in Neoproterozoic serpentinites (Bou Azzer ophiolite, Anti-Atlas, Morocco). Precamb. Res.300, 151-167

Ikenne, M., Souhassou, M., Saintilan, N.J., Karfal, A., El Hassani, A., Moundi, Y., Ousbih, M., Ezzghoudi, M., Zouhir, M., Maacha, L., 2020. Cobalt-Nickel-Copper arsenide, sulpharsenide and sulphide mineralization in the Bou Azzer window, Anti-Atlas, Morocco: One century of multi-disciplinary and geological investigations, mineral exploration and mining. Geological Society, London, Special Publications, DOI: https://doi.org/10.1144/SP502-2019-132.

Inglis, J.D., Samson, S., D'Lemos, R.S., Admou, H., 2003. Timing of regional greenschist facies deformation in the Bou Azzer Inlier, Anti-Atlas: U–Pb constraints from syn-tectonic intrusions. First meeting of IGCP 485, El Jadida, Morocco, 40–42.

Inglis, J.D., MacLean, J.S., Samson, S.D., D'Lemos, R.S., Admou, H., Hefferan, K., 2004. A precise U– Pb zircon age for the Bleida granodiorite, Anti-Atlas, Morocco: implications for the timing of deformation and terrane assembly in the eastern Anti-Atlas. J. Afr. Earth Sc, 39, 277–283.

Kimball, K.L., 1990. Effects of hydrothermal alteration on the composition of chromian spinels. Contrib Miner Petrol. 105 :337–346

Leblanc, M., 1975. Ophiolites précambriennes et gîtes arséniés de Cobalt (Bon Azzer. Maroc). PhD thésis, Univ. Paris VI, France, 329p.

Leblanc, M., 1981. Ophiolites précambriennes et gîtes arséniés de cobalt (Bou Azzer-Maroc). Notes et mém. Serv. Géol. Maroc, 280, 311p.

Maacha, L., 2013. Etude métallogénique et géophysiques des minéralisations cobaltifères et cuprifères de Bou-Azzer El Graara Anti Atlas Maroc (Tome 1). PhD thesis, Cadi Ayyad University, Marrakech, Morocco, 344p.

Mellini, M., Rumori, C., Viti, C., 2005. Hydrothermally reset magmatic spinels in retrograde serpentinites: formation of "ferritchromit" rims and chlorite aureoles. Contrib. Mineral. Petrol 149:266–275.

Merlini, A., Grieco, G., Diella, V., 2009. Ferritchromite and chromian chlorite formation in mélange-hosted Kalkan chromite (Southern urals, Russia). Am Miner 94 :1459–1467

Milton, C., Appleman, D. E., Appleman, M. H., Chao, E. C. T., Cuttitta, F., Dinnin, J. I., Dwornik, E. J., Ingram, B. L. and Rose, H. J., Jr., 1976. Merumite - a complex assemblage of chromium minerals from Guyana. U.S. Geol. Surv. Prof. Paper 887, 1-29.

Mrini, Z., 1993. Chronologie (Rb–Sr, U–Pb), traçage isotopique (Sr–Nd-Pb) des sources des roches Magmatiques éburnéennes, panafricaines et hercyniennes du Maroc PhD thésis, Cadi Ayad University, Marrakech, 227p.

Mukherjee, R., Mondal, S.K., Rosing, M.T., Frei, R., 2010. Compositional variations in the Mesoarchean chromites of the Nuggihalli schist belt, Western Dharwar Craton (India): potential parental melts and implications for tectonic setting. Contrib. Mineral. Petrol. 160 (6), 865–885.

Naïdoo, D.D., Bloomer, S.H., Saquaque, A., Hefferan, K., 1991. Geochemistry and significance of metavolcanic rocks from the Bou-Azzer-El Graara ophiolite (Morocco). Precamb. Res. 53, 79-97.

Prabhakar, N., Bhattacharya, A., 2013. Origin of zoned spinel by coupled dissolution– precipitation and inter-crystalline diffusion: evidence from serpentinized wehrlite, Bangriposi, Eastern India. Contrib. Mineral. Petrol. 166 (4), 1047–1066.

Proenza, J.A., Ortega-Gutiérrez, F., Camprubı, A., Tritlla, J., Elıas-Herrera, M., Reyes-Salas, M., 2004. Paleozoic serpentinite-enclosed chromitites from Tehuitzingo (Acatlán Complex, southern Mexico): a petrological and mineralogical study. J. S. Am. Earth Sci. 16 (8), 649–666.

Pujol-Solà, N., Domínguez-Carretero, D., Proenza, J. A., Haissen, F., Ikenne, M., González-Jiménez, J. M., Colás, V., Maacha, L., Garcia-Casco, A., 2021. The chromitites of the Neoproterozoic Bou Azzer ophiolite (Central Anti-Atlas, Morocco) revisited. Ore Geol. Rev. 134, 104166.

Samson, S.D., Inglis, J.D., D'Lemos, R.S., Admou, H., Blichert-Toft, J., Hefferan, K. 2004. Geochronological, geochemical, and Nd-Hf isotopic constraints on the origin of Neoproterozoic plagiogranites in the Tasriwine ophiolite, Anti-Atlas orogen, Morocco. Precamb. Res. 135, 133–147.

Satsukawa, T., Piazolo, S., González-Jiménez, J.M., Colás, V., Grifn, W.L., O'Reilly, S.Y., Gervilla, F., Fanlo, I., Kerestedjian, T.N., 2015. Fluid present deformation aids chemical homogenization in chromite: insights from chromites from Golyamo Kamenyane, SE Bulgaria. Lithos 228–229:78–89.

Saquaque, A., Admou, H., Karson, J.A., Hefferan, K., & Reuber, I., 1989. Precambrian accretionary tectonics in the Bou Azzer-El Graara region. Geology, 17, 1107–1110

Sergeeva, I.S., Kerestedjian, T.N., Nikolova, R.P., Gherkezova-Zhelena, Z.P., Gervilla, F., 2017. Crystal chemistry and structural characterization of natural Cr-spinels. Bulg Chem Commun 49 (special Issue A):7–20.

Singh, A.K., Singh, R.B., 2013. Genetic implications of Zn- and Mn-rich Cr-spinels in serpentinites of the Tidding Suture Zone, eastern Himalaya, NE India. Geol. J. 48 (1), 22–38.

Souiri, M., Aissa, M., Ahmed, A.H., El Azmi, M., Mezougane, H., Moussaid, A., El Basbas, A., 2021. Hydrothermal alterations of the Bou Azzer East Co-Ni-As-Au deposits (central Anti-Atlas, Morocco). Geosci. J. https://doi.org/10.1007/s12303-020-0063-2

Soulaimani, A., Ouanaimi, H., Saddiqi, O., Baidder, L., Michard, A., 2018. The Anti-Atlas Pan-African Belt (Morocco): Overview and pending questions. C. R. Geoscience. 350, 6, 278-288.

Subías, I., Fanlo, I., Hajjar, Z., Gervilla, F., Billström, K., 2022. Isotopic constraints on age, source of ore-forming fluids and genesis of the Bou Azzer arsenide ores (Morocco). Ore. Geol. Rev. Submited

Talukdar, M., Sanyal, S., Sengupta, P., 2017. Metasomatic alteration of chromite from parts of the late ArchaeanSittampundi Layered Magmatic Complex (SLC), Tamil Nadu, India. Ore Geol. Rev. 90, 148–165

Tekiout, B., 1991. Stratigraphie, pétrographie, géochimie et structure de l'ensemble arc/avant arc de la Boutonnière de Bou Azzer-El Graara (unité nord) Anti-Atlas Maroc. Thèse 3ème Cycle, Cadi Ayyad University, Marrakech, Morocco, 151p.

Traore, D., 2005. Serpentinisation hydrothermale et alteration lateritique des roches ultrabasiques en milieu tropical : evolution géochimique et minéralogique de la minéralisation en Platine de la rivière des Pirogues, (Nouvelle-Calédonie). Thèsis. Université de la Nouvelle-Calédonie, 222p

Triantafyllou, A., Berger, J., Baele, J.M., Diot, H., Ennih, N., Plissart, G., Monnier, C., Watlet, A., Bruguier, O., Spagna, P., Vandycke, S., 2016. The Tachakoucht–Iriri–Tourtit arc complex

(Moroccan Anti-Atlas): Neoproterozoic records of polyphased subduction-accretion dynamics during the Pan-African orogeny. J. Geodyn. 96, 81–103.

Triantafyllou, A., Berger, J., Baele, J.M., Bruguier, O., Diot, H., Ennih, N., Monnier, C., Plissart, G., Vandycke, S., Watlet, A., 2018. Intra-oceanic arc growth driven by magmatic and tectonic processes recorded in the Neoproterozoic Bougmane Arc complex (Anti-Atlas, Morocco). Precambrian Res. 304, 39–63.

Triantafyllou, A., Berger, J., Baele, J.M., Mattielli, N., Ducea, M.N., Sterckx S., Samson S., Hodel, F., Ennih, N., 2020. Episodic magmatism during the growth of a Neoproterozoic oceanic arc (Anti-Atlas, Morocco). Precamb. Res. 339, 105610

Wylie, A.G., Candela, P.A., Burke, T.M., 1987. Compositional zoning in unusual Zn-rich chromite from the Sykesville district of Maryland and its bearing on the origin of “ferritchromit”. Am. Mineral. 72, 413–422.

Chapter IV: Isotopic constraints on the age and source of ore forming fluids of the Bou Azzer arsenide ores (Morocco)

This chapter IV corresponds to a paper:

Subías, I., Fanlo, I., ***Hajjar, Z.,*** Gervilla, F., Billström, K., 2022. Isotopic constraints on age, source of ore-forming fluids and genesis of the Bou Azzer arsenide ores (Morocco). Ore geology review, 143, 104769. (IF. 3.714)

Abstract

The Bou Azzer district in Morocco has a long mining history since the beginning of the XXst century during which it has become the only world producer of Co from primary, hydrothermal Co arsenide ores. Orebodies are structurally controlled, and mainly distributed along fault contacts between Cryogenian ophiolite-related ser- pentinite bodies and intrusive quartz diorite or, locally, ophiolitic gabbros or Ediacaran volcanic rocks. Ore formation took place through a multi-stage mineralizing process that included an early stage composed by gold, quartz, chlorite, muscovite and calcite, followed by the main arsenide and sulfarsenide stage (subdivided into three substages, IIa: Ni-rich, Co ores, IIb: Co-Fe ores and IIc: Fe-Co ores), and ending with an epithermal stage characterized by the precipitation of sulfides along with quartz and calcite. Field relations and most previous geochronologic dating pointed to a post Pan-African age of ore formation, mainly coincident with the Hercynian orogeny.

The isotopic study presented in this paper includes S, Pb, Rb/Sr and Sm/Nd data of a set of ore mineral samples from three deposits (Aghbar, Tamdrost and Aït Ahmane), as well as of regional samples representative of the different lithologies occurring in the Bou Azzer area. The isotope data set was completed with S isotope analyses of arsenide and sulfarsenide minerals from five ore deposits (Filon 7/5, Aghbar, Tamdrost, Ightem and Aït- Ahmane) and of some whole-rock regional samples. Results show that ores formed during multi-episodic hydrothermal events connected with hercynian reactivation of Devonian-Carboniferous faults, supporting previous geochronologic dating. The obtained Pb, Sr, Nd and S isotopic signatures of ore minerals and regional rocks further show that ophiolite-related lithologies became isotopically modified by interaction with crustal material and afterwards acted as the main source of ore-forming elements. Nevertheless, isotopic data do not fully concur with such a simple scenario but are quite consistent with a rather complex interpretation based on multi-source origin of some elements and isotopes scavenged from a number of isotopically different lithologies both from the inferred basement and the volcanic and sedimentary cover.

Keywords: Co-Ni arsenide ores, Hydrothermal arsenides, Pb, Rb/Sr, Sm/Nd, and S isotopes, Bou Azzer

1 Introduction

Most cobalt production in the world comes from sediment-hosted copper deposits, magmatic Ni-Cu ores, five-element hydrothermal veins and laterite deposits, as a by-product. However, the Bou Azzer district in Morocco is nowadays the only locality in the world where cobalt is mined directly from Co-rich arsenide and sulfarsenide minerals as a primary ore. This world-class mining district includes more than 100 occurrences of Co-arsenide ores (Leblanc and Billaud, 1982) cor- responding to more than 2% of the world's cobalt production (U.S. Geological Survey, 2013). Currently, the mean annual production is about 150,000 t of ore (Ikenne et al., 2020) at an average grade of 1% Co and 1% Ni. In addition to Co and Ni, 3–4 g/t gold and silver are also recovered as by-products (Bouabdellah et al., 2016).

As a consequence of its huge economic potential, the district has been extensively studied over the last few decades, which has resulted in the release of research papers, theses, and unpublished mining company reports. In spite of the abundant literature, uncertainties still remain on the nature of mineral assemblages and paragenetic sequences (En- Naciri, 1995, Dolansky, 2007, Ahmed et al., 2009, Gervilla et al., 2012, Lasobras, 2012, L´azaro, 2012, Maacha, 2013, Bouabdellah et al., 2016, Ikenne et al., 2020), the physicochemical characteristics of ore-forming fluids (En-Naciri, 1995, Essarraj et al., 2005, Dolansky, 2007) and the timing of ore formation relative to the main tectonic events in the region (Clauer, 1976, Leblanc and Billaud, 1982, Gasquet et al., 2005, Dolan- sky, 2007, Oberthür et al., 2009, Blein et al., 2014, Bouabdellah et al., 2016, Tourneur et al., 2021).

Thus, the aim of this paper is to shed some light on the formation age of the Co-Ni arsenide ores of the Bou Azzer district as well as on the provenance of ore-forming fluids by means of a Pb, Sr, Nd and S isotope survey on a representative set of samples from different ore deposits and regional lithological units.

2 Geology and ore deposits of the Bou Azzer district

The Moroccan Anti-Atlas belt, separated from the High Atlas to the North by the South Atlas Fault, is constituted by several inliers of Pre- cambrian units within Late Ediacaran and younger units (Alvaro et al.,2014, Soulaimani et al, 2018; Table IV. 1). One of these inliers, the Bou Azzer-El Grâara inlier (Fig. IV. 1) is structurally the most complex portion of the whole

Anti-Atlas (Leblanc, 1981). The oldest formation located in the south-eastern part of the Bou Azzer inlier is made up of gneisses, pegmatites, schists, tholeiitic basalts, quartzites and carbonates. Such basement lithologies have been assigned to a Paleoproterozoic suite of rocks by Leblanc (1981); however, new U-Pb dating data for rocks gathered under the name Tachdamt Bleida group, and Tazegzaout group in Bou Azzer demonstrate Tonian and Early Cryogenian ages (900–700 Ma; Clauer, 1976, D'Lemos et al., 2006, Blein et al., 2014, Hefferan et al., 2014, Bouougri et al., 2020, Triantafyllou et al., 2020). In the North East Bou Azzer inlier outcrop a complex tectonic assemblage made up of metagreywackes and arc-related basalts, andesites, rhyolites and tuffs has been grouped under the name Tichinbanine Ben Lagrad group, and dated between 761 ± 7 Ma and 767 ± 7 Ma (Blein et al., 2014, Triantafyllou et al., 2018, 2020). An important Cryogenian terrane is defined by the Bou Azzer Group, which includes a mafic–ultramafic complex (serpentinized peridotites containing podi- form chromitites, layered gabbros, pillow lavas, diabase dykes and associated sedimentary rocks), interpreted by Leblanc (1981) as an ophiolite sequence. The above formations were intruded by syn- to post- kinematic stocks: *syn*-orogenic (640–660 Ma) quartz-diorite (Mrini, 1993, Samson et al., 2004, Inglis et al., 2003, El Hadi et al., 2010, Blein et al., 2014, Triantafyllou et al., 2020) and post-orogenic (594 ± 1.2 Ma) gabbrodiorite (Inglis et al., 2004, Blein et al., 2014). All the above formations were thrusted and folded during the Pan-African orogeny and were unconformably overlain by the molassic Tiddiline Group, the Ediacaran volcanoclastic pile (e.g. ignimbrites, andesites, conglomer- ates, sandstones dated at 606 ± 5 Ma; Blein et al., 2014), the Ouarzazate Supergroup (567 ± 5 Ma and 566 ± 4 Ma; Blein et al., 2014) and the lower Cambrian Taroudant Group (541 ± 6 Ma; Blein et al., 2014). According to Gasquet et al. (2005) a regional N–S shortening that occurred during the Variscan orogeny reactivated the major Pan-African faults.

Most Co–Ni–Fe arsenide (±Au ± Ag) deposits are structurally controlled and distributed along the boundaries of the serpentinite massifs which display vertical contacts with the quartz diorites and locally Ediacaran volcanic rocks of the Ouarzazate Group (Tourneur et al., 2021). From the west to the east (Fig. IV. 1), the studied deposits are: Mechoui, Filon 7/5, Aghbar, Tamdrost, Ambed, Ightem, Agoudal, and Aït-Ahmane. Co-Ni-Fe ores in the Bou Azzer inlier display variable shapes: *trans*-tensional, sub-vertical fault-jogs, flame-shaped orebodies, flat lensoidal and pocket-like masses, lodes, veins, veinlets, cemented breccias within veins, and fillings. Further, ores occur in various settings as: i) veins and lodes with sharp wall-rocks along

the contacts between serpentinites and other rocks. Locally, arsenide mineralization may extend into serpentinite and quartz diorite wall rocks for 10 m or more (En-Naciri, 1995, Levresse, 2001, El Ghorfi, 2006, Dolansky, 2007, Maacha, 2013, Tourneur et al., 2021); ii) veins and irregular replace- ment bodies hosted by serpentinites with diffuse, gradational contacts with the host (Hajjar et al. 2021); iii) mineralized veins secant to this contact, hosted mainly in quartz-diorite and rhyolite from the Ouarza- zate group (En-Naciri, 1995, Levresse, 2001, El Ghorfi, 2006, Dolansky, 2007, Maacha, 2013, Tourneur et al., 2021). The mineralized structures of the Bou Azzer cobalt district can be grouped into four main directions. E-W, NE-SW, NW-SE and N-S. No consistent paragenetic sequence can be defined owing to multiple overlapping pulses of mineralization; never- theless, according to Maacha (2013) and Bouabdellah et al. (2016) the sequence of mineral deposition shows three main stages: (I) the early pre-arsenide stage composed by gold, quartz, chlorite, muscovite and calcite, (II) the Co–, Ni-, Fe-rich main arsenide and sulfarsenide stage and (III) an epithermal stage marked by the precipitation of sulfides associated to late quartz and calcite. Mineralogy and micro-textures of stage II (En-Naciri, 1995, Dolansky, 2007, Ahmed et al., 2009, Gervilla et al., 2012, Lasobras, 2012, L´azaro, 2012) allow a subdivision into three sub-stages (Fig. IV. 2): (IIa) precipitation of arsenide ores starting with the formation of Ni-rich ores including nickeline, rammelsbergite, Ni-rich skutterudite, members of the rammelsbergite-safflorite-löllingite solid solution series and sulfarsenides (gersdorffite and minor cobaltite), (IIb) formation of Co-Fe rich ore assemblages made up of Co-rich skutter- udite, Co-Ni-Fe diarsenides deeply evolving from Co– and Ni-rich com- positions to the löllingite corner of the rammelsbergite-safflorite- löllingite ternary system, members of the safflorite-löllingite solid so- lution series and cobaltite, and (IIc) precipitation of Fe-Co rich ores composed of a third generation of skutterudite, safflorite, löllingite, cobaltite, alloclasite, arsenopyrite and molybdenite that may evolve locally to nearly monomineralic löllingite ores (Hajjar et al., 2021). It also needs to be mentioned that gold and silver are highly concentrated in some ore zones (Bouabdellah et al., 2016), and that a post-ore su- pergene stage comprising rare arsenides and arsenates is characterizing the upper parts of mineralized structures.

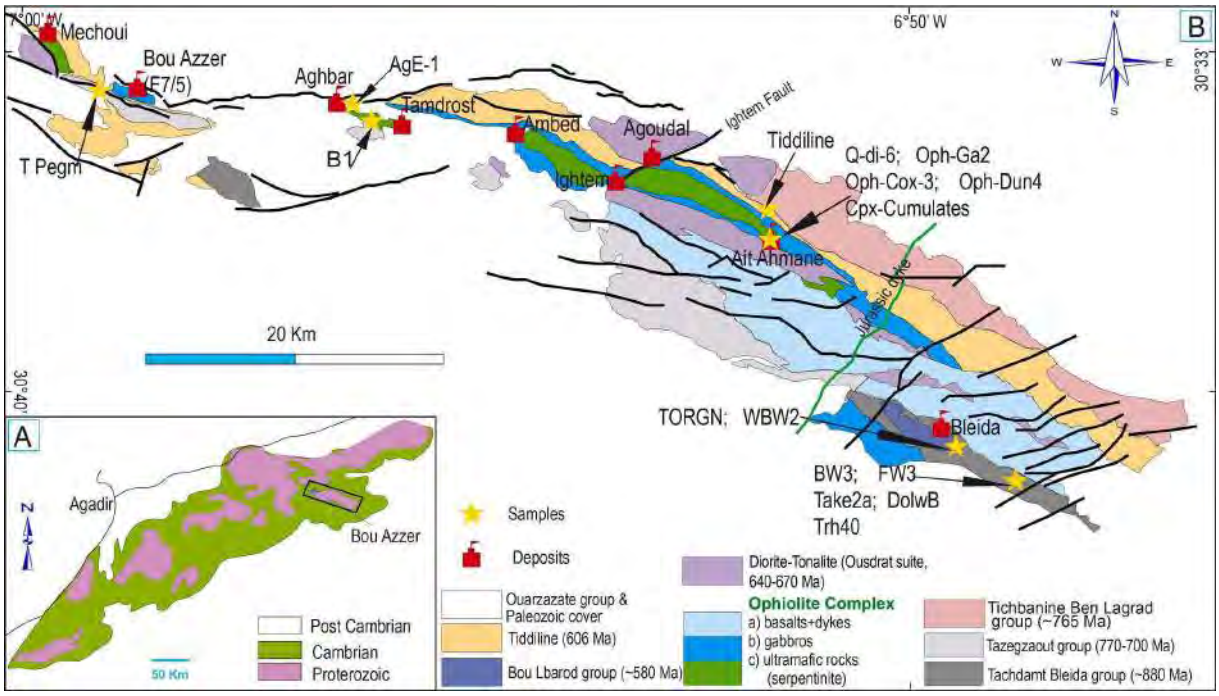

Fig. IV. 1. (A). Simplified geological map of the Anti-Atlas belt. (B). Geological map of Bou Azzer inlier (Central Anti Atlas, Morocco) (modified from Soulaimani et al., 2018), showing the main Co-Ni deposit in the district

Information on the nature of ore-forming fluids comes from a few fluid inclusion studies performed on the Bou Azzer ores (En-Naciri, 1995, Essarraj et al., 2005, Dolansky, 2007) and from some C, O and H isotopic data (Dolansky, 2007, Maacha et al., 2015). The obtained results are controversial. En-Naciri (1995) reported fluid inclusions of pre- and post-ore quartz and post-ore calcite containing moderate to highly saline fluids (15–22 wt% NaCl and 16.5–20.5 wt% $CaCl_2$) trapped at low temperatures (120–240 ˚C) under variable pressures (0.4–1.2 kb) in both pre-ore quartz and post-ore calcite. Essarraj et al. (2005) described a Co-Fe-As ore related with a late stage of Ag-Hg characterized by fluid inclusions with large halite crystals indicative of hyper-saline Na-Ca brines (16–24 wt% NaCl and 21–23 wt% $CaCl_2$) trapped at lower tem- peratures (120–200 ˚C) under a pressure range of 40–80 MPa. In contrast Dolansky (2007) found highly saline brines (31–42 wt% NaCl and 6–13 wt% $CaCl_2$) trapped at relatively high temperature (298–409 ˚C) under relatively high pressures (1.6–2.5 kb) in primary inclusions in pre-ore quartz. Dolansky (2007) also determined the salinity of secondary fluid inclusions (36–45 wt% NaCl and 13–26 wt% $CaCl_2$) in pre-ore quartz and of primary fluid inclusions in post-ore calcite (15.5–19.1 wt% NaCl and 20.9–21.5 wt% $CaCl_2$). She considered the high salinity, the homogenization temperature (164–290 ˚C) and trapping pressure

(0.88–1.4 kb) of the former as representative of the ore-forming fluids. The lower salinity, temperature (≥200 ˚C) and pressure (~0.65 kb) of the inclusions in post-ore calcite indicate decreasing P-T trapping conditions over the course of mineral deposition. Maacha et al. (2015) and Dolansky (2007) also measured $\delta^{18}O$ and δD in quartz separates and a chlorite sample obtaining values of the precipitating fluids ranging from 7.9 to 9.6‰ $\delta^{18}O$ and from -62 to -30‰ δD with little variations among samples or deposits. These data were interpreted as signatures of magmatic water, whereas Maacha et al. (2015), on the basis of $\delta^{13}C$ (from -1.61 to -6.5‰) and $\delta^{18}O_{fluid}$ values (from -6.3 to 5.9‰) values in Bou Azzer calcite and dolomite, argued for the presence of exogenic water in the formation of the associated arsenide ore.

Published sulfur isotope data are scarce (Dolansky, 2007, Maacha et al., 2015) and hardly representative for the main ore-forming event as they provide a set of scattered $\delta^{34}S$ data from –32.3 to 9.9‰ obtained from galena, pyrite and chalcopyrite pertaining to the late epithermal stage.

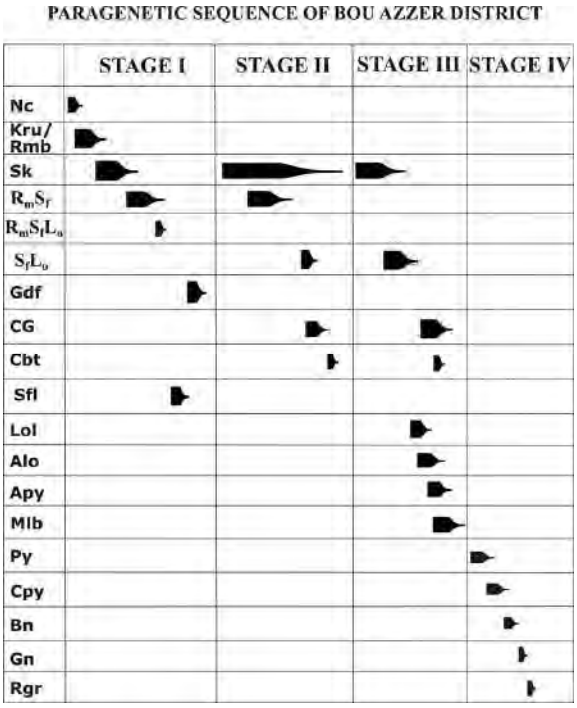

Fig. IV. 2. Paragenetic sequence of arsenide ores from Bou Azzer district. Nc: nickeline, Kru/Rmb: krutovite/rammelsbergite, Sk: skutterudite, R_mS_f: crystals of rammelsbergite-safflorite solid solution, $R_mS_fL_o$: crystals of rammelsbergite- safflorite-Löllingite solid solution, S_fL_o: crystals of safflorite-löllingite solid so- lution, Gdf: gersdorffite, CG: crystals of cobaltite-gersdorffite solid solution, Cbt: cobaltite, Sfl: safflorite, Lol: löllingite, Alo: alloclasite, Apy: arsenopyrite, Mlb: molybdenite, Py: pyrite, Cpy: chalcopyrite, Bn: bornite, Gn: galena, Rgr: realgar.

Table IV. 1. Rock samples age according to the geochronologic dating of the host formations

Rock Sample	Rock Type/Ores	Localization	Group	Age Ma	Reference
				Ediacarian	
AgE-1	Andesitic tuffs	Aghbar (PIII)	Ouarzazate	567 ± 5	Blein et al., 2014
Tiddiline	Sandstone	Near Aït Ahmane	Tidilline	606 ± 14	Blein et al., 2014
WBW2	Granodiorite	Bleida Far West		594 ± 1.2	Inglis et al., 2004
				Upper Cryogenian	
Q Diorite	Quarzt-diorite	Filon 7/5		640–660	Blein et al., 2014; Triantafyllou et al., 2020;
Q Di-6	Quarzt-diorite	Aït Ahmane		640–660	Inglis et al., 2003; Mrini, 1993
Rodingite	Rodingite	Filon 7/5			
OPH-Ga2	Gabbro	Aït Ahmane	Bou Azzer El Grara	697 ± 8	El Hadi et al., 2010
B1, serp.	Serpentinite	Bouismas	Bou Azzer El Grara		
cpx, cumulates	Clinopyroxenite	Aït Ahmane	Bou Azzer El Grara		
OPH-cpx3	Clinopyroxenite	Aït Ahmane	Bou Azzer El Grara		
OPH-DUN 4	Dunite	Aït Ahmane	Bou Azzer El Grara		
OPH-CR1	Chromitite	Aït Ahmane	Bou Azzer El Grara		
				Tonian to Lower Cryogenian	
T Pegm	Pegmatite veins	Ouest Bou Azzer	Tazegzaout	702 ± 5, 695 ± 7	Blein et al., 2014
T ORGN	Orthogneiss	Bleida Far West	Tazegzaout	753 ± 2; 755 ± 9	D'Lemos et al., 2006; Blein et al., 2014
TAK-2a	Rhyolite	Bleida Far West	Tichibanine	767 ± 7	Blein et al., 2014; Triantafyllou et al., 2020
Trh 40	Rhyolite	Bleida Far West	Tichibanine	767 ± 7	Blein et al., 2014
BW-3	Volcanosedimen ts	Bleida Far West	Tichibanine	767 ± 7	Blein et al., 2014
FW-3	Volcanosedimen ts	Bleida Far West	Tichibanine	767 ± 7	Blein et al., 2014
DOL WB	Dolomite	Bleida Far West	Tachdamt-Bleida	789 ± 10	Clauer, 1976

Crosscutting and offsetting relationships led Leblanc and Billaud (1982) to conclude that all the orebodies postdate the serpentinization and the structures of the major Pan-African tectonic phase during which ophiolite obduction and greenschist metamorphism took place (685 ± 15 Ma; Rb/Sr, Clauer, 1976; 660-640 Ma, Blein et al., 2014). Leblanc and Billaud (1982) also observed that the main orebodies are located along transcurrent sinistral faults belonging to the ultimate Pan-African phase, between 615 and 580 Ma ago. Therefore, they did not rule out that this time relate to mineralization events in the district. Bouabdellah et al. (2016) argued that the Bou Azzer mineralization is younger than the emplacement of the trachytic sills dated at 531 ± 5 Ma (U–Pb SIMS zircon ages) by Gasquet et al. (2005). A number of other radiometric studies aimed to date mineralization have yielded highly variable ages, from about 400 Ma down to 32 Ma, and their significance will be further discussed below. To sum up, a complex, telescoped and polymetallic (Co–Ni–As–Fe–Cu–Au–Ag) mineral district appears to be the result of late Pan-African and Variscan deformations and recrystallizations.

3 Sampling and analytical techniques

Specimens for microscopy and isotope investigations have been gathered from 5 Co-Ni deposits in the Bou Azzer area (

Table IV. 2). In particular, the study has mainly focused on three deposits Fig. IV. 3A-C); Tamdrost, Aghbar and Aït-Ahmane which are shortly described below as well as two other deposits (Filon 7/5 and Ightem) from which several samples were analysed for S isotopes. In addition, an examination of polished sections from Mechoui, Ambed and Agoudal added further support to the view that ores of the Bou Azzer district share a number of common features, such as a structural control and variable ore settings. Representative ore textures from some selected ores are shown in Fig. IV. 4. According to Maacha et al. (2015) the Tamdrost type ore bodies located at the discordant contact of serpentinites with felsic volcanic rocks of the Ouarzazate group are represented by veins and lenses filling fractures of extension and compression. A supergene alteration zone in serpentinite is the main ore-bearing structure hosting orebodies with maximum thickness at the contact of altered serpentinite.

Maacha et al. (2015) also show that the altered serpentinite is hosting ore veins at Aghbar that are related to synchronous fracturing and the ore body is restricted to the flanks of a serpentinite dome structure, whereas Dolansky (2007) pointed out that the mineralized structure at Aghbar is a broadly sub horizontal contact orebody with a concave-down form

draped over the serpentinite massif. The structure is commonly described as a complex shell, owing to numerous subvertical lenses referred to as flamelike structures, attributed to the Hercynian deformations (Leblanc, 1975).

Table IV. 2. Co-Ni-Fe ore samples age according to the geochronologic dating of the ore deposit Sample Localization Age Ma/Reference.

Sample	Ores	Localization	Age Ma	Reference
			Paleozoic	
759	Co-Ni-Fe ores	Filon 7/5	Brannerite associated to skuterudite (383 ± 7 to 355 ± 10, U/Pb, (Dolansky, 2007)); Brannerite associated to sulfide (257 ± 8 to 32 ± 2, U/Pb, (Dolansky, 2007)); Adularia associated to Sulfide (215 ± 8, Ar-Ar, (Leveresse, 2001) ; Molybdenite (350 - 400, Re-Os, (Oberthur et al., 2009)) ; Carbonates associated to sulfide (308 ± 31 Ma, Sn-Nd (Oberthur et al., 2009)	
972	Co-Ni-Fe ores	Filon 7/5		
1281	Co-Ni-Fe ores	Filon 7/5		
2456	Co-Ni-Fe ores	Filon 7/5		
2457	Co-Ni-Fe ores	Filon 7/5		
728	Co-Ni-Fe ores	Aghbar	Molybdenite (350 - 400, Re-Os, (j)); Carbonate associated to sulfide (308 ± 31 Ma, Re-Os, (Oberthur et al., 2009))	
727	Co-Ni-Fe ores	Aghbar		
726	Co-Ni-Fe ores	Aghbar		
819	Co-Ni-Fe ores	Aghbar		
1026	Co-Ni-Fe ores	Aghbar		
722	Co-Ni-Fe ores	Aghbar		
819	Co-Ni-Fe ores	Aghbar		
722	Co-Ni-Fe ores	Aghbar		
543	Co-Ni-Fe ores	Aghbar		
724	Co-Ni-Fe ores	Aghbar		
689	Co-Ni-Fe ores	Aghbar		
824	Co-Ni-Fe ores	Aghbar		
670a	Co-Ni-Fe ores	Aghbar		
805a3	Co-Ni-Fe ores	Aghbar		
843	Co-Ni-Fe ores	Aghbar		
2101	Co-Ni-Fe ores	Tamdrost	Muscovite present from Early stage to sulfide stage (392 ± 15; 356 ± 20, Ar-Ar (Leveresse, 2001)	
1551	Co-Ni-Fe ores	Tamdrost		
1643	Co-Ni-Fe ores	Tamdrost		
542	Co-Ni-Fe ores	Tamdrost		
79	Co-Ni-Fe ores	Ightem		
2418	Co-Ni-Fe ores	Aït-Ahmane	Carbonate associated to sulfide (308 ± 31 Ma, Re-Os, (Oberthur et al., 2009))	
2445	Co-Ni-Fe ores	Aït-Ahmane		
999	Co-Ni-Fe ores	Aït-Ahmane		

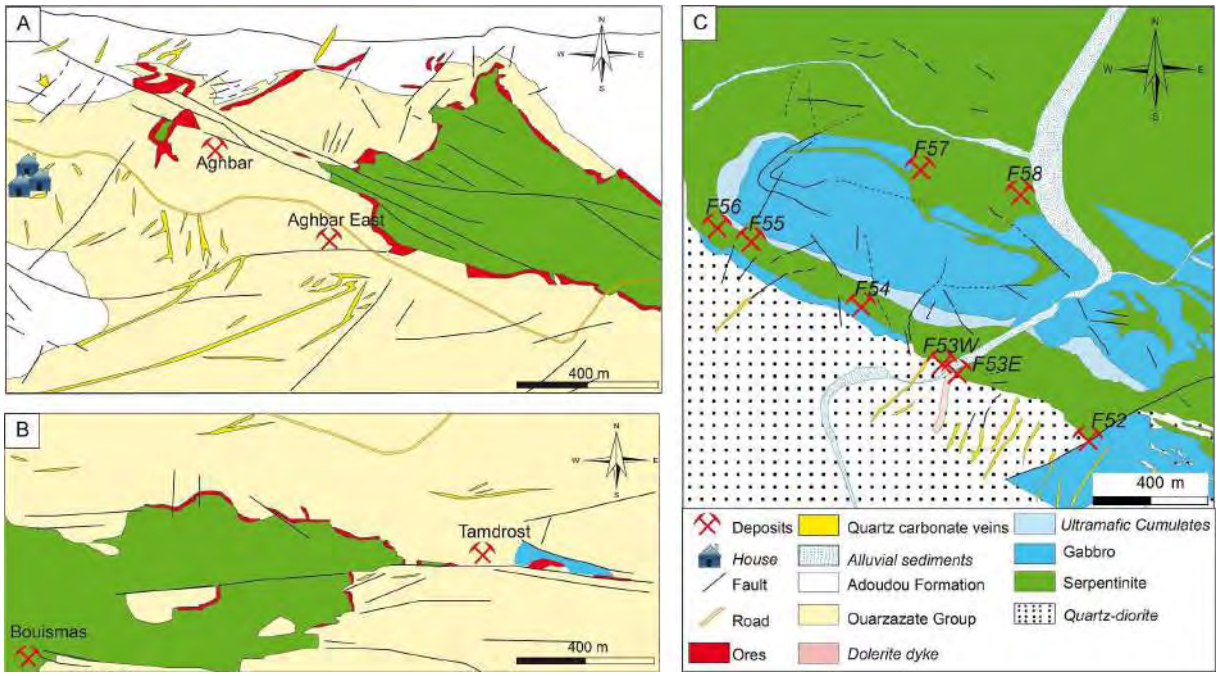

Fig. IV. 3. (A) Geological map of Aghbar deposit (modified after Leblanc, 1981). (B) Geological map of Tamdrost deposit (modified after Leblanc, 1981). (c) Geological map of Aït-Ahmane area (modified from Saquaque et al., 1992), showing the location of the differente ore deposits.

Aït-Ahmane does not refer to a single deposit but to an area in the easternmost part of the district where several ore veins are/were mined. The mineralization at Aït-Ahmane has been described as a "contact mineralization" that is hosted by lenses of calcified serpentinite located at the contact between serpentinite and quartz diorite or gabbro (En- Naciri, 1995) and as massive to disseminated bodies fully hosted by serpentinite (Hajjar et al., 2021). The former ore, taking the shape of disseminated, minute spherical aggregates, occurs essentially as an infilling in dissolution cavities within a mixture of clastic and chemical sediments. The latter ore fills intraserpentinite faults extending out- wards through the fault walls filling small entwined veins and partly replacing serpentinite (Hajjar et al., 2021). These authors pointed out that serpentinite-hosted ores are atypical in that they are mainly formed by Fe diarsenides (löllingite) with very low Ni and Co contents. Mineral textures show that ore-forming fluids partly have dissolved serpentine and, subsequently, precipitated Fe-rich arsenide ores.

Various types of samples have been analysed for their (Pb, Sr, Nd and S) isotopic and geochemical signatures. The fine-grained nature of the ores poses a challenge during the stage of sample selection for (S and Pb) isotope analyses. The di-, tri-arsenide and sulfarsenide minerals from different depositional stages, and encompassing all morphological types, were

selectively sampled from polished sections by using a rotatory tool (DremelTM) equipped with LascoTM 1.58 mm and 2.38 mm diamond core drills. As a complement, a few course Bou Azzer ore samples were also taken from the mineral collection of the Swedish Museum of Natural History. These specimens allowed separation of enough material for doing Sr-Nd isotope work, but their exact locality is not known. Regional rocks were selected to encompass plausible source rocks of mineralizing components at the time of ~~o~~re formation.

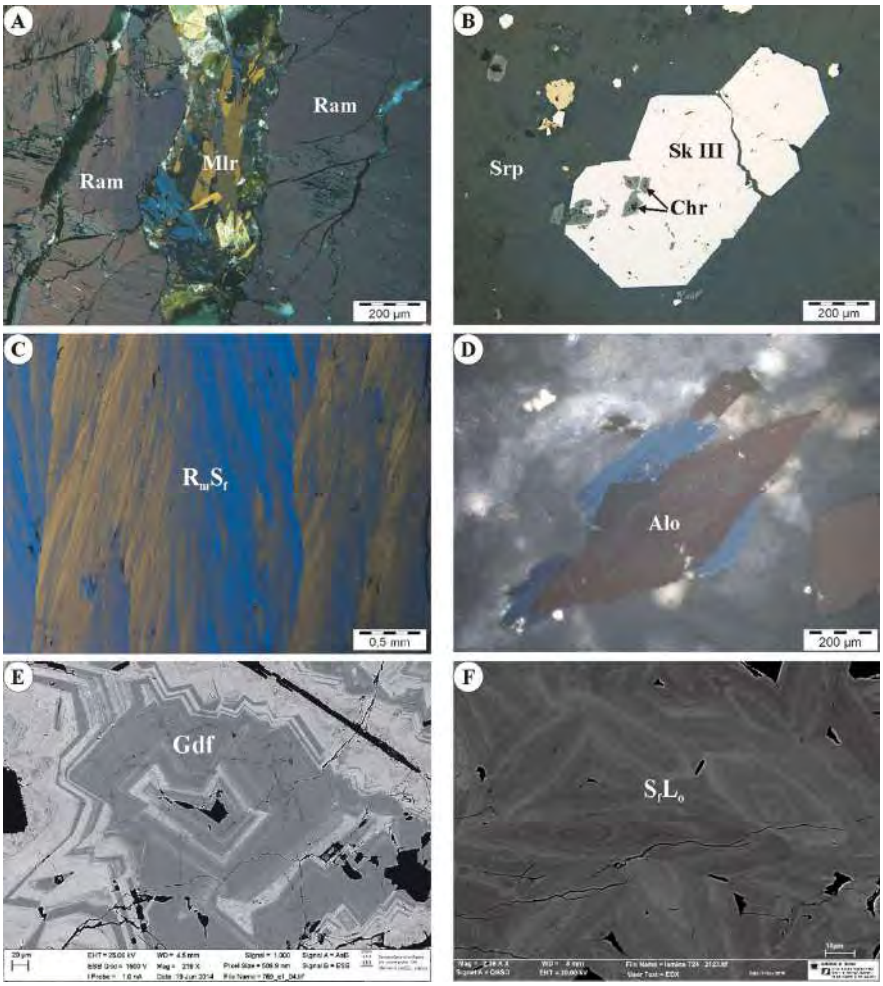

Fig. IV. 4. Reflected-light photomicrographs (A-D) and Back Scattered electron images (E-F) showing representative mineralogy of the studied ore deposits from Bou Azzer arsenide ores (Morocco). (A) Massive rammelsbergite exhibiting anisotropic colors with lamellae and inversion-induced polysynthetic twins; the crack in the middle of the masse is filled by millerite; #670a, Aghbar. (B) Euhedral crystals of skutterudite III, including small chromian spinel grains, scattered in serpentinite; #728, Aghbar. (C) Rammelsgergite-Safflorite solid-solution crystals with plumose textures; #1643–3, Tamdrost. (D) Idiomorphic crystals of alloclasite; #2449 Aït-Ahmane. (E) Crystals of arsenian- gersdorffite showing oscillatory replacement-induced zoning, very fine in scale along crystallographic directions; #759a, Filon7/5. (F) Rhythmic compositional zoning in löllingite–safflorite solid-solution crystals; #724, Aghbar. Abbreviations: Ram: rammelsbergite; Mlr: millerite; Sk III: skut- terudite from stage III; Chr: chromian spinel; Srp: serpentinite; R_mS_f: rammelsbergite-safflorite solid-solution series; Alo: alloclasite; Gdf: gersdorffite; S_fL_o: safflorite- löllingite solid-solution series.

Before the Sr-Nd-Pb-isotope ratio measurements, minerals and whole rock samples were spiked with a mixed $^{147}Sm/^{150}Nd$ spike solution (a mixed ^{84}Sr-^{87}Rb spike was also added to museum ore samples aimed for Rb-Sr analysis) and digested in nitric acid and a HF-$HClO_4$ acid mixture, respectively. Initially, dissolved samples went through an ion exchange column set-up using a mixture of TrueSpec® of AG1x8 resins. Sr was further purified in a second pass through the same columns now filled with SrSpec® resin, whereas Nd (and Sm) was isolated in Ln-spec col- umns (Pin and Zalduegui, 1997). The Pb fractions were re-dissolved in HBr, and treated further in columns with AG1 × 8, Cl^- form resin.

A Thermo-Finnigan Triton thermal ionization mass spectrometry (TIMS) instrument was used for the Sr and Nd isotope analyses and data were normalized to $^{88}Sr/^{86}Sr = 0.1194$ and $^{146}Nd/^{144}Nd = 0.7219$, respectively. Additionally, replicate analyses of the NBS-987 Sr standard analyzed during the course of the study yielded an average $^{87}Sr/^{86}Sr = 0.710221 \pm 0.000011$ (2σ external precision). Corresponding analyses of the La Jolla Nd standard yielded an average $^{143}Nd/^{144}Nd = 0.511848 \pm 0.000009$ (2σ external precision). Estimated external uncertainties amount to ca. ± 0.4 and ± 0.00005 for the calculated εNd and Sr initial isotope values, respectively. Pb isotope analyses were performed with a Nu Plasma II ICP-MS instrument (hosted by the Vegacenter facility), with Tl added to allow for an internal correction of the mass bias, and the measured intensities were corrected for background and Hg inter- ference on mass 204. The NBS-981 Pb standard was run at regular in- tervals and all unknowns were analyzed in duplicate. The obtained values for the standard are within error of those given by Todt et al. (1996), and the external reproducibility is between 0.04% ($^{206}Pb/^{204}Pb$) and 0.08% ($^{208}Pb/^{204}Pb$).

Sulfur isotope analyses were performed at the Laboratorio de Iso´topos Estables (University of Salamanca, Spain). Sulfur isotopic ratios of arsenide and sulfarsenide minerals were obtained by pyrolysis on an Elemental Analyzer (Eurovector EA3000) coupled on line with an Iso- prime (Micromass) continuous flow mass spectrometer. The SO_2 liber- ated by standard stable isotopic extraction techniques (Coleman and Moore, 1978) was analyzed using a dedicated SITA-II (VGIsogas) dual inlet mass spectrometer. Due to the small SO_2 quantities produced in both methods, V_2O_5 was added to favour combustion.

Sulfur from regional rocks was separated using a chemical extraction technique based on the works of Canfield et al. (1986) and Hall et al. (1988), with modifications as described by Recio et al. (1991). Results are reported in the standard delta per mil notation relative to

Canyon Diablo Troilite (CDT). Replicate analysis of reference standards gave an average reproducibility of ± 0.3‰.

Element concentrations of whole rock samples were determined at Intertek Laboratories (Australia). Sample preparation was performed by four acid digestion offering a near total dissolution of all mineral species. All elements were analyzed by combined ICP-OES and ICP-MS methods for ultra-trace levels under the control of certified international stan- dards. Further details on the latter, as well as calibration, detection limits, etc., can be found at http://www.intertek.com/minerals.

4 Results

Ore samples were analyzed mainly for their lead and sulfur isotope composition, and for a few of these also Sr and Nd isotope analyses were carried out. Further, to establish the source of metals in nearby Bou Azzer ores, radiogenic (Pb-Sr-Nd) isotope data, along with some S isotope analyses and geochemical results, have been acquired from a suite of potential source rocks. Most of the sampled rocks are Neo- proterozoic, comprising either a Cryogenian ophiolitic suite or are sedimentary, volcano-sedimentary and granitic rocks of a similar age (Table IV. 1). Others formed during the Ediacaran period.

4.1 Pb isotopes:

The results of Pb-isotope analysis of twenty-four ore samples and nineteen regional rock samples are given in Tables 3 and 4 and presented on conventional Pb-isotope diagrams in Figs. 5 and 6. $^{206}Pb/^{204}Pb$, $^{207}Pb/^{204}Pb$ and $^{208}Pb/^{204}Pb$ ratios of the arsenide and sulfide ores cover a wide range between 15.79 and 56.93, 15.13–17.71 and 34.85–38.66, respectively. One löllingite sample (#1643/10) from Tamdrost has a remarkably unradiogenic composition ($^{206}Pb/^{204}Pb$ =15.79), and an arsenopyrite sample (#819) from Aghbar has also a deviating, unradiogenic composition ($^{206}Pb/^{204}Pb$ = 16.71). Another outstanding feature is that a significant number of ore samples from the Aghbar and Tamdrost deposits are strongly radiogenic and tend to define linear uranogenic trends with relatively flat slopes (Fig. IV. 5A, inset). Other ore samples display a relatively limited data variation with e.g. $^{206}Pb/^{204}Pb$ between ca 17.9 and 18.1, but since this group of samples show a significant range in their $^{207}Pb/^{204}Pb$ ratios for a given $^{206}Pb/^{204}Pb$ ratio it becomes somewhat ambiguous to tell exactly which samples define the flat trends. Yet, if

such trends are interpreted as isochrones originating from an approximative bulk ore signature, and by excluding two Tamdrost (1643/34 and 1643/10) and three of the Aghbar samples (724, 819 löll and 1026) plotting below reasonable arrays, their slopes suggest ages at 392 ± 48 Ma (MSWD = 3.2) and 400 ± 150 Ma (MSWD = 30) for Aghbar (n = 10 samples) and Tamdrost (n = 6), respectively. A combined regression involving Aghbar and Tamdrost samples yields an age of 382 ± 52 (MSWD = 12). Although there is a clear variation in $^{207}Pb/^{204}Pb$ data from the Aït-Ahmane deposit ($^{206}Pb/^{204}Pb$ close to 18.0) that exceeds the analytical precision, the compositional range is narrower compared to the other deposits, although this could be the result of the restricted number of samples collected from this deposit (Table IV. 3). The thorogenic lead systematics of ore minerals (Fig. IV. 5B) seem also quite complex given that a range of specimens have significantly radiogenic, and variable, $^{206}Pb/^{204}Pb$ in combination with comparatively low $^{208}Pb/^{204}Pb$, in consistency with very low apparent Th/U ratios of these minerals. The remaining ore minerals cluster in a comparatively unradiogenic region and tend to form a crude linear, steep array.

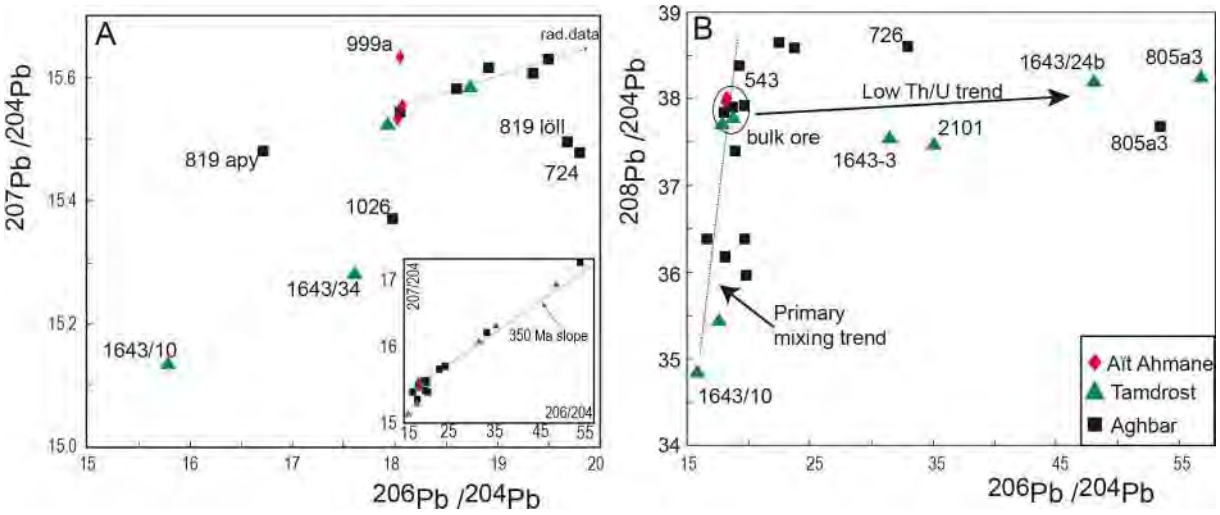

Fig. IV. 5. Lead isotopic compositions of ore phases from three deposits in the Bou Azzer area. A) a $^{207}Pb/^{204}Pb$ versus $^{206}Pb/^{204}Pb$ plot. The inset shows the full range of obtained compositions. Added is a reference line with a slope corresponding to the preferred ore formation age (350 Ma); B) a $^{208}Pb/^{204}Pb$ versus $^{206}Pb/^{204}Pb$ plot. The hatched line is likely depicting a potential syn-ore mixing effect, whereas the flat line illustrates the effect of an in-situ effect controlled by U-rich and Th- poor inclusions.

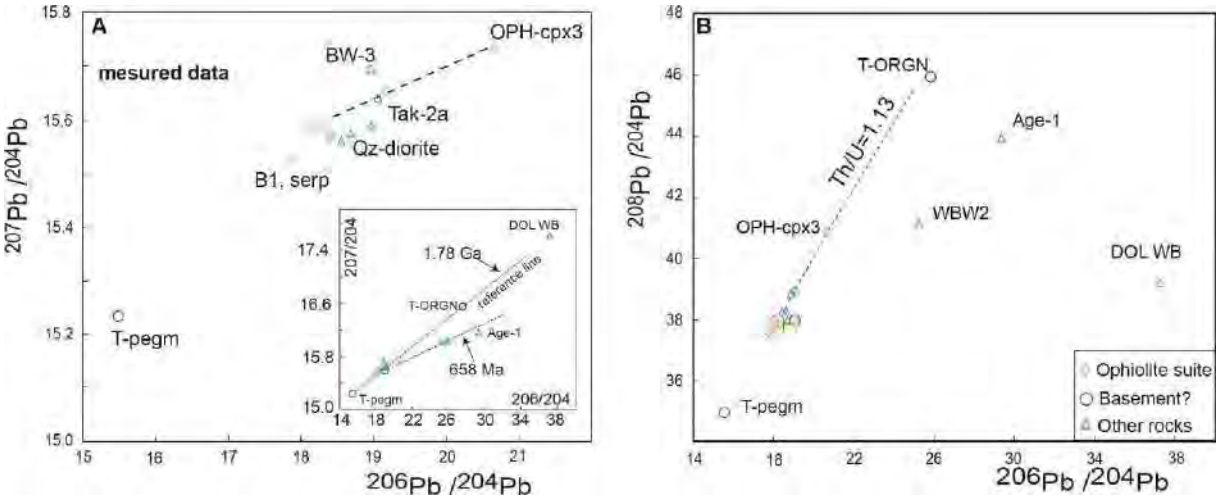

Fig. IV. 6. Lead isotopic compositions of selected whole rocks, occurring at distal positions from known ore occurrences, in the Bou Azzer area. The encircled areas in diagrams approximate the isotopic signature of the ophiolite magma ($^{206}Pb/^{204}Pb$ = 18, $^{207}Pb/^{204}Pb$ = 15.6 and $^{208}Pb/^{204}Pb$ = 38), and this composition is also used as a starting point of a line connecting samples with an ophiolitic chemistry. A) a $^{207}Pb/^{204}Pb$ versus $^{206}Pb/^{204}Pb$ plot. The steep dotted line in the inset aligns three samples (T-pegm, Tak-2a and T-ORGN) that might exemplify isolated remnants of a Proterozoic basement, whereas the hatched line in the main diagram is drawn to connect rocks with an ophiolitic chemistry; B) a $^{208}Pb/^{204}Pb$ versus $^{206}Pb/^{204}Pb$ plot.

Rocks of the ophiolite suite (e.g. gabbro and serpentinite) and associated rocks (e.g. Qz-diorite and rodingite) have relatively unra- diogenic compositions with $^{206}Pb/^{204}Pb$ between ca. 18.0 and 18.4 (Table IV. 4) that are similar to, or slightly more radiogenic, than the bulk of ore data. However, in analogy with the situation for some ore specimens, data for certain rock samples span a large Pb isotope interval (Fig. IV. 6). The extreme values are defined by an unradiogenic composition of a pegmatite (T-pegm; $^{206}Pb/^{204}Pb$ = 15.49) and radiogenic data for a dolomite (WB-Dol; $^{206}Pb/^{204}Pb$ = 37.25), respectively. There is no systematic isotope pattern to be seen if the inferred stratigraphic ages for different rocks are taken into account; yet, e.g. the composition of the T- peg sample would argue for an Early Proterozoic time of emplacement. Tentatively, certain rock data form crude linear arrays in the uranogenic diagram (Fig. IV. 6A), but their significance is not obvious as further dis- cussed below. With regard to the thorogenic lead, rock data tend to develop an array defining a steep slope (stippled line in Fig. IV. 6B) and the bulk ore composition plots close to this array whose end-members are defined by basement rocks. As also noted for the ore minerals, there is a tendency for a few rocks to show high $^{206}Pb/^{204}Pb$ ratios but without correspondingly elevated $^{208}Pb/^{204}Pb$ values.

4.2 Sr isotopes:

Only a few Rb-Sr analyses were carried out on museum ore speci- mens; two skutterudite, one erythrite and one carbonate. The obtained $^{87}Sr/^{86}Sr$ values are quite homogeneous and close to 0.710 (Table IV. 5). The calculation of their initial Sr isotope values is not obvious to carry out since the age of mineralization is still a debated issue. However, the obtained Rb/Sr ratios are generally low implying that the back- calculation to a desired time(s) of ore formation is not critically dependent on the exact age. By using an average ore mineralization age of 350 Ma (see discussion below), the calculated initial values of ore minerals fall between 0.709 and 0.710 (Table IV. 5). A first order approx- imation suggests these values to be a good estimate of the strontium isotope signature carried by Bou Azzer ore-forming solutions.

Rock data, on the other hand, are more heterogeneous which is an expected feature given that the data set involves rocks of different ages and origin and data scatter a lot in a conventional Rb-Sr isochron dia- gram (not shown). Partly, the scatter may be due to possible distur- bances of the Rb-Sr system which in turn would affect calculated initial Sr isotope compositions. Such compositions, calculated using the infer- red emplacement ages tabulated in Table IV. 5, are between 0.7019 and 0.7060 for the dolomite, the rhyolite, a Qz-diorite and three rocks (serpentinite, dunite and gabbro) believed to belong to the ophiolite suite. No Sr concentration data is available for the analyzed clinopyr- oxenite (OPH-cpx3); however, its Rb concentration is low (0.29 ppm) and knowing that clinopyroxene is usually a Ca-rich phase (by inference also with an elevated Sr content) it is suggested that the initial Sr isotope composition is close to the measured value of 0.7107. Knowing that the Rb-Sr system is susceptible to isotopic disturbances induced by meta- morphic and hydrothermal processes one should treat initial values, whether calculated for an emplacement age or a mineralization age, with caution. This uncertainty is further accentuated by the question mark regarding the emplacement ages of some rocks (see discussion) and also by the calculated initial value of ca. 0.7025 for the analyzed carbonate rock of the ~ 789 Ma Tachdamt-Bleida group which is well below that of contemporaneous seawater (0.7068, Asmerom et al., 1991). Probably, this reactive type of sample has also suffered some kind of disturbance, or carries minute inclusions of potassium-rich clay minerals, which is supported by its unusually high 87Rb/86Sr ratio of 0.656.

4.3 Nd isotopes:

The analyses of five ore samples (two carbonates, two skutterudites and one erythrite) yielded highly variable results (Table IV. 6). The spiking procedure turned out to be a major problem and the reason is probably the presence of variable amounts of REE-rich inclusions, such as bran- nerite, in the analyzed minerals which led to both over- and underspiked sample mixtures. Therefore, ore mineral results must be treated with caution and the calculated span of ƐNd (ore, 350 Ma) values between -6.5 and 11 is highly uncertain. The analyses of rocks involved eleven samples and obtained Nd isotope compositions and calculated parameter values are shown in Table IV. 6 and displayed on Fig. IV. 7. ƐNd values were calculated both for an inferred emplacement age (using ages in Table IV. 1) and an ore event at 350 Ma. ƐNd (658 Ma) values for rocks of the ophiolite suite, except for the serpentinite (B1 serp) yielding a negative value, have values between 3.06 and 5.05 that are similar, or slightly lower, than published data of similar rocks (D'Lemos et al., 2006). Also, an andesitic tuff (Age-1), and a quartz-diorite (Qz-Di6) have similar values, whereas data for other rocks (pegmatite, volcanic sedi- ment, rhyolite, orthogneiss and carbonate) have more variable and negative values. At the time of the inferred 350 Ma ore-forming event, negative ƐNd values characterize most rocks except for the quartz- diorite, the andesitic tuff (Age-1) and the ophiolitic rock types (except B1 serp.).

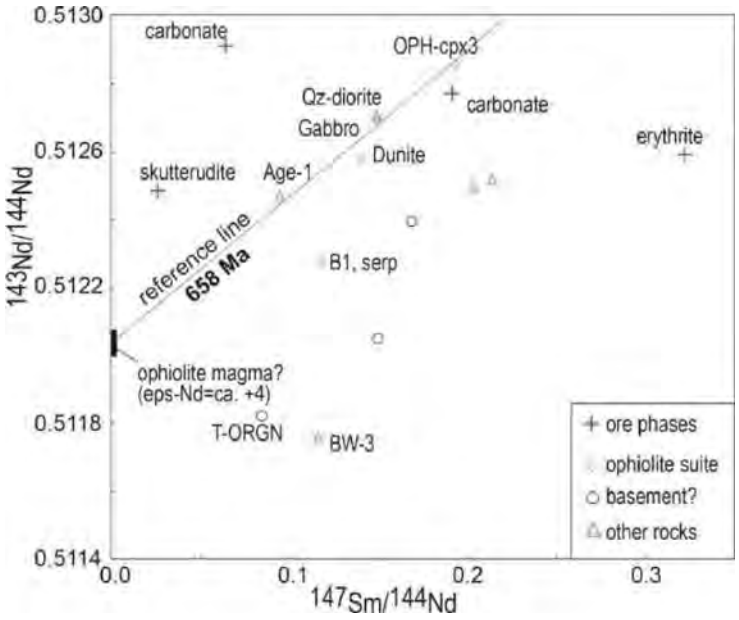

Fig. IV. 7. A Sm-Nd isotope plot of selected whole rocks and ore minerals from the Bou Azzer area. Rocks of the ophiolite suite have a common age of ca. 658 Ma, and this age is also indicated by the slope of an added reference line that crudely connects some rocks of this suite.

Table IV. 3. Pb isotope compositions of ore minerals from selected Co-Ni arsenide ores in the Bou Azzer area

Sample	Mineral	Deposit	$^{206}Pb/^{204}Pb$	2σ	$^{207}Pb/^{204}Pb$	2σ	$^{208}Pb/^{204}Pb$	2σ
1026	skutterudite	Aghbar	17.978	0.011	15.371	0.011	36.177	0.035
726	arsenopyrite	Aghbar	32.989	0.011	16.396	0.011	38.599	0.035
819	arsenopyrite	Aghbar	16,706	0.011	15,481	0.011	36,399	0.035
805a3	rammelsbergite	Aghbar	53.511	0.025	17.477	0.006	37.694	0.018
724	löllingite	Aghbar	19.792	0.011	15.477	0.011	35.974	0.035
543	löllingite	Aghbar	19.354	0.011	15.609	0.011	38.376	0.035
722	skutterudite	Aghbar	18.588	0.020	15.583	0.015	37.903	0.046
728	skutterudite	Aghbar	19.485	0.016	15.630	0.011	37.920	0.035
843	skutterudite	Aghbar	18.061	0.019	15.544	0.015	37.855	0.048
670a	rammelsbergite	Aghbar	23.664	0.011	15.857	0.011	38.589	0.035
670a	nickel ore	Aghbar	22,664	0,037	15,829	0,015	38,664	0.035
728	rammelsbergite	Aghbar	18,916	0,027	15,616	0,011	37,406	0.035
819	löllingite	Aghbar	16.706	0.011	15,496	0.011	36,392	0.035
1643/34	skutterudite	Tamdrost	17.606	0.011	15.288	0.011	35.431	0.035
1643/24	skutterudite	Tamdrost	48.074	0.005	17.096	0.006	38.186	0.018
2101	skutterudite	Tamdrost	35.090	0.011	16.485	0.011	37.463	0.035
1643/10	löllingite	Tamdrost	15,789	0,011	15,132	0.011	34,855	0.035
1643/24b	skutterudite	Tamdrost	56.925	0.011	17.706	0.011	38.231	0.035
1643-3	skutterudite	Tamdrost	31.380	0.046	16.246	0.013	37.537	0.038
1551	löllingite	Tamdrost	17.924	0.011	15.524	0.011	37.703	0.035
1643-4	rammelsbergite	Tamdrost	18.729	0.011	15.580	0.011	37.789	0.035
999a	löllingite	Ait-Ahmane	18.045	0.011	15.636	0.011	37.996	0.035
999b	löllingite	Ait-Ahmane	18.078	0.016	15.558	0.011	38.003	0.035
2415	löllingite	Ait-Ahmane	18.039	0.011	15.533	0.011	37.964	0.035

Table IV. 4. Pb isotope compositions of selected country rocks from the Bou Azzer area.

Rock Sample	Rock	System	$^{206}Pb/^{204}Pb$		$^{207}Pb/^{204}Pb$		$^{208}Pb/^{204}Pb$		Init-206/204	Init-207/204	Init-206/204	Init-207/204
				2σ		2σ		2σ	t=350 Ma	t=350 Ma	t=658 Ma	t=658 Ma
AgE-1	Andesitic tuff	Ediacaran	29,341	0,013	16,149	0,011	43,91	0,035	22,393	15,778	15,959	15,326
Tiddiline	Sandstone	Ediacaran	18,548	0,011	15,999	0,011	38,264	0,035	18,124	15,536	17,73	15,509
WBW2	granodiorite	Ediacaran	25,276	0,005	15,999	0,011	41,159	0,035	21,392	15,791	17,795	15,539
Q Diorite	Qz-diorite	Upper Cryogenian	18,679	0,017	15,572	0,011	38,042	0,026	18,398	15,557	15,859	15,326
Q Di-6	Qz-diorite	Upper Cryogenian	18,629	0,011	15,59	0,011	38,326	0,035	18,347	15,557	18,086	15,557
Rodingite	Rodingite	Upper Cryogenian	18,423	0,011	15,57	0,011	38,304	0,035	18,188	15,558	18,416	15,57
B1, serp.	Serpentinite	Upper Cryogenian	17,866	0,011	15,523	0,011	37,666	0,035	17,862	15,522	17,86	15,522
cpx, cumulates	Clynopiroxenite	Upper Cryogenian	19,161	0,058	15,652	0,006	37,885	0,026	18,946	15,641	18,747	15,627
OPH-cpx3	Clinopyroxenite	Upper Cryogenian	20,636	0,018	15,731	0,011	40,868	0,035	20,425	15,719	20,229	15,705
OPH-DUN 4	Dunite	Upper Cryogenian	18,186	0,011	15,586	0,011	37,87	0,035	17,654	15,558	17,162	15,523
OPH-CR1	Chromitite	Upper Cryogenian	18,278	0,011	15,588	0,011	37,881	0,035	18,268	15,587	18,258	15,587
OPH-Ga2	Gabbro	Upper Cryogenian	18,395	0,011	15,569	0,011	38,23	0,035	18,093	15,552	17,813	15,533
T Pegm	Pegmatite	Lower Cryogenian	15,488	0,005	15,233	0,007	34,987	0,018	15,44	15,231	15,396	115,227
T ORGN	Orthogneiss	Lower Cryogenian	27,61	0,011	16,545	0,011	46,499	0,051	24,948	16,384	21,813	16,189
TAK-2a	Rhyolite	Lower Cryogenian	19,036	0,011	15,582	0,011	37,956	0,035	18,326	15,544	17,669	15,497
Trh 40	Rhyolite	Lower Cryogenian	25,849	0,011	16,02	0,011	46,002	0,051	21,611	15,794	17,686	15,518
BW-3	Vol, Sediments	Lower Cryogenian	18,958	0,005	15,693	0,006	38,886	0,018	18,44	15,665	17,959	15,632
FW-3	Vol, Sediments	Lower Cryogenian	19,06	0,013	15,639	0,011	38,969	0,035	18,54	15,611	18,058	15,577
DOL WB	Dolomite	Lower Cryogenian	37,251	0,011	17,597	0,006	39,211	0,018	35,662	17,512	34,19	17,409

Table IV. 5. Rb-Sr isotope data of selected rocks and ore specimens from the Bou Azzer area

	Lithology	Rb	Sr	$^{87}Sr/^{86}$ Sr, mean	2 sigma	$^{67}Rb/^{86}Sr$	Rock age	$^{87}Sr/^{86}Sr$, i(rock)	$^{87}Sr/^{86}Sr$, i(ore)
Whole rock									
AgE-1	Andesitic tuff	114,70	19,58	0,793744	8	17,087	567	0,665561	0,70861
Q Di-6	Qz-diorite	8,52	235,10	0,704365	8	0,105	650	0,70339	0,70384
B1, serp.	Serpentinite	4,02	4,47	0,726406	14	2,607	658	0,70194	0,71342
OPH-cpx3	Clinopyroxenite	0,29	No data	0,710715	27	0,008	658	0,71062	0,7107
OPH-DUN 4	dunite	2,03	14,81	0,709713	7	0,397	658	0,70599	0,70774
OPH-Ga2	gabbro	20,26	510,60	0,704392	6	0,115	697	0,70325	0,70382
T Pegm	pegmatite	201,40	217,70	0,781318	8	2,696	2.0Ga ?	0,70366	0,76789
T Pegm	pegmatite	201,40	217,70	0,781318	8	2,696	700	0,75439	0,76789
T ORGN	orthogneiss	266,80	46,80	1,029491	5	17,013	2.0Ga ?	0,53939	0,94472
T ORGN	orthogneiss	266,80	46,80	1,029491	5	17,013	754	0,84635	
TAK-2a	Rhyolite	41,90	208,16	0,708510	6	0,582	2.0Ga ?	0,69173	0,70561
TAK-2a	Rhyolite	41,90	209,16	0,708510	6	0,582	767	0,70211	0,70561
BW-3	Vol, Sediments	99,82	40,29	0,790322	9	7,226	2.0Ga ?	0,58216	0,75432
BW-3	Vol, Sediments	99,82	40,29	0,790322	9	7,226	767	0,71115	0,75432
DOL WB	Dolomite	8,24	36,36	0,709938	10	0,656	789	0,70255	0,70667
Mineral									
M1 Erytrite		0,10	5,48	0,710198	<0.001				0,7102
M2 skutterudite		1,90	53,00	0,709459	0,102				0,70895
M3 Carbonate		0,14	161,00	0,709192	0,003				0,70918
M3 skutterudite		0,05	36,00	0,710203	0,004				0,71018

Table IV. 6. Sm-Nd data for selected rocks and ore specimens from the Bou Azzer area.

	Lithology	Sm	Nd	$^{143}Nd/^{144}Nd$	2 sigma	$^{147}Sm/^{144}Nd$	T-DM (91)	Rock age	eNd (cryst)	eNd (ore)
Whole rock										
AgE-1	Andesitic tuff	2,85	18,19	0,512472	6	0,0947	0,79	567	4,2	1,3
Q Di-6	Qz-diorite	4,04	16,41	0,512707	5	0,1489	0,91	650	5,3	3,5
B1. serp.	Serpentinite	0,16	0,83	0,512281	10	0,1179	1,30	658	-0,4	-3,5
OPH-cpx3	Clinopyroxenite	2,81	8,76	0,512861	6	0,1941	1,92	658	4,6	4,5
OPH-DUN 4	dunite	0,03	0,13	0,512578	8	0,1401	1,07	658	3,6	1,4
OPH-Ga2	gabbro	2,61	10,54	0,512694	5	0,1497	0,95	658	5,1	3,2
T Pegm	pegmatite	1,24	5,03	0,512050	6	0,1495	2,52	2.0Ga ?	0,6	-9,4
T Pegm	pegmatite	1,24	5,03	0,512050	d:0	0,1495	2,52	700	-7,3	-9,4
T ORGN	orthogneiss	5,61	39,72	0,511824	7	0,0854	1,52	2.0Ga ?	12,0	10,9
T ORGN	orthogneiss	5,61	39,72	0,511824	d:0	0,0854	1,52	754	-5,3	
TAK-2a	Rhyolite	0,44	1,58	0,512395	7	0,1690	2,45	2.0Ga ?	2,4	-3,5
TAK-2a	Rhyolite	0,44	1,58	0,512395	d:0	0,1690	2,45	767	-2,0	-3,5
TAK-2a (Dupl.)	Rhyolite	0,44	1,65	0,512359	6	0,1603	2,14	767	-1,9	-3,8
BW-3	Vol, Sediments	6,27	32,48	0,511760	7	0,1166	2,11	2.0Ga ?	3,4	-13,6
BW-3	Vol, Sediments	6,27	32,48	0,511760	d:0	0,1166	2,11	767	-9,3	-13,6
DOL WB	Dolomite	0,83	2,35	0,512518	7	0,2139	n.d	789	-4,1	-3,1
DOL WB (Dupl.)	Dolomite	0,72	2,15	0,512496	4	0,203	n.d	789	-3,4	-3,8
Mineral										
M1 Erytrite		3,27	6,14	0,512591	6	0,3224	n.d			-6,5
M2 skutterudite		0,14	3,24	0,512485	12	0,0258	0,49			4,7
M2 Carbonate		16,27	51,58	0,512773	3	0,1908	2,26			2,9
M3 Carbonate		5,07	47,94	0,512912	6	0,0640	0,17			11,3
M3 skutterudite		4,46	3,00	0,512887	11	0,8986	n.d			-26,6

4.4 S isotopes:

The S isotope study includes in-situ analyses of ore stage samples from Filon 7/5 and Ightem in addition to samples from those three de- posits (Aghbar, Tamdrost and Aït-Ahmane) for which Pb isotope data exist (Table IV. 7). The results are the first-ever S isotope analysis obtained from minor amounts of sulfur contained in arsenides and sulfarsenides. The set of analyzed samples covers the three sub-stages in which the main Co–, Ni-, Fe-rich arsenide and sulfarsenide stage (stage II; Bouab- dellah et al., 2016) can be subdivided: Ni-Co dominant (IIa), Co-Fe dominant (IIb) and Fe-Co dominant (IIc). The heterogeneous impres- sion yielded by the relatively few published S isotope data obtained from the post-ore, epithermal stage (a $\delta^{34}S$ range from + 10 to –32 ‰; Maacha et al., 2015, Dolansky, 2007) is reinforced by the new data from the main ore-forming stage. The entire $\delta^{34}S$ data range defined by thirty-six stage II specimens is from + 11.2 to –22.5 ‰, with no easily discernible distinction between data representing different ores and different sub-stages (Fig. IV. 8). For instance, there is a large data spread characterizing both Filon 7/5 and Aghbar (the range in both cases is more than 22 ‰, involving both negative and positive values), with a mode fairly close to zero per mille. Aït-Ahmane samples also display a large spread in data, but all numbers are negative, whereas Tamdrost and Ightem (few data) have values clustering around zero. Whenever related data exist from two nearby spots hitting the same mineral (e.g. 759a and 759b gers- dorffite in Table IV. 7), a relatively minor isotopic difference is noted although it often exceeds the analytical precision.

Five analyses correspond to whole rocks representing the ophiolite suite. Apart from one negative value (-2.2‰ for a gabbro), the remaining values are clearly positive defining a range between 6.2 and 9.0 ‰.

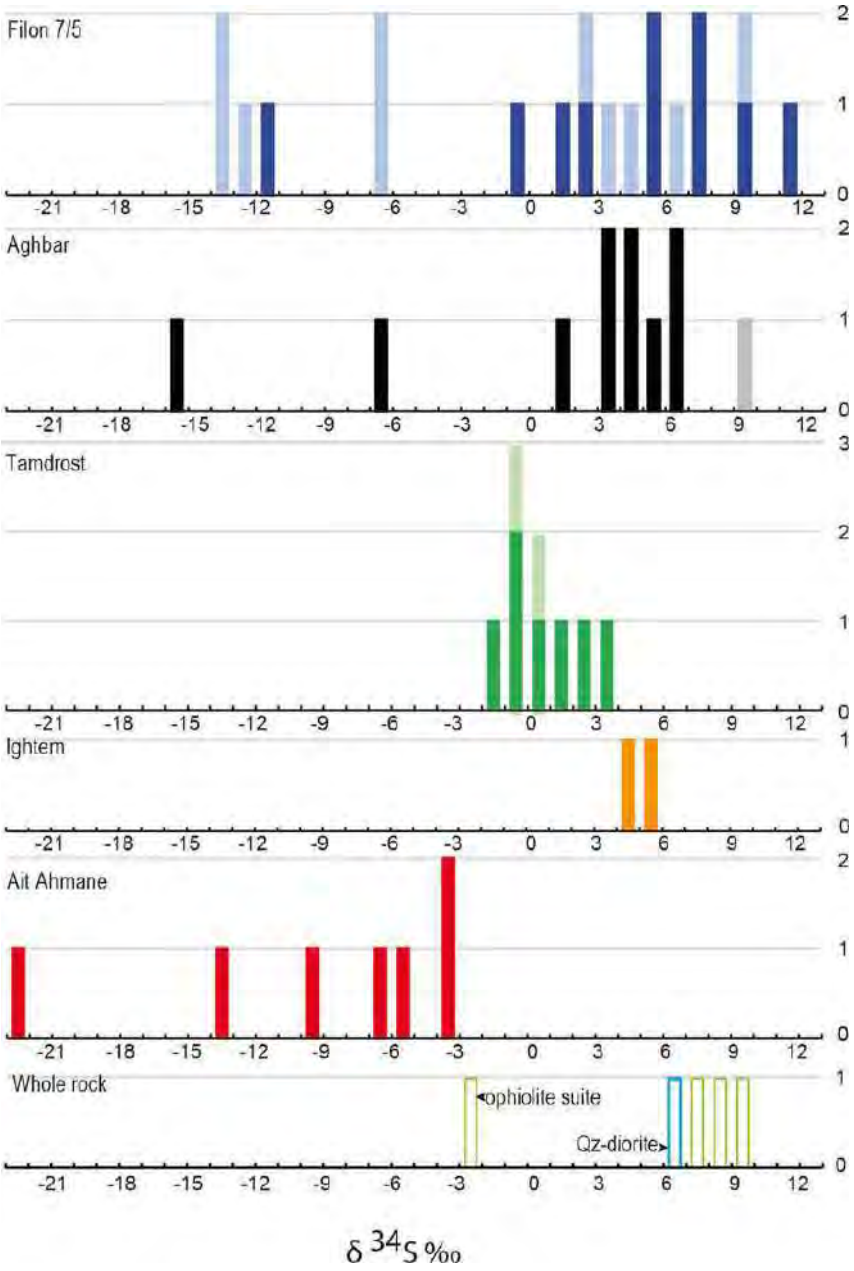

Fig. IV. 8. Frecuency histogram showing S isotope compositions of ore phases and associated whole rocks. Arsenide data (this study) are shown in dark blue, black, green, orange and red colors, and epithermal sulphides (Levresse, 2001; Dolansky, 2007, Maacha et al., 2015) in light blue, gray and green colors.

Table IV. 7: Sulfur isotope composition of ore minerals and country rocks

Deposit	Sample	Stage	Mineral	$\delta\ ^{34}S$
F7/5	759a	St II a	Gersdorffite	9.6
	759b	St II a	Gersdorffite	11.2
	972a	St II a	Rammelsbergite-Löllingite	-11.1
	972b	St II a	Skutterudite	-0.1
	972b	St II a	Gersdorffite	7.5
	972c	St II a	Gersdorffite	1.4
	1281a	St II a	Skutterudite	5.4
	1281b	St II a	Skutterudite	5.3
	2456	St II a	Skutterudite-Rammelsbergite	2.2
	2457	St II a	Nickeline	7.7
Aghbar	728	St II a	Skutterudite I	-6.5
	727	St II a	Skutterudite I	4.9
	726	St II b	Skutterudite II	4.3
	819	St II b	Skutterudite II	6
	1026	St II b	Skutterudite II	3.8
	722	St II c	Arsenopyrite	6.3
	819	St II c	Löllingite	-16
	722	St II c	Arsenopyrite	1.3
	543	St II c	Löllingite	3
	724	St II c	Löllingite	5.6
Tamdrost	2101	St II a	Skutterudite I	1.7
	1551	St II a	Skutterudite I	3.6
	1643/3	St II b	Skutterudite I	2.3
	1643/3	St II b	Skutterudite II	-0.5
	1643/34	St II b	Skutterudite II	-0.1
	1643/24b	St II b	Rammelsbergite-pararammelsbergite	0.7
	1643/4	St II a	Löllingite	-1.8
Ait Ahmane	2418	St II a	Skutterudite I	-3.3
	2445	St II b	Skutterudite II	-22.5
	999a	St II c	Löllingite	-5.1
	999b	St II c	Löllingite	-3.7
	2415	St II c	Löllingite	-6.5
	999a	St II c	Arsenopyrite	-9.9
	2449	St II c	Alloclasite	-13.1
Ightem	79		Skutterudite	5.4
	79b		Skutterudite	4.7
Regional	Qdi-6		diorite	6.2
Rock	OPH-Dun4		ophiolite	7.5
	OPH-Ser		ophiolite	9
	OPH-Ga2		ophiolite	-2.2
	Rodingite		ophiolite	8.7

St II a Ni-Co rich ores

St II b Co-Fe rich ores

St II c Fe-Co rich ores

Stage assignment from Gervilla et al. (2012; Aghbar), Lázaro, (2012; Tamdrost) and Lasobras, (2012; Aït Ahmane).

Table IV. 8. Major element contents (wt.%) in the selected country rocks from the Bou Azzer area.

	Al2O3	CaO	FeO	K2O	MgO	MnO	Na2O	TiO2
AgE-1	13,61	0,15	2,30	9,37	0,95	0,01	0,10	0,31
Tiddiline	12,24	1,28	5,21	0,69	0,67	0,06	5,78	0,88
WBW-2	15,00	2,84	3,36	2,36	1,66	0,07	3,50	0,42
Q-diorite	16,51	3,44	4,26	1,47	2,64	0,08	4,37	0,49
Qdi-6	18,48	3,29	5,13	0,44	3,88	0,12	7,06	0,60
Rodingite	15,54	6,02	5,25	1,49	3,13	0,61	4,29	0,48
B1, srp	0,92	0,08	6,02	0,09	34,01	0,09	0,02	0,01
OPH-DUN4	0,80	0,24	6,93	0,14	35,34	0,10	0,04	0,02
CPx-cumulate	10,10	8,60	9,83	0,23	15,46	0,21	0,85	0,27
OPH-CPx3	15,33	22,02	5,81	0,01	10,53	0,19	0,04	0,87
OPH-Ga2	18,25	8,54	8,84	0,90	4,97	0,18	2,83	0,73
OPH-CR1	7,06	0,05	7,46	0,02	9,89	0,31	0,02	0,04
	0,00	0,00	0,00	0,00	0,00	0,00	0,00	0,00
Tpegm	15,77	0,22	0,67	8,74	0,20	0,01	2,40	0,05
TAK-2a	14,87	0,62	1,74	2,31	3,55	0,02	4,57	0,14
BW-3	13,46	0,35	5,04	3,15	1,91	0,06	1,39	0,58
FW-3	14,39	1,67	5,88	1,82	4,08	0,16	2,55	0,78
Trh40	13,41	0,22	3,02	7,38	0,43	0,03	0,12	0,29
T ORGN	18,25	0,28	5,26	6,00	0,88	0,01	0,12	0,64
DoIWB	1,20	22,67	0,86	0,31	15,43	0,18	0,17	0,05

X: Under detection limit

Table IV. 9B. Trace elements contents (ppm) in the selected country rocks from the Bou Azzer area.

	As	S	Co	Cr	Cu	Ni	Pb	Zn	Ag	Hf	Mo	Nb	Rb	Sr	Tl	U	Zr
AgE-1	28,3	X	4,2	172	2,4	13,7	1,7	6	X	2,99	1,8	7,5	114,67	19,58	0,53	2,71	104,3
Tiddiline	10,9	X	5,4	399	3,2	10,3	4	21	X	2,75	0,8	3,47	19,11	116,04	0,09	0,48	97,3
WBW-2	4,5	X	9,6	174	120,6	16,3	2,6	41	0,15	1,38	0,9	6,73	58,08	468,05	0,29	2,51	40,4
Q-diorite	11	X	13,3	135	535,7	13,3	3,9	75	1,23	0,37	0,8	4,48	30,84	472,46	0,12	0,62	4,3
Qdi-6	26,5	X	12,9	237	136	21,8	7,8	142	0,23	0,53	0,4	3,8	8,52	235,05	0,03	0,62	8,8
Rodingite	571,9	X	13	166	24,9	17,7	8,6	277	6,37	0,42	0,5	4,88	30,93	381,95	0,15	0,57	5,3
B1, srp	0,9	X	196,7	5638	19,4	2008,7	43,7	54	0,06	X	0,4	0,3	4,02	4,47	0,08	0,04	1,2
OPH-DUN4	5,6	0,05	129,8	3731	12,1	1932,6	2,9	44	0,51	0,07	0,7	0,17	2,03	14,81	0,09	0,44	2
CPx-cumulate	3	X	74	1680	3,5	152,9	3,3	100	X	0,61	0,3	0,89	3,3	203,85	0,03	0,2	21,8
OPH-CPx3	4	X	39,1	362	42,9	169,1	X	31	0,05	2,35	0,5	1,5	0,29	X	X	0,14	69,1
OPH-Ga2	2,6	X	32,3	1592	67,2	32,2	2,1	83	0,12	0,81	0,5	1,79	20,26	510,63	0,05	0,18	25,5
OPH-CR1	X	X	114,2	>20000	3,1	743,8	3,4	644	X	X	0,2	X	0,36	3,74	X	0,01	1
Tpegm	5,8	X	3	206	2,5	6,9	25,8	6	X	1,13	1,1	1,31	201,42	217,68	0,98	0,38	37,5
TAK-2a	34,7	X	13,5	437	4,9	172,3	1,5	18	0,06	0,3	1	0,6	41,9	208,16	0,13	0,3	8,1
BW-3	3	X	15,8	151	3,5	34,4	9,5	32	X	2,08	0,6	14,29	99,82	40,29	0,33	1,37	94,9
FW-3	5,1	X	31	224	8,1	106	4,5	96	0,29	2,67	0,6	7,55	39,5	125,19	0,18	0,65	104,3
Trh40	4	X	3,2	162	10	5,5	2,7	17	X	4,92	2	14,36	117,92	15,51	0,56	2,67	155,8
T ORGN	6,7	X	2,9	236	10,7	10,2	4	19	X	0,99	1,4	18,17	266,76	46,83	1,38	2,72	33,7
DoIWB	3,9	X	7,7	78	24,8	9,9	1,7	9	X	0,23	0,5	0,87	8,24	36,36	0,07	0,59	8

X: below detection limit.

Table IV. 10*C. Rare Earth Element contents (ppm) in the selected country rocks from the Bou Azzer area.*

	La	Ce	Pr	Nd	Sm	Eu	Gd	Tb	Dy	Ho	Er	Tm	Yb	Y
AgE-1	37,13	46,71	5,82	19,56	3,01	0,5	2,51	0,4	2,54	0,49	1,52	0,24	1,6	13,07
Tiddiline	10,29	23,06	3,51	16,11	3,96	0,98	4,1	0,59	4	0,78	2,49	0,36	2,95	19,65
WBW-2	22,48	41,88	4,76	16,92	2,97	0,82	2,38	0,31	1,75	0,31	0,87	0,12	0,87	8,44
Q-diorite	9,04	19,51	2,7	11,98	2,62	0,87	2,33	0,33	1,74	0,32	0,85	0,12	0,69	8,11
Qdi-6	10,94	25,42	3,55	15,93	4,06	1,19	4,06	0,63	4,01	0,77	2,23	0,29	1,96	19,73
Rodingite	21,43	42,89	5,14	18,87	3,08	0,91	2,47	0,33	1,72	0,3	0,83	0,1	0,73	7,85
B1, srp	0,72	1,55	0,16	0,48	0,11	0,02	0,1	X	0,04	0,01	0,01	X	0,02	0,15
OPH-DUN4	0,85	1,11	0,13	0,47	0,1	0,03	0,12	0,02	0,12	0,03	0,08	0,02	0,07	0,65
CPx-cumulate	3,33	6,94	0,94	4,3	1,19	0,41	1,36	0,23	1,51	0,29	0,9	0,13	0,79	7,36
OPH-CPx3	4,97	12,32	1,87	9,54	3,19	0,64	4,36	0,77	5,53	1,18	3,76	0,55	3,92	32,53
OPH-Ga2	7,56	16,8	2,36	10,74	2,79	0,99	3,02	0,43	2,82	0,53	1,58	0,23	1,59	14,51
OPH-CR1	0,1	0,19	0,03	0,09	0,02	X	0,03	X	0,04	0,01	0,02	X	0,07	0,17
Tpegm	6,63	12,79	1,6	6,14	1,44	1,1	1,13	0,11	0,37	0,06	0,12	0,02	0,1	1,2
TAK-2a	0,99	1,62	0,23	1,05	0,28	0,13	0,43	0,06	0,38	0,07	0,19	0,03	0,17	2,13
BW-3	32,76	63,7	7,83	29,5	5,56	1	4,54	0,62	3,46	0,6	2,27	0,26	1,73	14,96
FW-3	8,93	25,05	2,93	12,47	3,21	0,92	3,33	0,6	4,16	0,82	2,37	0,35	2,44	19,51
Trh40	79,85	172,97	22,39	86,11	16,89	1,69	10,47	1,11	5,97	1,06	4,13	0,54	3,86	28,36
T ORGN	75,73	156,5	15,95	50,77	9,65	1,67	7,8	0,86	2,81	0,28	0,5	0,07	0,36	5,22
DoIWB	2,82	5,79	0,69	2,86	0,94	0,24	0,96	0,13	0,72	0,14	0,35	0,05	0,27	3,64

X: Under detection limit

4.5 Geochemistry of rocks

Nineteen rocks were analyzed for major and trace elements. The purpose of this work that involves fifthteen rock types taken from out- crops in the vicinity of ore deposits (see Tables 8(A-C); Fig. IV. 1) was basically to provide basic information about samples also used for isotope analyses. In the current context, it is crucial that selected sam- ples were not affected by post-emplacement ore-bearing fluids in order to enable a meaningful interpretation of isotope data of rocks and their possible role as sources of ore elements. For instance, although the Co contents in two samples also used for isotope work (B1, serpentinite; 197 ppm and OPH-Dun4 dunite; 130 ppm) are much higher than in remaining samples (*Table IV. 9*B), these numbers are not especially high in comparison with average Co concentrations in ultramafic rocks in general (110 ppm; Stueber and Goles, 1967) and with previous ophiolite data from Bou Azzer (Hajjar et al., 2021). Hence, there is little evidence to suggest that samples used for isotope work have suffered an isotopic over-printing effect in relation to the ore-forming event(s). However, it is less certain that e.g. the Rb-Sr isotope whole-rock system has stayed closed ever since the time of rock crystallization given that e.g. volcanic rocks of the ophiolite suite were affected by regional metamorphism, obduction-related metamorphism and basalt-seawater interaction (Naidoo et al., 1991). Geochemical Rb, Sr, U, Th and Pb concentrations were also used for calculating initial Sr and Pb isotope compositions both at the inferred time of rock emplacement and that of ore formation.

5 Discussion

Published field, mineralogical, petrological, fluid inclusion and iso- topic data indicate that ore depositional conditions have varied across the Bou Azzer district. Although our study is focused on only three, geographically spread out, ores (Tamdrost, Aghbar and Aït-Ahmane), these ores share features in different types of isotope (Pb, Sr and Nd) diagrams, as further discussed below. This is suggesting that elements in different deposits have a similar origin and that the conclusions drawn thus have a regional significance. The radiogenic isotope systematics are clearly complex for rocks and minerals analyzed from the sampled ores in this

study; however, it is still possible to use isotopic, mineralogical and field information to constrain the sources of ore components, and to discuss the timing and general processes leading to ore formation. Two features are of outmost importance for controlling radiogenic (Pb, Nd and Sr) isotope systematics pertinent to ore-forming conditions; assim- ilation of probably both sedimentary cover rocks and basement rocks during Neoproterozoic magma formation and the common incorpora- tion of (U- and REE-bearing) brannerite inclusions in arsenides and sulfarsenides, and related in-situ growth of radiogenic lead isotopes ever since ore mineral formation.

1.1. *Lead isotope constraints on the ore-forming conditions*

The lead isotope systematics of ore minerals and rocks show some unusual features involving e.g. highly evolved isotopic compositions and linear data trends having different slopes. These features will form the basis for discussing two main aspects; the age of the ores and the source of ore lead. It is suggested here that the variable lead isotopes of Bou Azzer minerals reflect both in-situ decay and source mixing effects and their respective influence on data becomes ambiguous. This implies that in order to assign values of e.g. the average ore lead composition, the influence of these two processes must be clarified and this is best done by examining the total data set derived from the three studied ores.

In-situ decay and the age of ores: Not much is known about the ten- dency for common Ni and Co arsenides to incorporate U and Th in their lattices, a process governing an in-situ growth of the radiogenic lead isotopes. Yet, this tendency is probably marginal given the small ionic radius of the cations in relation to the large size of uranium and thorium ions. Arsenopyrite, on the other hand, is a phase known to mimic a true common lead mineral (i.e. having very low U/Pb and Th/Pb ratios). Nonetheless, one arsenopyrite analysis (#726) yielded exceptional high $^{206}Pb/^{204}Pb$ ratios (Table IV. 3), whereas another arsenopyrite (#819) plots far away from other samples in the Pb-Pb diagrams. Arsenopyrite is a late phase of the main arsenide stage (stage II) and it is difficult to avoid the conclusion that the radiogenicity of arsenopyrite #726 is controlled by the presence of U-rich mineral inclusions. Such inclusions, dominated by brannerite (UTi_2O_6) have been recognized in e.g skutterudite from the Bou Azzer

area (Dolansky, 2007, this study). Following this, it is reasonable to suggest that also other arsenides and sulfarsenides with elevated $^{206}Pb/^{204}Pb$ observed from Tamdrost and Aghbar obtained their radiogenic signature due to the presence of such inclusions. An in- situ U-Pb decay effect active ever since ore mineral formation will pri- marily affect the $^{206}Pb/^{204}Pb$ ratio and to a much less degree the $^{207}Pb/^{204}Pb$ ratio, implying that samples with a significant content of brannerite will be displaced along a flat slope towards the radiogenic end. The slope of the straight line, connecting mineral samples from different deposits in Fig. IV. 5A, is not well constrained although an age in the 300–400 Ma time span is indicated. The age of ore formation re- mains a debated issue, and e.g. independent dating of brannerite and also molybdenite (Dolansky, 2007, Oberthür et al., 2009) have yielded ≤ 400 Ma ages which are comparable to the combined Aghbar and Tamdrost Pb-Pb age of 382 ± 56 Ma (this study). Other age estimates are close to 310 Ma (Oberthür et al., 2009). As it appears possible that mineralization ages vary across the district, we choose an intermediate value of 350 Ma for the purpose of setting an approximate age of district- scale ore formation. This model age corresponds to a slope value of 0.0542 (see the stippled lines in Fig. IV. 5A) and the least radiogenic ore samples along this slope (i.e. those which are least affected by in-situ decay effects) have $^{206}Pb/^{204}Pb$ values between 17.9 and 18.0 and are defined by a group of four samples involving Aghbar #1026 skutter- udite; Tamdrost #1551 löllingite; and Aït-Ahmane #999b and 2415 löllingite.

Mixing: The group of unradiogenic samples with comparatively constrained $^{206}Pb/^{204}Pb$ around 18 (Fig. IV. 5A), which is defined by specimens from all three studied deposits, can be assumed not have been significantly influenced by in-situ decay processes. Hence, such values should represent essentially undisturbed ore lead signatures since ore formation; yet, there is a substantial variation of about 0.4 units in $^{207}Pb/^{204}Pb$ developed for these samples. A probable explanation to deviating $^{207}Pb/^{204}Pb$ values is an incomplete mixing mechanism involving ore sources with contrasting isotopic compositions. This finds support from the steep trends noted in the thorogenic diagram (Fig. IV. 5B) for the considered group of samples. Such trends cannot result from the presence of brannerite inclusions (known to have very low Th/U values of about 0.0025 in the Bou Azzer area; Dolansky, 2007) as this would lead to markedly high $^{206}Pb/^{204}Pb$ ratios but not very elevated $^{208}Pb/^{204}Pb$ values. To sum up, the steeply aligned ^{207}Pb-^{206}Pb and

^{208}Pb-^{206}Pb isotope patterns at the low-radiogenic end of the data spectrum are probably an effect of mineralizing fluids acquiring lead from isotopically distinct sources.

Average ore lead: Given the noted ore lead isotope variability, and the existence of probable mixing effects, it is likely that no unique lead isotope signature represents the entire ore district. Rather, it is mean- ingful to try and define an average type of ore lead, and it was previously proposed that four unradiogenic samples could approximate the bulk ore lead in the district having a $^{206}Pb/^{204}Pb$ ratio of ca 17.9. The com- plementary $^{207}Pb/^{206}Pb$ and $^{208}Pb/^{206}Pb$ ratios can be derived from the relationships between the group of least radiogenic ore samples and the radiogenic samples displayed in Fig. IV. 5. Leaving out five samples with extreme compositions (Tamdrost #1643/https://doi.org/10,1643/34 and Aghbar #819, 724 and 1026), the data of which will be shown not to reflect typical arsenide and sulfarsenide ore-forming conditions, the tentative flat trends aligning a large number of samples from Tamdrost and Aghbar, are actually passing near the field of unradiogenic data with $^{206}Pb/^{204}Pb$ close to 17.9. This adds support to the idea that the bulk of ore samples crystallized with this $^{206}Pb/^{204}Pb$ value; some of them (free from U-rich inclusions) are still reflecting this signature, whereas others (carrying inclusions) evolved with time and at the present time, their values define a flat slope in Fig. IV. 5A. The intersection between the flat trend and the unradiogenic sample cluster define an average $^{207}Pb/^{204}Pb$ value of around 15.55. We are suggesting that the urano- genic 17.9/15.55 composition corresponds to a general situation where two or more end-components were thoroughly mixed prior to mineral deposition giving rise to an ore lead component typical of the Bou Azzer district (Fig. IV. 5). By analogy, the appropriate (thorogenic) $^{208}Pb/^{204}Pb$ value, set by the group of samples with matching $^{206}Pb/^{204}Pb$ and $^{207}Pb/^{204}Pb$ values close to 17.9 and 15.55, is close to 38, or slightly lower (Fig. IV. 5B). Hence, in further modelling, we will refer to an average type of ore lead with $^{206}Pb/^{204}Pb$, $^{207}Pb/^{204}Pb$ and $^{208}Pb/^{204}Pb$ at 17.9/ 15.55/37.9, respectively. By applying Stacey and Kramers (1975) two- stage model for terrestrial lead isotope evolution, this average lead composition yields a model age of about 440 Ma and a related my-value ($^{238}U/^{204}Pb$) of 9.58.

1.2. *Source(s) of lead in ore fluids*

Two samples can be distinguished as defining the previously outlined mixing array(s); Tamdrost #1643/10 (contains a marked proportion of an unradiogenic source; low in ^{207}Pb), and Aït Ahmane #999 (contains a significant amount of a more radiogenic source; high in ^{207}Pb). Tentatively, these samples reflect a binary mixing process involving two isotopically, rather well-defined end-members existing at the approximate time (350 Ma) of ore formation. Although this is probably an oversimplification, their isotopic compositions can still be used to discuss the nature of rocks that delivered the lead component to the ores. Fig. IV. 9 shows calculated lead isotope compositions of potential source rocks at 350 Ma and, with respect to a proposed mixing array, three rock types are relevant to discuss further; 1) an inferred basement, 2) ophiolites and 3) sedimentary rocks.

Basement-Pb: Two ore minerals, #819 arsenopyrite and #1643/10 löllingite, and some rocks have 206Pb/204Pb values less than 17 (Fig. IV. 5A) that are isotopically less evolved than lead typically existing during Neoproterozoic or Devonian-Carboniferous times. Although a much older formation age cannot completely be ruled out, the favored explanation is that Hercynian tectonic processes led to an incorporation of a very significant (#1643/10) to significant (#819) basement component characterized by unradiogenic lead that has resided in an environment with very low Th/Pb and U/Pb ratios. The analyzed pegmatite (T-pegm) has an extremely low $^{206}Pb/^{204}Pb$ value of about 15.5 which argues for an old emplacement age. The lead in this rock is mostly contained in K-feldspar that is a comparatively lead-rich phase and also considered to be a common Pb mineral (with a very low U/Pb concentration ratio) that keeps its primary magmatic composition intact over time. Therefore, this rock type is an obvious supplier of a distinctly unradiogenic component to an evolving ore-forming fluid, and its extremely unradiogenic composition implies that this rock must have formed in the early Proterozoic. From this it is inferred that there are old basement rocks present in the Bou Azzer-El Grâara inlier which contributed ore lead to the Ni-Co deposits. Tentatively, the analyzed orthogneiss (T-ORGN) is also early Proterozoic and may have formed from a similar magma source as the pegmatite, but its lead isotope composition changed moderately over time due to in-situ decay of uranium (and thorium) fixed in phases like biotite and amphibole. Supporting

this is the ~ 1.8 Ga reference line drawn to connect the pegmatite and orthogneiss data points in Fig. IV. 6A. Such an age is similar to detrital zircon ages obtained from sediments sampled in the same region (Bouougri et al., 2020; Lahna et al., 2020).

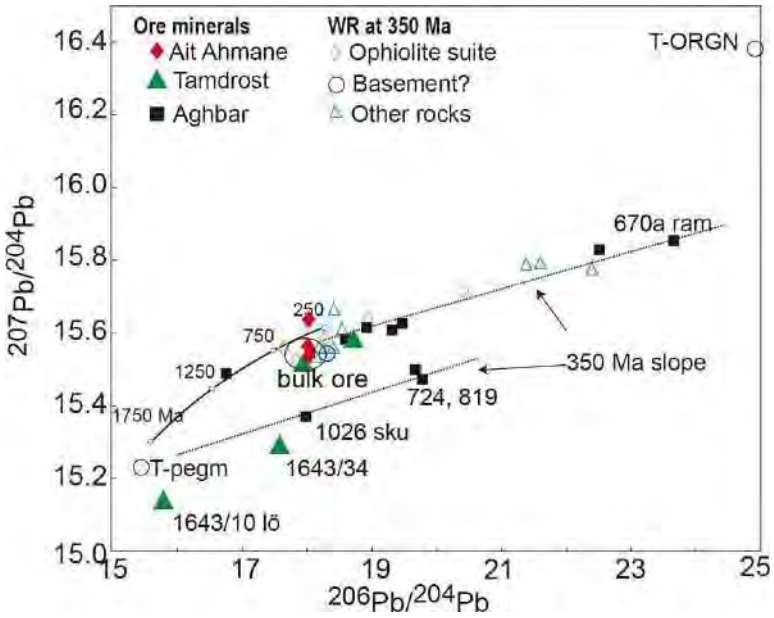

Fig. IV. 9. A $^{207}Pb/^{204}Pb$ versus $^{206}Pb/^{204}Pb$ plot showing values representing the situation at the time of the inferred ore formation at t = 350 Ma. Ore mineral data correspond to the present-day ratios (cf. Table IV. 1), whereas rock data are re- calculated to t = 350 Ma. The indicated ore signature defined by the least radiogenic ore data (encircled area) overlaps with the least radiogenic values of rocks of the ophiolite suite, and there are also other rock types sharing this isotopic signature. Part of the Stacey-Kramers (1975) two-stage curve is added as a reference.

Ophiolite-Pb: Whereas a basement component is probably not commonly available and therefore more rarely involved in ore-forming processes, the Upper Cryogenian ophiolite sequence of rocks is clearly spatially associated with Co-Ni ore deposits. Given that also a number of ophiolitic rocks have a lead isotope composition (at 350 Ma) that quite well matches the average ore lead composition (cf. Fig. IV. 9) is a strong evidence for a genetic connection as well. Ultramafic rocks (such as dunites and pyroxenites) are quite low in lead (Faure, 1986), and possibly serpentinites that often are intimately associated with ore-bearing structures have been the dominant ophiolitic rock type supplying lead, as well as Co and Ni (Hajjar et al., 2021), to the ores. Qz-diorite is another rock type with a common spatial relationship to ores. Noting that both analyzed samples of this type had an initial (350 Ma) Pb isotope composition that

plots relatively close to "average" ore lead (Fig. IV. 9), therefore this rock type may indeed have supplied part of the lead.

Sediment-Pb: As also the analyzed Tiddiline rock shows a good match with average ore lead as seen from a comparison (at t = 350 Ma) in both the ^{207}Pb-^{206}Pb (Fig. IV. 9) and ^{208}Pb-^{206}Pb diagrams, clastic rocks should also be considered as a supplier of ore lead. Carbonates are reactive and prone to interact with invading hot fluids, but the details of this suggested process are not clear and the significance of the highly radiogenic lead isotope composition of the analyzed carbonate rock (DOL-WB, Table IV. 4) remains obscure. It might also be briefly mentioned that there are some odd lead isotope compositions (with low ^{207}Pb in relation to the content of ^{206}Pb) recognized. For instance, three samples from Aghbar (# 724, 819 and 1026) may be interpreted as containing a significant old common Pb component, similar to that observed for the pegmatite (T-pegm), that controlled the composition attained during mineral deposition; in addition, these samples probably contain brannerite inclusions that over time (350 – 0 Ma interval) pushed the data points towards more radiogenic compositions (Fig. IV. 5).

In summary, it is believed that ore-forming fluids have picked up lead from a range of source rocks with serpentinites and quartz-dioritic rocks as the main suppliers. Besides, basement rocks are likely to have supplied an unradiogenic component, and possibly sediments contributed a minor, more radiogenic (high in ^{207}Pb) type of lead.

1.3. *Sources of Sr, Nd ore components*

Source(s) of strontium in ore fluids: Sr isotope data of ore specimens are relatively few, but it seems that contrary to the Pb (and Nd) isotopes, quite homogeneous $^{87}Sr/^{86}Sr$ compositions of around 0.709–0.710 (Fig. IV. 10, calculated for t_{ore} = 350 Ma) characterize the strontium con- tained in arsenides and carbonates. Contrary to the mineral phases, which have low Rb/Sr element ratios, some rocks show quite elevated Rb contents and since the Rb-Sr system is relatively susceptible to post- crystallization disturbances, back-calculated $^{87}Sr/^{86}Sr$ values, both to the time of rock crystallization and to the inferred ore formation (350 Ma), may become uncertain. This effect is normally insignificant for mafic rocks, known to generally have low Rb/Sr concentration ratios, and therefore the spread in Sr isotope compositions (350

Ma) with values as low as 0.7038 for a gabbro and an extreme value above 0.712 for the analyzed serpentinite, is not expected. The elevated value for the serpentinite, featuring an unusually high Rb/Sr ratio (Table IV. 5), may suggest interaction with crustal fluids as part of the serpentinization process close in time to the magma emplacement, but also e.g. a dunite and a clinopyroxenite have elevated ratios at t = 350 Ma.

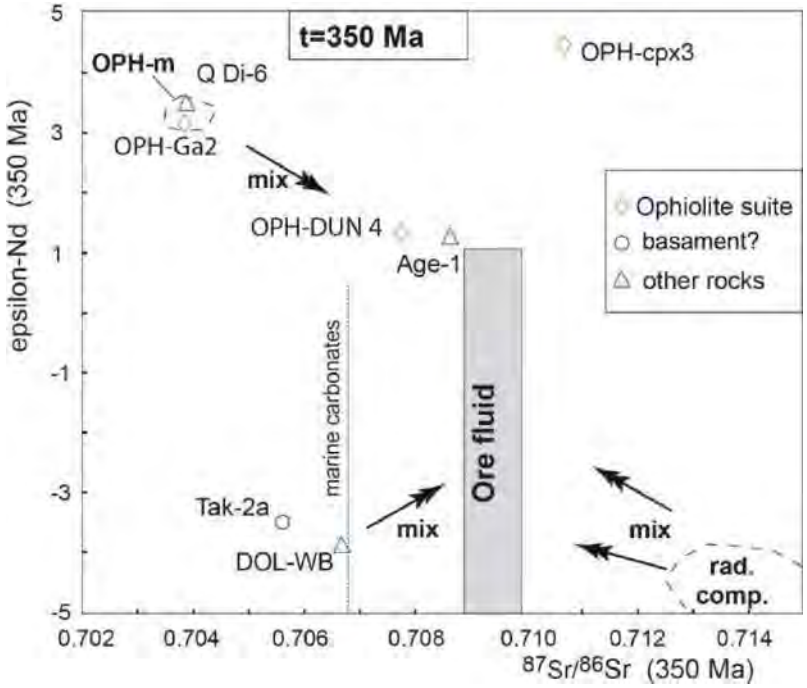

Fig. IV. 10. An epsilon-Nd versus Sr plot based on rock data calculated at the time of the inferred ore formation (350 Ma). Available mineral data do not allow the Nd isotope character of the ore-forming solutions to be constrained, however, its Sr isotopic signature is indicated (grayish field). Added is also the Sr isotope composition of Carboniferous carbonate rocks (vertical stippled line).

Given the available results, only the analyzed gabbro and the quartz- diorite, with $^{87}Sr/^{86}Sr$ values of ≤ 0.704 at t = 350 Ma, have a strontium isotope composition typical for a rock of a mantle origin. Two hypotheses may be put forward to explain the $^{87}Sr/^{86}Sr$ values (t = 350 Ma) well above 0.705 for most mafic rocks; one of them is that crustal assimilation during magma generation introduced radiogenic strontium into most magmas. Another possibility, which is in line with the near- deposit location for several of the analyzed rocks and the identified radiogenic strontium in ore-forming fluids, is that evolved mineralizing fluids have interacted with juvenile mafic rocks ($^{87}Sr/^{86}Sr$ below 0.704). Irrespective of the mechanisms

that controlled the strontium isotope signatures in rocks, the isotope range (0.709–0.710) indicated for the ultimate fluids depositing ore minerals is suggesting an isotopic ex- change between mineralizing fluids and country rocks prior to ore deposition. It is noteworthy that the homogeneous ore strontium values imply that a relatively thorough mixing preceded ore formation. How- ever, such an effect that equalizes contrasts in source end-member compositions is not indicated from lead isotope data. To overcome this apparent discrepancy, it may be that a single, relatively homogeneous source with a high concentration of strontium dominated ore-forming fluids and controlled their Sr isotopic composition.

Source(s) of neodymium in ore fluids: Due to the described problems related to analyses of ore minerals their corrected Nd isotope values, as shown in Fig. IV. 7, are uncertain. More attention can be given to Nd isotope data provided for ore carbonates sampled in three areas across the Bou Azzer district (Oberthür et al., 2009). When calculated for an approxi- mate ore formation age, these values (eps-Nd, t = 350 Ma) suggest that ore fluids carry neodymium of a highly variable composition, but dominantly with negative eps-Nd values (Fig. IV. 7). Such values are not consistent with a pure origin from a mantle-derived source which is likely to have values near + 7 to + 8.

The Nd isotope data of the analyzed rocks in this study produce a scattered impression when present-day compositions are plotted (Fig. IV. 7). Three ophiolite-type samples (dunite, OPH-cpx3 and the gab- bro), the Qz-diorite and the andesitic tuff scatter around a reference line drawn for a 658 Ma age. These data indicate that certain samples may have originated from a magma source with an approximate + 4 eps-Nd value, i.e. not as deleted as expected from a pure mantle-derived melt. A logical implication is that crustal assimilation processes may have affected the magma-generating event leading to deposition of ophiolite- type rocks. Other rock types indicate generally even less positive eps-Nd values, i.e. a formation from a quite evolved magma source. Notably, some rocks (Tak-2a, BW-3, T-ORGN and T-pegm), several of them sit- uated in the region close to the Bleida Far West occurrence (Fig. IV. 1), have more CHUR-like or even enriched ƐNd values and their model ages are much older than their emplacement ages (Table IV. 6). The high Nd model ages may be interpreted in two ways; either the rocks are Neo- proterozoic and incorporated a very significant old basement compo- nent, or they

represent truly early Proterozoic magmas. In the absence of new radiometric data, but irrespective of the preferred interpretation, the local existence of an old basement is nevertheless indicated.

Our interpretation of available data is that ophiolite-related rocks and certain crustal, felsic rocks were involved in the ore-forming pro- cesses at 350 Ma. Fig. IV. 10 is a combined Nd-Sr diagram constructed to illustrate the situation at this time using Nd data for ore carbonates (Oberthür et al., 2009) and Sr data for ore phases and rocks (this study). From the available data, the shaded box constrains possible Nd and Sr isotope values for ore fluids, and clearly the ore fluid composition is not consistent with an origin from a pure juvenile source with a depleted Sr and Nd isotope character. Thus, although ore fluids may have originated from a depleted source, equal to an ophiolite-related component (marked by ophiolite magma? in Fig. IV. 7), it appears that other, isotopi- cally contrasting and evolved sources are required to explain the range in the Sr-Nd isotopic signatures of ore fluids. The available depleted component may be reflected by the mantle-derived gabbro which will be shown to have a magmatic S isotope composition and hence may have escaped an (crustal) assimilation effect. Relatively few isotope data exist for crustal rocks and this inhibits the possibility to quantify crustal assimilation processes and to draw tentative mixing hyperbolas illus- trating the possible interaction between different sources and ore fluids. Nonetheless, arrows are to Fig. IV. 10 to simply illustrate that ore-forming fluids likely picked up Sr and Nd from both mantle-derived and crus- tal rocks in agreement with the conclusion drawn on basis of the lead isotope systematics.

1.4. *Source (s) of sulphur in ore fluids*

Like e.g. fluid inclusion and Pb isotope evidence, S isotope data of ore minerals give a complex impression (Fig. IV. 8). Available data cover a range of deposits but neither relatively few data from base metal sul- phides (Maacha et al., 2015, Dolansky, 2007) representing a late epi- thermal mineralization stage (Bouabdellah et al., 2016) nor a more exhaustive data set from the arsenide-sulfarsenide parageneses (this study) are conclusive. Basically, both data sets

involve distinctly nega- tive as well as positive values, and we are not able to see patterns relating obtained S isotope values to e.g. paragenetic stage, mineralogy or structural setting.

The S isotopic fractionation between arsenides/sulfarsenides and S species like H_2S is not easy to quantify because fractionation factors are not always known for pure phases and because metal substitution (Fe- Co-Ni) can take place (Liu et al., 2016). Generally, large isotopic dif- ferences are seen among analyzed samples, and the indicated relatively high hydrothermal temperatures (Dolansky, 2007) suggest that isotopic equilibrium is approached and that a fractionation between e.g. a sul- farsenide and H_2S will be limited and less than a few per mil. Therefore, an exact knowledge of mineral-dependent fractionation is considered less important and will not affect conclusions to be drawn.

Mineral deposition in the Bou Azzer area involved rare barite along with a massive presence of sulphides, arsenides and sulfarsenides, and this argues for a total dominance of reduced sulphur in ore-forming fluids. This in turn is suggesting that the dependence of S isotope data on changes in pH and fO_2 will not be very large. From this follows that an analyzed S isotope value for a sample will be similar to that of locally available, dissolved H_2S and also approximatively equal to the value of the total sulphur in solution (Ohmoto, 1972). In other words, the ob- tained (and variable) $\delta^{34}S$ values imply that the isotopic composition of locally available dissolved sulphur is highly heterogeneous.

The metals, in particular, Ni and Co are likely to have been derived from a magmatic source, e.g. the ophiolite suite of rocks, and magmatic sulphur has $\delta^{34}S$ values that cluster around zero per mil. Tamdrost has the simplest distribution with $\delta^{34}S$ data that cluster around zero and hence could reflect a component totally dominated by magmatic sulphur. On the other hand, magmatic sulphur alone cannot explain the isotopic patterns from other deposits in the ore district, as for instance the bulk of S isotope data from Filon 7/5 and Aghbar deposits are around + 6 ‰. Besides, the occasionally negative values found at Filon 7/5 and Aghbar, and the strongly negative values characterizing the Aït Ahmane deposit cannot be reconciled with a simple magmatic origin of sulphur. Some input of locally/regionally available sedimentary sulphur into a magmatic-type fluid carrying nickel and cobalt seems inevitable. There are no data available that help delineate if TSR (thermochemical sulphate reduction) or BSR (bacterial

sulphate reduction) processes, or a combination of both, were responsible for producing reduced sulphur of variable isotopic composition. The most negative values are probably best explained by BSR processes and there are e.g. scattered sedimentary country rocks, like pelitic schists and black shales, that are likely to contain organic material that could drive a bacterial reduction process.

Interestingly, the analyzed rocks, including four ophiolite-related rocks and one Qz-diorite, are also isotopically variable with one $\delta^{34}S$ value (-2.2 ‰) for a gabbro that could reflect an undisturbed mantle signature, whereas the remaining values are clearly positive in the range six to nine per mil. This range of data is suggesting that the S isotopic compositions of ultramafic rocks and the rodingite must have been modified during serpentinization-related, hydrothermal alteration, or that mafic magmas assimilated sedimentary material. More data are needed to further understanding of the variable ore mineral signatures, but one important contribution was probably from isotopically variable mafic to ultramafic rocks. On the other hand, at least the clearly negative ore mineral values seem to demand a direct input of locally available sedimentary sulphur to a magmatic fluid at depositional sites.

1.5. *Crustal assimilation of ophiolite-forming magmas*

The previous discussion, based on S, Sr and Nd isotope data, point out mafic ophiolite-type of rocks as the source of metals and that ore- forming fluids carry a sedimentary component. One way to bring these observations together is to argue that ore-forming fluids interacted with sedimentary units, but another option is that mafic rocks actually assimilated sedimentary material already during magma generation. A way to shed more light on this issue is to use the lead isotope data set, and Fig. IV. 11 shows initial lead isotope compositions for the individual ophiolite-related and other rock magmas, back-calculated to a common emplacement age of 658 Ma. In the frame-work of the plumbotectonics model (Zartman and Doe, 1981), such compositions are apparently slightly variable with some samples defining a data cluster between a mantle component and an upper crustal component (M and UC, respectively in Fig. IV. 11), whereas others are seemingly linearly aligned. The data cluster (OPH-m in Fig. IV. 11) is interpreted to represent an originally fairly homogeneous juvenile, mantle-derived magma

source that has assimilated variable amounts of crustal rocks. Tentatively, this data cluster represents the lead isotope compositions of all analyzed ophiolite-rocks at the time of their emplacement. Nonetheless, certain mafic samples apparently plot outside this cluster and either this discrepancy is due to post-crystallization processes whereby minor amounts of lead or uranium was added, or lost, to the rock system. Such a process would compromise the back-calculation procedure that is based on a closed-system behavior, and instead of creating a narrow data cluster in the used diagram type, certain data would fall along a 658 Ma isochron (indicated to the dotted trend line in Fig. IV. 11). Alternatively, the generalized crustal component depicted in the plumbotectonics model is not appropriate to consider. Instead, a more complex crustal assimilation affecting a mafic magma chamber, involving pre-658 Ma rocks in the area, may be a more viable process. The latter option finds some support from the overall pattern in Fig. IV. 11 where some country rocks, e. g. Trh-40 (rhyolite) and the pegmatite (T-pegm), have calculated iso- topic compositions at 658 Ma which plot at the extreme ends of the linear trend line, and thereby may comprise tentative assimilants into a magma chamber. To conclude, the inferred crustal assimilation event can explain why e.g. published Nd isotope data of ophiolites and asso- ciated rocks (Ikenne et al., 2020) are not typical for a pure, juvenile mantle component and why isotopically heavy sulphur is characterizing most ophiolites (this study).

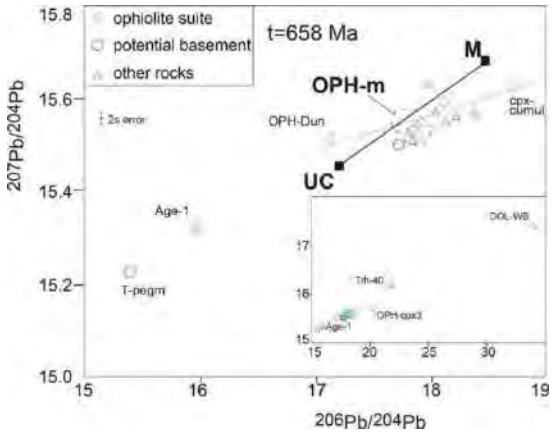

Fig. IV. 11. A $^{207}Pb/^{204}Pb$ versus $^{206}Pb/^{204}Pb$ plot representing the situation at the time of ophiolite formation (at 658 Ma), with a complementary inset covering the more extreme isotopic compositions. The range of values for rocks of the ophiolite suite may indicate a variable contamination of the ophiolite magma (cf. the dotted line). Symbols M and UC stand for the approximative Pb isotope composition at t = 658 Ma of the mantle and upper crust, respectively. To illustrate the possible role of deep-seated (basement?) and more surficial contamination (dolomite?) of the ophiolite -forming magma, calculated isotope values of other rock types (at 658 Ma) are also shown. However, the latter are uncertain given that certain rocks are believed to be younger than 658 Ma.

1.6. *Ore-forming model*

A range of investigations have been carried out on several Co-Ni ores of the Bou Azzer area. Such data together with new results from this study enable the construction of an updated model with emphasis on isotopic constraints on the timing and nature of ore-forming processes. *Timing*: Available geochronological and field data are offering various possible ages of mineralization. Generally, radiometric ages may, except for representing real ore-forming events, signify e.g. hy- drothermal alteration, late veining and isotopic resetting. Ikenne et al. (2020) did not rule out the possibility of a primary Pan-African miner- alization event followed by remobilization of metals during Hercynian events. Supporting a temporal relationship between Pan-African and mineralization events is the structural setting where the main orebodies are located along transcurrent sinistral faults belonging to the ultimate Pan-African phase, active between 615 and 580 Ma ago. However, no published radiometric dating of ore components supports a Pan-African connection, and crosscutting and offsetting relationships imply that orebodies postdate the serpentinization (Fanlo et al., 2015) and the structures of the major Pan-African tectonic phase (Leblanc and Billaud, 1982).

Basically, the geochronological evidence suggests two age modes; an older mode between ca. 380 and 355 Ma is defined by U-Pb brannerite ages at Filon 7/5 (Dolansky, 2007), which represent "chemical dates" obtained by using an electron microprobe. Similar ages, ≤400 Ma, were obtained from Pb-Pb relationships defined by ore minerals from Aghbar and Tamdrost (this study), and from Ar-Ar dating of muscovite from a barren quartz vein at Tamdrost (Levresse, 2001). Also, Re-Os molyb- denite ages from Filon 7 and Aghbar fall in the 400–350 Ma interval (Oberthür et al., 2009). However, it must be recalled that although this system usually yields robust age information the presented dates are model ages that rely on certain assumptions, and Oberthür et al. (2009) and Ikenne et al. (2020) raised doubts about their relevance. A younger age mode at ~ 310 Ma is indicated by laser ablation, ICPMS U-Pb brannerite ages of Filon 7 samples (Oberthür et al., 2009), and similar ages were obtained from ore carbonates sampled in three different areas of the district using the Sm-Nd method (Oberthür et al., 2009). However, ages significantly younger than about 300 Ma, e.g. ca. 220 Ma Ar-Ar muscovite ages at Tamdrost (Levresse, 2001), 260 Ma, or lower, U-Pb ages of altered

brannerite from Filon 7/5 (Dolansky, 2007, Oberthür et al., 2009), might reflect later over-printing events that did not involve any new addition of metals.

Apparently, brannerite is a key mineral for putting age constraints on ore formation, but its high U content makes this phase susceptible for post-crystallization lead loss as also seen in partly discordant U-Pb data defining a lower intercept age at 65 Ma (Oberthür et al., 2009). It is viable that post-crystallization processes could also explain why there is a bimodal brannerite U-Pb age distribution. One possibility is that analyzed brannerite clusters (Oberthür et al., 2009) have suffered a complete lead loss during Hercynian peak-metamorphism, and that the obtained 310 Ma date is a reset age. If so, 385–350 Ma brannerite ages (Dolansky, 2007) of unaltered brannerite inclusions in skutterudite are the best estimate of brannerite crystallization, and by inference ore formation. Also, similar ≤ 400 Ma Pb-Pb dates of arsenides (this study), essentially controlled by coeval brannerite inclusions, may be significant if arsenide grains have acted as a shield preventing the Pb-Pb system of brannerite to become disturbed by later hydrothermal-tectonic events. Altogether, radiometric evidences do not allow any tight age constraint to be set on ore formation. Probably, the 400–300 Ma period witnessed a series of tectonic and hydrothermal events, and given the variability in e.g. isotopic and fluid inclusion results it seems feasible that several episodes of ore mineral deposition occurred in this time interval.

Ore-forming scenario: Our working hypothesis is that the primary introduction of metals took place during Devonian-Carboniferous, dis- trict-scale events that reactivated old Pan-African tectonic structures as a result of N-S shortening (Gasquet et al., 2005). An episode of ore deposition may have involved repeated re-activation of old faults along with concurrent vein formation and initiation of hydrothermal fluid flow. Lead isotope data of ore minerals (this study) point out ophiolite- related rocks, e.g. serpentinites, and also quartz-diorites as major sour- ces of metals. Both rock types have a strong spatial relationship to ore bodies and show isotopic signatures at the proposed average (350 Ma) time of ore formation that match the inferred lead isotope composition of the bulk ore. Serpentinites are also often showing dissolution textures as a result of fluid interaction (Hajjar et al., 2021) which argue for a direct involvement in ore formation. Probably, competence contrasts between serpentinites and

surrounding wall rocks have governed the development of weakness zones (e.g. fault zones; Tourneur et al., 2021) that have acted as conduits for mineralizing fluids.

It is likely that tectonic activity triggered the percolation of fluids along shears and faults across a large area. Such fluids probably inter- acted with mafic magmatic rocks, thereby leaching nickel and cobalt, but substantial amounts of other elements were also picked from country rocks. Following earlier suggestions (En-Naciri, 1995, En-Naciri et al., 1997, Dolansky, 2007), ore fluids comprised reduced brines that became more oxidized at later stages. This view is basically consistent with hydrogen and oxygen isotope evidence (Dolansky, 2007, Maacha et al., 2015) which were interpreted to support the presence of hot, saline fluids of magmatic origin, and that cooler, dilute meteoric fluids sub- sequently entered mineralization sites. The complex picture arising from fluid inclusion studies is also in agreement with fluid mixing and asso- ciated changes in e.g. temperature and salinity. Fluids of meteoric origin that progressively invaded ore sites, and perhaps also triggered mineral precipitation, may have released reduced sulphur from e.g. pelitic schists that locally cap the ophiolite sequence. Carbonate rocks are reactive and locally abundant and the Sr isotope composition of an analyzed single sample appears to have been modified by percolating fluids suggesting that e.g. strontium and calcium were released from carbonates and picked up by percolating hydrothermal fluids.

Obviously, fluids that have experienced this geologic history could have passed, and interacted with, a range of rocks having different isotopic signatures before reaching a final site of ore deposition. Partly strongly negative ƐNd values of analyzed carbonates (Oberthür et al., 2009; this study), indicate a systematic variation with geographical location suggesting that at certain sites ore-forming fluids must have interacted to a significant degree with an old, enriched source, as also indicated e.g. by an early Proterozoic lead isotope signature for a löllingite (#1643/10) from Tamdrost. When summarizing field and other data, a magmatic (ophiolitic) source of e.g. sulphur, lead and strontium probably was important at all sites, but ore elements were released also from various country rocks and this created heterogeneous ore isotope characteristics. Not least the suggested assimilation/alter- ation history for the ophiolitic-type

rocks, that led to isotopic hetero- geneities, played a role in creating partly erratic analytical results.

6 Conclusions

Overall, new data from the present study, and other evidence, support Devonian-Carboniferous mineralization events operating on a large regional scale as a response to N-S shortening. Probably, the fea- tures of different deposits are the ultimate result of multi-episodic ore- forming events in connection with repeated re-activation of old faults along with concurrent vein formation and initiation of hydrothermal fluid flow.

Although derived from the mantle, the ophiolite-related rocks do not exhibit typical mantle isotopic signatures. This might be explained by assimilation processes where crustal material may have been incor- porated during crystallization of discrete magmas.

It is suggested that ophiolites of a mantle origin rocks have been the main supplier of ore elements. Yet, Pb, Sr, Nd and S isotope data generate a quite consistent picture where ore fluids have scavenged el- ements from a number of isotopically different crustal sources including both inferred basement lithologies and sedimentary rocks.

The presence of minute, coeval brannerite inclusions in arsenides and sulfarsenides excerpts a strong control on their lead and neodymium isotope behavior.

Pb isotope results suggest that certain of the studied felsic rocks represent early Proterozoic lithologies. Based on old Nd model ages, it is possible that also additional rocks may be much older than hitherto believed; an alternative interpretation is that these rocks have incor- porated significant amounts of old basement components. New radio- metric dating is required in order to shed further light on this issue.

Declaration of Competing Interest

The authors declare that they have no known competing financial interests or personal relationships that could have appeared to influence the work reported in this paper.

Acknowledgements

The authors greatly acknowledge the geological survey of CTT-Bou Azzer mine for facilitating our geological field campaigns and specially to Clemente Recio (University of Salamanca) for his invaluable help to IS during the development of the analytical procedure to mea- sure S isotope compositions from the minor amounts of S extracted from arsenides and sulfarsenides. Authors would like to acknowledge the use of Servicio General de Apoyo a la Investigación-SAI, Universidad de Zaragoza. This research was financially supported by the Spanish project RTI2018- 099157-A-I00 granted by the "Ministerio de Ciencia, Innovación y Universidades". The Swedish Research Council (infrastructure grant: Dnr. 2017-00671) is thanked for financial support to the Vegacenter national laboratory. This is Vegacenter publication number 124

References

Ahmed, A.H., Arai, S., Ikenne, M., 2009. Mineralogy and paragenesis of the Co-Ni arsenide ores of Bou Azzer, Anti-Atlas, Morocco. Econ. Geol. 104 (2), 249–266.

A´lvaro, J.J., Benziane, F., Thomas, R., Walsh, G.J., Yazidi, A., 2014. Neoproterozoic-Cambrian stratigraphic framework of the Anti-Atlas and Ouzellagh promontory (High Atlas), Morocco. J. Afr. Earth Sci. 98, 19–33.

Asmerom, Y., Jacobsen, S.B., Knoll, A.H., Butterfield, N.J., Swett, K., 1991. Strontium isotopic variations of Neoproterozoic seawater: Implications for crustal evolution. Geochim. Cosmochim. Acta 55 (10), 2883–2894.

Blein, O., Baudin, T., Ch`evremont, P., Soulaimani, A., Admou, H., Gasquet, P., Cocherie, A., Egal, E., Youbi, N., Razin, P., Bouabdelli, M., Gombert, P., 2014. Geochronological constraints on the polycyclic magmatism in the Bou Azzer-El Graara inlier (Central Anti-Atlas Morocco). J. Afr. Earth Sci. 99, 287–306.

Bouabdellah, M., Maacha, L., Levresse, G., Saddiqi, O., 2016. The Bou Azzer Co–Ni–Fe–As (±Au ± Ag) District of Central Anti-Atlas (Morocco): A Long-Lived Late Hercynian to Triassic Magmatic-Hydrothermal to Low-Sulphidation Epithermal System. In: Bouabdellah, M., Slack, F.J. (Eds.), Mineral Deposits of North Africa. Springer International Publishing, pp. 229–247.

Bouougri, E.H., Lahna, A.A., Tassinari, C.C.G., Basei, M.A.S., Youbi, N., Admou, H., Saquaque, A., Boumehdi, M.A., Maacha, L., 2020. Time constraints on early Tonian Rifting and Cryogenian Arc terrane-continent convergence along the northern margin of the West African craton: insights from SHRIMP and LA-ICP-MS zircon geochronology in the Pan-African Anti-Atlas belt (Morocco). Gondwana Res. 85, 169–188.

Canfield, D.E., Raiswell, R., Westrich, J.T., Reaves, C.M., Berner, R.A., 1986. The use of chromium reduction in the analysis of reduced inorganic sulfur in sediments and shales. Chem. Geol. 54 (1-2), 149–155.

Clauer, N., 1976. G´eochimie isotopique du strontium des milieux s´edimentaires Application `a la g´eochronologie du craton ouest africain: Th´ese Doct. Etat, Sci. G´eol. Univ. Strasbourg, 45, 256 p.

Coleman, M.L., Moore, M.P., 1978. Direct reduction of sulfates to sulfur dioxide for isotopic analysis. Anal. Chem. 50, 1594–1595.

D'Lemos, R.S., Inglis, J.D., Samson, S.D., 2006. A newly discovered orogenic event in Morocco: neoproterozoic ages for supposed Eburnean basement of the Bou Azzer inlier, Anti-Atlas Mountains. Precambr. Res. 147 (1–2), 65–78.

Dolansky, L.M., 2007. Controls on the genesis of hydrothermal cobalt mineralization: insights from the mineralogy and geochemistry of the Bou Azzer deposits, Morocco. McGill University, Montreal, Canada, p. 162. Unpublished Master Thesis.

El Ghorfi, M., 2006. Etude g´eochimique et m´etallogenique des m´etaux pr´ecieux (or, argent et platinoïdes) associes aux min´eralisations a` Co, Ni, Cr de Bou Azzer-El Graara, et dans la s´erie de Bleida Far West, Anti-Atlas, Maroc. Cadi Ayyad University, Marrakech, Morocco, p. 256 p.. PhD thesis.

El Hadi, H., Simancas, J.F., Martínez-Poyatos, D., Azor, A., Tahiri, A., Montero, P., Fanning, C.M., Bea, F., Gonza´lez-Lodeiro, F., 2010. Structural and geochronological constraints on the evolution of the Bou Azzer Neoproterozoic ophiolite (Anti-Atlas, Morocco). Precambr. Res. 182 (1-2), 1–14.

En-Naciri, A., 1995. Contribution 'a l'etude du district 'a Co., As (Ni, Au, Ag) de Bou Azzer. Anti-Atlas (Maroc) Donn´ees min´eralogiques et g´eochimiques. Universite d'Orl´eans, France, p. 245. PhD thesis.

En-Naciri, A., Barbanson, L., Touray, J.C., 1997. Brine inclusions from the Co-As (Au) Bou Azzer district, Anti-Atlas, Morocco. Econ. Geol. 92, 360–367.

Essarraj, S., Boiron, M.-C., Cathelineau, M., Banks, D.A., Benharref, M., 2005. Penetration of surface-evaporated brines into the Proterozoic basement and deposition of Co and Ag at Bou Azzer (Morocco): evidence from fluid inclusions. J. African Earth Sc. 41 (1-2), 25–39.

Fanlo, I., Gervilla, F., Colas, V., Subías, I., 2015. Zn-, Mn-, Co-enriched chromian spinels from the Bou-Azzer mining district (Morocco): constraints on their relationship with the mineralizing process. Ore Geol. Rev. 71, 82–98.

Faure, G., 1986. Principles of isotope geology, 2nd edition. John Wiley and Sons. Gasquet, D., Levresse, G., Cheilletz, A., Azizi-Samir, M.R., Mouttaqi, A., 2005. Contribution to a geodynamic reconstruction of the Anti-Atlas (Morocco) during Pan-African times with the emphasis on inversion tectonics and metallogenic activity at the Precambrian-Cambrian transition. Precambr. Res. 140 (3-4), 157–182.

Gervilla, F., Fanlo, I., Colas, V., Subias, I., 2012. Mineral compositions and phase relations of Ni–Co–Fe arsenide ores from the Aghbar mine, Bou Azzer, Morocco. Can. Mineral. 50 (2), 447–470.

Hajjar, Z., Gervilla, F., Fanlo, I., Jiménez, J.-M., Ilmen, S., 2021. Formation of serpentinite-hosted, Fe-rich arsenide ores at the latest stage of mineralization of the Bou-Azzer mining district (Morocco). Ore Geol. Rev. 128, 103926. https://doi.org/ 10.1016/j.oregeorev.2020.103926.

Hall, G.E.M., Pelchat, J.-C., Loop, J., 1988. Separation and recovery of various sulfur species in sedimentary rocks for stable sulfur isotopic determination. Chem. Geol. 67, 35–45.

Hefferan, K., Soulaimani, A., Samson, S.D., Admou, H., Inglis, J., Saquaque, A., Latifa, C., Heywood, N., 2014. A reconsideration of Pan African orogenic cycle in the Anti-Atlas Mountains, Morocco. J. Afr. Earth Sci. 98, 34–46.

Ikenne, M., Souhassou, M., Saintilan, N.J., Karfal, A., El Hassani, A., Moundi, Y., Ousbih, M., Ezzghoudi, M., Zouhir, M., Maacha, L., 2020. Cobalt-Nickel-Copper arsenide, sulpharsenide and sulphide mineralisation in the Bou Azzer window, Anti-Atlas, Morocco: One century of multi-

disciplinary and geological investigations, mineral exploration and mining. Geological Soc., London, Spec. Publ. 502. https://doi. org/ 10.1144/SP502-2019-132.
Inglis, J.D., Samson, S., D'Lemos, R.S., Admou, H., 2003. Timing of regional greenschist facies deformation in the Bou Azzer Inlier, Anti-Atlas: U–Pb constraints from syn- tectonic intrusions. First meeting of IGCP 485, El Jadida, Morocco, pp. 40–42.
Inglis, J.D., MacLean, J.S., Samson, S.D., D'Lemos, R.S., Admou, H., Hefferan, K., 2004. A precise U– Pb zircon age for the Bleida granodiorite, Anti-Atlas, Morocco: implications for the timing of deformation and terrane assembly in the eastern Anti- Atlas. J. Afr. Earth Sci. 39, 277–283.
Lahna, A.A., Youbi, N., Tassinari, C.C.G., Basei, M.A.S., Ernst, R.E., Chaib, L., Barzouk, A., Mata, J., G¨artner, A., Admou, H., Boumehdi, M.A., So¨derlund, U., Bensalah, M.K., Bodinier, J.-L., Maacha, L., Bekker, A., 2020. Revised stratigraphic framework, for the lower Anti-Atlas Supergroup based on U-Pb geochronology of magmatic and detrital zircons (Zenaga and Bou Azzer-El Graara inliers, Anti-Atlas Belt, Morocco. J. Afr. Earth Sci. 171, 103946. https://doi.org/10.1016/j. jafrearsci.2020.103946.
Lasobras, E., 2012. Composicio´n mineral y relaciones de fase de los arseniuros de Co- Fe- Ni del yacimiento de Aït-Ahmane (Bou-Azzer, Marruecos). Diferencias con otros depo´sitos. TFM. Universidad de Zaragoza, Spain, p. 53.
La´zaro, M., 2012. Mecanismos de reequilibrio mineral en arseniuros de Co-Fe-Ni en Tamdrost (Bou Azzer, Marruecos). TFM. Universidad de Zaragoza, Spain, p. 53.
Leblanc, M., 1975. Ophiolites pr´ecambriennes et gîtes ars´eni´es de Cobalt (Bou Azzer. Maroc). PhD Thesis. Univ, Paris VI, France, p. 329.
Leblanc, M., 1981. The late Proterozoic ophiolites of Bou Azzer (Morocco): evidence for Pan-African plate tectonics. In: Kro¨ner, A. (Ed.), Precambrian plate tectonics. Elsevier Amsterdam, pp. 451–455.
Leblanc, M., Billaud, P., 1982. Cobalt arsenide orebodies related to an Upper Proterozoic ophiolite: Bou Azzer (Morocco). Econ. Geol. 77 (1), 162–175.
Levresse, G., 2001. Contribution a` letablissement d'un mod`ele g´en´etique des gisements d'Imiter (Ag-Hg), Bou Madine (Pb-Zn-Cu-Ag-Au) et Bou Azzer (Co-Ni-As-Ag-Au) dans l'Anti-Atlas marocain. CRPG-CNRS, Nancy, France, p. 191. Ph.D. thesis.
Liu, S., Li, Y., Gong, H., Chen, C., Liu, J., Shi, Y., 2016. Frist-principles calculations of sulphur isotope fractionation in MX2 minerals, with M=Fe Co, Ni and X2=AsS. SbS. Chem. Geol. 441, 204–211.
Maacha, L., 2013. Etude m´etallog´eniques et g´eophysiques des min´eralisations cobaltif´eres et cuprif´eres de Bou-Azzer El Graara Anti Atlas Maroc (Tome 1). Cadi Ayyad University, Marrakech, Morocco, p. 344. PhD Thesis.
Maacha, L., El Ghorfi, M., En-Naciri, A., Sadiqqi, O., Soulaimani, A., Alansari, A., Bhilisse, M., 2015. Nouvelles donn´ees isotopiques et d'inclusions fluides des min´eralisations cobaltif´eres de Bou Azzer. Apport a` la g´eologie ´economique de la boutonni`ere. (Anti-Atlas central, Maroc). Notes et m´em. Serv. G´eol. Maroc 579, 133–139.
Mrini, Z., 1993. Chronologie (Rb–Sr, U-Pb), traçage isotopique (Sr–Nd-Pb) des sources des roches Magmatiques ´eburn´eennes, panafricaines et hercyniennes du Maroc. Cadi Ayad University, Marrakech, p. 227. PhD thesis.
Naidoo, D.D., Bloomer, S.H., Saquaque, A., Hefferan, K., 1991. Geochemistry and significance of metavolcanic rocks from the Bou-Azzer-El Graara ophiolite (Morocco). Precambr. Res. 53 (1-2), 79–97.
Oberthür, T., Melcher, F., Henjes-Kunst, F., Gerdes, A., Stein, H., Zimmerman, A., El Ghorfi, M., 2009. Hercynian age of the cobalt-nickel-arsenide-(gold) ores, Bou Azzer, Anti-Atlas, Morocco: Re-Os, Sm-Nd, and U-Pb age determinations. Econ. Geol. 104 (7), 1065–1079.

Ohmoto, H., 1972. Systematics of sulfur and carbon isotopes in hydrothermal ore deposits. Econ. Geol. 65 (5), 551–578.
Pin, C., Zalduegui, J.S., 1997. Sequential separation of light rare-earth elements, thorium and uranium by miniaturized extraction chromatography: application to isotopic analyses of silicate rocks. Anal. Chim. Acta 339 (1-2), 79–89.
Recio, C., Fallick, A.E., Ugidos, J.M., 1991. Sulfur isotope systematics of granitoids and associated rocks from the Avila-La Alberca area (western Sistema Central, Spain). Rev. Soc. Geol. Espan˜a 4, 371–381.
Saquaque, A., Benharref, M., Abia, H., Mrini, Z., Reuber, I., Karson, J.A., 1992. Evidence for a Panafrican volcanic arc and wrench fault tectonics in the Jbel Saghro, Anti- Atlas, Morocco. Geologische Rundschau 81 (1), 1–13.
Samson, S.D., Inglis, J.D., D'Lemos, R.S., Admou, H., Blichert-Toft, J., Hefferan, K., 2004. Geochronological, geochemical, and Nd-Hf isotopic constraints on the origin of Neoproterozoic plagiogranites in the Tasriwine ophiolite, Anti-Atlas orogeny, Morocco. Precambr. Res. 135, 133–147.
Stacey, J.S., Kramers, J.D., 1975. Approximation of terrestrial lead isotope evolution by a two-stage model. Earth Planet. Sci. Lett. 26 (2), 207–221.
Stueber, A.M., Goles, G.G., 1967. Abundances of Na, Mn, Cr, Sc and Co in ultramafic rocks. Geochim. Cosmochim. Acta 31, 75–93.
Soulaimani, A., Ouanaimi, H., Saddiqi, O., Baidder, L., Michard, A., 2018. The Anti-Atlas Pan-African Belt (Morocco): overview and pending questions. C. R. Geosci. 350 (6), 279–288.
Todt, W., Cliff, R.A., Hanser, A., Hofmann, A.W., 1996. Evaluation of a 202Pb-205Pb double spike for high-precision lead isotope analysis, in Earth Processes: Reading the Isotopic Code. In: Basu, A., Hart, S.R. (eds), Geophys. Monogr. Ser. AGU, Washington, D.C. 95, 429–437.
Tourneur, E., Chauvet, A.m Kouzmanov, K., Tuduri, J., Paquez, C., Sizaret, S., Darfal, A., Moundi, Y., El Hassani, A. 2021. Co-Ni-arsenide minealisation in the Bou Azzer district (Anti-Atlas, Morocco): Genetic model and tectonic implications. Ore Geol. Rev. 10.1016/j.oregeorev.2021.104128.
Triantafyllou, A., Berger, J., Baele, J.-M., Bruguier, O., Diot, H., Ennih, N., Monnier, C., Plissart, G., Vandycke, S., Watlet, A., 2018. Intra-oceanic arc growth driven by magmatic and tectonic processes recorded in the Neoproterozoic Bougmane arc complex (Anti-Atlas, Morocco). Precambr. Res. 304, 39–63.
Triantafyllou, A., Berger, J., Baele, J.-M., Mattielli, N., Ducea, M.N., Sterckx, S., Samson, S., Hodel, F., Ennih, N., 2020. Episodic magmatism during the growth of a Neoproterozoic oceanic arc (Anti-Atlas, Morocco). Precambr. Res. 339, 105610. https://doi.org/10.1016/j.precamres.2020.105610.
U.S. Geological Survey, 2013. Mineral commodity summaries 2013. U.S. Geological Survey, p. 198.
Zartman, R.E., Doe, B.R., 1981. Plumbotectonics – the Model. Techtonophysics 75 (1-2), 135–162.

Chapter V: Concluding remarks

The identification in this Ph.D. Thesis of the serpentinite-hosted ores as a new morphological type of arsenide ores complete the complex metallogenic framework of the Bou Azzer district. Unlike the more common contact-type ores occurring as flame-shaped bodies, flat lenses and pocket-like masses along the contact between ophiolite-related serpentinite and quartz-diorite, gabbro or volcano-sedimentary rocks (e.g., Leblanc, 1975; Leblanc and Billaud, 1982; En-Naciri, 1995; El Ghorfi, 2006; Maacha, 2013; Tourneur et al., 2021), the studied serpentinite-hosted ores of the Ait Ahmane area consist of flat lenses enveloped by carbonated serpentinite within barren, poorly-altered serpentinite (Hajjar et al. 2021). Additional differences between both types of ores lie in the nature of the arsenide assemblage, being the serpentinite-hosted ores basically composed of Fe diarsenides with minor amounts of Co and Ni di- and tri-arsenides in contrast to contact-type ores which show a more complex mineral assemblage made up of mono-, di- and triarsenides of Co, Ni and Fe (e.g., En-Naciri, 1995; En-Naciri et al., 1997; El Ghorfi, 2006; Ahmed et al., 2009a; Gervilla et al., 2012a; Lasobras, 2012; Maacha, 2013; Fanlo et al., 2017). These distinctive mineral assemblages arrange in different zoning patterns in both types of ores. Contact-type ores consist of massive and banded Co-Ni arsenides at the nearest zone of the contact between serpentinite and quartz diorite, gabbro or volcano-sedimentary rocks, evolving towards the serpentinite body, initially as massive Co-Fe

arsenide ores and later, as disseminated and veinlet-filling Fe-Co ores (Gervilla et al., 2012; Hajjar et al., 2022). The zoning pattern of serpentinite-hosted ores, exemplified by the F55 deposit from Aït Ahmane is simpler, consisting of massive ores enveloped by disseminated ores both composed of löllingite arranged in aggregates of zoned spindle-like crystals or rosettes. Host-rock predominant alteration also varies from silicification in contact-type ores to carbonation in serpentinite-hosted ores.

Most authors agree on the multiphase nature of the mineralizing process at Bou Azzer (e.g., Leblanc, 1975; En-Naciri, 1995; El Ghorfi, 2006; Maacha, 2013; Bouabdellah et al., 2016) connected with the reactivation of ancient, Pan-African faults during the Hercynian Orogeny, which acted as pathways for hydrothermal fluids (e.g., Dolansky, 2007; Maacha, 2013; Tourneur et al., 2021; Subias et al., 2021). Thus, any metallogenic model of the district must account for the potential role played by any pre-arsenide ores process, the nature and provenance of the hydrothermal ore-forming fluids, the source of the main ore-forming metals and semimetals and the mechanisms of ore formation either by precipitation in open spaces or by replacement of pre-existing lithologies.

1 Pre-arsenide ores processes?

Co-Ni-Fe arsenide orebodies in the Bou Azzer district mainly occurs associated to serpentinite which formed by pervasive alteration of mantle rocks belonging to a suboceanic lithospheric section (the ophiolite sequence) (Bhilisse et al., 2019). Serpentinization at Bou Azzer gave rise to the formation of serpentine minerals, after olivine and pyroxenes, and induced partial alteration of Cr-spinel. The later became zoned with core-to-rim decreasing amounts of Al and Mg, and increasing atomic proportions of Fe^{2+} and Fe^{3+} (Gahlan and Arai, 2007; Hodel et al., 2017). This Cr-spinel show unusual high MnO, ZnO, and CoO contents (Ahmed et al., 2005, 2009; Gahlan et al., 2006; Gahlan and Arai, 2007; El Ghorfi et al., 2008; Fanlo et al., 2015; Hodel et al., 2017) which was related to the continental hydrothermal system responsible for the formation of the Co-Ni arsenide ores (e.g., El Ghorfi et al., 2008). Nevertheless, Fanlo et al (2015) proved that both zoning and the anomalously high MnO and ZnO contents of Cr-spinel were clearly pre-ore features developed during subsea floor

serpentinization in Neoproterozoic times, in a metal-rich environment caused by the presence of nearby black smoker-type hydrothermal vents.

Serpentinization processes were later overprinted by several stages of hydrothermal alteration (talcification, carbonation, silicification, Souiri et al., 2021), assumed to be linked with early stages of formation of Co-Ni-Fe arsenide ores. Alteration resulted in a varied set of mineral assemblages depending on the existence of different altering-, variably evolved fluids and/or the nature of protolith. Thus, quartz-diorite adjacent to serpentinites in most contact-types ores shows intense chloritization (locally with epidote) and silicification, with less common carbonatization. Ignimbrite also became altered to chlorite but associated to various clay mineral assemblages (Leblanc, 1975; En-Naciri, 1995; Dolansky, 2007; Maacha, 2013; Souiri et al., 2021). The alteration of serpentinite (from both contact-type, and serpentinite-hosted ores) was characterized by the development of low temperature (220-320ºC), talc- and carbonate-rich assemblages, consisting of talc-rich and chlorite-bearing serpentinite cut by a network of calcite veinlets (<1 cm thick) which becomes tighter towards the ore zone resulting in carbonate rocks with minor remnants of serpentine and/or chromian spinel (En-Naciri, 1995; El Ghorfi, 2006; Souiri et al., 2021; Hajjar et al., 2021). Leblanc (1981) and Leblanc and Billaud (1982) relate this alteration halos to meteoric alteration of serpentinite which should become folded and pinched tectonically during the last Pan-African (B2) and Hercynian orogenic phases. According to these authors, mineralisation could start previously to, and evolve coeval with the B2, Pan-African deformation stage (c. 615 Ma) but became later remobilised during the Hercynian orogeny (e.g., Leblanc, 1981; Ikenne et al., 2021).

The hypothesis of an early, Pan-African onset of ore deposition in some contact-type ores, was supported by U-Pb dating of brannerite which yielded 550 Ma (En-Naciri et al., 1997). However, new data based on diverse dating methods confirmed much younger ages (380-355 Ma) coincident with the early stages of the Hercynian Orogeny (e.g., Levresse, 2001; Gasquet et al, 2005; Dolansky, 2007; Oberthür et al., 2009). These results are further supported by the intersection of a trachyte dyke from the Ouarzazate group dated between 533 and 531 Ma (Gasquet et al., 2005; Levresse, 2001) by Co-Ni-Fe orebodies, and by the fact that in some

contact-type ores (e.g., Aghbar) these orebodies are located at the contact between serpentinite and post Pan-African volcano-sedimentary rocks of the Ouarzazate group.

Pb isotope data obtained in arsenide minerals (Stage II) from the Aghbar and Tamdrost deposits also yield Hercynian ages (around 382 Ma; Subías et al., 2022). This age contrasts with that obtained by Oberthür et al. (2009) who reported a younger one (~310 Ma) in post-arsenide carbonates and brannerite suggesting late over-printing events that did not involve any new addition of metals.

Most isotopic and geochronologic data now allow suggesting that although some alteration could pre-date ore-forming processes, the main mineralizing event took place around 350 Ma. involving multi-source hydrothermal fluids (Subías et al., 2022) channelled through reactivated ancient (probably Pan-African) faults (Tourneur et al., 2021) and new faults mainly affecting serpentinites (Hajjar et al., 2021). The hypothesis of Hercynian hydrothermal remobilization can successfully be used to interpret the formation of the crosscutting-type ores (Lebanc 1981; Maacha et al., 1998; Tourneur et al., 2021).

2 Sources of ore-forming fluids

The origin of the mineralizing fluids has attracted the interest of most researchers working in the Bou Azzer district (e.g., Leblanc, 1975; Essarraj et al., 2005; Dolansky, 2007, Maacha et al., 2015; Bouabdellah et al., 2016; Ikenne et al., 2020). The few available data on O, H, and C stable isotopes point to a dual origin of ore-forming fluids: magmatic and exotic (probably meteoritic) water (Dolansky, 2007; Maacha et al., 2015). This fluid mixing model was also supported by the fluid inclusions study conducted by Dolansky (2007) who proposed mixing between As-bearing, NaCl-dominated saline brines probably derived from a felsic magmatic source and CO_2-bearing meteoric waters. The radiogenic (Pb, Sr, Rb and Nd) and stable (S) isotope data provided in this Ph.D. Thesis (see. Subías et al., 2022) confirm the multi-source origin of ore forming fluids (Fig. V. 1).

Pb Isotopes data of ores minerals from the Bou Azzer district, suggest that these samples reflect a binary mixing process involving two distinct isotopic signatures at the approximate time (350 Ma) of ore formation. Fig. V. 1A shows calculated lead isotope compositions of

potential source rocks at 350 Ma. Unradiogenic isotopic signature of two ore minerals from Bou Azzer ($^{206}Pb/^{204}Pb$ < 17) are comparable to that obtained for a Tortonian-Lower Cryogenian pegmatite ($^{206}Pb/^{204}Pb$ = 15.5) suggesting that ancient basement rocks of the Bou Azzer-El Graara inlier, could contributed to the formation of the Co-Ni ores. The lead isotopic composition of ophiolitic rocks (including serpentinite), approximates the average lead composition of ores (Fig. V. 1A), providing strong evidence for a genetic link. Therefore, serpentinite (which is spatially associated with Co-Ni-Fe orebody) had supplied lead, as well as Co and Ni to the ore. Similarly, the initial isotopic signature of Pb (at t_{ore} =350 Ma) of quartz diorite and sandstone from Tidilline group are relatively close to the "average" lead of ores (Fig. V. 1A) suggesting that these rock types may indeed have provided some lead to the ore-forming system. In summary, Pb isotope data show that most lead of Co-Ni-Fe ores was mainly captured from serpentinites and quartz diorite although some other sources (basement rocks) must be taken into account to understand the lead isotopic signature of mineralizing fluids. Basement igneous rocks could likely have provided a non-radiogenic component, and sediments could contribute with a minor, more radiogenic type of lead (rich in ^{207}Pb).

During the ore-forming event, inferred at 350 Ma, the analysed gabbro and quartz-diorite have $^{87}Sr/^{86}Sr$ values ≤ 0.704, consistent with the Sr isotopic signature of rocks of mantle origin. In addition, quartz diorite and andesitic tuff and rocks of the ophiolite suite, gave positive εNd values at 350 Ma. The compilation of Nd (ore-associated carbonates; Oberthür et al., 2009) and Sr (ore minerals and rocks; Subías et al., 2022) isotopes clearly demonstrate that Sr-Nd isotopic composition of ore fluids is not consistent with an origin from a pure juvenile source (Fig. V. 1B) but have a depleted source origin, equal to an ophiolite-related component. Nevertheless, these data also show that other sources are required to explain the obtained range of Sr-Nd isotopes. Certain crustal, felsic rocks could be involved in ore-forming processes at 350 Ma.

The sulfur isotopic signature of ore minerals from Tamdrost ($\delta^{34}S$ data cluster around zero) as well as the positive values measured in the F7/5, Aghbar and Ightem deposits (up to $\delta^{34}S$ =11.2 in a gersdorffite sample from F7/5) could be explained assuming a magmatic, ophiolite-related source since the analysed samples from the ophiolite suite yielded $\delta^{34}S$ values

varying from 9 to -2.2. Nevertheless, this interpretation cannot apply for the S isotopic composition of the Ait Ahmane deposits and some samples from F7/5 and Aghbar, in which $\delta^{34}S$ values are negative (down to $\delta^{34}S$=-22.5 in a skutterudite sample from Ait Ahmane) (Subías et al. 2022). The achievement of such a light isotopic composition of sulfur requires thermochemical sulphate reduction (TSR) or bacterial sulphate reduction (BSR) processes, or a combination of both, but no data are available to help delineate such processes. The heterogeneous values of $\delta^{34}S$ suggest some input of locally/regionally available sedimentary sulfur into a magmatic-type fluid. The most negative values are probably best explained by BSR processes and there are scattered from sedimentary country rocks, like pelitic schists and black shales, that are likely to contain organic material that could drive a bacterial reduction process.

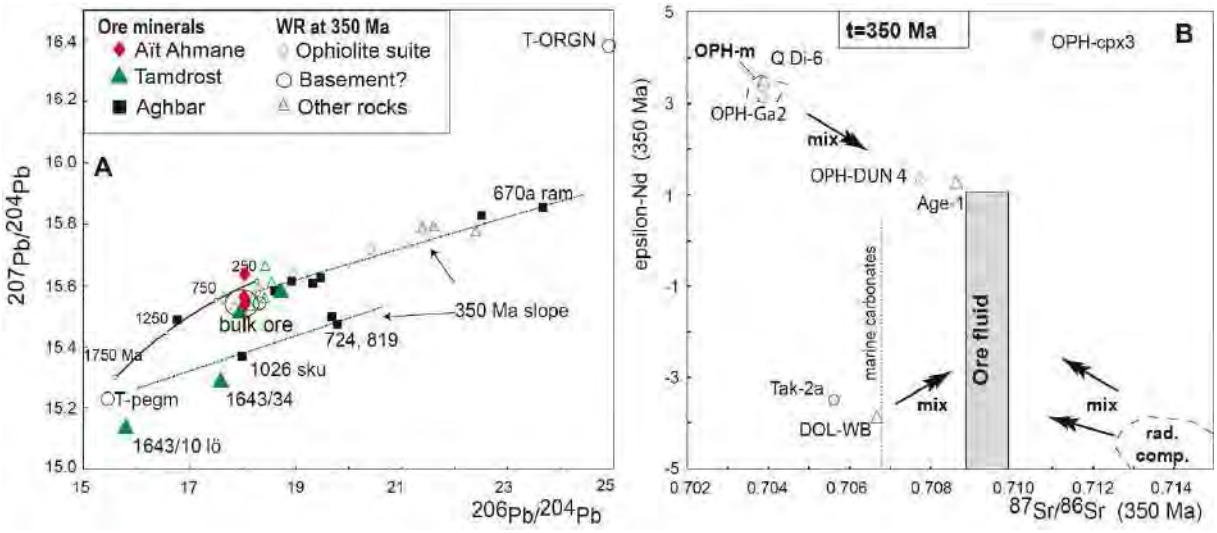

Fig. V. 1. (A) A 207Pb/204Pb versus 206Pb/204Pb plot showing values representing the situation at the time of the inferred ore formation at t = 350 Ma. Ore mineral data correspond to the present-day ratios (cf. Table IV. 1), whereas rock data are recalculated to t = 350 Ma. The indicated ore signature defined by the least radiogenic ore data (encircled area) overlaps with the least radiogenic values of rocks of the ophiolite suite, and there are also other rock types sharing this isotopic signature. Part of the Stacey and Kramers (1975) two-stage curve is added as a reference. (B) An epsilon-Nd versus Sr plot based on rock data calculated at the time of the inferred ore formation (350 Ma). Available mineral data do not allow the Nd isotope character of the ore-forming solutions to be constrained, however, its Sr isotopic signature is indicated (grays field). Added is also the Sr isotope composition of Carboniferous carbonate rocks (vertical stippled line).

The results of the multi-isotope survey (Pb, Nd, Sr and S) performed on ores and regional country rocks of the Bou Azzer mining district show that ore-forming fluids have

mainly a depleted source origin, equal to an ophiolite-related component, combined with a felsic rock (mainly quartz-diorite). However, basement igneous and sedimentary rocks (most probably carbonaceous pelitic schists and black shales) should partly contribute to the bulk, complex isotopic signature of fluids. This interpretation is consistent with the published hydrogen and oxygen isotope evidences (Dolansky, 2007; Maacha et al., 2015) which are better explained assuming a magmatic origin (from serpentinite and quart-diorite) of ore-forming fluids progressively mixed with varied exotic fluids of meteoric origin.

3 Source of ore forming metals

Serpentinite mostly matches the source of Co-Ni, while origin of As remain controversial (e.g., Leblanc, 1975; Leblanc and Billaud, 1982; Leblanc and Fischer, 1990; En-Naciri, 1995; En-Naciri et al., 1997; Dolansky, 2007; Ahmed et al., 2009a; Maacha, 2013; and Bouabdellah et al., 2016). Monitoring of Co, Fe, Ni, and As composition from barren serpentinite to alteration halo (talc-rich serpentinite, and carbonated serpentinite) and finally to massive ores from F55 orebody, provided arguments for a possible exchange of As, Co, Ni and Fe via fluids between the serpentinite and the ores.

The still very high As values measured in the serpentinite from the Ait Ahmane area (up to 644 ppm) suggest that these serpentinites cannot have suffered extensive leaching. These values are 10^4 higher than primitive mantle (Lyubetskaya and Korenag, 2007) and As-rich serpentinites described in literature (e.g., 6–275 ppm As, Hattori et al., 2005). So, even assuming that these values are residual after leaching of serpentinite anomalously enriched in As, this cannot be the unique source of As. That is why Bouabdellah et al. (2016) proposed that Neoproterozoic organic-rich black shales occurring in several inliers of the region could bring As to the Co-Ni-Fe ores in the Bou Azzer district; some of these rocks have really high As contents (up to 6180 ppm; Pašava, 1994). This finding can now be supported by the abundance of highly negative $\delta^{34}S$ values in different ores (especially in those occurring in the Aït Ahmane area), which are indicative of BSR processes commonly developed in organic matter-rich shales (black shales).

Assuming that Co, Ni, and Fe contents in peridotites were not affected by serpentinization, it is possible to evaluate the extent of leaching of such elements from serpentinites to evaluate the role of these rocks as source of metals of the Bou Azzer arsenide ores. Co, and Ni contents in serpentinite, talc-rich serpentinite and carbonated serpentinites, are below the values expected in depleted mantle peridotite (~142 ppm Co; ~2905 ppm Ni; Machesi et al., 2016), the most frequent peridotites in the tectonite section of ophiolites. However, the exceptionally high concentration of Co (and high Co/Ni ratio) in the Bou Azzer ores, is much higher than that expected from leaching of serpentinite alone. Therefore, an additional source of Co should be considered, pointing again to black shales. Some rocks of this type in the region have a Co contents around 36,8 ppm (Pašava, 1994), turning them into a suitable source of the additional Co needed to account for the high volume of Co (with very high Co/Ni ratios) concentrated in the Bou Azzer arsenide ores. Although the Fe depletion of serpentinite is comparable to that of depleted peridotite (Machesi et al., 2016), the presence of magnetite veins associated to bleached serpentinite walls (Hodel et al., 2017), support the idea that Fe was extensively leached too from serpentinite in the Ait Ahmane area. Hodel et al. (2017) proposed that magnetite veins formation was due to the involvement of Cl-rich acidic hydrothermal fluids comparable to those involved in the formation of the Co-Ni-As ores of the Bou Azzer district (Dolansky, 2007). This suggest that Fe leaching should be heterogeneous, giving rise to highly depleted zones associated to magnetite veins and moderate- to low-depleted zones (like the one studied here) which provided the necessary Fe to form the Co-Fe and Fe arsenide ores.

The slight PGE enrichment detected in the different types of ores (according to Leblanc and Fisher, 1990) with respect to serpentinite, as well as the strong PGE depletion of talc-rich serpentinites allow consider serpentinites as the most probable source of PGE, scavenged from these rocks during silicic alteration. Although it has not been studied in detail in this Ph.D. Thesis, the anomalous Au enrichment of most contact-type, Co-Ni arsenide ores of Bou Azzer could be related with hydrothermal fluids from acid/intermediate igneous rocks (granodiorite, monzonite, pegmatite…) of Lower Cryogenian age occurring in the Bou Azzer inlier.

4 Mechanisms of ore formation: Vein filling versus replacement

Co-Ni-Fe arsenide ores in the Bou Azzer district contains inclusions of serpentine, chlorite, and fractured Cr-spinel (Gervilla et al., 2012; Fanlo et al., 2015; Tourneur et al., 2021). Zoned Cr-spinel in disseminated arsenide ores in serpentinites from Aghbar, Tamdrost and Ait Ahmane deposits (i.e., Type 1A) display fracturation patterns, related to the Variscan orogeny (Gervilla et al., 2012; Fanlo et al., 2015). Textural relationship of Cr-spinel grains studied by Gervilla et al. (2012), Fanlo et al. (2015) and Tourneur et al. (2021) indicate that precipitation of arsenide ores (and the late epithermal sulfides) overprints the fracturation events affecting Cr-spinel minerals; leaving Cr-spinel fragments as inclusions in arsenide minerals. Cr-spinel minerals are largely admitted as a high-temperature magmatic mineral and exhibits low solubility under most geological conditions (Oze et al., 2007). Thus, their presence as inclusions in Co-Fe arsenide ores from the Bou Azzer district questioned their genetic link with arsenide ores, suggesting that Cr-spinel cannot be formed by hydrothermal ore-forming fluids. As argued in the previous section, the chemical composition of Type 1A Cr-spinel associated to disseminated arsenide ores hosted in serpentinite, is not chemically modified, preserving a zoning pattern originated during ocean-floor serpentinization during Neoproterozoic times (Fanlo et al., 2015; Hodel et al., 2017; Fig. V. 2). These evidences support the interpretation of Type 1A Cr-spinels as unaltered remnants left after the replacement of the ophiolitic serpentinite by Co-Ni-Fe arsenide ores in the Bou Azzer district (Hajjar et al., 2021, 2022). Therefore, arsenide ore assemblages in the Bou Azzer district should form by a combined effect of dissolution of serpentinite coupled with precipitation of mono-, di- and triarsenides, especially in Co-Fe and Fe arsenide ores where skutterudite, löllingite-safflorite and löllingite with variable amounts of calcite predominate.

Other textural feature of Cr-spinels from disseminated arsenide ores occurs as zoned crystals made up of a porous core surrounded by ferrian chromite (i.e., Type 1B; Fig. V. 2). This textural type of Cr-spinel formed by a crack-related replacement mechanism that led to the formation of Cr-Fe hydroxide in the core of fractured crystals. This replacement process likely took place coeval with Fe-Co ore and calcite precipitation (Fig. V. 2). Chlorite composition allow estimate the temperature at which Type 1B Cr-spinel formed. Calculi by Ares et al. (2018)

showed temperatures in the range of 187 and 269 °C which coincides with the lower temperature estimates proposed by Dolansky (2007) (from >400 ◦C to >200 ◦C) from fluid inclusions data, representing the latest arsenide mineralization events. Fluid inclusion results further suggest that these late events formed from $CaCl_2$-rich hydrothermal solutions, which infiltrate through serpentinite, reaching Cr-spinel grains and becoming channelled along fractures of homogenous Type 1A Cr-spinel. Such fluids were more reactive with the nearly magmatic composition of core (richer in Al and Mg) than with the ferrian chromite rim giving rise to the formation of the Cr-Fe hydroxide core of Type 1B Cr-spinel (Hajjar et al., 2022) (Fig. V. 2). Rise of the $CaCl_2$/NaCl ratio in the mineralizing fluid, led to the dissolution of the newly formed Cr-Fe hydroxide nuclei and of small grains and fragments of Cr-spinel, coeval with progressive precipitation of calcite, giving rise to a new textural type of Cr-spinel (i.e., Type 3; Fig. V. 2). This dissolution of Cr-spinel mainly affected zoned Type 1B Cr-spinel grains and fractured Type 1A grains relics and coincided with progressive precipitation of Fe-rich diarsenides (mainly löllingite). It's worth mentioning that ore-forming fluids comprised reduced brines that became more oxidized at later stages (En-Naciri, 1995, En-Naciri et al., 1997, Dolansky, 2007). Some fractured Fe-rich, Cr-spinel grains included in Fe-arsenide minerals were not affected by this dissolution stage remaining homogenous ferrian chromite (i.e., type 3; Fig. V. 2).

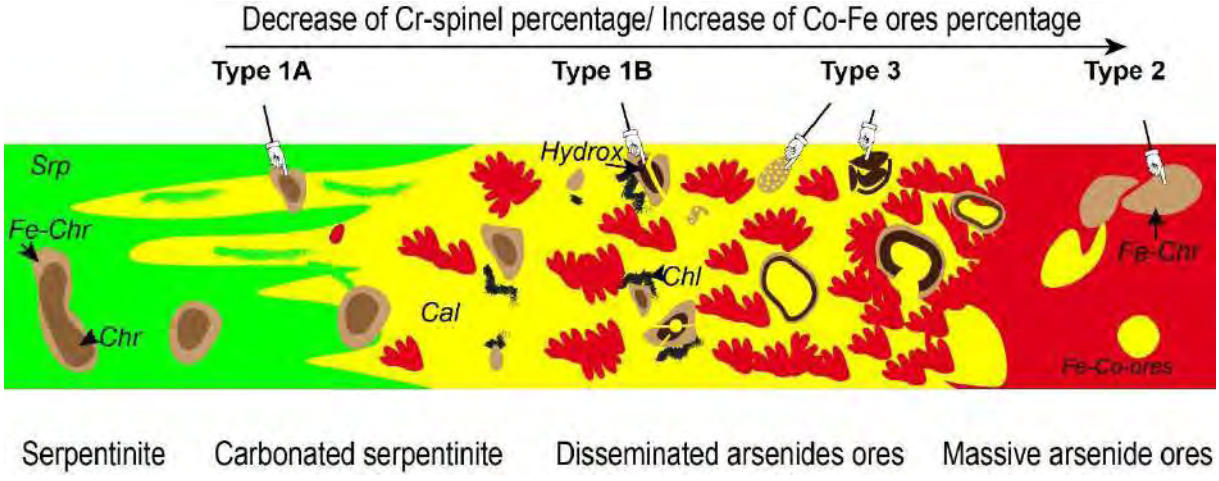

Fig. V. 2. Schematic diagram of ores zoning in the serpentinite hosted ores, showing the distribution of different Cr-spinel texture over this cross section.

5 Ore forming model

The genetic model for Co-Ni-Fe arsenide ores establishment in the Bou Azzer district predicts that the primary introduction of metals took place during Devonian-Carboniferous (e.g., Levresse, 2001; Gasquet et al., 2005; Dolansky, 2007; Oberthür et al., 2009; Saintilan et al., 2022; this study); where a N-S shortening (Gasquet et al., 2005) reactivated old Pan-African tectonic structures. The re-activated Pan-African faults, and the contact between serpentinites and the surrounding wall rocks (Quartz-diorite, Gabbro, and volcano-sedimentary rocks) (Tourneur et al., 2021) acted as conduits for the mineralizing fluids. These fluids reacted with these surrounding rocks but mainly with serpentinite (pointed out by lead isotope data) which show signs of dissolution immediately followed by precipitation of arsenide ores, highlighted by the presence of remnants of zoned Cr-spinel grains disseminated all types of arsenide ores but mainly in those rich in Co and Fe (i.e., Type 1A; Gervilla et al., 2012; Fanlo et al., 2015; Hajjar et al., 2021, 2022).

The infiltration of high temperature (most probably well above 400 ◦C), reduced, and saline fluids, leached Co, Ni, Fe and PGE from serpentinite (and other country rocks), became channelised through quartz-diorite and serpentinite contacts and extended through the serpentinite side promoting the formation of contact-type ore (Fig. V. 3A). Ni- and Ni-Co-rich ores precipitated along the fault separating serpentinite and quartz-diorite, under extremely high fluid/rock ratios. The resulting Ni-depleted fluid evolved through serpentinite, maintaining high fluid/rock ratios, and precipitated Co-Fe ores replacing both the previously formed Ni-Co ores and adjacent serpentinite. Over the course of ore formation, the mineralizing fluid cooled down (~200 °C) and became oxidized and enriched in $CaCl_2$. The late Co-Fe and Fe arsenide ores formed from extensive replacement of serpentinite by precipitating Co-Fe arsenides ± calcite assemblage (Fig. V. 3). These late Fe-arsenide ores do not occur as contact-type ores but develop within along fault walls in serpentinite, giving rise to what has been defined in this Ph.D. Thesis as a new type of arsenide ores in the Bou Azzer district: the serpentinite-hosted ores (Fig. V. 3B).

During the formation of contact-type ores, small amounts of mineralizing fluids could be able of migrate through transverse faults intersecting the contact, forming the cross cutting-ore type (Tourneur et al., 2021).

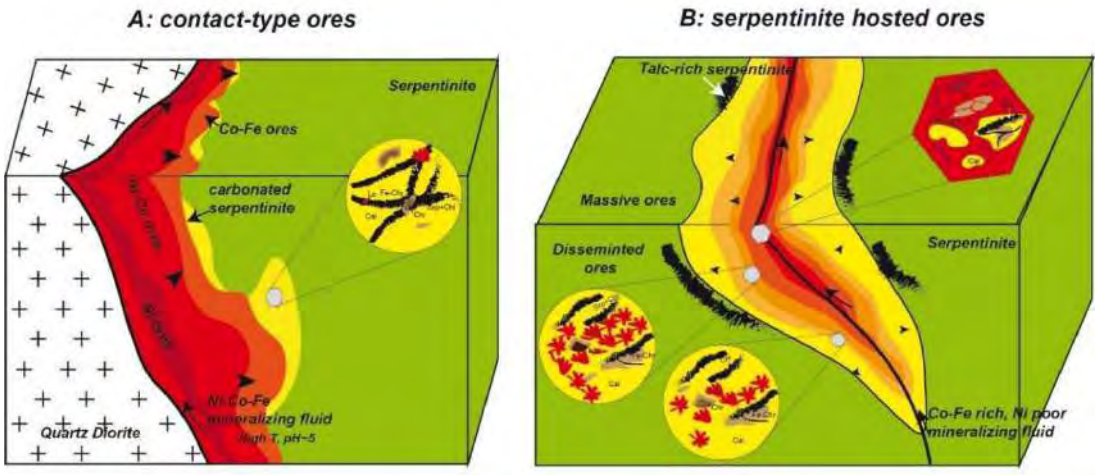

Fig. V. 3. Schematic bloc diagram of ores zoning in the serpentinite hosted ores (F55 lens, A), and in contact-type ores (B).

References

Admou, H., Razin, P., Egal, E., Youbi, N., Soulaimani, A., Blein, O., Chèvremont, P., Gasquet, D., Barbanson, L., Bouabdelli, M., Anzar-Conseil, 2013. Notice explicative carte géol. Maroc (1/50 000), feuille d'Aït Ahmane. Notes et Mem. Serv. Geol. Maroc, 533.

Ahmed, A.H., Arai, S., Abdel-Aziz, Y.M., Ikenne, M., Rahimi, A., 2009b. Platinum-group elements distribution and spinel composition in podiform chromitites and associated rocks from the upper mantle section of the Neoproterozoic Bou Azzer ophiolite, Anti-Atlas, Morocco. J. Afr. Earth Sci. 55, 92–104.

Ahmed, A.H., Arai, S., Ikenne, M., 2009a. Mineralogy and Paragenesis of the Co-Ni Arsenide Ores of Bou Azzer, Anti-Atlas, Morocco. Econ Geol, 104, 249–266.

Alves-Dias, P., Blagoeva, D., Pavel, C., Arvanitidis, N., 2018. Cobalt: demand-supply balances in the transition to electric mobility. JRC Science for Policy Report. European Commision.https://publications.jrc.ec.europa.eu/repository/bitstream/JRC112285/jrc112285_cobalt.pdf

Ares, A., 2018. Las espinelas cromíferas del fil´on 7/5 del distrito minero de Bou Azzer (Marruecos): residuos del reemplazamiento de serpentinitas. TFM. Universidad de Huelva-Universidad Internacional de Andalucía, p. 54.

Barnes, S.J., 2000. Chromite in Komatiites, II. Modification during greenschist to mid-amphibolite facies metamorphism. J. Petrol. 41, 387–409.

Barra, F., Gervilla, F., Hern´andez, E., Reich, M., Padr´on-Navarta, J.A., González-Jiménez, J.M., 2014. Alteration patterns of chromian spinels from La Cabaña peridotite, southcentral Chile. Mineral. Petrol. Times 108 (6), 819–836.

Bouabdellah, M., Maacha, L., Levresse, G., Saddiqi, O., 2016. The Bou Azzer Co–Ni–Fe–As (– Au – Ag) District of Central Anti-Atlas (Morocco): A Long-Lived Late Hercynian to Triassic Magmatic-Hydrothermal to Low-Sulphidation Epithermal System, Mineral Deposits of North Africa, (eds.), Mineral Deposits of North Africa, Mineral Resource Reviews, 229-247

Dolansky, LM., 2007. Controls on the genesis of hydrothermal cobalt mineralization: insights from the mineralogy and geochemistry of the Bou Azzer deposits, Morocco. Master, McGill University, Montréal, Canada, 162p

EL Ghorfi, M., 2006. Etude géochimique et métallogenique des métaux précieux (or, argent et platinoïdes) associes aux minéralisations à Co, Ni, Cr de Bou Azzer-El Graara, et dans la série de Bleida Far West, Anti-Atlas, Maroc. PhD thesis, Cadi Ayyad University, Marrakech, Morocco, 256 p.

El Ghorfi, M., Melcher, F., Oberth€ur, T., Boukhari, A.E., Maacha, L., Maddi, A., Mhaili, M., 2008. Platinum group minerals in podiform chromitites of the Bou Azzer ophiolite, Anti Atlas, Central Morocco. Mineral. Petrol. 92, 59–80.

EL Hadi, H.E., Simancas, J.F., Martinez-Poyatos, D., Azor, A., Tahiri, A., Montero, P., Bea, C.M., González-lodeiro, F., 2010. Structural and geochronological constraints on the evolution of the Bou Azzer Neoproterozoic ophiolite (Anti-Atlas, Morocco). Precamb. Res. 182, 1–14.

En-Naciri, A., 1995. Contribution à l'étude du district à Co. As (Ni, Au, Ag) de Bou Azzer. Anti- Atlas (Maroc) Données minéralogiques et géochimiques. PhD thesis, Université d'Orléans. France 245 p.

En-Naciri, A., Barbanson, L., Touray, J.C., 1997. Brine inclusions from the Co-As (Au) Bou Azzer district, Anti-Atlas, Morocco. Econ Geol, 92, 360-367.

Essarraj, S., Boiron, M.-C., Cathelineau, M., Banks, D.A., Benharref, M., 2005. Penetration of surface-evaporated brines into the Proterozoic basement and deposition of Co and Ag at Bou Azzer (Morocco): evidence from fluid inclusions. J. African Earth Sc. 41 (1-2), 25–39.

Fanlo, I., Gervilla, F., Colás, V., Subías, I., 2015. Zn-, Mn- and Co-rich chromian spinels from the Bou-Azzer mining district (Morocco): Constraints on their relationship with the mineralizing process. Ore Geol. Rev. 71, 82–98.

Fanlo, I., Arranz, E., Subías, I., Gervilla, F., 2017. The Filon 7/5 (Bou Azzer district, Morocco): an example of Co-Ni ores formation under disequilibrium conditions. In: Mineral Resources to Discover. Proceedings of the 14th Biennial SGA Meeting, 1, 1531-1534.

Gahlan, H., Arai, S., 2007. Genesis of peculiarly zoned Co, Zn and Mn-rich chromian spinel in serpentinite of Bou Azzer ophiolite, Anti Atlas, Morocco. J. Miner. Petrol. Sci, 102, 69-85.

Gasquet, D., Levresse, G., Cheilletz, A., Azizi-Samir, M.R., Mouttaqi, A., 2005. Contribution to a geodynamic reconstruction of the Anti-Atlas (Morocco) during Pan-African times with the emphasis on inversion tectonics and metallogenic activity at the Precambrian-Cambrian transition. Precamb. Res.140, 157–182.

Gasquet, D., Ennih, N., Lie´ geois, J.-P., Soulaimani, A., Michard, A., 2008. The Pan-African belt. In: Michard, A., Saddiqi, O., Chalouan, A., Frizon Lamotte, D. (Eds.), Continental

Evolution: The Geology of Morocco. Lecture Notes in Earth Sciences, vol. 116, Springer, pp. 33–64.

Gervilla, F., Fanlo, I., Colás, V., Subías, I., 2012a. Mineral compositions and phase relations of Ni–Co–Fe arsenide ores from the Aghbar mine, Bou Azzer, Morocco. Can. Mineral. 50, 2, 447–470.

Gervilla, F., Padron-Navarta, J.A., Kerestedjian, T., Sergeeva, I., González-Jiménez, J.M., Fanlo, I., 2012b. Formation of ferrian chromite in podiform chromitites from the Golyamo Kamenyane serpentinite, Eastern Rhodopes, SE Bulgaria: a two-stage process. Contrib. Mineral. Petrol. 164 (4), 643–657.

Gervilla, F., Asta, M.P., Fanlo, I., Grolimund, D., Ferreira-S´anchez, D., Samson, V.A., Hunziker, D., Colas, V., González-Jiménez, J.M., Kerestedjian, T.N., Sergeeva, I., 2019. Diffusion pathways of Fe2+ and Fe3+ during the formation of ferrian chromite: a μXANES study. Contrib. Mineral. Petrol. 174, 65.

González-Jiménez, J.M., Kerestedjian, T., Proenza Fern´andez, J.A., Gervilla, F., 2009. Metamorphism on chromite ores from the Dobromirtsi ultramafic massif, Rhodope Mountains (SE Bulgaria). Geol. Acta 7 (4), 413–429.

Hajjar, Z. 2011. Contribution à l'étude des Filons F53, F54, F55, champs minier d'Aït Ahmane (Bou Azzer, Anti Atlas, Maroc). Master, Cadi Ayyad University, Marrakech, Morocco, 105p.

Hajjar, Z., Ares, G., Fanlo, I., Gervilla, F., González-Jiménez, J.M., 2022. Textural changes in Cr-spinel fingerprints the genesis of Co-Fe ores at Bou Azzer (Morocco). Journal of African Earth Science, 188, 104471.

Hajjar Z., Gervilla F., Fanlo I., González-Jiménez J.M., Ilmen S., 2021. Formation of serpentinite-hosted, Fe-rich arsenide ores at the latest stage of mineralization of the Bou-Azzer mining district (Morocco). Ore Geology Reviews 128, 103926.

Hattori, K., Takahashi, Y., Guillot, S., Johanson, B., 2005. Occurrence of arsenic (V) in forearc mantle serpentinites based on X-ray absorption spectroscopy study. Geochim. Cosmochim. Acta, 69, 23, 5585–5596.

Hefferan, K., Soulaimani, A., Samson, S.D., Admou, H., Inglis, J., Saquaque, A., Chaib, L., Heywood, N., 2014. A reconsideration of Pan African orogenic cycle in the Anti-Atlas Mountains, Morocco. J. Afr. Earth Sc. 98, 34-46

Hodel, F., Macouin, M., Triantafyllou, A., Carlut, J., Berger, J., Rousse, S., Ennih, N., Trindade, R.I.F., 2017. Unusual massive magnetite veins and highly altered Cr-spinels as relics of a Clrich acidic hydrothermal event in Neoproterozoic serpentinites (Bou Azzer ophiolite, Anti-Atlas, Morocco). Precamb. Res. 300, 151-167

Ikenne, M., Souhassou, M., Saintilan, N.J., Karfal, A., El Hassani, A., Moundi, Y., Ousbih, M., Ezzghoudi, M., Zouhir, M., Maacha, L., 2020. Cobalt-Nickel-Copper arsenide, sulpharsenide and sulphide mineralisation in the Bou Azzer window, Anti-Atlas, Morocco: One century of multi-disciplinary and geological investigations, mineral

exploration and mining. Geological Society, London, Special Publications, 502, https://doi.org/10.1144/SP502-2019-132

Kimball, K.L., 1990. Effects of hydrothermal alteration on the composition of chromian spinels. Contrib. Mineral. Petrol. 105, 337–346.

Lasobras, E., 2012. Composición mineral y relaciones de fase de los arseniuros de Co-Fe-Ni del yacimiento de Aït-Ahmane (Bou-Azzer, Marruecos). Diferencias con otros depósitos. TFM., Universidad de Zaragoza. Spain, 53p.

Lázaro, M., 2012. Mecanismos de reequilibrio mineral en arseniuros de Co-Fe-Ni en Tamdrost (Bou Azzer, Marruecos). TFM. Universidad de Zaragoza, Spain, p. 53.

Lebedev, V.I., Borovikov, A.A., Borisenko, A.S., Azizi, R., Ishkov, Y.M., Borisenko, D.A., 1999, Physicochemical constraints of cobalt ore formation in the Bou Azzer Deposit, Morocco: Doklady Earth Sciences, 368, 985-988.

Leblanc, M., 1975. Ophiolites précambriennes et gîtes arséniés de Cobalt (Bon Azzer. Maroc). PhD thesis, Univ. Paris VI, France, 329p.

Leblanc, M., 1981. Ophiolites précambriennes et gîtes arséniés de cobalt (Bou Azzer-Maroc). Notes et mém. Serv. Géol. Maroc, 280, 311p.

Leblanc, M., Billaud, P., 1982. Cobalt arsenide orebodies related to an Upper Proterozoic ophiolite: Bou Azzer (Morocco). Econ Geol. 77, 162-175.

Leblanc, M., Fischer, W., 1990. Gold and platinum group elements in cobalt-arsenide ores: Hydrothermal concentration from a serpentinite source-rock (Bou Azzer, Morocco). Miner. Petrol., 42, 197-209.

Ledent, D., 1960, Âge absolu d'une brannérite de Bou-Azzer (Sud-Marocain): Academie des [Paris] Comptes Rendus, Série D, 250, 1309-1311.

Levresse, G., 2001, Contribution à l'établissement d'un modèle génétique des gisements d'Imiter (Ag-Hg), Bou Madine (Pb-Zn-Cu-Ag-Au) et Bou Azzer (Co-Ni-As-Ag-Au) dans l'Anti-Atlas marocain. Ph.D. thesis, CRPG-CNRS, Nancy, France, 191p.

Lorand, J.P., Luguet, A. Alard, O., 2008, Platinum-group elements: a new set of key tracers for the Earth's interior. Elements 4, 247-252.

Lyubetskaya, T., Korenag, J., 2007. Chemical composition of Earth's primitive mantle and its variance. J. Geophys. Res., 112, B03211. 21p

Maacha, L., 2013. Etude méallogéniques et géophysiques des minéralisations cobaltifères et cuprifères de Bou-Azzer El Graara Anti Atlas Maroc (Tome 1). PhD thesis, Cadi Ayyad University, Marrakech, Morocco, 344p.

Maacha, L., Azizi, R., Bouchta, R., 1998, Gisements cobaltifères du district de Bou Azzer (Anti-Atlas) : structure, minéralogie et conditions de genèse: Chronique de la Recherche Minière, 530-533, 65-75.

Maacha, L., En-Naciri, O., El Ghorfi, M., Saquaque, A., Alansari, A., Soulaimani, A., 2011. Le district à cobalt, nickel et arsenic de Bou Azzer (Anti-Atlas central). Notes et mém. Serv. Géol. Maroc, 9, 91-97.

Maacha, L., Lebedev, V.I., Saddiqi, O., Zouhair, M., El Ghorfi, M., Borissenko, A.S., Pavlova, G.G., 2015. Arsenide deposits of the Bou Azzer ore district (anti-atlas metallogenic province) and their economic outlook. editor acad. RAS, doctor of geology V.V. Yarmolyuk – Kyzyl: TuvIENR SB RAS, 66p.

Marchesi, C., Garrido, C.J., Proenza, J.A., Hidas, K., Varas-Reus, M.I., Butjosa, L., Lewis, J.F., 2016. Geochemical record of subduction initiation in the sub-arc mantle: Insights from the Loma Caribe peridotite (Dominican Republic). Lithos 252–253, 1–15.

Mellini, M., Rumori, C., Viti, C., 2005. Hydrothermally reset magmatic spinels in retrograde serpentinites: formation of "ferritchromit" rims and chlorite aureoles. Contrib. Mineral. Petrol. 149, 266–275.

Merlini, A., Grieco, G., Diella, V., 2009. Ferritchromite and chromian chlorite formation in melange-hosted Kalkan chromite (Southern urals, Russia). Am. Mineral. 94, 1459–1467.

Mukherjee, R., Mondal, S.K., Rosing, M.T., Frei, R., 2010. Compositional variations in the Mesoarchean chromites of the Nuggihalli schist belt, Western Dharwar Craton (India): potential parental melts and implications for tectonic setting. Contrib. Mineral. Petrol. 160 (6), 865–885.

Nataf, F., 2003. Jean epinat. Un homme, une aventure au Maroc. Souffles, 160p.

Ohmoto, H., Goldhaber, M.B., 1997. Sulfur and carbon isotopes. In: Barnes H (ed.) Geochemistry of Hydrothermal Ore Deposits, pp. 517–612. New York, NY: Wiley.

Oberthür, T., Melcher, F., Henjes-Kunst, F., Gerdes, A., Stein, H., Zimmerman, A., El Ghorfi, M., 2009. Hercynian age of the cobalt-nickel-arsenide-(gold) ores, Bou Azzer, Anti-Atlas, Morocco : Re-Os, Sm-Nd, and U-Pb age determinations. Econ Geol. 104, 1065–1079.

Oze, C., Bird, D.K., Fendorf, S., 2007. Genesis of hexavalent chromium from natural sources in soil and groundwater. PNAS 104 (16), 6544–6549.

Pasava, J., 1994. Geochemistry and role of anoxic sediments in the origin of the Imiter silver deposit in Morocco. Czech Geol. Surv. Bull. 69, 1–11.

Proenza, J.A., Ortega-Guti´errez, F., Camprubı, A., Tritlla, J., Elıas-Herrera, M., Reyes- Salas, M., 2004. Paleozoic serpentinite-enclosed chromitites from Tehuitzingo (Acatl´an Complex, southern Mexico): a petrological and mineralogical study. J. S. Am. Earth Sci. 16 (8), 649–666.

Saintilan N.J., Bernasconi S.M., Ikenne M., Allaz J.M., Souhassou M., Karfal A., Maacha L., Spangenberg J.E., 2022. Giant Co-Ni arsenide mineralization resulting from cold hydrocarbon seep and upper Devonian brine circulation in Neoproterozoic serpentinite

(Bou Azzer, Morocco). Edt. The critical role of minerals in the carbon-neutral future. 16th biennal meeting SGA 2022. pp160.

Saquaque, A., Admou, H., Karson, J.A., Hefferan, K., Reuber, I., 1989. Precambrian accretionary tectonics in the Bou Azzer-El Graara region. Geology, 17, 1107–1110.

Souiri, M., Aissa, M., Ahmed, A.H., El Azmi, M., Mezougane, H., Moussaid, A., El Basbas, A., 2021. Hydrothermal alterations of the Bou Azzer East Co-Ni- As-Au deposits (central Anti-Atlas, Morocco). Geosciences Journal, https://doi.org/10.1007/s12303-020-0063-2

Soulaimani, A., Hefferan, K., 2017. Le Précambrien à la bordure nord du craton ouest-africain (Anti-Atlas et Haut Atlas, Maroc). Geologues 194, 33–36.

Soulaimani, A., Ouanaimi, H., Saddiqi, O., Baidder, L., Michard, A., 2018. The Anti-Atlas Pan-African Belt (Morocco): overview and pending questions. C. R. Geosci. 350 (6), 279–288.

Stacey, J.S., Kramers, J.D., 1975. Approximation of terrestrial lead isotope evolution by a two-stage model. Earth Planet. Sci. Lett. 26 (2), 207–221.

Subías, I., Fanlo, I., Hajjar, Z., Gervilla, F., Billström, K., 2022. Isotopic constraints on age, source of ore-forming fluids and genesis of the Bou Azzer arsenide ores (Morocco). Ore geology review, 143, 104769.

Talukdar, M., Sanyal, S., Sengupta, P., 2017. Metasomatic alteration of chromite from parts of the late Archaean Sittampundi layered magmatic complex (SLC), Tamil Nadu, India. Ore Geol. Rev. 90, 148–165.

Tourneur, E., Chauvet, A.m Kouzmanov, K., Tuduri, J., Paquez, C., Sizaret, S., Darfal, A., Moundi, Y., El Hassani, A. 2021. Co-Ni-arsenide minealisation in the Bou Azzer district (Anti-Atlas, Morocco): Genetic model and tectonic implications. Ore Geol. Rev. 134, 104128

Triantafyllou, A., Berger, J., Baele, J.M., Diot, H., Ennih, N., Plissart, G., Monnier, C., Watlet, A., Bruguier, O., Spagna, P., Vandycke, S., 2016. The Tachakoucht–Iriri–Tourtit arc complex (Moroccan Anti-Atlas): Neoproterozoic records of polyphased subduction-accretion dynamics during the Pan-African orogeny. J. Geodyn. 96, 81–103.

Triantafyllou, A., Berger, J., Baele, J.-M., Bruguier, O., Diot, H., Ennih, N., Monnier, C., Plissart, G., Vandycke, S., Watlet, A., 2018. Intra-oceanic arc growth driven by magmatic and tectonic processes recorded in the Neoproterozoic Bougmane arc complex (Anti-Atlas, Morocco). Precambr. Res. 304, 39–63.

Triantafyllou, A., Berger, J., Baele, J.M., Mattielli, N., Ducea, M.N., Sterckx S., Samson S., Hodel, F., Ennih, N., 2020. Episodic magmatism during the growth of a Neoproterozoic oceanic arc (Anti-Atlas, Morocco). Precamb. Res. 339, 105610

Ulrich, M., Munöz, M., Guillot, S., Cathelineau, M., Picard, C., Quesnel, B., Boulvais, P., Couteau, C., 2014. Dissolution–precipitation processes governing the carbonation and

silicification of the serpentinite sole of the New Caledonia ophiolite. Contrib Mineral Petrol. 167: 952, 1-19.

U.S. Geological Survey, 2013. Mineral commodity summaries 2013. U.S. Geological Survey, 198 p.

Appendix

Appendix A: Chemical composition of arsenide

Appendix B: chemical composition of chromite

Appendix A: Chemical composition of arsenide

Sample	As	Co	Ni	Fe	S	Bi	Sb	Total
F55 Lens								
Disseminated ores								
Loellingite								
AA-17-C1-12	71,47	0,24	0,00	27,92	0,53	0,00	0,00	100,16
AA-17-C1-13	71,41	0,37	0,04	27,79	0,61	0,00	0,05	100,27
AA-17-C1-14	71,44	0,26	0,04	27,84	0,62	0,00	0,01	100,21
AA-17-C1-26	69,71	0,07	0,01	28,76	1,69	0,00	0,03	100,26
AA-17-C1-27	69,32	0,07	0,00	28,75	1,96	0,00	0,06	100,16
AA-17-C1-28	69,74	0,08	0,00	28,58	1,80	0,00	0,00	100,20
AA-17-C1-29	69,61	0,62	0,01	27,97	1,88	0,00	0,06	100,14
AA-17-C1-30	69,51	0,09	0,00	28,59	1,88	0,00	0,03	100,10
AA-17-C1-31	71,83	0,27	0,01	27,82	0,29	0,00	0,02	100,23
AA-17-C1-32	71,63	0,48	0,01	27,65	0,36	0,00	0,00	100,13
AA-17-C1-34	71,31	0,23	0,03	28,12	0,63	0,05	0,05	100,40
AA-17-C1-36	68,72	0,06	0,02	28,83	2,56	0,00	0,00	100,18
AA-17-C1-47	70,12	0,09	0,00	28,54	1,46	0,00	0,04	100,25
AA-17-C1-48	69,78	0,12	0,02	28,56	1,82	0,00	0,00	100,29
AA-17-C2-11	71,68	0,42	0,02	27,56	0,42	0,00	0,00	100,10
AA-17-C2-15	71,44	0,47	0,04	27,65	0,52	0,00	0,00	100,11
AA-17-C2-18	69,72	0,28	0,00	28,30	1,84	0,00	0,00	100,14
AA-17-C2-9	70,96	0,97	0,11	27,12	0,95	0,00	0,00	100,10
AA-17-C5-10	71,62	0,30	0,01	27,80	0,28	0,00	0,05	100,06
AA-17-C5-11	69,30	0,42	0,00	28,40	1,90	0,00	0,01	100,03
AA-17-C5-12	71,50	0,09	0,01	28,22	0,49	0,00	0,03	100,34
AA-17-C5-13	71,10	0,26	0,02	28,13	0,79	0,00	0,00	100,31
AA-17-C5-2	71,94	0,23	0,00	28,02	0,24	0,00	0,06	100,49
AA-17-C5-3	71,59	0,26	0,02	27,85	0,25	0,06	0,08	100,09
AA-17-C5-4	71,49	0,19	0,01	28,08	0,53	0,00	0,00	100,30
AA-17-C5-6	71,28	0,12	0,00	28,03	0,55	0,14	0,10	100,22
AA-17-C5-7	70,05	0,06	0,00	28,68	1,45	0,00	0,07	100,31
AA-17-C5-8	70,78	0,18	0,02	28,20	1,09	0,00	0,00	100,28
AA-17-C6-1	71,97	0,36	0,02	27,92	0,24	0,00	0,00	100,51
AA-17-C6-11	71,69	0,20	0,00	28,03	0,19	0,05	0,00	100,16
AA-17-C6-12	71,37	0,16	0,00	28,21	0,44	0,00	0,02	100,20
AA-17-C6-13	71,56	0,14	0,04	28,37	0,46	0,00	0,04	100,60
AA-17-C6-16	71,67	0,12	0,00	28,07	0,34	0,00	0,01	100,21
AA-17-C6-17	69,17	1,38	0,01	27,44	2,05	0,02	0,08	100,15
AA-17-C6-19	71,55	0,15	0,00	27,90	0,34	0,10	0,08	100,11
AA-17-C6-2	71,60	0,29	0,00	27,92	0,37	0,11	0,00	100,28
AA-17-C6-20	71,37	0,12	0,00	28,09	0,48	0,00	0,05	100,12
AA-17-C6-21	71,40	0,10	0,00	28,06	0,52	0,00	0,02	100,10
AA-17-C6-22	70,49	0,05	0,00	28,40	0,99	0,11	0,02	100,07
AA-17-C6-3	71,57	0,22	0,00	28,01	0,36	0,00	0,03	100,19
AA-17-C6-4	69,16	0,29	0,00	28,77	2,07	0,00	0,01	100,31
AA-17-C6-5	70,64	0,12	0,01	28,33	0,99	0,00	0,06	100,15
AA-17-C6-6	70,88	0,46	0,00	27,94	0,87	0,00	0,00	100,15
AA-17-C6-8	71,57	0,26	0,01	27,98	0,32	0,07	0,01	100,22
Rm-Lo								
AA-17-C1-3	69,70	2,26	10,58	16,09	1,55	0,00	0,03	100,21
AA-17-C1-7	69,35	2,12	9,94	16,92	1,83	0,00	0,00	100,16
AA-17-C1-6	68,07	2,00	7,98	19,50	2,77	0,00	0,06	100,38

Sample	As	Co	Ni	Fe	S	Bi	Sb	Total
AA-17-C1-8	69,91	1,87	10,26	16,99	1,60	0,00	0,00	100,63
AA-17-C1-42	69,44	1,54	10,34	17,17	1,75	0,00	0,05	100,29
AA-17-C2-3	70,53	1,54	11,83	15,21	0,88	0,00	0,07	100,05
AA-17-C1-41	69,18	1,28	9,08	18,78	1,89	0,00	0,03	100,24
AA-17-C1-1	71,57	1,26	8,66	18,35	0,18	0,14	0,07	100,24
AA-17-C1-21	70,66	1,19	11,49	15,99	0,78	0,05	0,05	100,21
AA-17-C1-2	70,42	1,06	11,90	15,83	1,11	0,00	0,00	100,32
AA-17-C1-39	70,46	1,00	12,72	15,08	0,87	0,00	0,01	100,15
AA-17-C1-22	70,15	0,99	11,25	16,68	1,13	0,00	0,05	100,25
AA-17-C1-40	70,65	0,96	12,64	15,16	0,89	0,00	0,02	100,31
AA-17-C1-38	71,20	0,95	6,16	21,12	0,58	0,00	0,07	100,08
AA-17-C1-4	70,72	0,88	12,92	14,97	0,90	0,00	0,00	100,38
AA-17-C1-5	70,41	0,84	12,13	15,84	0,96	0,00	0,12	100,30
AA-17-C1-20	70,78	0,57	12,49	15,60	0,70	0,00	0,00	100,14
AA-17-C2-2	71,55	0,47	10,82	16,83	0,23	0,11	0,05	100,07
Rm-Sf-Lo								
AA-17-C1-44	69,85	14,52	6,71	7,79	1,22	0,00	0,04	100,13
AA-17-C1-43	70,20	13,09	8,22	7,60	0,96	0,00	0,00	100,07
AA-17-C1-45	70,63	11,45	5,36	11,94	0,74	0,00	0,04	100,16
AA-17-C1-46	71,18	9,84	5,95	12,87	0,26	0,00	0,01	100,12
AA-17-C1-10	71,36	9,54	8,22	10,78	0,27	0,00	0,00	100,17
AA-17-C1-24	70,58	9,40	6,04	13,33	0,74	0,00	0,00	100,09
Massive ores								
Lo								
AA-19-C2-1	71,37	0,11	0,04	28,28	0,67	0,03	0,00	100,50
AA-19-C2-11	71,20	0,09	0,00	28,25	0,81	0,01	0,00	100,36
AA-19-C2-14	70,78	0,04	0,00	28,69	1,28	0,00	0,00	100,79
AA-19-C2-15	70,94	0,06	0,01	28,51	0,95	0,00	0,00	100,47
AA-19-C2-16	70,97	0,07	0,01	28,29	0,88	0,12	0,08	100,42
AA-19-C2-2	71,33	0,33	0,01	27,98	0,56	0,00	0,04	100,26
AA-19-C2-3	70,24	0,04	0,00	28,52	1,54	0,00	0,00	100,34
AA-19-C2-4	71,43	0,07	0,01	28,46	0,57	0,00	0,06	100,60
AA-19-C2-5	71,14	0,27	0,00	28,19	0,74	0,00	0,01	100,35
AA-19-C2-6	70,16	0,16	0,00	28,45	1,41	0,00	0,00	100,18
AA-19-C2-7	71,52	0,05	0,00	28,11	0,48	0,00	0,00	100,16
AA-19-C2-8	70,13	0,05	0,01	28,56	1,59	0,00	0,00	100,34
AA-19-C2-9	70,11	0,06	0,01	28,63	1,51	0,13	0,00	100,44
AA-19-C4-1	71,73	0,55	0,02	27,72	0,34	0,00	0,05	100,41
AA-19-C4-10	71,73	0,24	0,03	27,98	0,35	0,00	0,00	100,33
AA-19-C4-11	70,53	1,28	0,00	27,11	1,18	0,00	0,00	100,10
AA-19-C4-12	71,74	0,11	0,00	28,10	0,35	0,00	0,03	100,33
AA-19-C4-13	71,76	0,12	0,00	28,03	0,35	0,06	0,00	100,31
AA-19-C4-14	68,83	0,20	0,00	29,12	2,34	0,00	0,07	100,55
AA-19-C4-15	68,73	1,57	0,01	27,51	2,38	0,00	0,02	100,22
AA-19-C4-17	71,38	0,28	0,00	28,12	0,56	0,00	0,05	100,39
AA-19-C4-18	69,89	0,23	0,00	28,48	1,69	0,00	0,00	100,29
AA-19-C4-2	71,50	0,23	0,01	28,33	0,55	0,05	0,04	100,72
AA-19-C4-20	69,64	0,68	0,00	28,08	1,92	0,00	0,00	100,32
AA-19-C4-21	71,44	0,13	0,00	27,98	0,48	0,16	0,00	100,19
AA-19-C4-22	71,34	0,13	0,02	28,20	0,46	0,00	0,00	100,14
AA-19-C4-3	71,58	0,16	0,01	28,06	0,44	0,11	0,00	100,36
AA-19-C4-4	71,57	0,65	0,00	27,71	0,46	0,00	0,00	100,39
AA-19-C4-5	71,58	0,49	0,00	27,90	0,34	0,24	0,00	100,54

Sample	As	Co	Ni	Fe	S	Bi	Sb	Total
AA-19-C4-6	71,78	0,12	0,00	28,15	0,25	0,00	0,00	100,30
AA-19-C4-7	71,42	0,80	0,00	27,55	0,57	0,00	0,00	100,35
AA-19-C4-8	71,61	0,24	0,01	27,97	0,48	0,00	0,00	100,31
AA-19-C4-9	71,60	0,09	0,02	28,12	0,40	0,00	0,00	100,23
AA-18-C2-26	71,27	0,67	0,63	27,02	0,65	0,00	0,01	100,25
AA-18-C2-27	70,55	0,72	0,29	27,68	1,17	0,00	0,02	100,42
AA-18-C2-28	71,65	0,24	0,11	28,04	0,28	0,00	0,05	100,37
AA-18-C3-1	71,63	0,16	0,01	28,05	0,39	0,00	0,00	100,24
AA-18-C3-11	71,80	0,45	0,00	27,71	0,32	0,00	0,00	100,29
AA-18-C3-12	71,38	0,13	0,00	28,26	0,59	0,00	0,08	100,43
AA-18-C3-13	71,59	3,21	0,01	25,21	0,36	0,02	0,00	100,41
AA-18-C3-14	71,02	0,27	0,00	28,06	0,76	0,00	0,02	100,12
AA-18-C3-15	69,00	0,41	0,07	28,34	2,41	0,00	0,00	100,22
AA-18-C3-16	71,64	0,17	0,02	27,90	0,38	0,00	0,00	100,11
AA-18-C3-17	71,71	0,34	0,01	27,88	0,36	0,02	0,00	100,32
AA-18-C3-18	71,77	0,13	0,03	28,16	0,37	0,00	0,07	100,52
AA-18-C3-19	68,90	0,93	0,00	27,99	2,48	0,00	0,03	100,34
AA-18-C3-2	71,09	0,27	0,01	28,35	0,89	0,00	0,00	100,62
AA-18-C3-20	69,03	0,21	0,00	28,89	2,42	0,00	0,10	100,65
AA-18-C3-22	71,66	0,15	0,01	27,99	0,37	0,00	0,03	100,21
AA-18-C3-3	71,78	1,99	0,01	26,18	0,31	0,22	0,08	100,57
AA-18-C3-5	71,58	0,12	0,00	28,48	0,39	0,00	0,00	100,57
AA-18-C3-6	71,34	0,10	0,00	28,17	0,58	0,00	0,00	100,19
AA-18-C3-7	69,23	1,26	0,00	27,80	2,12	0,00	0,01	100,42
AA-18-C3-8	71,48	0,43	0,00	27,85	0,56	0,00	0,03	100,35
Sf-Lo								
AA-18-C2-14	71,24	14,17	0,42	14,05	0,23	0,00	0,01	100,12
AA-18-C2-20	71,08	16,85	0,23	11,67	0,25	0,16	0,00	100,24
AA-18-C2-21	71,28	15,70	0,18	12,74	0,25	0,00	0,01	100,17
AA-18-C2-23	70,56	19,49	0,05	9,37	0,59	0,00	0,10	100,16
AA-18-C2-24	70,81	13,28	0,06	15,51	0,62	0,00	0,05	100,33
AA-18-C2-29	71,50	12,51	0,04	15,94	0,06	0,00	0,00	100,05
F56 lens								
sk								
F56-AA-7-c2-10	76,09	14,17	5,32	2,06	1,30	0,00	0,00	98,94
F56-AA-7-c2-13	75,58	15,15	4,48	2,04	1,64	0,00	0,05	98,94
F56-AA-7-c2-2	76,41	14,36	5,45	1,92	1,35	0,00	0,00	99,49
F56-AA-7-c2-3	76,25	14,18	5,40	1,95	1,47	0,00	0,03	99,28
F56-AA-7-c2-4	76,77	12,66	6,31	2,28	0,92	0,00	0,00	98,95
F56-AA-7-c2-5	76,90	12,68	6,34	2,24	0,94	0,00	0,09	99,20
F56-AA-7-c2-6	76,75	13,06	6,06	2,29	1,04	0,00	0,00	99,20
F56-AA-7-c2-7	76,74	12,73	6,43	2,24	0,89	0,00	0,01	99,05
F56-AA-7-c2-8	76,97	12,71	6,47	2,26	0,95	0,00	0,00	99,36
F56-AA-7-c3-10	76,16	13,33	6,40	1,61	1,19	0,00	0,04	98,73
F56-AA-7-c3-11	76,44	12,15	7,33	1,77	0,73	0,01	0,02	98,45
F56-AA-7-c3-12	76,16	13,07	6,50	1,49	0,96	0,00	0,00	98,18
F56-AA-7-c3-13	76,54	12,51	6,92	1,83	0,92	0,00	0,00	98,72
F56-AA-7-c3-14	76,63	12,52	6,86	1,74	0,90	0,06	0,05	98,76
F56-AA-7-c3-15	76,25	14,12	6,06	1,61	1,27	0,00	0,05	99,36
F56-AA-7-c3-19	75,24	18,15	2,54	1,38	2,09	0,00	0,02	99,42
F56-AA-7-c3-21	75,70	15,61	4,46	1,56	1,49	0,00	0,05	98,87

Sample	As	Co	Ni	Fe	S	Bi	Sb	Total
F56-AA-7-c3-22	75,67	15,62	4,42	1,59	1,46	0,00	0,00	98,76
F56-AA-7-c3-24	75,77	17,12	3,37	1,42	2,00	0,00	0,00	99,68
F56-AA-7-c3-3	76,00	12,45	7,13	1,76	0,85	0,11	0,03	98,32
F56-AA-7-c3-7	76,75	12,23	7,28	1,74	0,82	0,00	0,00	98,82
F56-AA-7-c3-8	75,63	13,29	6,33	1,71	1,13	0,00	0,00	98,09
F56-AA-7-c3-9	76,72	12,89	6,84	1,81	0,93	0,00	0,00	99,19
F56-AA-7-c4-1	76,53	13,90	5,85	1,82	1,25	0,00	0,00	99,35
F56-AA-7-c4-2	76,66	13,72	6,22	1,72	1,18	0,00	0,01	99,51
F56-AA-7-c4-3	76,86	13,06	6,64	1,85	1,10	0,01	0,00	99,52
F56-AA-7-c4-4	76,71	13,16	6,48	1,77	1,19	0,18	0,10	99,59
F56-AA-7-c4-6	75,80	14,19	5,66	1,63	1,40	0,00	0,06	98,74
F56-AA-7-c5-1	75,32	15,49	1,87	3,76	1,68	0,00	0,05	98,17
F56-AA-7-c5-10	76,06	15,48	4,13	1,93	1,96	0,07	0,01	99,64
F56-AA-7-c5-11	75,88	15,34	4,32	1,87	1,78	0,00	0,07	99,26
F56-AA-7-c5-12	76,66	13,31	5,92	2,11	1,13	0,00	0,02	99,15
F56-AA-7-c5-13	77,31	12,95	6,53	2,24	1,11	0,00	0,01	100,15
F56-AA-7-c5-14	76,77	14,21	5,83	1,85	1,45	0,00	0,04	100,15
F56-AA-7-c5-15	76,73	14,27	5,71	1,84	1,52	0,00	0,03	100,10
F56-AA-7-c5-16	77,06	12,92	6,87	1,78	1,15	0,00	0,00	99,78
F56-AA-7-c5-18	77,17	13,47	6,38	1,88	1,31	0,00	0,01	100,22
F56-AA-7-c5-19	77,06	13,14	6,84	1,75	1,21	0,00	0,00	100,00
F56-AA-7-c5-2	75,56	14,81	3,07	3,15	1,55	0,00	0,00	98,14
F56-AA-7-c5-22	76,11	15,70	3,66	2,44	1,94	0,00	0,01	99,86
F56-AA-7-c5-23	76,82	13,26	5,66	2,49	1,32	0,00	0,00	99,55
F56-AA-7-c5-24	76,05	14,00	5,28	2,34	1,38	0,00	0,00	99,05
F56-AA-7-c5-25	76,69	13,79	5,57	2,23	1,40	0,00	0,02	99,70
F56-AA-7-c5-3	75,19	15,44	3,87	1,95	1,89	0,00	0,00	98,34
F56-AA-7-c5-4	75,74	14,85	4,82	1,76	1,66	0,00	0,03	98,86
F56-AA-7-c5-6	75,97	14,49	5,25	1,63	1,58	0,00	0,06	98,98
F56-AA-7-c5-7	77,06	11,66	7,25	2,14	0,88	0,00	0,00	98,99
F56-AA-7-c5-8	76,25	12,79	6,73	1,75	1,26	0,00	0,07	98,85
F56-AA-7-c5-9	75,81	16,32	2,98	2,38	2,08	0,00	0,00	99,57
F56-AA-8-c3-1	75,24	18,51	1,54	1,70	2,22	0,00	0,06	99,27
F56-AA-8-c3-23	74,85	19,24	0,72	1,63	2,46	0,00	0,00	98,90
F56-AA-8-c3-24	75,84	16,99	0,62	3,49	1,65	0,13	0,00	98,72
F56-AA-8-c3-25	76,17	16,71	3,08	1,68	1,78	0,00	0,06	99,48
F56-AA-8-c3-26	76,43	16,31	2,69	2,14	1,52	0,00	0,00	99,09
F56-AA-8-c3-27	76,14	16,63	2,61	2,09	1,70	0,00	0,05	99,22
F56-AA-8-c3-28	76,68	14,77	3,68	2,85	1,13	0,00	0,01	99,12
F56-AA-8-c3-29	76,28	15,05	3,72	2,44	1,36	0,00	0,10	98,95
F56-AA-8-c3-8	74,92	18,87	1,04	2,09	2,17	0,00	0,04	99,13
Lo								
F56-AA-8-c2-8	70,73	1,20	0,88	25,78	0,61	0,00	0,00	99,20
F56-AA-8-c2-5	69,25	1,73	0,53	25,98	1,80	0,00	0,01	99,30
F56-AA-8-c1-25	68,16	0,18	0,03	28,58	2,49	0,00	0,02	99,46
F56-AA-8-c1-26	68,68	0,13	0,02	28,49	2,24	0,00	0,00	99,55
F56-AA-8-c1-4	67,59	0,70	0,01	28,21	3,04	0,00	0,01	99,56
F56-AA-8-c1-35	70,92	0,07	0,00	27,86	0,61	0,00	0,09	99,56
F56-AA-8-c1-53	67,72	0,05	0,01	28,59	3,08	0,00	0,12	99,57

Sample	As	Co	Ni	Fe	S	Bi	Sb	Total
F56-AA-8-c1-18	67,89	0,44	0,00	28,27	2,92	0,00	0,07	99,58
F56-AA-8-c1-1	67,52	0,47	0,00	28,46	3,15	0,00	0,02	99,62
F56-AA-8-c1-29	70,67	0,14	0,00	27,94	0,91	0,00	0,00	99,65
F56-AA-8-c1-32	67,31	0,09	0,02	28,95	3,29	0,00	0,00	99,66
F56-AA-8-c1-7	67,52	0,19	0,00	28,94	3,02	0,00	0,00	99,67
F56-AA-8-c1-34	70,64	0,11	0,03	27,99	0,84	0,00	0,07	99,69
F56-AA-8-c1-8	68,33	0,07	0,00	28,68	2,60	0,00	0,04	99,72
F56-AA-8-c1-37	70,81	0,17	0,00	27,91	0,83	0,00	0,01	99,73
F56-AA-8-c1-44	68,09	0,15	0,02	28,51	2,97	0,00	0,01	99,75
F56-AA-8-c1-20	67,94	0,27	0,00	28,57	2,99	0,00	0,00	99,77
F56-AA-8-c1-13	68,29	0,23	0,00	28,57	2,60	0,00	0,08	99,78
F56-AA-8-c1-28	71,39	0,06	0,00	27,96	0,39	0,00	0,00	99,81
F56-AA-8-c1-14	69,53	0,38	0,00	28,10	1,81	0,00	0,00	99,82
F56-AA-8-c1-36	70,59	0,08	0,00	28,13	1,02	0,00	0,00	99,82
F56-AA-8-c1-50	71,17	0,15	0,00	27,91	0,59	0,00	0,01	99,83
F56-AA-8-c1-3	71,51	0,41	0,01	27,47	0,41	0,00	0,04	99,85
F56-AA-8-c1-40	71,13	0,12	0,00	27,98	0,63	0,00	0,00	99,86
F56-AA-8-c1-33	70,99	0,11	0,00	28,04	0,60	0,10	0,02	99,86
F56-AA-8-c1-30	70,66	0,08	0,00	28,18	0,93	0,00	0,03	99,87
F56-AA-8-c1-52	69,66	0,06	0,01	28,37	1,71	0,00	0,07	99,88
F56-AA-8-c1-41	70,66	0,05	0,02	28,10	1,03	0,00	0,03	99,90
F56-AA-8-c1-9	70,99	0,15	0,01	27,81	0,91	0,03	0,00	99,90
F56-AA-8-c1-16	68,45	0,15	0,00	28,64	2,60	0,00	0,08	99,92
F56-AA-8-c1-42	70,69	0,05	0,02	28,12	1,04	0,00	0,00	99,92
F56-AA-8-c1-49	71,15	0,18	0,01	28,03	0,53	0,00	0,05	99,94
F56-AA-8-c1-5	71,20	0,52	0,02	27,70	0,48	0,00	0,03	99,94
F56-AA-8-c1-31	67,75	0,10	0,01	29,05	3,05	0,00	0,00	99,97
F56-AA-8-c1-6	71,44	0,06	0,01	27,97	0,48	0,00	0,04	100,00
F56-AA-8-c1-38	70,95	0,15	0,00	27,95	0,80	0,04	0,14	100,02
F56-AA-8-c1-46	71,42	0,10	0,01	27,91	0,56	0,00	0,04	100,04
F56-AA-8-c1-15	68,31	0,41	0,00	28,45	2,79	0,00	0,08	100,04
F56-AA-8-c1-17	68,61	0,34	0,00	28,57	2,50	0,00	0,03	100,05
F56-AA-8-c1-21	71,42	0,35	0,01	27,86	0,42	0,00	0,02	100,07
F56-AA-8-c1-2	71,11	0,18	0,00	28,14	0,61	0,00	0,03	100,08
F56-AA-8-c1-51	68,57	0,07	0,03	28,73	2,70	0,00	0,00	100,09
F56-AA-8-c1-27	70,93	0,07	0,01	28,17	0,79	0,06	0,09	100,10
F56-AA-8-c1-23	71,32	0,08	0,00	28,04	0,67	0,00	0,03	100,14
F56-AA-8-c1-19	68,74	0,32	0,01	28,67	2,40	0,00	0,00	100,14
F56-AA-8-c1-12	71,38	0,09	0,00	28,03	0,51	0,05	0,09	100,14
F56-AA-8-c1-47	69,12	0,09	0,00	28,65	2,25	0,00	0,04	100,15
F56-AA-8-c1-43	68,28	0,11	0,03	29,02	2,72	0,00	0,00	100,16
F56-AA-8-c1-22	71,60	0,14	0,00	28,04	0,39	0,00	0,04	100,22
F56-AA-8-c1-24	71,15	0,11	0,00	28,16	0,70	0,10	0,03	100,26
F56-AA-8-c1-39	71,23	0,09	0,00	28,25	0,61	0,00	0,08	100,26
F56-AA-8-c1-48	71,53	0,16	0,00	28,09	0,51	0,00	0,02	100,30
F56-AA-8-c1-10	71,55	0,07	0,00	28,13	0,49	0,12	0,00	100,36
F56-AA-8-c1-11	67,81	0,18	0,00	29,21	3,26	0,00	0,04	100,50

Sample	As	Co	Ni	Fe	S	Bi	Sb	Total
Sf-Lo								
F56-AA-8-c1-14	70,52	12,97	0,35	15,14	0,43	0,00	0,00	99,41
F56-AA-7-c6-4	70,83	13,27	0,60	14,38	0,41	0,00	0,04	99,54
F56-AA-8-c1-19	69,63	14,68	0,39	13,68	0,96	0,00	0,00	99,34
F56-AA-8-c1-11	70,79	18,19	0,45	9,90	0,26	0,00	0,00	99,59
F56-AA-8-c3-15	70,18	20,62	1,20	6,98	0,54	0,01	0,06	99,59
F56-AA-8-c1-9	70,02	20,90	0,26	7,43	0,73	0,00	0,00	99,35
F56-AA-8-c1-10	70,13	22,04	0,62	6,07	0,53	0,00	0,00	99,40
F56-AA-8-c2-20	69,43	22,92	0,53	5,36	0,74	0,00	0,00	98,99
F56-AA-8-c2-6	69,21	23,00	3,24	2,53	0,92	0,00	0,11	99,01
F56-AA-8-c2-12	68,29	23,47	1,83	3,90	1,68	0,00	0,03	99,20
F56-AA-8-c2-5	68,17	24,38	2,00	2,85	1,74	0,00	0,01	99,15
F56-AA-8-c3-17	69,14	24,39	2,34	2,47	1,38	0,00	0,01	99,73
F56-AA-8-C2-60	68,65	22,09	1,22	5,12	1,33	0,00	0,00	98,41
F56-AA-8-C2-27	70,07	12,44	0,82	14,90	1,20	0,00	0,10	99,53
F56-AA-8-C2-57	67,28	22,09	0,54	6,07	2,43	0,00	0,04	98,46
F56-AA-8-C2-28	68,48	17,61	0,37	10,43	1,86	0,00	0,00	98,75
F56-AA-8-C2-58	70,56	11,34	0,29	16,43	0,53	0,00	0,04	99,19
Rm-Lo								
F56-AA-8-C2-2	68,62	0,85	4,83	22,65	2,06	0,00	0,00	99,01
F56-AA-8-C2-1	69,21	2,31	4,14	21,86	1,58	0,00	0,00	99,10
F56-AA-8-C2-3	69,66	1,69	4,01	22,40	1,36	0,00	0,00	99,12
F56-AA-8-C2-18	69,94	1,53	3,81	22,43	1,13	0,00	0,04	98,88
F56-AA-8-C2-13	69,35	0,84	2,19	24,72	1,41	0,00	0,00	98,51

Appendix B: chemical composition of chromite

		SiO_2	TiO_2	V_2O_3	Al_2O_3	Cr_2O_3	FeO	Fe_2O_3	MnO	MgO	CoO	NiO	ZnO	Total	Mg#	Cr#	Fe3+#
Talc -rich serpentinite																	
Associated to talc																	
AA-3-28	R	0,06	0,12	0,25	3,72	34,89	23,67	31,45	0,94	4,75	0,11	0,21	0,38	100,6	0,26	0,86	0,43
AA-3-21	R	0,74	0,08	0,26	4,09	38,66	23,49	27,13	1,00	4,91	0,12	0,09	0,37	100,9	0,27	0,86	0,37
AA-3-1-2	R	1,82	0,10	0,24	3,22	35,65	22,92	29,72	0,93	4,79	0,13	0,14	0,28	100,0	0,27	0,88	0,41
AA-3-1-7	R	0,10	0,15	0,27	2,84	33,90	23,85	32,27	1,10	4,05	0,11	0,18	0,70	99,5	0,23	0,89	0,45
AA-3-4-13	R	0,16	0,10	0,32	3,10	32,98	24,60	32,77	0,68	3,95	0,14	0,36	0,23	99,4	0,22	0,88	0,45
AA-3-4-9	R	0,14	0,10	0,34	2,93	31,72	24,97	33,74	0,70	3,55	0,15	0,37	0,29	99,0	0,20	0,88	0,47
AA-3-1-5	C	0,03	0,01	0,16	15,25	43,09	22,36	11,44	0,60	7,18	0,14	0,13	0,47	100,8	0,36	0,65	0,14
AA-3-1-6	C	0,03	0,02	0,13	14,55	42,91	22,29	12,32	0,67	7,07	0,13	0,11	0,50	100,7	0,36	0,66	0,15
AA-3-25	C	0,03	0,03	0,15	14,43	42,62	22,50	12,83	0,66	7,00	0,15	0,11	0,46	100,9	0,36	0,66	0,16
AA-3-1-14	C	0,04	0,03	0,14	14,49	42,84	22,56	12,61	0,63	6,98	0,13	0,14	0,48	101,1	0,36	0,66	0,16
AA-3-24	C	0,04	0,04	0,15	13,94	42,65	22,79	13,27	0,65	6,76	0,16	0,11	0,47	101,0	0,35	0,67	0,17
AA-3-1-4	C	0,04	0,04	0,15	13,71	42,52	22,84	13,55	0,64	6,69	0,16	0,12	0,46	100,9	0,34	0,68	0,17
AA-3-23	C	0,04	0,07	0,20	11,30	41,63	23,35	16,52	0,75	5,99	0,14	0,15	0,40	100,5	0,31	0,71	0,21
AA-3-1-12	C	0,03	0,07	0,21	11,08	41,97	23,46	16,44	0,79	5,88	0,13	0,14	0,43	100,6	0,31	0,72	0,21
AA-3-26	C	0,24	0,06	0,17	10,87	42,59	23,40	16,31	0,73	5,98	0,14	0,14	0,40	101,0	0,31	0,72	0,21
AA-3-1-17	C	0,26	0,07	0,22	7,09	44,74	24,19	17,96	0,67	5,10	0,15	0,20	0,32	101,0	0,27	0,81	0,24
AA-3-4-11	C	0,27	0,02	0,17	8,07	49,00	22,44	13,23	0,66	6,37	0,14	0,06	0,42	100,8	0,34	0,80	0,17
AA-3-4-4	C	0,04	0,03	0,10	7,89	49,73	22,52	12,09	0,81	6,06	0,13	0,06	0,41	99,9	0,32	0,81	0,16
Carbonated serpentinite																	
Associated to serpentinite																	
AA-6-3-2	R	0,08	0,09	0,32	3,89	35,98	24,39	29,57	0,58	4,38	0,15	0,42	0,21	100,1	0,24	0,86	0,40
AA-6-3-1	R	0,07	0,08	0,34	3,79	36,16	24,09	29,12	0,60	4,44	0,14	0,42	0,22	99,5	0,25	0,86	0,40
AA-6-3-3	R	0,07	0,07	0,28	4,10	37,22	24,23	28,09	0,56	4,51	0,13	0,38	0,24	99,9	0,25	0,86	0,38
AA-6-3-6	R	0,07	0,08	0,32	3,83	37,51	23,86	28,20	0,84	4,51	0,14	0,41	0,35	100,1	0,25	0,87	0,38
AA-6-3-4	R	0,06	0,08	0,33	4,00	37,30	23,71	28,02	0,61	4,78	0,15	0,38	0,22	99,6	0,26	0,86	0,38
AA-6-3-9	R	0,05	0,09	0,30	3,85	37,30	23,75	28,31	0,53	4,79	0,15	0,38	0,23	99,7	0,26	0,87	0,39
AA-6-4-6	R	0,04	0,14	0,26	11,44	36,53	21,65	21,74	0,57	7,21	0,14	0,26	0,18	100,2	0,37	0,68	0,28
AA-6-4-16	R	0,04	0,14	0,23	10,98	41,41	21,76	17,78	0,52	7,29	0,13	0,22	0,19	100,7	0,37	0,72	0,23
AA-6-4-15	R	0,03	0,16	0,28	12,55	36,59	21,35	21,00	0,52	7,71	0,10	0,29	0,16	100,7	0,39	0,66	0,27
AA-6-4-14	R	0,04	0,09	0,21	10,83	43,97	21,01	15,55	0,60	7,70	0,12	0,14	0,20	100,5	0,40	0,73	0,20
AA-6-4-4	R	0,03	0,08	0,16	11,21	45,35	21,12	13,98	0,54	7,77	0,12	0,15	0,19	100,7	0,40	0,73	0,18
AA-6-4-5	R	0,04	0,05	0,17	12,47	46,09	21,16	11,81	0,52	7,90	0,12	0,12	0,19	100,6	0,40	0,71	0,15
AA-6-4-3	R	0,07	0,07	0,17	12,16	46,21	20,91	12,22	0,50	8,04	0,11	0,12	0,25	100,8	0,41	0,72	0,15
AA-6-4-8	R	0,03	0,12	0,25	11,80	39,57	20,51	18,68	0,55	8,02	0,14	0,23	0,19	100,1	0,41	0,69	0,24
AA-6-4-13	R	0,04	0,07	0,18	12,33	45,98	20,63	12,20	0,53	8,21	0,12	0,13	0,23	100,6	0,41	0,71	0,15
AA-6-4-1	R	0,74	0,07	0,17	12,07	44,48	19,83	13,27	0,53	8,41	0,14	0,11	0,23	100,1	0,43	0,71	0,17
AA-6-7-3	R	0,04	0,09	0,22	9,21	42,48	22,83	18,07	0,58	6,22	0,14	0,27	0,20	100,4	0,33	0,76	0,23
AA-6-7-6	R	0,03	0,08	0,19	9,49	41,48	22,85	18,92	0,59	6,25	0,15	0,25	0,20	100,5	0,33	0,75	0,24
AA-6-7-5	R	0,04	0,08	0,21	9,88	40,74	22,80	19,18	0,61	6,30	0,13	0,27	0,21	100,4	0,33	0,73	0,25
AA-6-7-2	R	0,29	0,07	0,21	8,87	43,29	22,46	17,83	0,64	6,43	0,13	0,21	0,21	100,6	0,34	0,77	0,23
AA-6-7-1	R	1,09	0,08	0,20	8,90	41,29	21,58	18,97	0,57	6,70	0,13	0,28	0,22	100,0	0,36	0,76	0,25
AA-6-7-10	R	0,03	0,05	0,16	10,16	44,68	22,09	15,42	0,52	6,93	0,14	0,22	0,19	100,6	0,36	0,75	0,20
AA-6-8-14	R	0,28	0,09	0,20	11,49	35,93	21,94	21,92	0,63	6,66	0,13	0,43	0,34	100,0	0,35	0,68	0,28
AA-6-8-8	R	0,04	0,05	0,15	9,76	45,76	22,25	14,69	0,50	6,77	0,13	0,21	0,24	100,5	0,35	0,76	0,19
AA-6-8-24	R	0,04	0,03	0,14	10,59	45,94	22,07	13,83	0,52	6,98	0,13	0,20	0,26	100,7	0,36	0,74	0,18
AA-6-8-23	R	0,05	0,05	0,17	12,03	40,43	22,09	17,52	0,47	6,99	0,15	0,35	0,28	100,6	0,36	0,69	0,22
AA-6-8-15	R	0,03	0,04	0,18	10,14	44,88	21,60	15,05	0,52	7,13	0,12	0,22	0,25	100,2	0,37	0,75	0,19

Appendix B: chemical composition of chromite

		SiO_2	TiO_2	V_2O_3	Al_2O_3	Cr_2O_3	FeO	Fe_2O_3	MnO	MgO	CoO	NiO	ZnO	Total	Mg#	Cr#	Fe3+#
AA-6-8-10	R	0,04	0,04	0,16	10,89	44,11	21,66	15,18	0,52	7,22	0,11	0,24	0,23	100,4	0,37	0,73	0,19
AA-6-8-20	R	0,03	0,04	0,14	11,45	43,61	21,77	15,31	0,47	7,28	0,13	0,24	0,23	100,7	0,37	0,72	0,19
AA-6-8-10	R	0,19	0,07	0,17	12,11	37,52	21,48	20,59	0,49	7,37	0,13	0,38	0,27	100,8	0,38	0,68	0,26
AA-6-8-11	R	0,06	0,07	0,17	13,18	36,93	21,43	19,89	0,47	7,49	0,13	0,42	0,24	100,5	0,38	0,65	0,29
AA-6-8-17	R	0,04	0,06	0,20	12,39	39,77	21,35	17,97	0,53	7,52	0,13	0,34	0,22	100,5	0,39	0,68	0,23
AA-6-8-13	R	0,04	0,03	0,11	11,49	46,34	21,31	12,69	0,49	7,60	0,12	0,18	0,27	100,7	0,39	0,73	0,16
AA-6-8-1	R	0,03	0,04	0,13	11,27	45,61	21,04	12,89	0,49	7,54	0,13	0,15	0,28	99,6	0,39	0,73	0,16
AA-6-8-22	R	0,03	0,03	0,14	11,70	46,04	21,26	12,59	0,50	7,64	0,10	0,19	0,24	100,5	0,39	0,73	0,16
AA-6-8-11	R	0,03	0,04	0,15	12,02	45,34	21,34	13,32	0,52	7,73	0,11	0,16	0,24	101,0	0,39	0,72	0,17
AA-6-8-28	R	0,04	0,05	0,12	14,74	46,38	20,90	9,39	0,48	8,33	0,12	0,11	0,33	101,0	0,42	0,68	0,12
AA-6-8-16	R	0,04	0,06	0,17	10,24	44,88	21,98	15,57	0,50	7,11	0,11	0,25	0,23	101,1	0,37	0,75	0,20
AA-6-3-5	C	0,05	0,08	0,31	4,05	37,84	23,79	27,81	0,63	4,83	0,13	0,38	0,22	100,1	0,27	0,86	0,38
AA-6-3-11	C	0,05	0,08	0,28	4,08	39,07	23,52	26,50	0,59	5,02	0,12	0,35	0,20	99,9	0,28	0,87	0,36
AA-6-3-8	C	0,07	0,08	0,27	4,18	40,13	23,50	25,44	0,56	5,09	0,13	0,32	0,23	100,0	0,28	0,87	0,34
AA-6-3-10	C	0,05	0,07	0,26	4,41	40,76	23,22	24,47	0,61	5,23	0,15	0,29	0,21	99,7	0,29	0,86	0,33
AA-6-4-10	C	0,04	0,15	0,22	13,58	37,44	20,70	18,55	0,48	8,08	0,11	0,23	0,22	99,8	0,41	0,65	0,23
AA-6-4-11	C	0,03	0,06	0,19	14,21	46,70	19,67	9,56	0,50	9,05	0,14	0,08	0,22	100,4	0,45	0,69	0,12
AA-6-4-2	C	0,04	0,08	0,15	12,16	46,33	20,98	12,05	0,50	8,01	0,12	0,14	0,21	100,8	0,40	0,72	0,15
AA-6-4-9	C	0,04	0,13	0,22	13,99	37,53	20,28	18,72	0,48	8,51	0,13	0,24	0,21	100,5	0,43	0,64	0,23
AA-6-4-12	C	0,03	0,06	0,19	14,37	46,84	19,72	9,35	0,48	9,07	0,11	0,08	0,24	100,5	0,45	0,69	0,12
AA-6-4-2	C	0,03	0,06	0,19	15,58	47,73	19,65	7,31	0,51	9,31	0,12	0,07	0,23	100,8	0,46	0,67	0,09
AA-6-4-2	C	0,03	0,06	0,21	16,39	47,77	19,29	6,23	0,45	9,58	0,14	0,07	0,26	100,5	0,47	0,66	0,08
AA-6-7-8	C	0,03	0,06	0,20	11,76	43,11	22,23	15,16	0,57	6,99	0,13	0,23	0,22	100,7	0,36	0,71	0,19
AA-6-7-8	C	0,04	0,04	0,18	11,05	44,26	22,11	14,69	0,56	6,96	0,14	0,19	0,20	100,4	0,36	0,73	0,19
AA6-7-12	C	0,03	0,05	0,17	11,09	43,59	21,77	15,39	0,52	7,19	0,12	0,23	0,18	100,3	0,37	0,73	0,20
AA-6-7-15	C	0,10	0,08	0,22	12,80	38,64	21,85	18,49	0,53	7,28	0,14	0,30	0,21	100,7	0,37	0,67	0,23
AA-6-7-11	C	0,22	0,05	0,15	10,48	43,77	21,49	15,60	0,52	7,17	0,11	0,23	0,25	100,1	0,37	0,74	0,20
AA-6-7-13	C	0,03	0,05	0,15	10,89	45,24	21,68	14,58	0,53	7,38	0,12	0,19	0,22	101,0	0,38	0,74	0,18
AA-6-7-14	C	0,06	0,07	0,23	12,48	39,84	21,66	17,74	0,51	7,39	0,11	0,30	0,25	100,6	0,38	0,68	0,22
AA-6-8-12	C	0,08	0,06	0,18	13,43	37,20	21,77	18,93	0,62	7,07	0,12	0,41	0,40	100,3	0,37	0,65	0,24
AA-6-8-5	C	0,03	0,03	0,14	11,89	46,54	21,50	11,85	0,49	7,49	0,14	0,18	0,29	100,6	0,38	0,72	0,15
AA-6-8-7	C	0,04	0,03	0,12	11,81	46,57	21,45	12,17	0,49	7,57	0,14	0,19	0,29	100,9	0,39	0,73	0,15
AA-6-8-25	C	0,03	0,04	0,15	13,06	46,69	21,05	10,54	0,47	7,96	0,14	0,15	0,27	100,6	0,40	0,71	0,13
AA-6-8-26	C	0,06	0,06	0,18	15,41	47,84	20,47	7,29	0,45	8,76	0,11	0,13	0,32	101,1	0,43	0,68	0,09
AA-6-8-26	C	0,03	0,07	0,20	15,44	47,35	20,28	7,44	0,45	8,80	0,12	0,10	0,34	100,6	0,44	0,67	0,09
AA-6-8-21	C	0,03	0,08	0,21	16,01	48,00	20,10	5,91	0,44	8,94	0,13	0,11	0,31	100,3	0,44	0,67	0,07
AA-6-8-18	C	0,03	0,07	0,17	15,82	47,90	20,06	6,40	0,46	8,96	0,11	0,09	0,33	100,4	0,44	0,67	0,08
AA-6-8-27	C	0,11	0,08	0,21	16,44	47,51	20,14	5,99	0,44	9,00	0,09	0,08	0,34	100,4	0,44	0,66	0,07
AA-6-8-4	C	0,04	0,07	0,22	16,23	48,41	19,87	5,07	0,48	9,04	0,10	0,10	0,33	100,0	0,45	0,67	0,06
AA-6-8-2	C	0,03	0,07	0,18	16,15	47,93	19,72	5,64	0,46	9,10	0,13	0,09	0,32	99,8	0,45	0,67	0,07
AA-6-8-3	C	0,03	0,07	0,21	16,82	48,53	19,74	4,32	0,47	9,18	0,13	0,07	0,34	99,9	0,45	0,66	0,05
Associated to calcite																	
AA-6-10-1	R	0,51	0,06	0,20	8,00	45,70	23,14	15,44	0,65	5,68	0,15	0,19	0,28	100,0	0,30	0,79	0,20
AA-6-10-5	R	1,28	0,07	0,19	7,69	45,18	21,88	16,69	0,65	6,45	0,16	0,19	0,27	100,7	0,34	0,80	0,22
AA-6-10-6	R	1,19	0,04	0,14	8,05	46,45	21,64	15,33	0,64	6,71	0,14	0,12	0,26	100,7	0,36	0,79	0,20
AA-6-11-1	R	0,04	0,06	0,18	14,51	47,24	21,90	8,03	0,58	7,48	0,14	0,10	0,47	100,7	0,38	0,69	0,10
AA-6-11-5	R	0,14	0,09	0,31	7,02	36,13	24,18	25,83	0,95	4,65	0,15	0,25	0,35	100,0	0,26	0,78	0,35
AA-6-11-5	R	0,16	0,10	0,28	7,06	36,31	24,30	25,89	0,96	4,64	0,14	0,27	0,35	100,5	0,25	0,78	0,34
AA-6-11-7	R	0,05	0,08	0,25	6,79	41,07	24,06	21,89	0,64	5,13	0,15	0,24	0,24	100,6	0,28	0,80	0,29
AA-6-11-10	R	0,04	0,08	0,21	10,58	45,22	22,87	14,18	0,61	6,43	0,14	0,14	0,39	100,9	0,33	0,74	0,18
AA-6-11-11	R	0,87	0,08	0,17	8,31	45,06	22,53	16,31	0,69	6,19	0,14	0,13	0,33	100,8	0,33	0,78	0,21

Appendix B: chemical composition of chromite

		SiO_2	TiO_2	V_2O_3	Al_2O_3	Cr_2O_3	FeO	Fe_2O_3	MnO	MgO	CoO	NiO	ZnO	Total	Mg#	Cr#	Fe3+#
AA-6-10-3	C	0,77	0,08	0,23	6,17	46,55	22,81	16,86	0,67	5,79	0,14	0,16	0,24	100,5	0,31	0,84	0,22
AA-6-10-2	C	1,07	0,09	0,21	6,36	45,22	22,19	18,29	0,64	6,21	0,13	0,20	0,26	100,9	0,33	0,83	0,24
AA-6-10-7	C	0,28	0,05	0,19	8,44	44,57	22,32	16,58	0,60	6,38	0,12	0,14	0,24	99,9	0,34	0,78	0,22
AA-6-11-2	C	0,04	0,06	0,21	15,20	47,87	21,45	6,81	0,52	7,94	0,13	0,06	0,44	100,7	0,40	0,68	0,08
AA-6-11-3	C	0,03	0,07	0,23	15,98	48,06	21,01	6,00	0,52	8,39	0,13	0,06	0,42	100,9	0,42	0,67	0,07
AA-6-11-4	C	0,04	0,06	0,23	15,92	48,24	20,88	5,93	0,50	8,45	0,10	0,06	0,47	100,9	0,42	0,67	0,07
AA-6-11-6	C	0,04	0,06	0,20	14,54	47,72	20,99	7,83	0,56	8,13	0,14	0,08	0,42	100,7	0,41	0,69	0,10
AA-6-11-8	C	0,05	0,06	0,21	11,32	45,37	22,23	13,27	0,57	6,90	0,15	0,15	0,37	100,6	0,36	0,73	0,17
Disseminated ores																	
Associated to calcite																	
AA-8-6-3	R	0,04	0,00	0,22	0,18	18,24	28,93	50,82	0,93	0,79	0,18	0,30	0,11	100,7	0,05	0,99	0,72
AA-8-6-9	R	0,07	0,02	0,24	0,15	18,72	28,47	50,57	0,77	1,23	0,16	0,30	0,11	100,8	0,07	0,99	0,72
AA-8-6-21	R	0,05	0,01	0,21	0,09	15,15	28,46	53,79	0,83	1,06	0,15	0,29	0,06	100,2	0,06	0,99	0,77
AA-8-6-5	R	0,06	0,00	0,18	0,11	20,80	28,84	48,04	1,54	0,44	0,15	0,27	0,14	100,6	0,03	0,99	0,69
AA-8-6-15	R	0,04	0,01	0,21	0,10	19,97	28,81	48,42	1,21	0,54	0,17	0,27	0,13	99,9	0,03	0,99	0,70
AA-8-6-18	R	0,05	0,02	0,22	0,13	14,98	28,37	54,67	0,69	1,37	0,14	0,35	0,05	101,0	0,08	0,99	0,77
AA-8-6-20	R	0,05	0,01	0,21	0,11	14,24	28,14	55,32	0,67	1,46	0,14	0,33	0,06	100,7	0,08	0,99	0,79
AA-8-6-17	R	0,04	0,00	0,25	0,10	14,89	28,74	54,50	0,72	1,08	0,14	0,32	0,06	100,8	0,06	0,99	0,78
AA-8-6-14	R	0,04	0,01	0,23	0,09	16,62	29,45	52,44	1,05	0,39	0,15	0,34	0,11	100,9	0,02	0,99	0,75
AA-8-6-12	R	0,05	0,01	0,20	0,09	16,23	29,57	52,91	0,88	0,43	0,14	0,33	0,08	100,9	0,03	0,99	0,75
AA-8-3-4	R	0,06	0,01	0,19	0,56	22,77	26,20	46,21	0,96	2,47	0,15	0,29	0,19	100,1	0,14	0,96	0,65
AA-8-3-5	R	0,05	0,01	0,16	0,39	20,66	26,22	48,47	0,68	2,56	0,13	0,33	0,13	99,8	0,15	0,97	0,68
AA-8-3-15	R	0,05	0,01	0,18	0,25	20,91	25,97	48,62	0,76	2,73	0,13	0,29	0,14	100,0	0,16	0,98	0,69
AA-8-3-12	R	0,09	0,01	0,18	0,21	21,62	25,59	48,00	0,91	2,86	0,13	0,26	0,22	100,1	0,17	0,99	0,68
AA-8-3-7	R	0,05	0,02	0,16	0,13	20,22	25,71	49,82	0,71	2,98	0,14	0,26	0,13	100,3	0,17	0,99	0,70
AA-8-3-6	R	0,05	0,00	0,15	0,11	19,34	25,60	50,90	0,67	3,09	0,13	0,26	0,14	100,4	0,18	0,99	0,71
AA-8-3-9	R	0,04	0,01	0,18	0,13	19,80	25,59	50,45	0,70	3,12	0,14	0,26	0,11	100,5	0,18	0,99	0,71
AA-8-3-13	R	0,05	0,01	0,15	0,23	24,30	24,90	45,44	0,90	3,34	0,16	0,21	0,17	99,9	0,19	0,99	0,64
AA-8-4-10	R	0,31	0,01	0,22	0,80	31,82	23,76	37,24	1,06	4,03	0,12	0,24	0,27	99,9	0,23	0,96	0,52
AA-8-4-9	R	0,04	0,01	0,20	0,69	31,01	24,39	38,45	0,96	3,77	0,15	0,22	0,25	100,2	0,22	0,97	0,53
AA-8-4-4	R	0,03	0,01	0,27	0,35	24,55	25,47	45,18	0,75	3,20	0,15	0,27	0,14	100,4	0,18	0,98	0,63
AA-8-4-12	R	0,05	0,01	0,26	0,32	23,73	25,44	45,54	0,80	3,02	0,13	0,29	0,21	99,8	0,17	0,98	0,64
AA-8-4-15	R	0,10	0,03	0,29	0,31	21,83	26,33	47,19	0,88	2,41	0,14	0,33	0,17	100,0	0,14	0,98	0,67
AA-8-6-7	C	0,04	0,01	0,21	0,26	24,13	27,86	45,14	1,12	1,46	0,15	0,29	0,13	100,8	0,09	0,98	0,64
AA-8-6-7	C	0,04	0,01	0,21	0,26	24,13	27,86	45,14	1,12	1,46	0,15	0,29	0,13	100,8	0,09	0,98	0,64
AA-8-6-2	C	0,05	0,02	0,23	0,38	25,90	27,83	43,20	1,16	1,50	0,16	0,25	0,16	100,8	0,09	0,98	0,61
AA-8-6-6	C	0,06	0,00	0,03	4,59	55,96	22,49	10,09	1,16	5,57	0,11	0,04	0,58	100,7	0,31	0,89	0,13
AA-8-6-4	C	0,05	0,01	0,19	0,64	33,48	25,63	36,13	1,09	3,08	0,15	0,17	0,24	100,9	0,18	0,97	0,50
AA-8-6-6	C	0,04	0,01	0,03	5,96	47,62	22,79	16,65	1,07	5,46	0,13	0,09	0,50	100,4	0,30	0,84	0,22
AA-8-6-1	C	0,08	0,00	0,02	4,47	54,92	23,10	11,08	1,07	5,23	0,14	0,03	0,51	100,6	0,29	0,89	0,15
AA-8-6-8	C	0,05	0,00	0,02	5,02	53,16	22,59	12,25	1,08	5,49	0,16	0,06	0,58	100,5	0,30	0,88	0,16
AA-8-4-5	C	0,03	0,01	0,22	0,28	23,01	25,99	46,97	0,73	2,90	0,14	0,29	0,15	100,7	0,17	0,98	0,66
AA-8-4-4	C	0,03	0,01	0,25	0,47	27,26	25,15	42,43	0,80	3,42	0,14	0,24	0,18	100,4	0,19	0,97	0,59
AA-8-4-1	C	0,03	0,01	0,16	3,07	39,46	23,20	28,00	1,07	4,88	0,15	0,15	0,35	100,5	0,27	0,90	0,38
AA-8-4-3	C	0,07	0,00	0,06	4,76	54,63	21,53	10,55	1,18	5,97	0,12	0,01	0,58	99,5	0,33	0,88	0,14
AA-8-4-8	C	0,03	0,00	0,20	1,59	37,06	23,54	31,77	1,08	4,43	0,17	0,17	0,33	100,4	0,25	0,94	0,43
Associated to loellingite																	
AA-8-10-10	R	0,06	0,01	0,09	0,03	9,17	24,25	62,30	0,56	2,03	0,17	0,73	0,05	99,4	0,12	1,00	0,86
AA-8-10-3	R	0,05	0,01	0,10	0,03	8,84	23,95	62,46	0,33	2,60	0,14	0,73	0,07	99,3	0,15	0,99	0,87

Appendix B: chemical composition of chromite

		SiO_2	TiO_2	V_2O_3	Al_2O_3	Cr_2O_3	FeO	Fe_2O_3	MnO	MgO	CoO	NiO	ZnO	Total	Mg#	Cr#	Fe3+#
AA-8-10-8	R	0,08	0,00	0,10	0,03	9,45	23,89	62,59	0,29	2,65	0,15	0,74	0,06	100,0	0,15	0,99	0,86
AA-8-10-4	R	0,07	0,01	0,10	0,04	8,80	23,83	62,19	0,28	2,84	0,19	0,74	0,09	99,2	0,17	0,99	0,87
AA-8-10-5	C	0,08	0,01	0,11	0,02	9,28	22,69	63,95	0,29	2,90	0,21	0,70	0,00	100,2	0,17	1,00	0,86
AA-8-10-7	C	0,06	0,00	0,07	0,03	9,65	23,43	63,14	0,31	2,90	0,18	0,77	0,06	100,6	0,17	1,00	0,86
AA-8-10-6	C	0,06	0,01	0,09	0,03	9,57	23,31	63,34	0,29	2,91	0,19	0,75	0,05	100,6	0,17	1,00	0,86
AA-8-10-2	C	0,06	0,00	0,08	0,03	9,22	23,31	62,94	0,28	2,92	0,17	0,75	0,05	99,8	0,17	1,00	0,86
AA-8-10-1	C	0,06	0,01	0,08	0,03	9,42	22,74	63,87	0,30	2,95	0,19	0,74	0,02	100,4	0,17	0,99	0,86
Massive ores																	
Associated to calcite																	
AA-18-5-1	R	0,16	0,04	0,28	3,95	19,95	25,22	41,45	1,22	1,97	0,14	0,78	0,42	95,6	0,12	0,77	0,60
AA-18-5-2	R	0,20	0,03	0,29	4,22	20,08	24,93	41,03	1,30	2,15	0,13	0,69	0,47	95,5	0,13	0,76	0,60
AA-18-5-4	R	0,09	0,03	0,21	4,13	18,72	25,88	44,69	0,64	2,53	0,14	0,83	0,18	98,1	0,15	0,75	0,63
AA-18-5-5	R	0,30	0,03	0,21	3,76	17,35	24,44	45,55	1,99	2,30	0,17	0,78	0,16	97,0	0,14	0,76	0,65
AA-18-5-11	R	0,17	0,04	0,27	3,73	18,70	24,04	43,39	2,52	1,98	0,16	0,81	0,32	96,1	0,13	0,77	0,63
AA-18-5-17	R	0,12	0,04	0,28	5,08	23,02	25,36	38,86	1,13	2,57	0,13	0,71	0,47	97,7	0,15	0,75	0,55
AA-18-5-25	R	0,12	0,03	0,24	3,75	20,16	26,18	43,57	1,07	2,02	0,15	0,77	0,36	98,4	0,12	0,78	0,62
AA-18-5-12	C	0,12	0,03	0,27	3,57	18,14	25,47	46,75	1,45	2,47	0,16	0,87	0,15	99,5	0,15	0,77	0,65
AA-18-5-20	C	0,22	0,04	0,25	3,61	19,23	26,45	45,29	0,93	2,13	0,14	0,80	0,28	99,4	0,13	0,78	0,64
AA-18-5-26	C	0,22	0,04	0,26	3,99	22,08	26,32	41,94	0,98	2,17	0,14	0,79	0,41	99,3	0,13	0,79	0,59
AA-18-5-27	C	0,07	0,03	0,21	4,53	20,24	24,68	44,21	1,65	3,12	0,15	0,75	0,14	99,8	0,18	0,75	0,61
AA-18-5-28	C	0,11	0,03	0,24	3,66	18,81	26,14	46,27	0,53	2,68	0,18	0,83	0,18	99,7	0,15	0,77	0,64
AA-18-5-29	C	0,07	0,03	0,22	4,90	20,91	24,94	44,17	0,62	3,87	0,15	0,79	0,12	100,8	0,22	0,74	0,60
AA-18-5-30	C	0,15	0,04	0,26	4,35	20,24	25,85	44,33	0,67	2,85	0,17	0,77	0,45	100,1	0,16	0,76	0,61
Associated to loellingite																	
AA-18-1-24	R	0,15	0,05	0,28	1,56	22,78	26,96	41,87	1,93	0,62	0,14	0,58	0,42	97,3	0,04	0,91	0,61
AA-18-1-21	R	0,17	0,06	0,29	1,70	21,53	26,14	42,79	2,48	0,73	0,15	0,53	0,48	97,0	0,05	0,89	0,63
AA-18-1-7	R	0,06	0,04	0,25	1,61	19,95	26,53	46,78	3,25	0,74	0,13	0,57	0,14	100,0	0,05	0,89	0,67
AA-18-1-20	R	0,12	0,05	0,24	1,71	21,60	27,30	43,99	1,88	0,77	0,12	0,57	0,33	98,7	0,05	0,89	0,63
AA-18-1-5	R	0,11	0,05	0,25	1,58	20,51	25,44	44,92	3,17	0,98	0,14	0,58	0,30	98,0	0,06	0,90	0,65
AA-18-1-11	R	0,08	0,04	0,24	1,61	19,84	25,92	46,54	3,08	1,07	0,12	0,58	0,17	99,3	0,07	0,89	0,67
AA-18-1-8	R	0,08	0,04	0,21	1,45	19,11	25,22	46,43	3,22	1,08	0,13	0,58	0,14	97,7	0,07	0,90	0,68
AA-18-1-25	R	0,11	0,05	0,25	1,57	21,54	26,42	44,55	1,51	1,57	0,13	0,59	0,25	98,5	0,10	0,90	0,64
AA-18-1-2	R	0,22	0,06	0,30	1,58	21,82	26,65	42,80	2,26	0,59	0,11	0,53	0,57	97,5	0,04	0,90	0,63
AA-18-1-1	R	0,10	0,05	0,26	1,60	21,65	26,77	43,77	2,25	0,80	0,13	0,56	0,28	98,2	0,05	0,90	0,63
AA-18-1-4	R	0,16	0,05	0,27	1,57	21,67	25,41	43,07	3,08	0,90	0,12	0,57	0,32	97,2	0,06	0,90	0,63
AA-18-1-10	R	0,08	0,05	0,25	1,52	20,10	26,48	46,73	1,13	1,94	0,12	0,57	0,20	99,2	0,12	0,90	0,67
AA-18-1-66	R	0,09	0,04	0,25	1,46	19,05	26,28	46,04	3,39	0,24	0,13	0,47	0,40	97,8	0,02	0,90	0,67
AA-18-1-63	R	0,13	0,04	0,30	1,42	22,99	25,94	41,62	3,25	0,44	0,14	0,56	0,30	97,1	0,03	0,92	0,61
AA-18-1-44	R	0,11	0,05	0,30	1,49	20,50	26,97	44,65	2,15	0,60	0,13	0,55	0,40	97,9	0,04	0,90	0,65
AA-18-1-45	R	0,12	0,05	0,27	1,62	20,76	25,70	44,02	3,37	0,58	0,15	0,62	0,27	97,5	0,04	0,90	0,64
AA-18-1-68	R	0,06	0,03	0,25	1,58	19,56	25,97	46,74	3,72	0,68	0,14	0,56	0,10	99,4	0,04	0,89	0,67
AA-18-1-65	R	0,09	0,05	0,24	1,36	21,06	27,15	44,69	1,27	1,15	0,15	0,59	0,18	98,0	0,07	0,91	0,65
AA-18-1-62	R	0,09	0,04	0,25	1,50	22,37	26,13	43,26	2,44	1,11	0,12	0,53	0,24	98,1	0,07	0,91	0,63
AA-18-3-5	R	0,08	0,03	0,17	1,32	20,07	24,57	45,38	3,73	0,85	0,68	0,40	0,18	97,5	0,06	0,91	0,66
AA-18-1-12	C	0,07	0,05	0,25	1,63	20,64	26,37	45,61	3,03	0,83	0,12	0,57	0,20	99,4	0,05	0,89	0,65
AA-18-1-9	C	0,07	0,05	0,26	1,42	19,10	25,96	47,71	2,71	1,30	0,16	0,56	0,13	99,4	0,08	0,90	0,68
AA-18-1-17	C	0,08	0,04	0,29	1,74	22,02	27,25	44,95	1,19	1,60	0,13	0,57	0,28	100,1	0,09	0,89	0,63
AA-18-1-27	C	0,10	0,04	0,26	1,76	23,04	26,84	43,42	0,95	1,86	0,15	0,55	0,25	99,2	0,11	0,90	0,62

Appendix B: chemical composition of chromite

	SiO_2	TiO_2	V_2O_3	Al_2O_3	Cr_2O_3	FeO	Fe_2O_3	MnO	MgO	CoO	NiO	ZnO	Total	Mg#	Cr#	Fe3+#
AA-18-1-40 C	0,08	0,04	0,28	1,41	18,77	25,84	48,15	1,80	1,90	0,12	0,64	0,13	99,2	0,12	0,90	0,69
AA-18-1-37 C	0,07	0,05	0,27	1,91	22,27	26,86	44,41	0,79	2,09	0,15	0,55	0,17	99,6	0,12	0,89	0,63
AA-18-1-14 C	0,15	0,06	0,24	1,91	22,50	26,11	44,30	0,82	2,49	0,14	0,57	0,22	99,5	0,15	0,89	0,62
AA-18-1-35 C	0,05	0,04	0,23	1,83	22,27	26,05	44,67	0,68	2,60	0,15	0,55	0,21	99,3	0,15	0,89	0,63
AA-18-1-34 C	0,06	0,03	0,26	1,77	22,01	26,07	45,22	0,55	2,74	0,16	0,59	0,11	99,6	0,16	0,89	0,64
AA-18-1-26 C	0,06	0,04	0,24	1,63	21,41	26,14	46,69	0,54	2,86	0,15	0,57	0,11	100,5	0,16	0,90	0,65
AA-18-1-13 C	0,07	0,05	0,26	1,79	21,11	25,59	46,83	1,13	2,86	0,14	0,58	0,15	100,6	0,17	0,89	0,65
AA-18-1-39 C	0,08	0,03	0,24	1,53	20,60	25,55	46,79	0,60	2,86	0,16	0,61	0,21	99,3	0,17	0,90	0,66
AA-18-1-38 C	0,05	0,04	0,25	1,61	20,18	25,39	47,38	0,72	2,99	0,17	0,64	0,11	99,5	0,17	0,89	0,67
AA-18-1-28 C	0,05	0,04	0,25	1,84	22,47	26,04	45,58	0,42	3,11	0,14	0,57	0,08	100,6	0,18	0,89	0,63
AA-18-1-16 C	0,06	0,04	0,27	1,77	21,20	25,87	47,06	0,42	3,19	0,16	0,57	0,11	100,7	0,18	0,89	0,65
AA-18-1-29 C	0,07	0,04	0,23	1,94	22,93	25,62	44,74	0,44	3,22	0,15	0,58	0,14	100,1	0,18	0,89	0,62
AA-18-1-31 C	0,05	0,04	0,30	1,87	22,21	25,65	45,87	0,38	3,37	0,14	0,59	0,09	100,6	0,19	0,89	0,64
AA-18-1-30 C	0,06	0,04	0,22	1,91	22,63	25,52	45,40	0,39	3,40	0,17	0,58	0,07	100,4	0,19	0,89	0,63
AA-18-1-36 C	0,06	0,03	0,26	2,04	23,10	25,36	44,73	0,47	3,46	0,15	0,58	0,12	100,4	0,20	0,88	0,62
AA-18-1-52 C	0,07	0,05	0,27	1,58	20,27	26,38	46,21	2,56	1,14	0,13	0,60	0,17	99,4	0,07	0,90	0,66
AA-18-1-64 C	0,06	0,04	0,22	1,36	21,22	26,44	45,70	1,65	1,68	0,11	0,56	0,13	99,2	0,10	0,91	0,65
AA-18-1-51 C	0,06	0,04	0,22	1,52	19,65	25,06	47,75	3,07	1,76	0,13	0,63	0,10	100,0	0,11	0,90	0,67
AA-18-1-58 C	0,05	0,04	0,25	1,50	19,54	25,12	47,95	1,77	2,54	0,11	0,60	0,07	99,5	0,15	0,90	0,68
AA-18-1-47 C	0,06	0,03	0,25	1,53	19,85	25,42	48,49	0,44	3,32	0,17	0,62	0,05	100,2	0,19	0,90	0,68
AA-18-1-54 C	0,05	0,04	0,28	1,70	20,02	24,59	48,28	0,71	3,70	0,14	0,63	0,12	100,2	0,21	0,89	0,67
AA-18-3-3 C	0,19	0,04	0,19	1,49	18,06	25,98	48,71	1,80	1,67	0,31	0,49	0,24	99,16	0,10	0,89	0,70
AA-18-1-55 C	0,06	0,03	0,26	1,49	19,74	26,20	48,11	0,46	2,73	0,14	0,61	0,10	99,93	0,16	0,90	0,68